TRANSPORTATION RESEARCH

RECORD

No. 1319

Highway and Facility Design;
Bridges, Other Structures, and
Hydraulics and Hydrology

Bridge and Hydrology Research 1991

A peer-reviewed publication of the Transportation Research Board

TRANSPORTATION RESEARCH BOARD
NATIONAL RESEARCH COUNCIL
WASHINGTON, D.C. 1991

Transportation Research Record 1319
Price: $26.00

Subscriber Categories
IIA highway and facility design
IIC bridges, other structures, and hydraulics and hydrology

TRB Publications Staff
Director of Publications: Nancy A. Ackerman
Senior Editor: Naomi C. Kassabian
Associate Editor: Alison G. Tobias
Assistant Editors: Luanne Crayton, Norman Solomon
Graphics Coordinator: Diane L. Ross
Production Coordinator: Karen S. Waugh
Office Manager: Phyllis D. Barber
Production Assistant: Betty L. Hawkins

Printed in the United States of America

Library of Congress Cataloging-in-Publication Data
National Research Council. Transportation Research Board.

Bridge and hydrology research, 1991.
p. cm.—(Transportation research record, ISSN 0361-1981 ; no. 1319)
Research papers from the 70th annual meeting of the Transportation Research Board held in Washington, D.C., in 1991.
ISBN 0-309-05157-6
1. Bridges—Design and construction. 2. Scour at bridges. I. National Research Council (U.S.). Transportation Research Board. Meeting (70th : 1991 : Washington, D.C.) II. Series: Transportation research record ; 1319.
TE7.H5 no. 1319
[TG300]
388 s—dc20
[624'.2] 92-9337
CIP

Sponsorship of Transportation Research Record 1319

GROUP 2—DESIGN AND CONSTRUCTION OF TRANSPORTATION FACILITIES
Chairman: Raymond A. Forsyth, Sacramento, California

General Design Section
Chairman: Jarvis D. Michie, Dynatech Engineering Inc.

Committee on Hydrology, Hydraulics, and Water Quality
Chairman: J. Sterling Jones, Federal Highway Administration, U.S. Department of Transportation
Secretary: Lawrence J. Harrison, Federal Highway Administration, U.S. Department of Transportation
Dennis Athayde, Charles W. Boning, Stanley R. Davis, David J. Flavell, Thomas L. Hart, John Owen Hurd, S. Bennett P. John, Kenneth D. Kerri, M. Dean Knighton, Floyd J. Lawmann, Norman Miller, Johnny L. Morris, Jerome M. Normann, Glenn A Pickering, Don L. Potter, Jean Reichert, Everett V. Richardson, H. Earl Shaver, Corwin L.Tracey, E. L. Walker, Jr., Ken Young, Michael E. Zeller

Structures Section
Chairman: Robert C. Cassano, Imbsen & Associates Inc.

Committee on General Structures
Chairman: John J. Ahlskog, Federal Highway Administration, U. S. Department of Transportation
Dan S. Bechly, Neal H. Bettigole, Amar Bhajandas, Charles H. Bryant, Edwin G. Burdette, Martin P. Burke, Jr., Paul F. Csagoly, Donald J. Flemming, Theodore V. Galambos, Frederick Gottemoeller, Richard P. Knight, Andrew Lally, Clellon Lewis Loveall, Dennis R. Mertz, Roy L. Mion, Andrzej S. Nowak, Richard V. Nutt, Andrew E. N. Osborn, William J. Rogers, Arunprakash M. Shirole, Michael S. Stenko, Stanley W. Woods

Committee on Steel Bridges
Chairman: Charles W. Roeder, University of Washington
John J. Ahlskog, David R. Anderson, Charles J. Arnold, Alfred G. Bishara, William G. Byers, William F. Crozier, Donald J. Flemming, Dan M. Frangopol, Geerhard Haaijer, Ray W. James, Theodore H. Karaspoulos, Michael J. Koob, Andrew Lally, Albert D. M. Lewis, Ayaz H. Malik, Richard A. Parmelee, Charles G. Schmidt, Charles Seim, Robert A. P. Sweeney, John A. Van Lund, Ivan M. Viest, Gerald M. White, Stanley W. Woods

Committee on Concrete Bridges
Chairman: Wayne Henneberger, Figg & Muller Engineers Inc.
J. C. Beauchamp, Robert N. Bruce, Jr., George A. Christian, John H. Clark, Anthony Ralph Cusens, C. Stewart Gloyd, H. Henrie Henson, James J. Hill, Roy A. Imbsen, John M. Kulicki, Charles M. Minervino, Mrutyunjaya Pani, Richard A. Parmelee, Philip C. Perdikaris, Walter Podolny, Jr., Henry G. Russell, Alex C. Scordelis, S. Srinivasan, John F. Stanton, Holger S. Svensson, Robert A. P. Sweeney, Man-Chung Tang, Julius F. J. Volgyi, Jr., Allan H. Walley

Construction Section
Chairman: Charles T. Edson, New Jersey Department of Transportation

Committee on Construction of Bridges and Structures
Chairman: Robert M. Barnoff, R. M. Barnoff & Associates Inc.
Ernest V. Acree, Jr., Ostap Bender, Neal H. Bettigole, D. Stephen Brown, Bruce M. Douglas, Jackson L. Durkee, Allan C. Harwood, James R. Hoblitzell, Ramankutty Kannankutty, Jai B. Kim, Thomas P. McCarthy, William T. Peckham, Charles H. Quandel, John P. Rutter, Charles V. Slavis, Michael S. Stenko, Francis E. Ward, James R. Wilder, Kenneth C. Wilson, Luis Ybanez

Frank R. McCullagh and Frederick D. Hejl, Transportation Research Board staff

Sponsorship is indicated by a footnote at the end of each paper. The organizational units, officers, and members are as of December 31, 1990.

Transportation Research Record 1319

Contents

Foreword

Hirsch et al. present a new steel-pipe bridge rail that is aesthetically pleasing and meets crash test criteria presented in *NCHRP Report 230: Recommended Procedures for the Safety Performance Evaluation of Highway Appurtenances*. Kim and Kim discuss the design analysis and testing of an A-frame timber bridge that meets the AASHTO standard specification for Highway Bridge requirements at a low cost. McLean et al. investigated the behavior of column specimens incorporating different moment-reducing hinge details, and they propose recommendations for the comprehensive design of moment-reducing hinge details at the bases of bridge columns. Stokes presents a unique approach to bridge inspection, rock climbing technology, that has proven safe and effective.

Weissmann and Harrison examine the impact on the rural interstate bridge system of double 48-ft trailers and triple 28-ft trailers. They predict greater bridge damage and extremely high user costs on key rural structures. Schelling et al. present the results of a study of the structural evaluation of the failure of the Harrison Bridge over the Great Miami River. James et al. studied the problem of cracking and dislocation of backwalls of reinforced concrete abutments. Vorster et al. discuss the development of a model for determining the optimum rehabilitation cycle for concrete bridge decks.

Marx et al. discuss the development of an analysis procedure for skem slab and girder bridges. Avent et al. summarize the results of a study of heat straightening repair for damaged steel bridge girders and recommend factors to be considered when contemplating a heat straightening repair. Van Lund describes lifting a steel bridge superstructure in Washington state to increase vertical clearance, to remove and replace defective bridge bearings, and to transfer the superstructure from one bridge substructure to another; and present case histories along with recommendations. Kaspar and Rowings present a variety of constructability concepts for cable-stayed bridges.

Helm uses cost comparisons of an actual construction project to compare AASHTO Type IV and Type IV Modified beams to bulb-tee beams. Dagher et al. developed design charts for skew angle bridges that relate the moments, shears, and deflections in a skew bridge to those in a 1-ft-wide plane frame taken along the longitudinal center line of the skew bridge.

Hurd uses experiences to demonstrate some of the misapplication of hydrologic regional regression equations and provides some information that clarifies the application of the equations. Tasker illustrates a method that allows a network manager to design a nearly optimal stream flow data network for collecting regional information. Santoro et al. experimentally investigated local scour around a model of the Schoharie bridge pier. Johnson and McCuen formulated and calibrated a time-dependent pier scour model with laboratory data and observations and with field observations. This model enables the engineer to estimate the scour depth at any time during the life of the bridge.

Aesthetically Pleasing Steel Pipe Bridge Rail

T. J. HIRSCH, C. E. BUTH, AND DARRELL KADERKA

Research has developed railings to withstand impact loads from vehicles of ever-increasing size; however, aesthetic considerations have been overshadowed by safety and structural requirements. The objective of this research study was to develop aesthetically pleasing, structurally sound railings that can serve as alternative railings in city or urban areas. A new steel pipe bridge rail—Texas Type T421—is introduced. This bridge rail is constructed of 5-in.-diameter steel pipe posts with a 5-in.-diameter steel pipe top rail 32 in. high and a 10-in.-diameter steel pipe lower rail. The bridge rail was crash-tested and evaluated in accordance with NCHRP Report 230. Two crash tests were required—a 4,500-lb passenger car at 60 mph and 25-degree impact angle and an 1,800-lb passenger car at 60 mph and 20-degree impact angle. In both tests, the bridge rail contained and redirected the test vehicle. There were no detached elements or debris to present undue hazard to other traffic. The vehicle remained upright and relatively stable during the collision. The occupant-compartment impact velocities and 10-msec occupant ridedown accelerations were within the normally accepted limits. The vehicle trajectory at loss of contact (exit angles of 5 and 7.6 degrees) indicated no intrusion into adjacent traffic lanes.

Research has developed railing to withstand impact loads from vehicles of ever-increasing size; however, aesthetic considerations have been overshadowed by safety and structural requirements. Engineers often fail to recognize the impact of their structures on the landscape, particularly in city or urban areas. Architects and developers often propose aesthetically pleasing railings that engineers cannot accept because of structural inadequacies. The objective of this research study was to develop aesthetically pleasing, structurally sound railings that can serve as alternative railings.

This study is developing one or more new concrete, steel, and aluminum railings or combination railings, some with curb and sidewalk.

A new steel pipe bridge rail—Texas Type T421—is introduced. The research study advisory committee reviewed design sketches of 22 different bridge rail designs before selecting the new Texas Type T421 as its second priority. The advisory committee was composed of two architects (private consultants from Dallas), two research engineers from Texas Transportation Institute, two highway design engineers from Dallas District, one bridge design engineer from Dallas District, and three bridge design engineers from Austin headquarters.

Texas Transportation Institute, Texas A&M University, College Station, Tex. 77843-3135.

DESCRIPTION OF TEXAS TYPE T421 BRIDGE RAIL

This bridge rail is constructed of standard steel pipe 5 or 10 in. in diameter. Figure 1 shows photographs of the steel pipe bridge rail installed on a typical simulated 8-in.-thick concrete bridge deck. Figures 2 and 3a show a cross section and side elevation, respectively, of the T421 bridge rail. The top rail was 32 in. high and used 5-in.-diameter standard steel pipe. The lower rail uses 10-in.-diameter standard steel pipe. The 5-in.-diameter posts are sloping at a 10-degree angle so that the traffic side or face of the two rails is a vertical plane.

The standard steel pipe was of ASTM A53, Type E, Grade B, with a yield strength of 35 kg/in.^{2} and minimum ductility of 15 percent in a 2-in. gauge length. The concrete reinforcing steel was ASTM A615, Grade 60. Concrete cylinders taken from the simulated concrete deck yielded a compressive strength of 3,370 psi at 28 days of age (design f'_c was 3,600 psi).

The anchor bolts were ASTM A-321 threaded rods with tack-welded nuts for heads and with hex nuts and washers. Nuts and washers for anchor bolts were of A-325 requirements. Nuts were tapped or chased after galvanizing. Bolts and nuts had Class 2A and 2B fit tolerances. Details of the base plate are shown in Figure 3b. All other steel was ASTM A36.

This pipe rail was originally designed using steel tubing with a wall thickness of 0.25 in. and a yield strength of 42 kg/in.^{2} with a ductility of 23 percent in a 2-in. gauge length (ASTM A500, Grade B). Plastic analysis of this design yielded a strength of 66 kips at an effective height of 17.5 in. When the rail was fabricated, standard steel pipe was used because it was readily available. Either material should perform satisfactorily.

In the original design, ten 7.5-ft-long bridge rail segments were to be installed for a total length of 75 ft. The fabricator chose to fabricate and install five 15-ft-long segments for a total length of 75 ft, as shown in Figure 4. Figure 3c shows the pipe splice details.

CRASH TESTS

In order to qualify this bridge rail for use on federal-aid highways, it was crash-tested and evaluated in accordance with NCHRP Report 230 (*1*). Two crash tests were required—Test Designation S13 with an 1,800-lb passenger car at 60 mph and 20-degree impact angle and Test Designation 10 with a 4,500-lb passenger car at 60 mph and 25-degree impact angle.

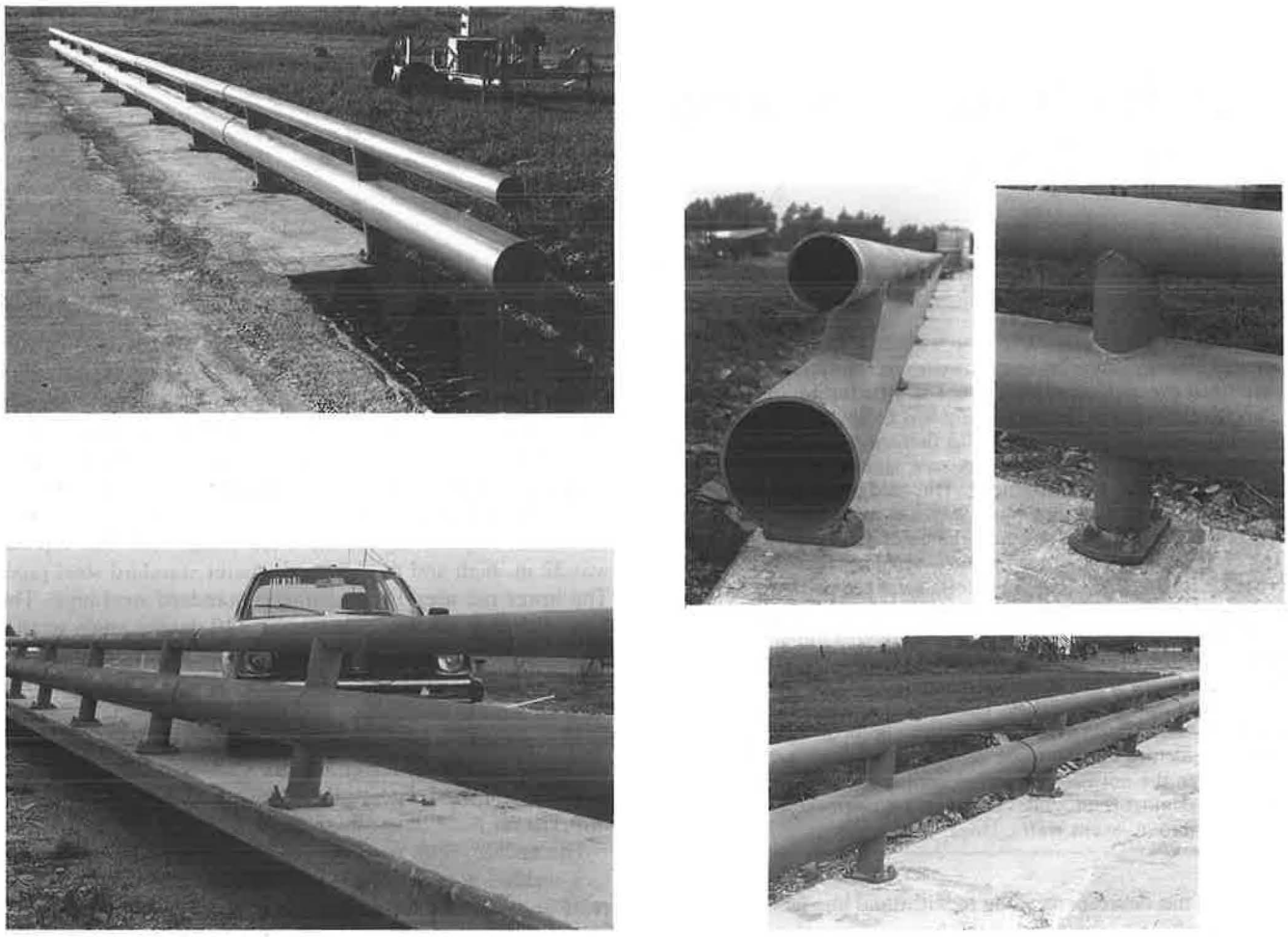

FIGURE 1 T421 bridge rail installation.

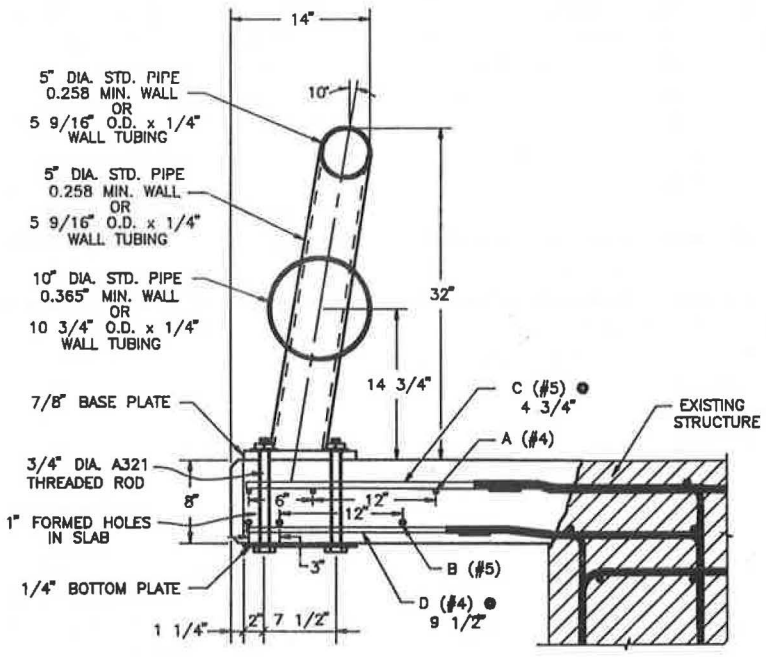

FIGURE 2 Cross-section of T421 bridge rail.

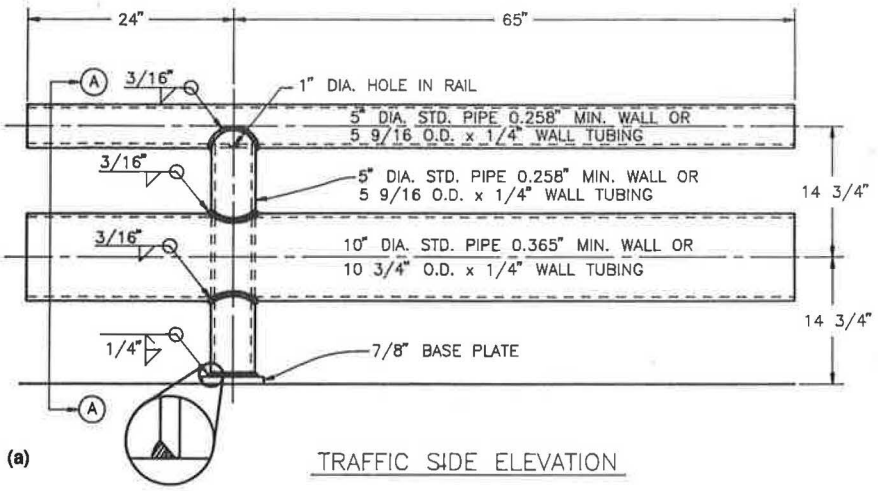

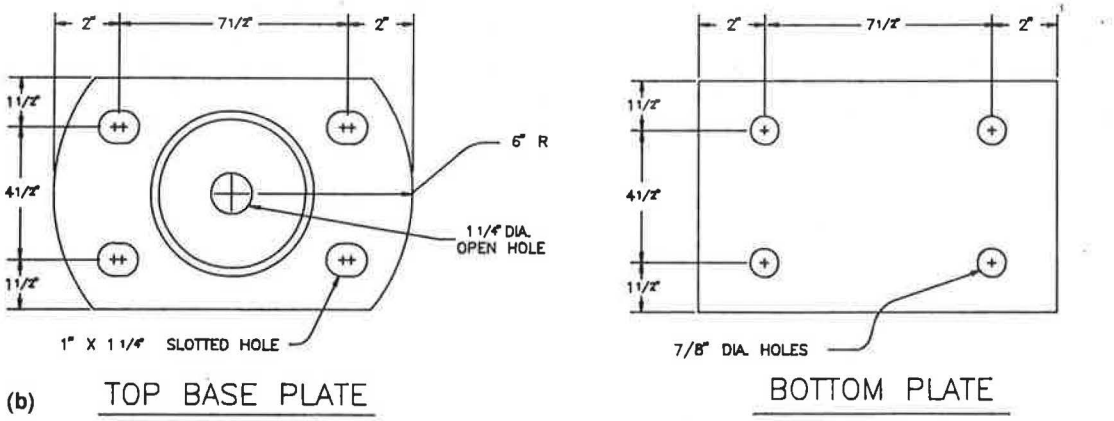

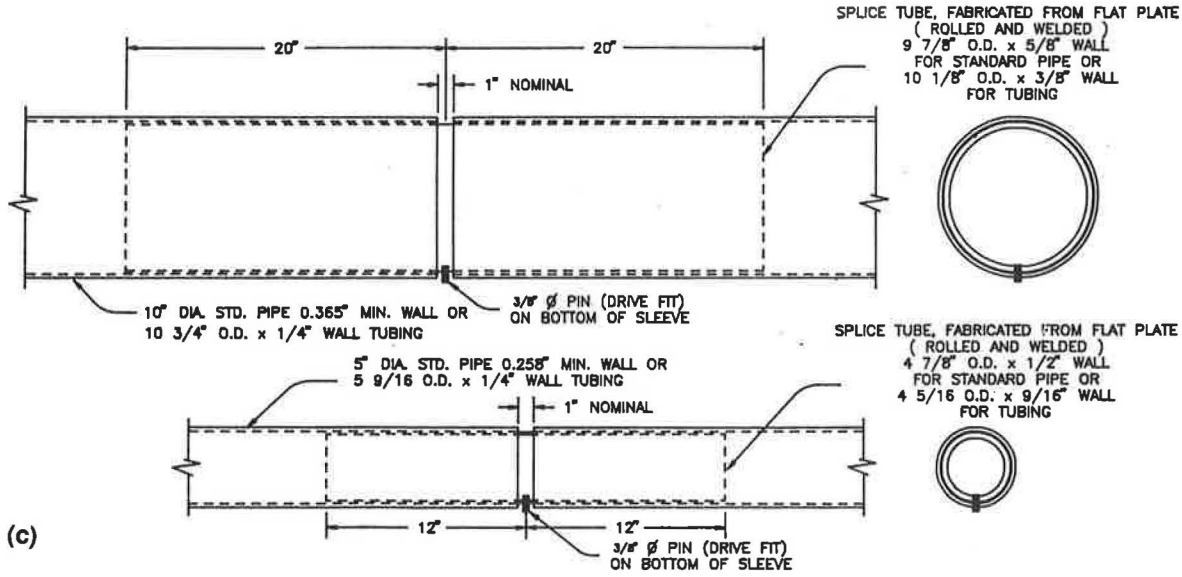

FIGURE 3 T421 bridge rail: (a) elevation of 7.5-ft-long segment, (b) base plate details, and (c) splice details.

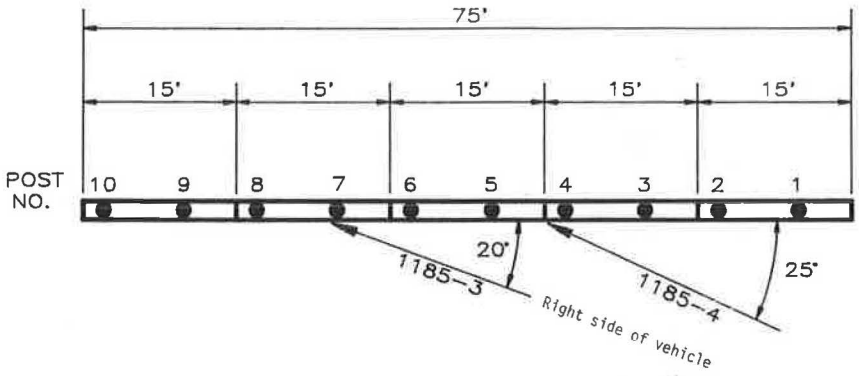

FIGURE 4 Plan view of T421 bridge rail installation and vehicle impact points.

The 1980 Honda Civic (Figure 1) was directed into the T421 bridge rail using a reverse tow and guidance system. Test inertia mass of the vehicle was 1,800 lb (808 kg). The height to the lower edge of the vehicle bumper was 15.0 in. (36.1 cm) and it was 20.0 in. (50.8 cm) to the top of the bumper. Other dimensions and information on the test vehicle are given in Figure 5. The vehicle was free wheeling and unrestrained just before impact.

The speed of the vehicle at impact was 59.7 mph (96.1 km/hr); the angle of impact was 21.4 degrees. The right front bumper of the vehicle impacted the bridge rail 5 ft (1.5 m) upstream of Post 7. The right front wheel made contact with the lower pipe member shortly after impact. The vehicle began to redirect at 0.042 sec. By 0.060 sec, the vehicle had deformed to the A-pillar, which caused the windshield to break. The right front wheel became wedged under the lower pipe member and impacted the lower part of Post 7. At 0.162 sec, the vehicle was traveling parallel with the bridge rail at a speed of 49.7 mph (79.2 km/hr). The vehicle exited the rail at 0.237 sec traveling at 49.2 mph (79.2 km/hr) and 5.0 de-

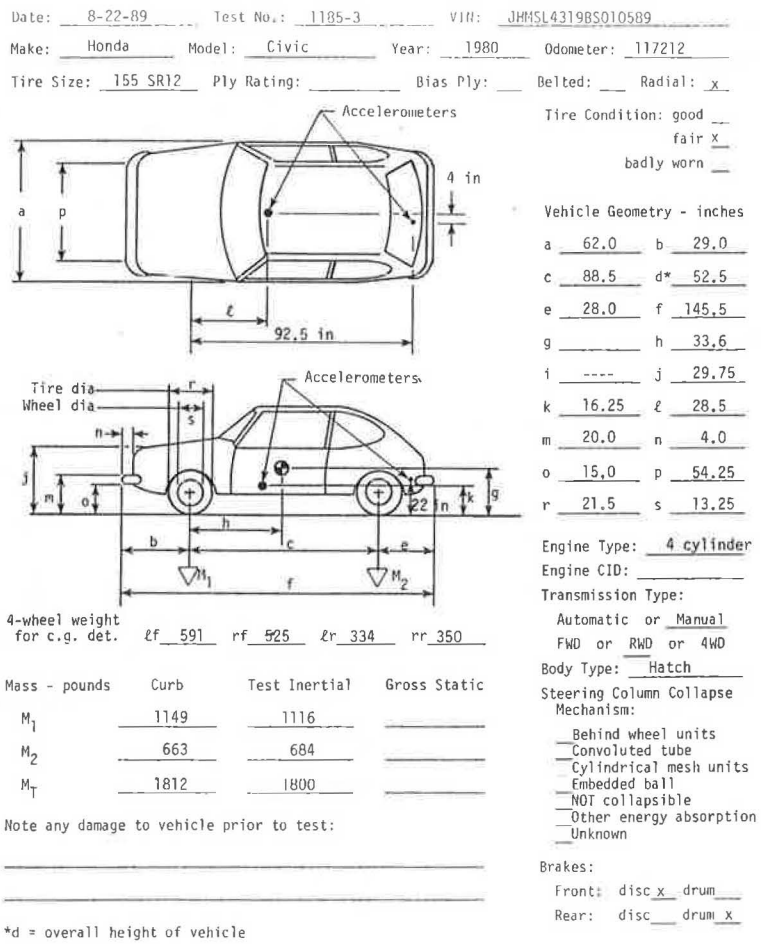

FIGURE 5 Vehicle properties (Test 1185–3).

grees. As the vehicle left the test site, the brakes were applied. The vehicle yawed clockwise almost 180 degrees and subsequently came to rest 270 ft (82 m) from the point of impact.

As can be seen in Figure 6, the rail received minimal cosmetic damage. Tire marks appeared 3 in. (7.6 cm) behind the traffic edge of the baseplate of Post 7 before impacting the lower part of the post and riding over the baseplate. The vehicle was in contact with the rail for 9.25 ft (2.8 m).

The vehicle sustained severe damage to the right side, as shown in Figure 7. Maximum crush at the right front bumper heights was 10.0 in. (25.4 cm). The constant velocity joint and right strut were damaged. The right front rim was bent and the tire damaged. The roof was bent and the windshield was broken. There was damage to the hood, grill, bumper, right front quarter-panel, the right door and glass, the right rear quarter-panel, and the rear bumper.

Impact speed was 59.7 mph (96.1 km/hr) and the angle of impact was 21.4 degrees. The vehicle was traveling 49.7 mph (80.0 km/hr) as it became parallel at 0.162 sec. The vehicle exited the rail at 0.237 sec traveling at 49.2 mph (79.2 km/hr) and 5.0 degrees. Occupant impact velocity was 21.8 ft/sec (6.6 m/sec) in the longitudinal direction and 24.5 ft/sec (7.5 m/sec) in the lateral direction. The highest 0.010-sec occupant ridedown accelerations were −3.9 g (longitudinal) and −6.3 g (lateral). These data and other pertinent information from the test are summarized in Figure 8 and Table 1.

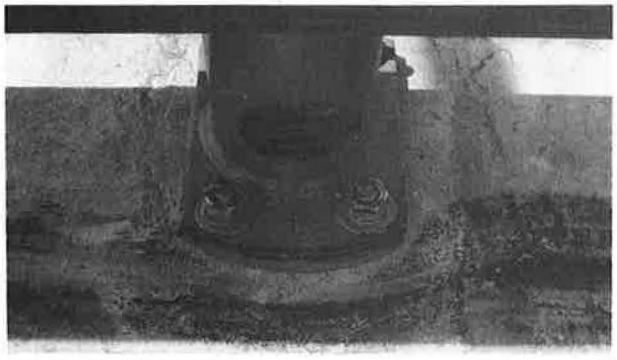

FIGURE 6 T421 bridge rail after Honda impact.

FIGURE 7 Honda before and after impact with T421 bridge rail.

These data were further analyzed to obtain 0.050-sec average accelerations versus time. The maximum 0.050-sec average accelerations at the center of gravity were −8.4 g (longitudinal) and 12.7 g (lateral).

CONCLUSIONS

The T421 bridge rail contained and redirected the test vehicle with no lateral movement of the bridge rail. There were no detached elements or debris to present undue hazard to other traffic. The vehicle remained upright and relatively stable during the collision. The longitudinal occupant-compartment impact velocity and 10-msec occupant ridedown accelerations were within the limits recommended in NCHRP Report 230. The vehicle trajectory at loss of contact was 5 degrees, which was less than the recommended limit of 60 percent of the impact angle (12.8 degrees for this test).

The 1982 Oldsmobile 98 (Figure 9) was directed into the T421 bridge rail using a reverse tow and guidance system. Test inertia mass of the vehicle was 4,500 lb (2,043 kg). The

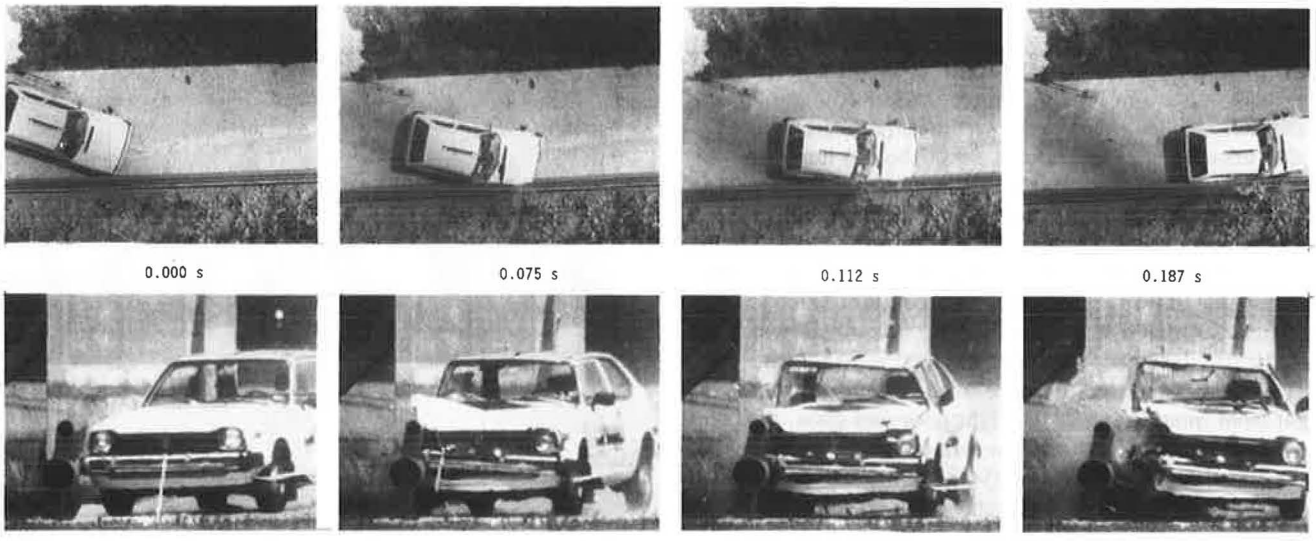

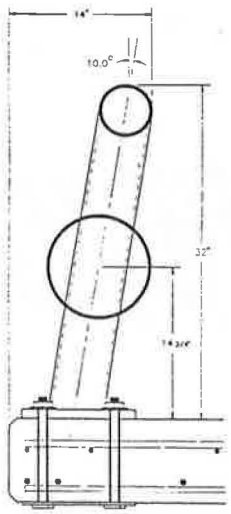

Test No. 1185-3
Date 08/22/89

Test Installation . . . T421 Bridge Rail
Length of Installation . 75 ft (23 m)

Vehicle . . . . . 1980 Honda Civic
Vehicle Weight
  Test Inertia . . . . . 1,800 lb (817 kg)
Vehicle Damage Classification
  TAD . . . . . 01FR6 & 01RD6
  CDC . . . . . 01FZEK4 & 01RDES4
Maximum Vehicle Crush . 10.0 in (25.4 cm)

Impact Speed . . . 59.7 mi/h (96.1 km/h)
Impact Angle . . . 21.4 degrees
Speed at Parallel . 49.7 mi/h (80.0 km/h)
Exit Speed . . . . 49.2 mi/h (79.2 km/h)
Exit Trajectory . . 5.0 degrees
Vehicle Accelerations
  (Max. 0.050-sec Avg)
  Longitudinal . . -8.4 g
  Lateral . . . . . 12.7 g
Occupant Impact Velocity
  Longitudinal . . 21.8 ft/s (6.6 m/s)
  Lateral . . . . . 24.5 ft/s (7.5 m/s)
Occupant Ridedown Accelerations
  Longitudinal . . -3.9 g
  Lateral . . . . . 6.3 g

FIGURE 8 Summary of results for Test 1185–3.

height of the lower edge of the vehicle bumper was 12.25 in. (31.1 cm) and the height to the top of the bumper was 20.0 in. (50.8 cm). Other dimensions and information on the test vehicle are given in Figure 10. The vehicle was free-wheeling and unrestrained just before impact.

The speed of the vehicle at impact was 62.4 mph (100.4 km/hr) and the angle of impact was 26.6 degrees. The right front bumper of the vehicle impacted the bridge rail 5 ft (1.5 m) upstream of Post 5. The right front wheel made contact with the lower pipe member shortly after impact. The vehicle began to redirect at 0.067 sec. By 0.075 sec, the vehicle had deformed to the A-pillar and the windshield broke. As the vehicle continued forward, the front bumper was forced between the upper and lower pipe member and impacted the middle portion of the post. At the same time, the right front wheel became wedged under the lower pipe element and impacted the lower portion of Post 5. At 0.204 sec, the vehicle traveling at a speed of 47.6 mph (76.6 km/hr) began to move parallel with the bridge rail. The rear of the vehicle impacted the bridge rail at 0.219 sec and the rear bumper was forced between the upper and lower pipe elements and impacted the middle portion of the post. The vehicle lost contact with the bridge rail at 0.348 sec traveling at 44.6 mph (71.8 km/hr) and 7.6 degrees. Shortly after the vehicle left the test site, the brakes were applied; the vehicle yawed clockwise and subsequently came to rest 225 ft (69 m) from the point of impact.

As shown in Figures 11–13, the rail received minor damage and the slab received moderate damage. The vehicle impacted the rail between Posts 4 and 5. The bases on both Posts 4 and 5 were pushed back approximately 0.25 in. (0.6 cm). The bridge deck behind Post 4 was cracked. Tire marks appeared 5 in. (12.7 cm) behind the traffic edge of the baseplate of Post 5 before the tire impacted the lower part of the post. The bridge deck around Post 5 was broken, as shown in Figure 12. There were tire marks on the base of Post 6 and, shortly thereafter, the vehicle left the rail. The vehicle was in contact with the bridge rail for 15.5 ft (4.7 m).

TABLE 1 EVALUATION OF CRASH TEST 1185–3

USUAL CRITERIA	TEST RESULTS	PASS/FAIL
Must contain vehicle	Vehicle was contained	Pass
Debris shall not penetrate passenger compartment	No debris penetrated passenger compartment	Pass
Passenger compartment must have essentially no deformation	Minimal deformation	Pass
Vehicle must remain upright	Vehicle did remain upright	Pass
Must smoothly redirect the vehicle	Vehicle was redirected	Pass
Effective coefficient of friction (9)		
# Assessment 0 - .25 Good .26 - .35 Fair > .35 Marginal	# Assessment .27 Fair	Pass
Shall be less than		
Occupant Impact Velocity - fps Longitudinal 30 Lateral 25	Occupant Impact Velocity - fps Longitudinal 21.8 Lateral 24.5	Pass
Occupant Ridedown Accelerations - g's Longitudinal 15 Lateral 15	Occupant Ridedown Accelerations - g's Longitudinal -3.9 Lateral 6.3	Pass
Exit angle shall be less than 12.8 degrees	Exit angle was 5.0 degrees	Pass

FIGURE 9 Oldsmobile before and after impact with T421 bridge rail.

The vehicle sustained severe damage to the right side, as shown in Figure 9. Maximum crush at the right front corner at bumper height was 18.0 in. (45.7 cm). The right front axle was pushed back 15.0 in. (38.1 cm). The right A-arm, sway bar, tie rod, and upper and lower ball joints were damaged and the subframe was bent. The instrument panel in the passenger compartment as well as the floor pan and roof was bent, and the windshield was broken. The right front and rear rims were bent and the tires were damaged. There was damage to the hood, grill, front bumper, right front quarter-panel, right front and rear doors, right rear quarter-panel, and rear bumper.

Impact speed was 62.4 mph (100.4 km/hr) and the angle of impact was 26.0 degrees. The vehicle was traveling at 47.6 mph (76.6 km/hr) as it began moving parallel to the bridge rail. The vehicle exited the rail at 44.6 mph (71.8 km/hr) and 7.6 degrees. Occupant impact velocity was 26.8 ft/sec (8.2 m/sec) in the longitudinal direction and 20.1 ft/sec (6.1 m/sec) in the lateral direction. The highest 0.010-sec occupant ridedown accelerations were −6.8 g (longitudinal) and 8.7 g (lateral). These data and other pertinent information from the test are summarized in Figure 14 and Table 2.

These data were then further analyzed to obtain 0.050-sec average accelerations versus time. The maximum 0.050-sec average accelerations at the center of gravity were −16.1 g (longitudinal) and 11.1 g (lateral).

The bridge rail contained and redirected the test vehicle with minimal lateral movement of the bridge rail. The vehicle remained upright and relatively stable during the collision. Occupant-compartment impact velocities and occupant ridedown accelerations were within the limits recommended in NCHRP Report 230. The vehicle trajectory at loss of contact was 7.6 degrees, which was less than the recommended limit of 60 percent of the impact angle (15.6 degrees in this case).

The new aesthetic bridge rail T421 performed well when crash-tested in accordance with NCHRP 230 Tests 10 and

Date: 8-24-89 Test No.: 1185-4 VIN: 1G3AW69N6CM141463

Make: Oldsmobile Model: 98 Year: 1982 Odometer: 29415

Tire Size: P225/75R-15 Ply Rating: _____ Bias Ply: ___ Belted: ___ Radial: x

Tire Condition: good __
fair x
badly worn __

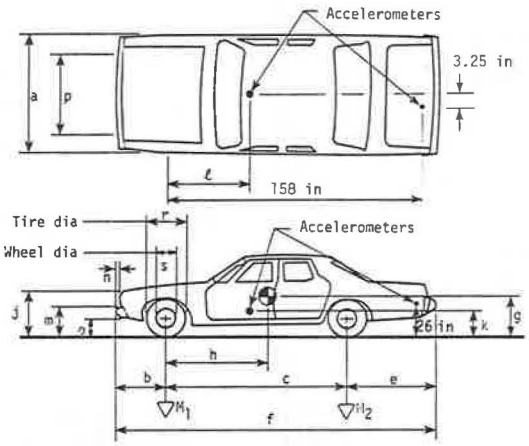

Vehicle Geometry - inches

a	76.0	b	42.0
c	119.0	d*	57.5
e	55.5	f	216.5
g	_____	h	51.7
i	----	j	32.0
k	20.0	ℓ	32.25
m	20.0	n	5.0
o	12.25	p	61.5
r	27.75	s	16.5

4-wheel weight for c.g. det. ℓf 1253 rf 1292 ℓr 992 rr 963

Mass - pounds	Curb	Test Inertial	Gross Static
M_1	2458	2545	_____
M_2	1563	1955	_____
M_T	4021	4500	_____

Note any damage to vehicle prior to test:

_____

_____

*d = overall height of vehicle

Engine Type: 8 - diesel
Engine CID: 5.7
Transmission Type:
Automatic or Manual
FWD or RWD or 4WD
Body Type: 4-door sedar
Steering Column Collapse Mechanism:
__Behind wheel units
__Convoluted tube
__Cylindrical mesh units
__Embedded ball
__NOT collapsible
__Other energy absorption
__Unknown

Brakes:
Front: discx drum___
Rear: disc___ drumx

FIGURE 10 Vehicle properties (Test 1185–4).

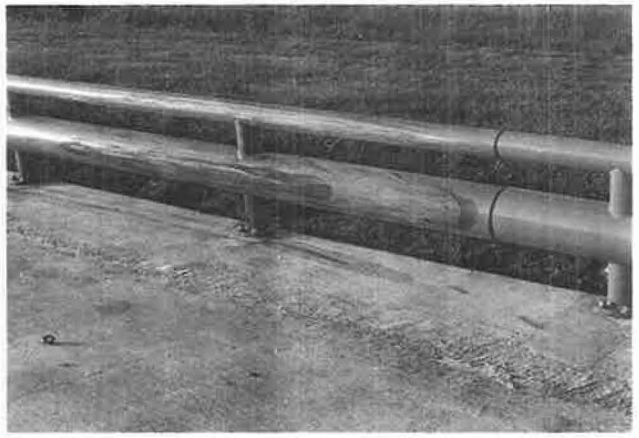

FIGURE 11 T421 bridge rail after Oldsmobile impact.

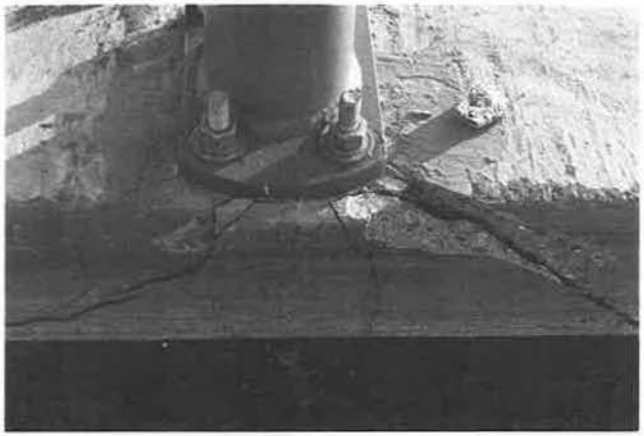

FIGURE 12 Damage at Post 5.

FIGURE 13 Posts 4 and 6 after Oldsmobile impact.

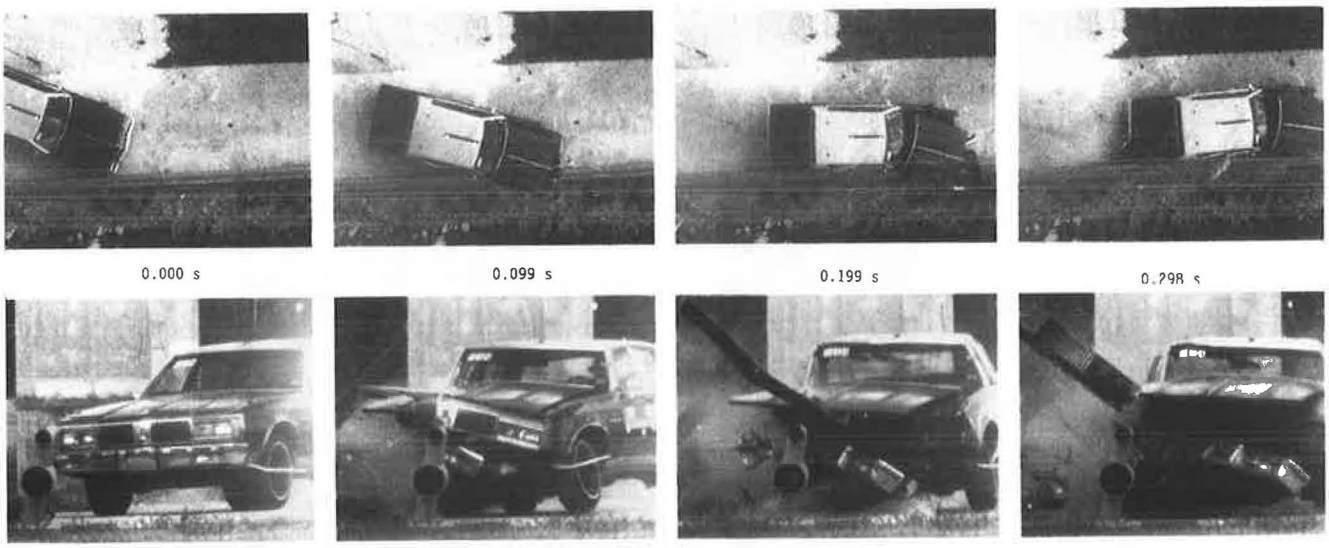

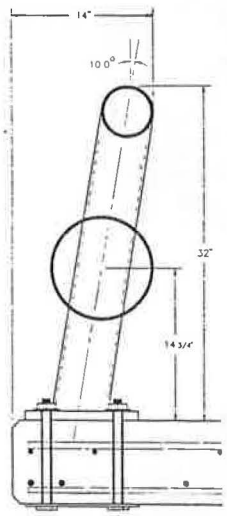

Test No. 1185-4
Date 08/24/89

Test Installation . . . T421 Bridge Rail
Length of Installation . 75 ft (23 m)

Vehicle . . . . . 1982 Oldsmobile 98
Vehicle Weight
  Test Inertia . . . . . 4,500 lb (2,043 kg)
Vehicle Damage Classification
  TAD . . . . . 01FR6 & 01RD6
  CDC . . . . . 01FZEK4 & 01RDES4
Maximum Vehicle Crush . 18.0 in (45.7 cm)

Impact Speed . . . 62.4 mi/h (100.4 km/h)
Impact Angle . . . 26.6 degrees
Speed at Parallel . 47.6 mi/h (76.6 km/h)
Exit Speed . . . . 44.6 mi/h (71.8 km/h)
Exit Trajectory . . 7.6 degrees
Vehicle Accelerations
  (Max. 0.050-sec Avg)
  Longitudinal . .-16.1 g
  Lateral . . . . . 11.1 g
Occupant Impact Velocity
  Longitudinal . . 26.8 ft/s (8.2 m/s)
  Lateral . . . . . 20.1 ft/s (6.1 m/s)
Occupant Ridedown Accelerations
  Longitudinal . . -6.8 g
  Lateral . . . . . 8.7 g

FIGURE 14 Summary of results for Test 1185–4.

TABLE 2 EVALUATION OF CRASH TEST 1185–4

USUAL CRITERIA	USUAL TEST RESULTS	PASS/FAIL
Must contain vehicle	Vehicle was contained	Pass
Debris shall not penetrate passenger compartment	No debris penetrated passenger compartment	Pass
Passenger compartment must have essentially no deformation	Minimal deformation	Pass
Vehicle must remain upright	Vehicle did remain upright	Pass
Must smoothly redirect the vehicle	Vehicle was redirected	Pass
Effective coefficient of friction (9)		
μ Assessment 0 - .25 Good .26 - .35 Fair > .35 Marginal	μ Assessment .29 Fair	Pass
Shall be less than		
Occupant Impact Velocity - fps Longitudinal 30 Lateral 25	Occupant Impact Velocity - fps Longitudinal 26.8 Lateral 20.1	Pass
Occupant Ridedown Accelerations - g's Longitudinal 15 Lateral 15	Occupant Ridedown Accelerations - g's Longitudinal -6.8 Lateral 8.7	Pass
Exit angle shall be less than 16.0 degrees	Exit angle was 7.6 degrees	Pass

S13. It met all of the safety evaluation guidelines of NCHRP 230 (Tables 1 and 2).

None of the pipes incurred any collapse nor was there any yielding of these members. The base plates in Test 10 moved without yielding by virtue of the rotation allowed at the splices. Therefore, repairs of the rail itself would consist of cleaning and repainting after an accident.

Punching shear cracks developed in the bridge deck typical of crash tests on steel beam and post bridge rails. These only occurred from the 4,500-lb car impacting at 62.4 mph and 26.6 degrees. This impact was a very severe impact that most bridge rail installations rarely experience.

The cracking of the concrete deck could be minimized by increasing the edge distance of the posts and base plate from the deck facia and adding some horizontally placed reinforcements perpendicular to the surface cracks.

ACKNOWLEDGMENTS

This research study was conducted under a cooperative program between the Texas Transportation Institute (TTI), the State Department of Highways and Public Transportation (SDHPT), and the FHWA. Dean Van Landuyt, John J. Panak, and Van M. McElroy were closely involved in all phases of this study.

REFERENCE

1. J. D. Michie. *NCHRP Report 230: Recommended Procedures for the Safety Performance Evaluation of Highway Appurtenances.* TRB, National Research Council, Washington, D.C., March 1981.

Publication of this paper sponsored by Committee on General Structures.

Oak A-Frame Timber Bridges Meeting the Modern Deflection Requirement

JAI B. KIM AND ROBERT H. KIM

One of the most difficult requirements for timber bridges has been meeting the live-load deflection limitation of *L*/500 (span length divided by 500) at competitive costs. An 18- × 18-ft all–Pennsylvania oak A-frame bridge has been designed in accordance with the 1991 AASHTO *Standard Specifications for Highway Bridges*, analyzed by a finite element method, and built and tested under an equivalent HS-20 truck loading at Bucknell University to satisfy this live-load deflection requirement at a low cost. An 18-ft-long timber A-frame bridge consisting of two timber A-frames, six timber stringers, two steel hanger rods suspended from the apex of the frames, one steel transverse beam at midspan supported by the hanger rods, and panelized timber decking met the *L*/500 deflection requirement. The total cost of the bridge was $1,500 for material and $2,500 for student labor (estimated). This same A-frame-type bridge can be built economically and also satisfy the *L*/500 live-load requirement for spans up to 50 ft in length.

The use of hardwood timber for modern highway bridges, regardless of span length, has been minimal, particularly with Pennsylvania hardwood. For stringer-type bridges, it is nearly impossible to build bridges with sawn lumber of hardwood species such as oak, because of the maximum live-load deflection requirement of *L*/500, coupled with the high costs caused by this requirement. All timber bridges must meet the *L*/500 live-load deflection requirement and still be economical to compete with other types of bridges.

In some regions, stressed timber bridges are prohibited because of the extensive maintenance required for prevention of adverse shrinkage-swelling and creep effects, which makes the application of timber bridges even more difficult. Another problem with hardwood timber bridges is that there is no available glulam technology for hardwood lumber.

The construction and load testing of an 18- × 18-ft Pennsylvania hardwood timber bridge constructed by students at a cost of $1,500 (material only) are described. The bridge was tested under an HS-20 truck loading and fulfilled the *L*/500 live-load deflection requirement.

DESIGN AND CONSTRUCTION OF BRIDGE

The 18- by 18-ft bridge was constructed with oak timber available from local sawmills at a cost of $0.24 per board foot (Figure 1). The bridge was first designed in accordance with the 1991 AASHTO *Standard Specifications for Highway Bridges* (*1*) to carry an HS20 truck loading.

J. B. Kim, Department of Civil Engineering, Bucknell University, Lewisburg, Pa. 17837. R. H. Kim, Department of Civil Engineering, Pennsylvania State University, University Park, Pa. 16802.

The bridge consisted of two 7- × 9-in. A-frames, six 7- × 9-in. stringers, and a series of 40-in.-wide 3- × 6-in. nail-laminated deck panels. For this test program, in order to simulate worst-case service conditions, the deck panels were not attached to each other or to the stringers below. The six stringers were supported at their midspan by a W10 × 26 steel beam, with ¾-in. cover plates welded to the flanges, which was supported by 1-in.-diameter A588 Grade 50 weathering-steel hanger rods from an A-frame apex (Figures 2–5).

The 7- × 9-in. A-frames and stringers were Grade 2 white oak members with moisture content values varying from 40 to 50 percent. The A-frame members were connected to the exterior stringers with 2½-in. split-ring timber connectors. Additional lateral support for the A-frames was provided by connecting each end of an A-frame to an exterior stringer with two steel angles (3½ × 3½ × ½ thick) and four ¾-in. bolts per angle.

The guide rails and wheel guards were made of 6- × 6-in. Grade 2 white oak with 7- × 9-in. posts spaced at 9 ft center to center.

TESTS

Before the present test program, 7- × 9-in. oak timber specimens were tested for flexure and the moduli of elasticity were determined experimentally as part of a research project funded by the Ben Franklin partnership program with the state of Pennsylvania (*2*) and the Burke, Parsons, and Bowlby Corporation (*3*). The values of the moisture content of these specimens varied from 40 to 50 percent and the values of Young's modulus averaged 1.45×10^6 psi. In accordance with the AASHTO design specifications for HS20 truck loading, a 6-ft rear-axle load of 30 kips at midspan with one wheel at a distance of 2 ft from a wheel guard was simulated with a bar joist loaded by a 600,000-lb universal testing machine in Bucknell University's Structural Testing Laboratory as shown in Figure 6. The load was increased in 1-sec intervals by a computer-controlled system from 0 to 32 kips. For each 1-sec load interval, the vertical deflections were measured at three points along the length of the transverse W10 × 26 steel beam (each end and midspan) with transducers at those points that would produce maximum deflections.

In an attempt to predict maximum live-load deflections at midspan, a finite element program (IMAGES 3D) was run during the bridge construction and load testing to compare the predicted deflections with the actual deflections. The value of Young's modulus used was 1.45×10^6 psi determined previously for the 7- × 9-in. timber tested. IMAGES 3D

FIGURE 1 18- × 18-ft oak A-frame timber bridge.

predicted the deflections to be much less than those during the load tests. Therefore, trial and error approaches had to be used to arrive at the as-built configuration that met the live-load deflection requirement.

TEST RESULTS AND CONCLUSIONS

The load test results are shown in Figure 7 (initial-cycle loading), Figure 8 (second-cycle loading), and Figure 9 (third-cycle loading). Figure 8 shows that, at the design load of 32 kips on the bridge, the transverse steel beam deflection was 0.431 in. in the middle of the beam, 0.179 in. at one end, and 0.104 in. at the other end. However, Figure 7 shows slightly higher values, 0.454 in. in the middle, and 0.126 and 0.004 in. at the ends of the steel transverse beam. The corresponding

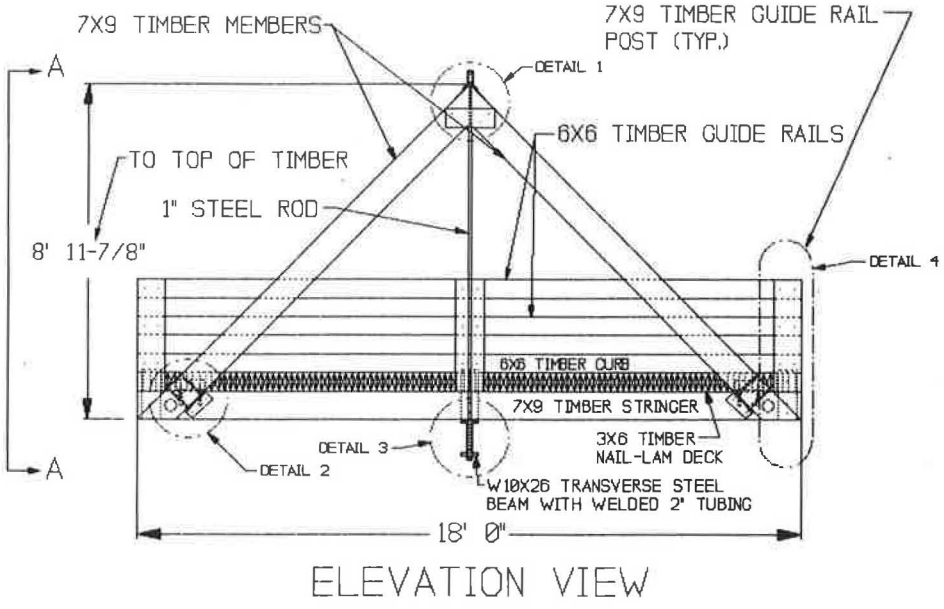

FIGURE 2 A-frame sideview detail.

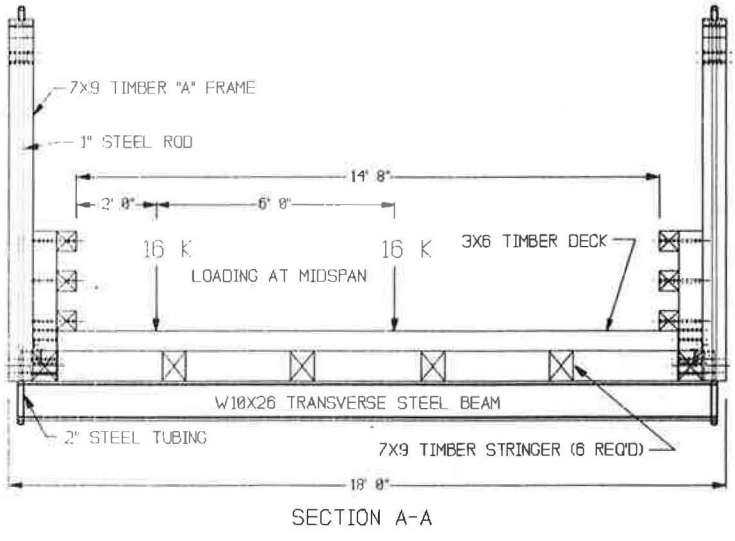

FIGURE 3 Bridge cross-section.

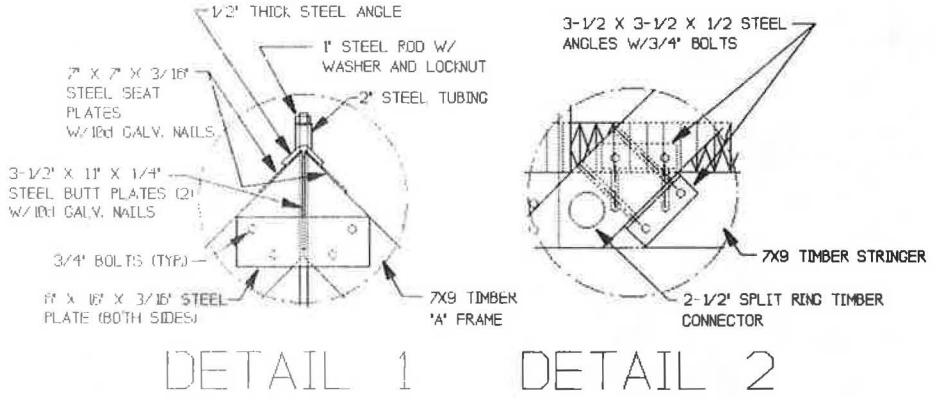

FIGURE 4 A-frame connection detail.

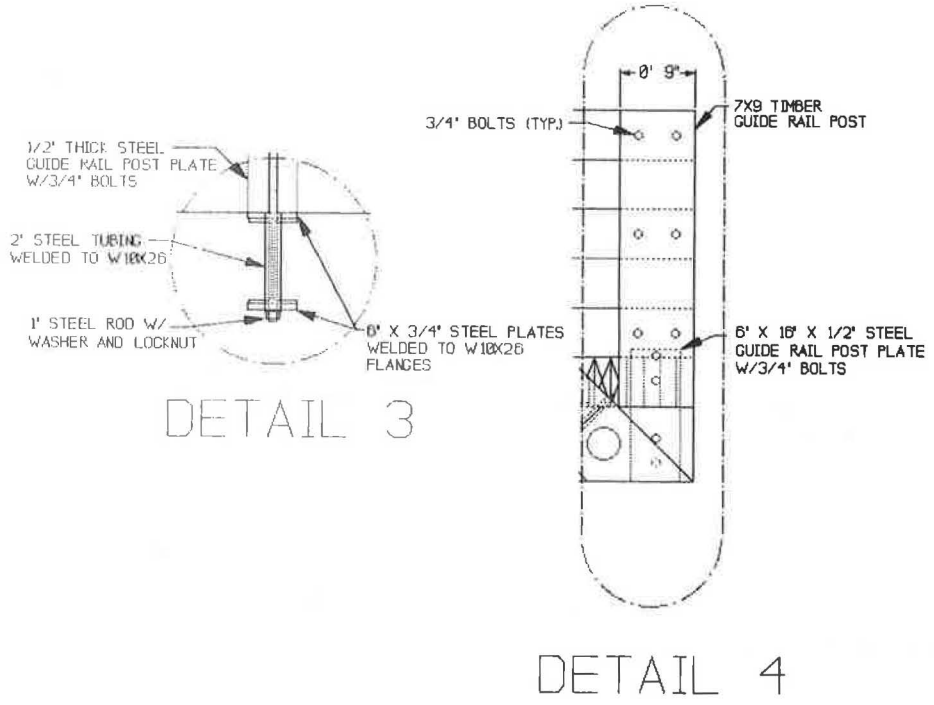

FIGURE 5 Other connection details.

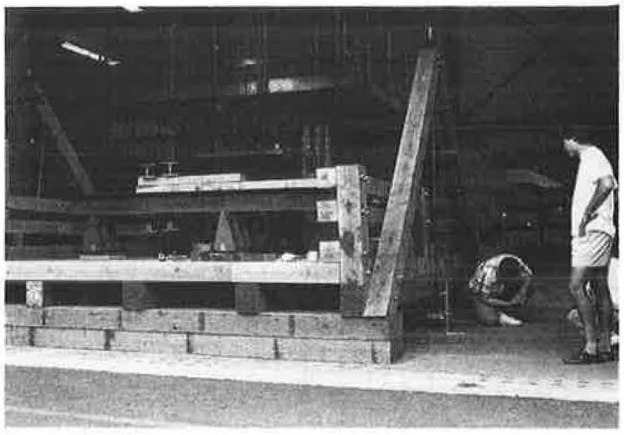

FIGURE 6 Load test set-up for an HS20 loading.

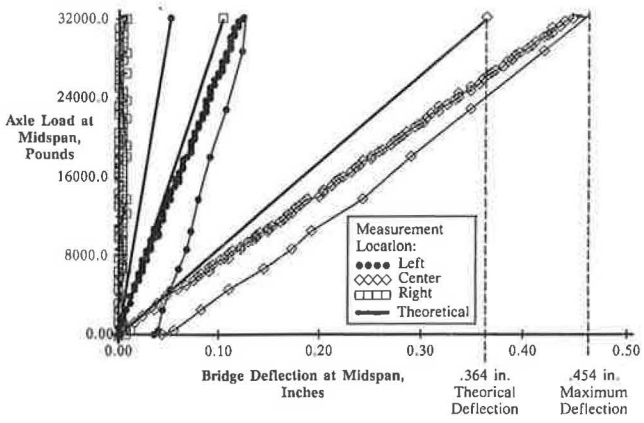

FIGURE 7 Load versus deflection for initial-cycle loading.

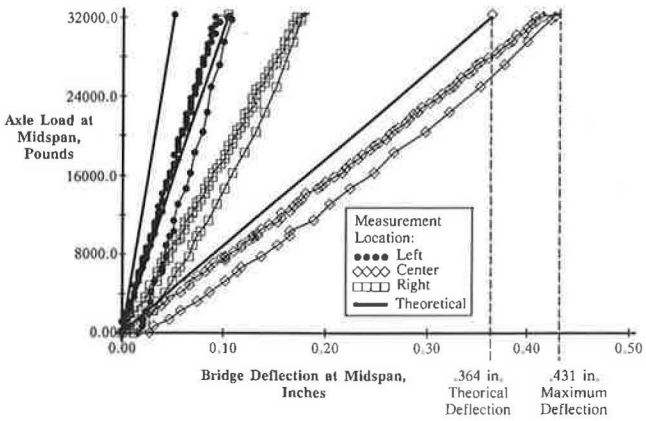

FIGURE 8 Load versus deflection during second-cycle loading.

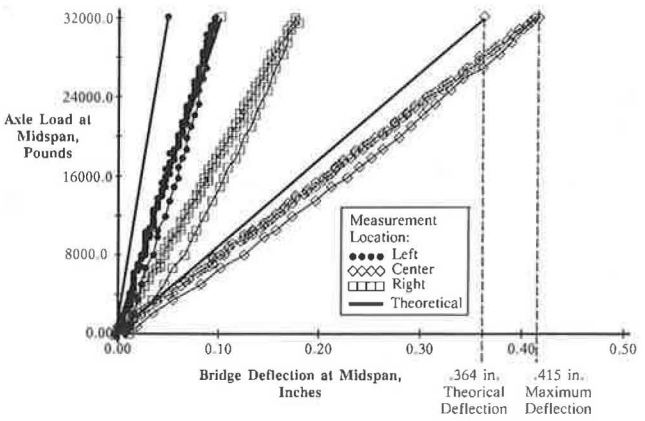

FIGURE 9 Load versus deflection during third-cycle loading.

values predicted by IMAGES 3D were 0.364, 0.104, and 0.051 in., respectively, as seen in the figure. Deflections during initial loadings were slightly greater than those during loadings after tightening the loosened connections. The bridge was then unloaded and reloaded with no significant changes in these deflections as demonstrated in the second cycle loading (Figure 8) and in the third cycle loading (Figure 9). The *L*/500 live-load deflection limitation for this test bridge is calculated to be 0.432 in. The load-deflection curves were linear (Figures 7–9), indicating a linear elastic behavior.

With stringer-type bridges, such as this A-frame bridge, the stresses in the timber members rarely control the design. For example, compressive stresses calculated by IMAGES 3D were less than 200 psi for the 7- × 9-in. A-frame members. The controlling factor was the live-load deflection restriction. Appropriately controlling live-load deflections with this type of A-frame timber bridge can be done easily and economically by varying the size of the transverse steel beam or varying the sizes of the steel hanger rods supporting this steel beam, or both.

The same A-frame bridge concept can be economically applied to longer spans in the range of 40 to 50 ft by lapping stringers at the transverse steel beam with a double A-frame system.

ACKNOWLEDGMENT

This bridge was constructed as a special student project funded by the Bureau of Forestry of the Pennsylvania Department of Environmental Resources and Bucknell University. The authors recognize the work performed by eight undergraduate civil engineering students. L. Henry Muller helped conduct the load tests for independent course work. Joseph V. Sinfield performed all the finite element analyses.

REFERENCES

1. *Standard Specifications for Highway Bridges*, 14th ed. (revised). AASHTO, Washington, D.C., 1991.
2. J. B. Kim. *Evaluation of Reinforced Bridge Oak Timber Girders*. Final report, Department of Civil Engineering, Bucknell University, Lewisburg, Pa., Sept. 1989.
3. J. B. Kim. *Flexure Test of 7" × 9" × 8'6" Oak Railroad Ties*. Final report, Department of Civil Engineering, Bucknell University, Lewisburg, Pa., March 1988.

Publication of this paper sponsored by Committee on General Structures.

Behavior and Design of Moment-Reducing Details for Bridge Column–Foundation Connections

DAVID I. MCLEAN, KUANG Y. LIM, AND EDWARD H. HENLEY, JR.

Bridge foundations in seismic regions are usually designed to withstand the plastic hinge moments that develop at the bases of the columns. Various hinge details have been proposed to reduce or even eliminate the plastic moments transferred to the foundations, and thereby, reduce the sizes and costs of the foundations. However, no code specifications for these moment-reducing hinge details currently exist. The behavior of column specimens incorporating different moment-reducing hinge details was investigated. Tests were performed on reinforced-concrete column specimens subjected to increasing levels of cycled inelastic displacements under constant axial load. The effects on hinge performance of several parameters were investigated, including providing vertical discontinuity in the hinge detail, level of axial load, low-cycle fatigue characteristics, column aspect ratio, and different amounts of longitudinal and transverse reinforcement. Using the test results, hinge details can be incorporated into columns to significantly reduce the moment capacity at the bases of the columns. The moments are not negligible, as is sometimes assumed for design with the moment-reducing hinge details. Providing vertical discontinuity in the moment-reducing hinge details results in reduced distress in the longitudinal reinforcement and improved performance of the hinge. Preliminary design recommendations are proposed for the comprehensive design of moment-reducing hinge details at the bases of bridge columns.

Bridge foundations in seismic regions are designed to withstand the plastic hinge moments that develop at the bases of bridge columns. In columns that are oversized for architectural or other reasons, this approach results in excessively large foundations. Various hinge details for the bases of bridge columns have been proposed to reduce the plastic moments transferred to the foundations, and hence, reduce foundation sizes and costs.

The basic concept inherent in the modified hinge details is to provide a reduced moment capacity in the plastic hinging region at the bases of the columns. This is accomplished by placing a layer of easily compressed material at the base of the column that provides partial discontinuity between the column and the foundation. The discontinuity results in a smaller effective cross section at the column base and, thus, in a reduced hinge capacity in the column. To a great extent, the modifications that have been suggested have been based on engineering judgment, and the behavior and safety of the moment-reducing details have not been fully established.

D. I. McLean, Department of Civil and Environmental Engineering, Washington State University, Pullman, Wash. 99164–2910. K. Y. Lim, Sverdrup Corporation, 1340 Treat Boulevard, No. 100, Walnut Creek, Calif. 94596. E. H. Henley, Jr., Bridge and Structures Branch, Washington State Department of Transportation, Transportation Building KF-01, Olympia, Wash. 98504.

The objectives of this study were to evaluate current design practices for incorporating moment-reducing hinge details at the bases of oversized bridge columns, to experimentally investigate the seismic performance of columns incorporating such details, to identify any symptomatic problems associated with the suggested details, and to develop design recommendations for the detailing of the hinge region of oversized columns to reduce the moment transfer between the columns and foundations. Details of the experimental program and preliminary findings were presented by Lim et al. (*1*). Herein, final conclusions from the study are presented and preliminary recommendations for the design of moment-reducing hinge details at the bases of bridge columns are proposed.

CURRENT PRACTICE

Codified guidelines for the design of moment-reducing hinge details do not currently exist. As a result, there is considerable variation in the specifications, and even the use, of these details.

One approach to the design of the moment-reducing hinge details is to determine the size of the hinge required from the pure axial compressive capacity of the section, and to design for shear across the section by providing the amount of longitudinal steel required as determined from shear friction theory. A horizontal joint consisting of ¼- to ½-in.-thick expansion joint material is provided at the throat region around the hinge perimeter to create partial discontinuity between the column and the footing. To further reduce the moment developed at the hinge section, the longitudinal bars are sometimes clustered at the center of the hinge, and the hinge is treated as a pin with no moment capacity. Both circular and rectangular arrangements of the reinforcement in the hinges have been used. Normally, only nominal transverse steel is provided. Occasionally, no transverse steel is used. An example design for a column incorporating a hinge of this type is shown in Figure 1 (left).

Several questions about the behavior of this hinge detail under seismic loading can be raised. The hinge is designed for the axial load capacity of the section, and research (*2*) has shown that reinforced-concrete columns tested under axial loads close to the maximum axial load allowed by American Concrete Institute (ACI) (*3*) exhibited significantly reduced ductility. Also, even though the hinge is assumed to be a pin connection, substantial moment actually develops at the hinge section even if the longitudinal bars are clustered. This process results in an increase in the shear and axial load in the column

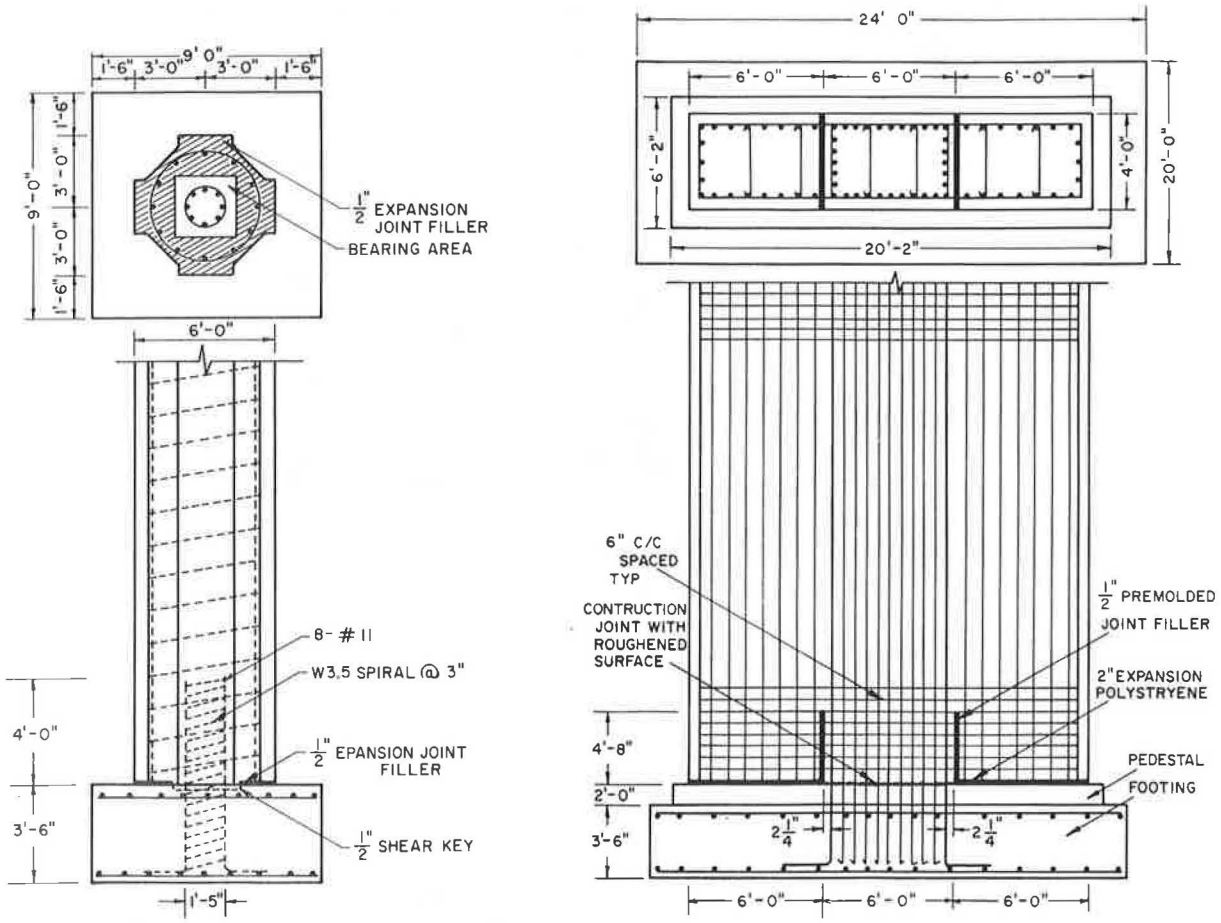

FIGURE 1 Moment-reducing hinge details for the bases of bridge columns.

over that assumed for design. Prying action, caused by contact of the column edges with the top of the footing, develops under inelastic loading if insufficient horizontal joint thickness is provided. This prying action leads to higher moments and increased degradation in the hinge. Because of the sharp changes in section properties at the hinge, plastic deformations in the hinge are concentrated at the location of the horizontal discontinuity, resulting in increased distress in the hinge. Finally, the assumed design forces for the footing are unconservative as the actual moment transferred by the hinge to the footing is not considered.

Other designs have been proposed to spread the zone of plastic action over a greater vertical length by providing both horizontal and vertical discontinuity in the moment-reducing hinge detail. Increased discontinuity joint thicknesses are also specified to prevent contact of the outer column with the footing. An example design for a hinge incorporating both horizontal and vertical discontinuity is shown in Figure 1 (right).

EXPERIMENTAL TESTING PROGRAM

Test Specimens and Parameters

Experimental tests were conducted on reinforced-concrete column specimens incorporating several different moment-reducing hinge details. The test specimens consisted of a single column member connected at the base to a rectangular footing. The specimens were subjected to increasing levels of cycled inelastic displacements under a constant axial load.

The specimens were arranged in groups of three: one specimen incorporating a hinge detail with horizontal discontinuity only (CA series), one specimen incorporating a hinge detail with both horizontal and vertical discontinuity (WA series), and one reference or control specimen consisting of a column with the same dimensions and reinforcement as the hinge connection of the specimens incorporating the moment-reducing hinge details (CON series). These three types of specimens are shown in Figure 2.

Tests were performed on two different sizes of specimens: small-scale specimens (approximately 1:20) and moderate-scale specimens (approximately 1:6). More than fifty 1:20-scale specimens were tested. The small-scale study provided a cost-efficient parametric study and also guided the selection of variables for the larger-scale tests. Fourteen 1:6-scale specimens were tested. The larger 1:6-scale tests resulted in a more realistic representation of the hinging behavior in actual bridge columns, and size effects were reduced when compared to the small-scale tests. Dimensions and reinforcement for a typical 1:6-scale column specimen are shown in Figure 3.

Parameters investigated in the experimental testing program included column aspect ratio, magnitude of axial load, amount of both longitudinal and transverse reinforcement,

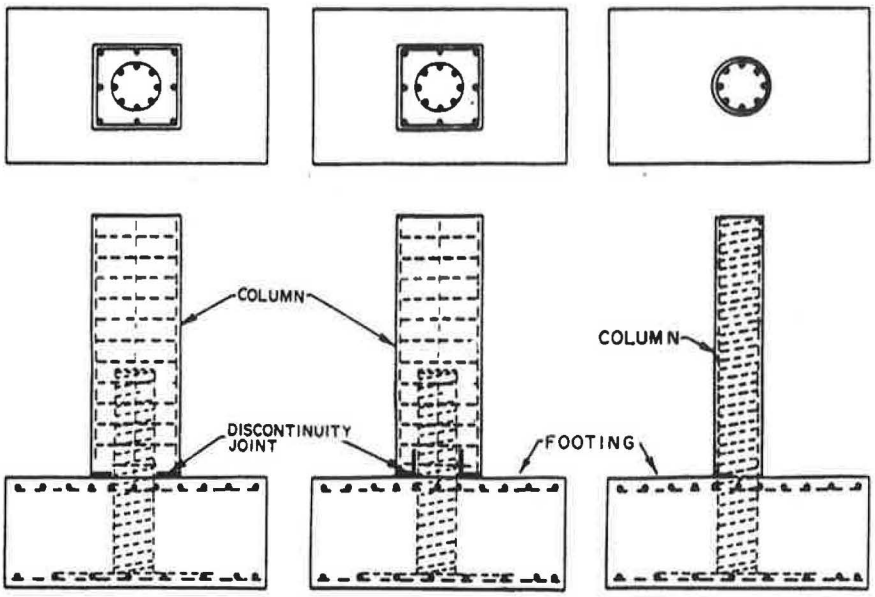

(a) CA detail (b) WA detail (c) CON detail

FIGURE 2 Hinge details studied.

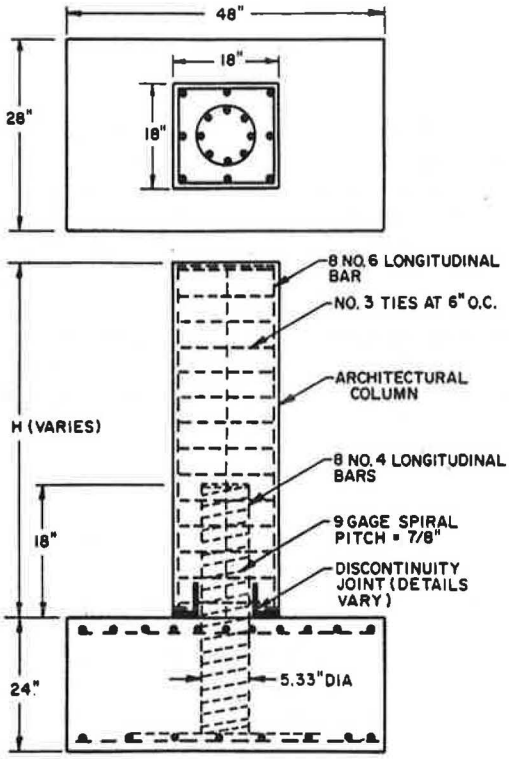

FIGURE 3 Typical 1:6-scale specimen dimensions and reinforcement.

vertical discontinuity length, thickness of horizontal discontinuity, column shape, hinge cross-sectional shape (circular and square), and low-cycle fatigue characteristics. A summary of the details of the specimens of the 1:6-scale testing program is presented in Table 1. Additional details of the testing program are provided by Lim et al. (*1,4,5*).

Test Setup and Procedures

The test setup and procedures for the 1:20- and 1:6-scale specimens were similar. Figure 4 shows the test setup for the 1:6-scale specimens. The footing of the test column was anchored to a laboratory strong floor. Axial load was first applied to the top of the column using a 55-kip actuator operated in force control. Axial loads were maintained at a constant level during a test. Lateral force was then applied slightly below the top of the column using a 22-kip actuator operated in displacement control. An analog signal of a prescribed ramp function was generated using a personal computer and sent to the servocontroller of the 22-kip actuator. Strain gages were used to monitor the strains in the longitudinal and transverse reinforcement within the hinging region, and linear variable displacement transformers (LVDTs) were mounted to the sides of the columns to measure rotations at the column base. All data were recorded intermittently on the same personal computer used to generate control signals for the horizontal actuator.

The determination of the yield displacement, Δ_y, and the loading sequence were similar to the procedures used by Priestley and Park (*6–8*). However, on the basis of preliminary tests, it was found that the ultimate moment capacities

TABLE 1 SUMMARY OF THE 1:6-SCALE TESTING PROGRAM

Specimen No.	Variable Studied	Aspect Ratio (H/D)	Axial Load (P/f'_cA_g)	Yield Displacement (in.)	Measured Yield Moment (in.-kips)	Measured Peak Moment (in.-kips)	Measured Peak Moment / ACI Predicted Moment	Maximum Applied Shear Load (kips)
CA1	hinge detail	2.50	0.24	0.30	181	270	1.52	6.0
WA1	"	2.50	0.24	0.30	133	212	1.19	4.7
CON1	"	*	0.24	0.30	72	179	1.01	4.0
CA2	aspect ratio	1.25	0.24	0.15	162	279	1.57	12.4
WA2	"	1.25	0.24	0.15	142	250	1.40	11.1
CON2	"	**	0.24	0.15	93	209	1.18	9.3
CA3	axial load	1.25	0.35	0.15	166	277	1.56	12.3
WA3	"	1.25	0.35	0.15	135	240	1.35	10.7
CON3	"	***	0.35	0.15	92	213	1.20	9.5
CA4	low-cycle fatigue	1.25	0.24	0.15	138	271	1.52	12.0
WA4	"	1.25	0.24	0.15	130	236	1.33	10.5
WA5	joint height	1.25	0.24	0.15	129	240	1.35	10.7
CA6	repeatability	2.50	0.24	0.15	164	276	1.55	6.1
WA6	"	2.50	0.24	0.15	140	229	1.29	5.1

* circular control column with the same height as Units CA1 and WA1
** circular control column with the same height as Units CA2 and WA2
*** circular control column with the same height as Units CA3 and WA3

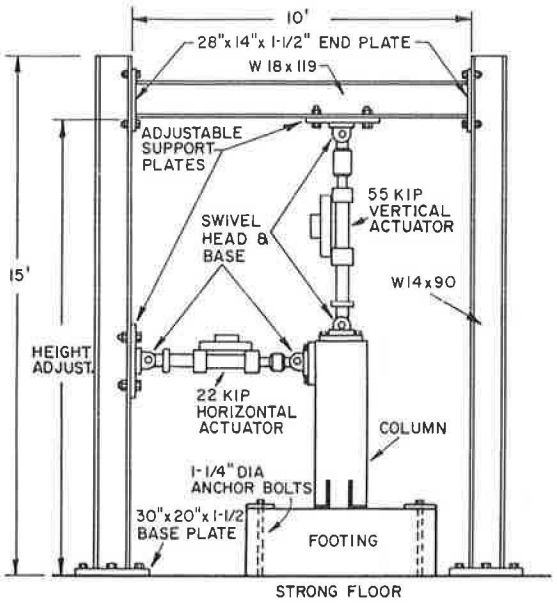

FIGURE 4 Test setup for the 1:6-scale specimens.

and stiffnesses, and hence the yield displacements, varied in columns with different details. However, to better compare the hinging behavior of columns with different hinge details, parallel sets of columns were subjected to the same displacement history. The typical loading sequences used for the tests was two cycles at displacement ductility factors (i.e., multiple values of Δ_y) of μ = 1, 2, 4, 6, 8, 10 and 12 unless premature failure of the specimen caused a halt to the testing.

TEST RESULTS AND DISCUSSION

A summary of the test results for all 1:6-scale test specimens is presented in Table 1. Column performance was evaluated with respect to the moment capacity and displacement ductility attained, the overall hysteresis behavior, and degradation and energy dissipation characteristics. Rather than discuss the results of each specimen individually, results of groups of specimens are presented to facilitate correlation of the influence of various parameters with column performance and to obtain behavioral trends.

General Behavior

Hysteresis Behavior

Figure 5 shows typical load-displacement hysteresis curves for 1:6-scale columns incorporating details CA and WA and a comparable control column (Units CA2, WA2, and CON2). These columns were subjected to an axial load level of $0.24f'_cA_g$. The aspect ratio for the columns incorporating the modified details was 1.25 measured with respect to the outer column, which corresponded to an aspect ratio of 3.75 for the control column. Longitudinal and volumetric reinforcing ratios in the hinges were 5.7 and 1.46 percent, respectively. The lateral loads presented in these plots are the true loads on

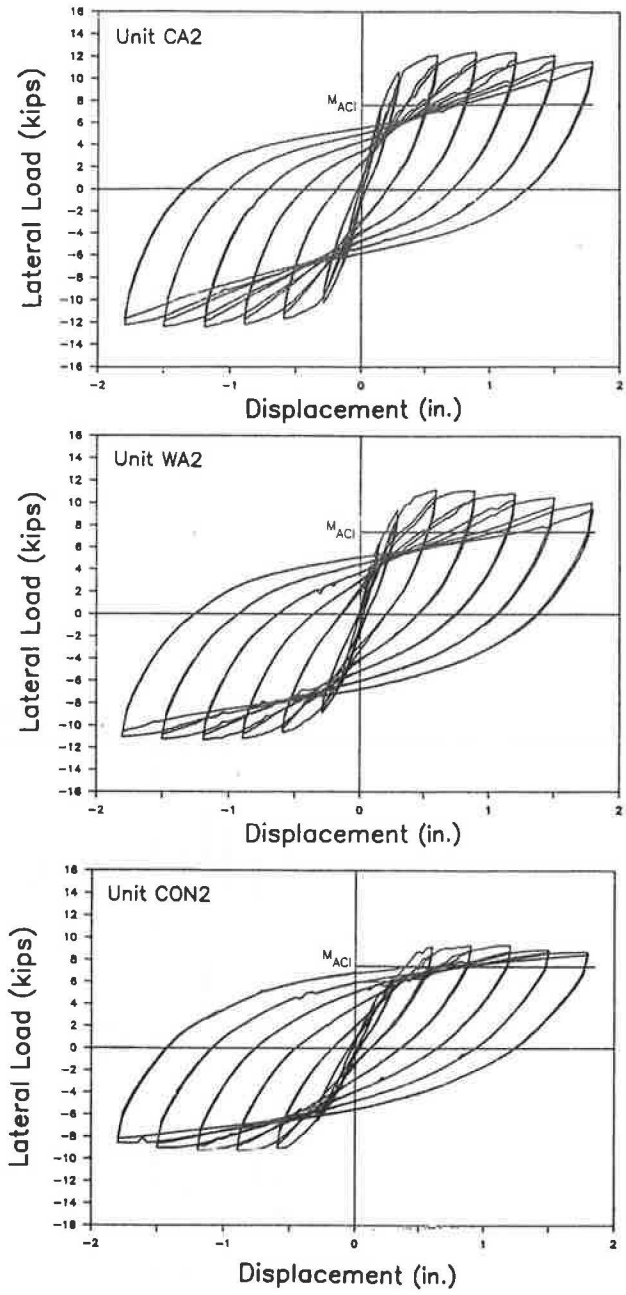

FIGURE 5 Load-displacement hysteresis curves for Units CA2, WA2, and CON2.

the specimens, including P–Δ effects and secondary effects from the axial load. The hysteresis curves for all three specimens are very stable even at displacement levels of μ = 12. No evidence of any sudden drop in load-carrying capability was observed, and the plastic hinges continued to absorb energy throughout the tests.

The theoretical ultimate lateral load, calculated from ACI methods and using measured material strengths with a material reduction factor of one, is also shown in each of these figures. Figure 5 indicates that substantial enhancement of the measured flexural strength above the ACI-predicted values was obtained for these columns. This strength enhancement is caused by increases in concrete strength and ductility

because of the confinement provided by the spiral, and by the increased strength of the steel in the strain-hardening region. Results from the 1:6-scale tests indicated average enhancement values of 1.17, 1.35, and 1.52 for control columns, columns with detail WA, and columns with detail CA, respectively. The greater strength enhancement in the columns with the modified hinge details is caused by the additional confinement provided by the outer column surrounding the hinge detail. Figure 5 also indicates that hysteresis curves for the column incorporating detail CA are somewhat narrower than those for the column with detail WA and for the control column. This result indicates a reduced energy dissipation capacity in the hinge with the CA detail.

Shear Degradation

Figure 6 shows the plots of the shear strength envelope curves for Units CA1, WA1, and CON1. The shear strength envelope curve is obtained by plotting the maximum shear force attained at each peak displacement level with respect to that displacement. The columns with the moment-reducing details exhibited less strength degradation than did the control column, possibly because of the additional confinement provided around the hinge region by the outer column. Figure 6 also indicates that the column with detail CA exhibited the greatest stiffness and that the control column exhibited the least stiffness. Two reasons can be cited for the difference in stiffnesses observed in these specimens. First, the elastic stiffness of the control column is less than that of the outer columns with the moment-reducing details. Second, the moment-reducing details produce pinching of the rebars crossing the column-to-foundation connection, thereby inducing larger strain values in the rebars of the moment-reducing details.

Strain profiles of the longitudinal bars measured at the base of these columns are shown in Figure 7, illustrating this pinching effect. The largest strains were measured in the column with detail CA; the strains in the column with detail WA and in the control column were considerably lower. Examining the distributions in the figure of the strains over the vertical height of the columns also indicates that the plastic hinging action in the column with detail CA was largely concentrated at the throat region of the hinge. In contrast, the plastic action

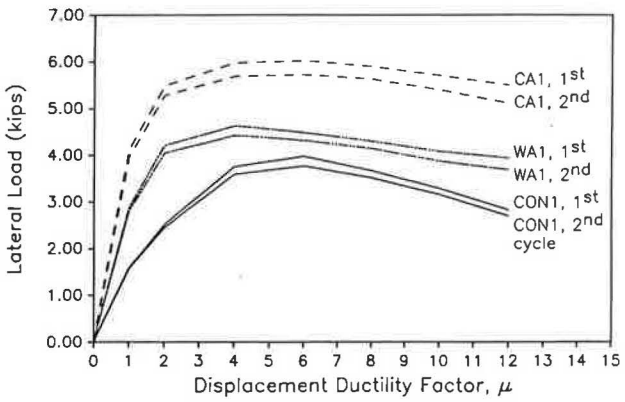

FIGURE 6 Shear strength envelope curves for Units CA1, WA1, and CON1.

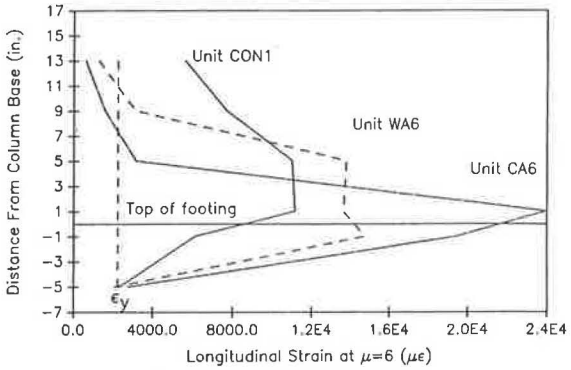

FIGURE 7 Longitudinal bar strain profiles.

was distributed over a greater vertical length of the hinge region in the column with the WA detail and in the control column.

Energy Dissipation

The energy dissipated by a column during a particular load cycle is represented by the area enclosed by the load-displacement hysteresis curve. The energy dissipated by a perfectly elastoplastic system during a complete displacement cycle, as shown in Figure 8, is the area of the parallelogram BCDE. For a particular displacement ductility factor, μ, the ideal plastic energy dissipated, E_p, can be computed as

$$E_p = 4(\mu - 1)\ V_p\Delta_y \qquad (1)$$

where V_p is the maximum shear force attained at that displacement level (7). In order to evaluate quantitatively the energy dissipation capability of the various hinge details, the measured energy dissipation was divided by the E_p value of the column for the same displacement ductility factor. This ratio is referred to as the relative energy dissipation index.

Values of the energy dissipation effectiveness of Units CA2, WA2, and CON2 are shown in Figure 9. The low values of

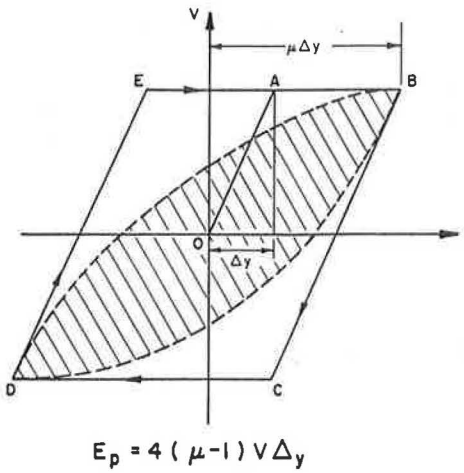

FIGURE 8 Actual and idealized perfectly elastoplastic hysteresis curves.

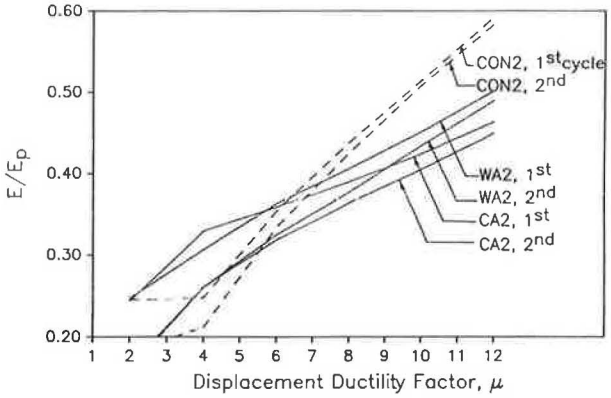

FIGURE 9 Relative energy dissipation index curves for Units CA2, WA2, and CON2.

E/E_p at $\mu = 2$ and 4 for the control column, Unit CON2, are caused by the inexactness in defining the actual yield displacement in the different columns, with the result that response of the control column is still largely elastic at these displacement levels. The figure indicates that the control column exhibited the greatest energy dissipation effectiveness and column with detail CA exhibited the least effectiveness. The reduced effectiveness in the column with moment-reducing details may be caused by the confining of the plastic action at the base of the column, particularly with the CA detail.

Effect of Various Parameters on Column Performance

Aspect Ratio

In order to evaluate the effects of column aspect ratio on the behavior of the hinge details, 1:6-scale test results for modified columns with aspect ratios of 2.5 (Units WA1 and CA1) and 1.25 (Units WA2 and CA2) and comparable control columns with aspect ratios of 7.5 (Unit CON1) and 3.75 (Unit CON2) are compared. The hysteresis curves for Units WA2, CA2, and CON2 and Units WA1, CA1, and CON1 are shown in Figures 5 and 10, respectively. The hysteresis curves for the two sets of specimens are similar, indicating that flexure dominated the behavior of the columns even with low aspect ratios.

The shear strength envelope curves for the two sets of specimens are shown in Figure 11. To account for the different lateral load levels associated with columns of different heights, the shear force, V, is plotted normalized with respect to the yield shear force, V_y. The figure indicates that greater strength degradation occurred in the columns with the higher aspect ratio.

Level of Axial Load

In order to examine the effect of level of axial load on hinge performance, 1:6-scale Units WA2, CA2, and CON2 and Units WA3, CA3, and CON3 were tested with axial load levels of $0.24f_c' A_g$ and $0.35f_c' A_g$, respectively. The shear strength envelope curves for these specimens are shown in Figure 12. From the figure, higher axial load resulted in greater

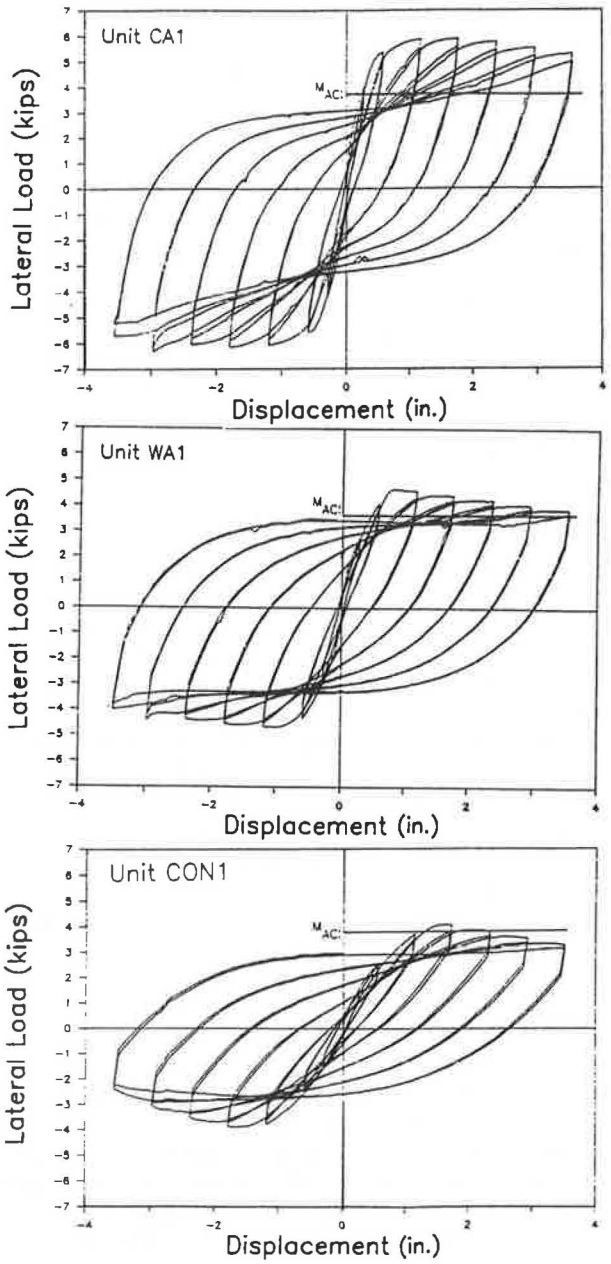

FIGURE 10 Load-displacement hysteresis curves for Units CA1, WA1, and CON1.

degradation in the control columns. However, axial load seemed to have little effect in the columns with the modified hinge details, particularly in the column with the CA detail. The reason that these columns are relatively unaffected by axial load level may be the confining effect provided around the hinge region by the outer column.

Horizontal Discontinuity Joint Thickness

When insufficient discontinuity joint thickness was provided in the moment-reducing hinge details, large prying forces developed from contact of the edges of the outer column with the top of the footing. This prying action resulted in greatly

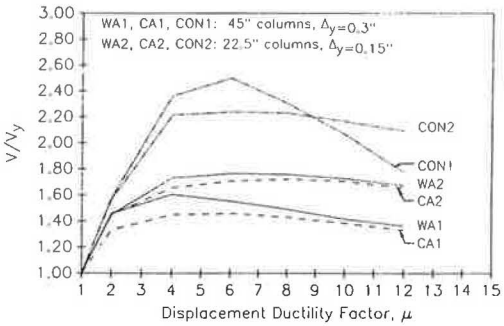

FIGURE 11 Shear strength envelope curves for Units CA1, WA1, and CON1 and Units CA2, WA2, and CON2.

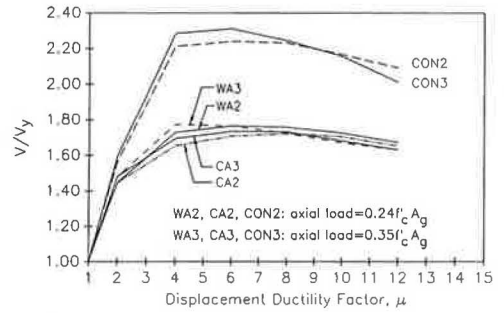

FIGURE 12 Shear strength envelope curves for Units CA2, WA2, and CON2 and Units CA3, WA3, and CON3.

increased strains in the longitudinal bars and larger moments than that in columns with no prying action. Energy dissipation effectiveness was also reduced because of the prying forces.

Detail WA Vertical Joint Height

The test results indicated that providing vertical discontinuity in the moment-reducing hinge detail resulted in a greater plastic hinge length and lower longitudinal bar strains when compared to that for the hinge detail providing only horizontal discontinuity. As the length of vertical discontinuity was increased from one to two hinge diameters, the behavior of the column approached that of the unmodified control columns.

Longitudinal Reinforcing Ratio

In order to evaluate the influence of the longitudinal reinforcing ratio on hinge performance, small-scale specimens with hinge reinforcing ratios of 4, 6, and 8 percent were tested. In general, the behavior of the specimens with the different longitudinal steel contents was similar. However, less degradation and greater energy dissipation effectiveness was observed in the columns with the larger reinforcing ratios.

Transverse Reinforcing Ratio

Small-scale specimens with spiral reinforcing ratios in the hinge of 0, 0.94, and 3.2 percent were tested. Greater degradation and less energy dissipation capability were observed in the specimens with no transverse reinforcement, particularly in the specimen incorporating both horizontal and vertical discontinuity in the hinge detail. However, no sudden failure occurred in the specimens because of the confinement provided around the hinge region by the outer column. There was little difference in behavior between the specimens with 0.94 and 3.2 percent transverse reinforcement.

Circular Versus Square Hinge Cross Section

The performance of columns incorporating square moment-reducing hinge details with tie reinforcement was compared to columns incorporating circular hinge details with spiral reinforcement in the small-scale study. Test results indicated that columns with square hinges experienced significantly more rapid strength degradation than that for columns with circular hinges.

Effects of Low-Cycle Fatigue

In the small-scale study, fracture of the longitudinal bars was observed in columns incorporating detail CA when subjected to repeated loadings at large displacement levels. This result was taken as evidence of greater distress in the longitudinal reinforcement in detail CA than in detail WA. To further examine the low-cycle fatigue characteristics of the moment-reducing hinge details, tests were conducted on Units WA4 and CA4 in the 1:6-scale study. Both units were cycled to a displacement level of $\mu = 10$ and then subjected to multiple cycles at this displacement level. The hysteresis curves for these specimens are shown in Figure 13. For both specimens, little degradation occurred after the completion of the second cycle at $\mu = 10$. The hinges continued to exhibit stable plastic behavior even after being cycled up to 16 times at that displacement level.

APPLICATIONS AND IMPLEMENTATION

Design Recommendations

On the basis of the results of this investigation and a survey of the literature, the following preliminary recommendations are proposed for the design of moment-reducing hinge details at the connection between the column and footing. There are two applications for the proposed hinge detail. The first application is to reduce the moment capacity in a column that has been oversized for architectural or other reasons. For this case, the column foundation connection is designed to carry the required forces resulting from the bridge analysis. The second application is to create as near as possible a pinned connection. For this case, the recommended procedures result in a hinge connection with the smallest possible moment capacity that is capable of carrying the required forces.

1. From equilibrium requirements for the column, determine the design shear force, V_u. For multiple column bents, V_u is determined on the basis of the flexural overstrength,

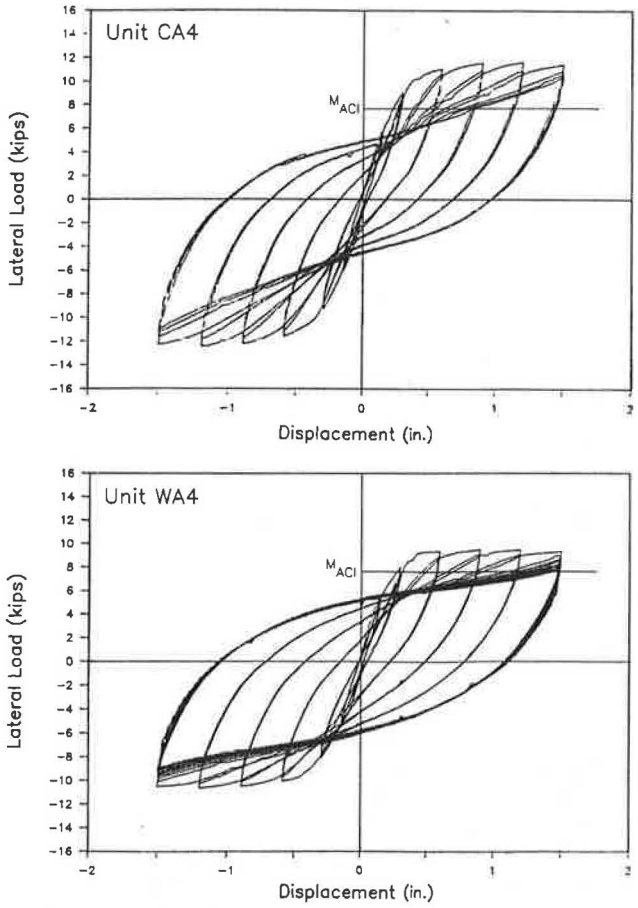

FIGURE 13 Load-displacement hysteresis curves for Units CA4 and WA4.

M_p, of the plastic hinging region at the top of the column. The overstrength moment is calculated as

$$M_p = \phi_0 M_n \tag{2}$$

where

M_p = plastic moment of section,
M_n = ACI nominal moment (of section), and
ϕ_0 = overstrength factor, specified by AASHTO as 1.3.

2. Determine the required hinge area on the basis of the greatest area from the following:

a. Shear friction theory:

$$A_g \geq V_u/(0.2\phi f_c') \tag{3}$$

$$A_g \geq V_u/(800\phi) \tag{4}$$

where

A_g = gross area of hinge section (in²);
V_u = design shear force (lb);
f_c' = concrete compressive strength (psi); and
ϕ = strength reduction factor, taken as 0.85.

b. Maximum allowable diagonal shear:

$$A_c = V_u/[10\ (f_c')^{1/2}\ \phi] \tag{5}$$

where A_c is the core area of section (A_g − cover area) (in²) and ϕ is 0.85.

c. Axial stress limit of $0.7f_c'$ (to ensure ductility):

$$A_g = P_u/(0.7\phi f_c') \tag{6}$$

where P_u is the factored design axial load (lb) and ϕ is 0.75 for circular, spirally reinforced sections.

3. Determine the longitudinal steel required on the basis of the greatest of the following:

a. Shear friction theory:

$$A_{vf} \geq V_u/(\phi\mu f_y) \tag{7}$$

where

A_{vf} = area of reinforcement required for shear fraction (in.²);
μ = coefficient of friction (1.0);
f_y = yield strength of longitudinal steel (psi); and
ϕ = 0.85.

b. Minimum longitudinal reinforcement permitted by AASHTO:

$$A_l = 0.01A_g \tag{8}$$

where A_l is the area of longitudinal reinforcement (in²).

c. For the case of a single column or an oversized column in which a reduced moment capacity is desired, the longitudinal steel area required on the basis of the design loads resulting from the bridge analysis.

4. Determine the plastic moment capacity of the column base hinge:

$$M_{pbh} = \phi_0 M_n \tag{9}$$

where

M_{pbh} = plastic moment capacity of the base hinge,
M_n = ACI nominal moment (of the hinge); and
ϕ_0 = overstrength factor (= 1.6 to account for the increased moment strength enhancement of the moment-reducing hinge detail).

5. As applicable, revise the calculated shear force and axial load (developed from framing action) to reflect the actual moment capacity of the hinge at the base of the column.

6. Repeat Steps 2 through 5 until the design loads converge within 10 percent.

7. Determine the spiral reinforcing ratio required on the basis of the greater of the following:

a. Confinement requirements:

$$\rho_s \geq 0.45\ [(A_g/A_c) - 1]\, f_c'/f_y'\, [0.5 + 1.25\ P_u/(\phi f_c' A_g)] \tag{10}$$

and

$$\rho_s \geq 0.12 \ (f_c'/f_y) \ [0.5 + 1.25 \ P_u/(\phi f_c' A_g)] \quad (11)$$

where $[0.5 + 1.25 \ P_u/(\phi f_c' A_g)]$ is greater than or equal to 1.0 and ϕ is 0.75.

b. Diagonal shear requirements ($V_u = \phi V_c + \phi V_s$):

$$\rho_s \geq 0.2/f_y \ [(V_u/\phi A_c) - 2(f_c')^{1/2}] \quad (12)$$

where

$s = 4 \ A_{sp}/(\rho_s d_c)$,
A_{sp} = cross-sectional area of spiral bar,
d_c = outside diameter of spiral,
s = spacing of spiral, and
ϕ = 0.85.

8. Detailing of the moment-reducing hinge:

a. Provide a ½-in.-thick vertical discontinuity joint with a height equal to the hinge diameter.

b. Provide a length of 1.25 times the rebar development length for the longitudinal bars above the top of the vertical discontinuity joint for anchorage into the column, and ensure proper anchorage into the footing.

c. Provide a horizontal discontinuity joint thickness of at least 2 in. (in some cases, greater thicknesses may be needed to prevent the contact of the outer column edge with the footing).

d. Provide clear spacing of the spiral reinforcement not greater than 6 times the hinge longitudinal bar diameter and not more than 3 in.

e. Provide a ½-in. shear key at the column-foundation connection.

9. Base the design of the footing on the maximum axial load and actual plastic moment at the base of the column.

Design Example

This example illustrates the application of the proposed design recommendations. The column section and design forces used in the example were obtained from the example problem presented in Appendix A of the 1983 AASHTO *Guide Specifications for Seismic Design of Highway Bridges* (*9*).

The column has a clear height of 22 ft and an overall diameter of 4 ft. The factored design axial load and moment for this column are P_u = 1,141 kips and M_u = 3,804 kip-ft. The specified concrete compressive strength, f_c', is 4,000 psi, and a yield strength of f_y = 60,000 psi is specified for both the longitudinal and transverse reinforcements. The slenderness ratio for the column selected for the example is slightly greater than that for which slenderness effects may be neglected, and thus slenderness effects should be considered. However, for simplicity, slenderness is not considered in this example.

Using the appropriate strength reduction factors and the ACI column chart, the column requires 43 No. 10 bars for longitudinal reinforcement. This yields a longitudinal reinforcing ratio of ρ_l = 0.03, which is within the limits specified by AASHTO (*9*).

The design for the moment-reducing hinge detail is presented in the step-by-step procedure of the recommendations outlined previously.

Step 1. The column shear force is obtained from the overstrength plastic moment capacity of the top of the column (initially, the column is considered pinned at the base):

$$V_u = M_p/L_u = \phi_0 M_n/L_u$$
$$= 1.3 \times 5{,}406/22 = 319 \text{ kips} \quad (13)$$

where L_u is the height of the column. The nominal moment capacity, M_n = 5,406 kip-ft, is obtained for the column using the ACI design chart for a longitudinal reinforcing ratio of 3 percent and a clear cover of 2 in., with the strength reduction factor taken as unity.

Step 2. The required circular hinge area is determined on the basis of the following:

a. Shear friction theory:

$$A_g \geq V_u/(0.2\phi f_c')$$
$$= 319/(0.2 \times 0.85 \times 4) = 469 \text{ in.}^2 \quad (14)$$

$$A_g \geq V_u/800\phi$$
$$= 319 \times 1{,}000/(0.85 \times 800) = 469 \text{ in.}^2 \quad (15)$$

b. Maximum allowable diagonal shear:

$$A_c \geq V_u \ [10(f_c')^{1/2}\phi]$$
$$= \frac{319{,}000}{0.85 \times 10 \times (4{,}000)^{1/2}} = 593 \text{ in.}^2 \quad (16)$$

On the basis of the required core area, a core diameter of 28 in. is required. With a 2-in. cover, the core and gross areas required are A_c = 615 in.^{2} and A_g = 804 in.^{2}, respectively.

c. Axial stress limit of $0.7f_c'$:

$$A_g \geq P_u/(0.7f_c'\phi)$$
$$= 1{,}141/(0.75 \times 0.7 \times 4) = 543 \text{ in.}^2 \quad (17)$$

Therefore, a gross hinge area of A_g = 804 in.^{2} should be provided.

Step 3. On the basis of shear friction theory, the longitudinal steel required is

$$A_{vf} \geq V_u/(\phi\mu f_y)$$
$$= 319/(0.85 \times 1 \times 60) = 6.25 \text{ in.}^2 \quad (18)$$

Because this value is less than 1 percent of the gross hinge area, a total of 8 No. 9 bars will be used to provide a longitudinal reinforcement ratio of 1 percent.

Step 4. The plastic moment capacity of the base hinge is

$$M_{pbh} = \phi_0 M_{nbh} = 1.6 \times 991 = 1{,}586 \text{ kip-ft} \quad (19)$$

Step 5. Using the preliminary design of the base hinge, the column shear force is revised to reflect the actual moment capacity at the base of the column. The revised column shear

force V_u' resulting from the plastic moments developed at both the top and bottom of the column is given by

$$V_u' = (M_{pth} + M_{pbh})/L_u$$
$$= (1.3 \times 5{,}406 + 1.6 \times 991)/22 = 392 \text{ kips} \quad (20)$$

where M_{pth} and M_{pbh} are the plastic moments at the top and bottom of the column, respectively.

Step 6. Because of the plastic moment at the base hinge, the column shear force is increased by 23 percent. The design of the base hinge is revised by repeating Steps 2 through 5 until the shear force converges within 10 percent. A final base hinge with a gross diameter of 35 in. and 10 No. 9 longitudinal bars is obtained. The plastic moment capacity of the hinge, $\phi_0 M_{nbh}$, is 2,035 kip-ft.

Step 7. The transverse reinforcement required based on confinement is the greater of

$$\rho_s \geq 0.45[(A_g/A_c) - 1]f_c'/f_y\,[0.5 + 1.25P_u/(\phi f_c' A_g)]$$
$$= 0.45\left(\frac{962}{755} - 1\right)\frac{4}{60}\left(0.5 + 1.25 \times \frac{1{,}141}{0.75 \times 4 \times 962}\right)$$
$$= 0.0082 \quad (21)$$

and

$$\rho_s \geq 0.12\,(f_c'/f_y)\,[0.5 + 1.25P_u/(\phi f_c' A_g)]$$
$$= 0.12 \times (4/60)\left(0.5 + 1.25 \times \frac{1{,}141}{0.75 \times 4 \times 962}\right)$$
$$= 0.008 \quad (22)$$

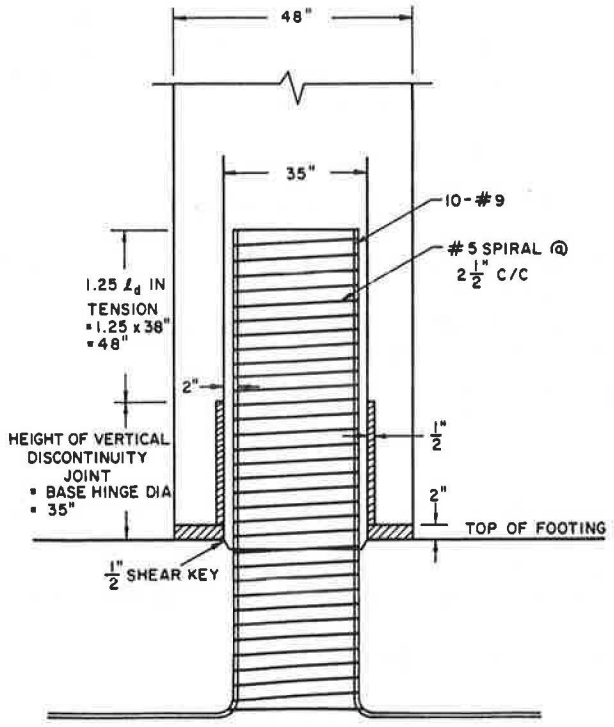

FIGURE 14 Cross-section of the moment-reducing hinge detail for the design example.

The volumetric ratio required based on shear considerations is

$$\rho_s \geq 2/f_y\,[(V_u/\phi A_c) - 2\,(f_c')^{1/2}]$$
$$= \frac{2}{60} \times \left(\frac{412}{0.85 \times 755} - \frac{2 \times (4{,}000)^{1/2}}{1{,}000}\right)$$
$$= 0.017 \quad (23)$$

Therefore, a transverse reinforcement ratio of 1.7 percent is provided using No. 5 spiral at a pitch of 2.5 in.

Step 8. A cross-sectional view showing the details of the moment-reducing hinge is shown in Figure 14.

For the column selected for the example, the plastic moment capacities of the column and the hinge, including the overstrength factors, are 7,028 and 2,035 kip-ft, respectively. Thus, a 70 percent reduction of moment transferred to the foundation is obtained by incorporating the moment-reducing hinge detail when compared to a foundation connection consisting of the constant cross section and reinforcement provided in the column.

CONCLUSIONS AND RECOMMENDATIONS

Conclusions

On the basis of the results of this investigation, the following conclusions are made:

1. Columns with the moment-reducing hinge details of this study exhibited stable hinging behavior similar to that of a conventional column with the same dimensions and reinforcement as that of the hinge.
2. Substantial enhancement of the measured flexural strength over that predicted by current design approaches was observed for all columns. Average enhancement values of 1.17, 1.35, and 1.52 were obtained for conventional columns, columns incorporating moment-reducing hinge details providing both horizontal and vertical discontinuity, and columns incorporating moment-reducing hinge details providing only horizontal discontinuity, respectively.
3. Greater distress in the longitudinal bars and reduced energy dissipation effectiveness was observed in the hinge detail with only horizontal discontinuity when compared to the other hinge details of this study.
4. Flexure controlled the behavior of all of the columns, including those with an aspect ratio of 1.25. However, greater strength degradation occurred in the columns with higher aspect ratios.
5. Higher axial load levels had only a minor effect on the performance of columns with the moment-reducing hinge details. This lack of effect was attributed to the confinement around the hinge provided by the outer column.
6. Columns tested with small horizontal discontinuity joint thicknesses experienced prying action because of contact of the column edges with the footing. This prying action resulted in increases in the hinge moments and reinforcement strains.
7. The concrete of the outer column provided significant lateral confinement around the hinge region in the columns

with the moment-reducing hinge details. However, adequate confining reinforcement was still required in order to obtain stable plastic hinging behavior and satisfactory energy dissipation in the column.

8. Columns with circular spirally reinforced hinge details exhibited better performance than did columns with square hinge details with tie reinforcement.

Recommendations

The following preliminary recommendations are made on the basis of the results of this study and a survey of the literature.

1. Both vertical and horizontal discontinuity should be provided in the moment-reducing hinge detail. The thickness of the discontinuity joint should be selected to accommodate the anticipated rotation requirements of the column base.
2. The column and the moment-reducing hinge detail should be designed on the basis of the actual moment capacity of the hinge detail. Rational procedures based on known principles of performance should be used in the design.
3. Circular hinge sections should be used in the moment-reducing hinge, and spiral reinforcement should be provided over the full length of the hinge detail.
4. The hinge section at the base of the column should be designed for a value lower than the maximum allowable axial load capacity to ensure ductility when subjected to seismic loadings.
5. Conservative evaluations were used for several parameters not investigated in this study, including anchorage requirements of the reinforcing bars, very high axial load levels, shear strength, and the effect of clustering the longitudinal bars. Further research is needed to precisely define the influence of these parameters on the behavior of the moment-reducing hinge details. The current information should also be supplemented by testing multiple column bents incorporating moment-reducing hinge details at the bases of the columns.

ACKNOWLEDGMENTS

The research presented in this paper was funded by the Washington State Transportation Center (TRAC). The authors acknowledge the valuable assistance of Umesh Vasishth of Exeltech Engineering.

REFERENCES

1. K. Y. Lim, D. I. McLean, and E. H. Henley. Moment-Reducing Hinge Details for the Bases of Bridge Columns. In *Transportation Research Record 1275*, TRB, National Research Council, Washington, D.C., 1990, pp. 1–11.
2. K. Sakai and S. A. Sheikh. What Do We Know about Confinement in Reinforcement Concrete Columns? (A Critical Review of Previous Work and Code Provisions). *ACI Structural Journal*, Vol. 86, No. 2, American Concrete Institute, Detroit, Mich., March–April 1989, pp. 192–207.
3. ACI Committee 318. *Building Code Requirements for Reinforced Concrete*. ACI 318-83. American Concrete Institute, Detroit, Mich., 1983.
4. D. I. McLean, K. Y. Lim, and E. H. Henley. *Moment-Reducing Hinge Details for the Bases of Bridge Columns*. Washington State Department of Transportation, Olympia, July 1990.
5. K. Y. Lim and D. I. McLean. Scale Model Studies of Moment-Reducing Hinge Details in Bridge Columns. *ACI Structural Journal*, Vol. 88, No. 4, American Concrete Institute, Detroit, Mich., July–Aug. 1991, pp. 465–474.
6. M. J. N. Priestley and R. Park. *Strength and Ductility of Bridge Substructures*. RRU Bulletin 71. National Roads Board, Wellington, New Zealand, 1984, 120 pp.
7. B. G. Ang, M. J. N. Priestley, and T. Paulay. *Seismic Shear Strength of Circular Bridge Piers*. Research Report 85-5. Department of Civil Engineering, University of Canterbury, New Zealand, 1985.
8. M. J. N. Priestley and R. Park. Strength and Ductility of Concrete Bridge Columns Under Seismic Loading. *ACI Structural Journal*, Vol. 84, No. 1, American Concrete Institute, Detroit, Mich., Jan.–Feb. 1987, pp. 61–76.
9. *Guide Specifications for Seismic Design of Highway Bridges*. AASHTO, Washington, D.C., 1983.

Publication of this paper sponsored by Committee on General Structures.

Abridgment

Climbing: A Unique and Effective Approach to Bridge Inspection

RAYMOND H. STOKES, JR.

Bridges are a critical part of this nation's infrastructure. Their thorough and regular inspection is vital to the safety of everyone who crosses them. However, gaining access to primary structural members of a high-level bridge presents a major dilemma. In 1981, Burgess and Niple Ltd. pioneered a unique approach to bridge inspection using rock-climbing technology. Trained structural engineers and technicians use standard climbing techniques to reach bridge components that are often difficult to access. By applying climbing skills, inspectors can ascend and descend, walk and climb on, swing and hang from, and maneuver around various bridge components. The climbing approach to bridge inspection offers several advantages over traditional methods. The equipment is lighter and less cumbersome than safety equipment used by iron workers. The techniques are often quicker, less expensive, and more effective than mechanical access methods. Inspection by climbing allows little or no disruption of vehicular traffic.

Bridges are a critical part of this nation's infrastructure. Their thorough and regular inspection is vital to the safety of everyone who crosses them. However, gaining access to primary structural members of a high-level bridge presents a major dilemma. Mechanical access methods (underbridge units, aerial lift units, scaffolds, etc.) are used with varying degrees of success. Iron workers hired specifically for their climbing skills lack the technical knowledge necessary to identify and evaluate structural defects. In 1981, Burgess and Niple Ltd. (B&N) pioneered a unique approach to bridge inspection using rock-climbing technology. Trained structural engineers and technicians use standard climbing techniques to reach bridge components that are often difficult to access. This approach not only allows hands-on inspection, but has been proven safe. B&N inspectors are provided with in-house training that includes climbing terminology, use of equipment, and techniques. By applying these learned skills, inspectors can ascend and descend, walk and climb on, swing and hang from, and maneuver around various bridge components. The climbing approach to bridge inspection offers several advantages over traditional methods. The equipment is lighter and less cumbersome than safety equipment used by iron workers. The techniques are often quicker, less expensive, and more effective than mechanical access methods. Inspection by climbing allows little or no disruption of vehicular traffic. B&N climbing techniques are looked on favorably by the Occupational Safety and Health Administration (OSHA), U.S. Department of Labor. B&N realizes the importance of a safe, hands-on inspection and takes the extra effort to perform an untraditional method of inspection.

Burgess & Niple, Ltd., 5085 Reed Road, Columbus, Ohio 43220.

TRAINING

B&N provides in-house training for inspectors that includes terminology, proper care and use of equipment, and techniques for safe, hands-on inspection. Climbing skills are developed through elevated rope exercises, scaling rock faces, and maneuvering on local bridges. Emphasis is placed on proper falling techniques, handling gear, and general safety procedures. Climbers develop trust in their equipment and in one another. Practice improves agility, coordination, and finesse.

EQUIPMENT

B&N uses the following basic climbing equipment, which is lightweight and durable (see Figure 1).

Rope

A nylon line that connects a two-man climbing team and is used during belaying, rappelling, ascending, and rescue operations. The rope has an 11-mm diameter and is of a kern-mantle construction consisting of an outer nylon-braided sheath surrounding a continuous stranded core. Two types of rope are used—dynamic and static. Dynamic ropes are used mainly for belaying.

Carabiner

An aluminum clip that connects climbing equipment to one another. Typically, carabiners are used to connect webbing slings to the rope or to the climber. A carabiner connected to a webbing sling is considered an anchor.

Webbing Sling

A nylon strip tied into a loop that is used primarily to anchor the climber or the rope to the bridge. The strip is 1 in. wide

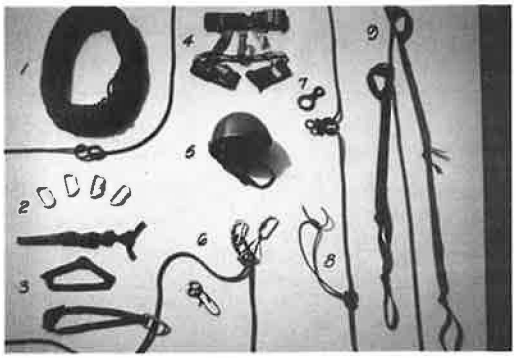

FIGURE 1 Standard climbing equipment.

and is of tubular construction. A water (wet) knot closes the sling's loop.

Sit Harness

A nylon body unit with adjustable waist and leg loops that secures the climber to the rope or webbing sling.

Helmet

A climber's protective headgear. It has safety features such as a bonded urethane foam liner and adjustable chin strap.

Sticht Plate

An aluminum device that rope is fed or retrieved through during belaying. The rope is looped through this plate and both are connected to an anchor.

Figure 8 Ring

An aluminum device that rope is fed through during rappelling. The rope is looped through the larger ring and over the smaller ring. The Figure 8 ring is attached to the rappeller's harness with a carabiner.

Prusik Sling

A nylon static line tied into a loop that secures the climber to the rope during rappelling or ascending. The line has a 5- to 7-mm diameter and is of the same construction as the climbing rope. A double grapevine (fisherman's) knot closes the loop of the sling. The sling is attached to the climbing rope with a prusik knot and to the climber's harness with a carabiner.

Ascenders

A pair of hand-held aluminum mechanical devices that slide along the rope during ascending. Webbing or prusik slings attached to the ascenders are used as footholds by the climber.

TECHNIQUES

B&N uses four standard techniques: climbing with rope, climbing with webbing, rappelling, and ascending.

Climbing with Rope (Belaying)

A method of providing security for a climber by controlling the play of the rope. This technique is typically used when climbing girders, arches, and large truss members. Each end of the rope is connected to a climber of a two-man team. One climber remains stationary (belayer) while the other climber moves about the bridge. The belayer and rope are secured to the bridge with an anchor. The belayer's function is to feed out and retrieve rope at a controlled rate through a sticht plate, so that any fall by the climber will be as short as possible.

As the climber moves away from the belayer, he sets anchors around the bridge components (floor beams, cross frames, diaphragms, bracing members, etc.). The rope is placed through the carabiner of each anchor. Once the climber has used the available length of rope, he secures himself to the bridge and becomes the belayer. The former belayer becomes the climber who removes and sets anchors as he moves toward and beyond the new belayer. By the team members alternating duties of climber and belayer, they are able to leap-frog their way along the bridge.

Climbing with Webbing

A method for climbers to move independently of each other while providing their own security by using webbing slings. This technique is generally used when climbing bracing members and small- to moderate-sized truss members. An anchor is looped around a bridge member and connected to the climber's harness. As the climber moves, the anchor is slid along the bridge member. A climber can hang from his anchors to reach the underside of bridge members. A long sling knotted into several loops can be used as a webbing ladder for ascending or descending.

Rappelling

A controlled means of descending a rope. Friction across the rappeller's Figure 8 ring and body controls the rate of descent. A prusik sling is attached to the rope and used as a safety brake for resting or if the descent rate gets out of control. When descending a single rope, the rappeller should be belayed with another rope as a safety precaution. However, if only one rope is available (generally the case), then it should be doubled and the rappeller descend both halves. In this case, each half of the rope should be secured to an anchor with a butterfly knot. Rappelling is used to descend truss verticals, arch columns, piers, etc., or to exit off a bridge.

The Figure 8 ring is limited to a rappel of less than 100 ft because it is difficult to increase or decrease friction of the rope around the ring. This situation requires the use of a rappel rack that varies the friction of the rope thereby con-

trolling the rappeller's rate of descent. The rack is a steel bar bent into a U-shape on which aluminum brake bars move freely up and down, and which attaches to the rappeller's harness with a carabiner. Passing the rope over and under successive bars creates the friction that controls the rappeller's rate of descent.

Ascending

A progressive method of climbing a rope by using ascenders with attached webbing or prusik slings. The climber alternately ratchets each ascender up the rope while using the slings as steps. A prusik sling is attached to the rope and used as a safety brake for resting. Ascending is used to return to a specific point of a bridge after rappelling or falling from it.

After mastering the techniques and applying his skills, some of the many things a climber can do are as follows:

- Walk on girder and floor beam flanges, arches, truss chords, and suspension cables with handrails;
- Climb arch columns, truss verticals and diagonals, bracing members, and suspension cables without handrails;
- Swing or hang from members of a floor system (stringer, floorbeams, and bracing), truss members, and arches;
- Maneuver around arch columns and girder stiffeners; and
- Descend truss verticals, arch columns, and piers.

The climber has many hand- and footholds available such as flanges, stiffeners, lacing, perforations, rivets, bolts, and various bracing members (see Figure 2).

ATTIRE

When an inspector is preparing for a bridge climb, he must dress according to the environment. Layered, loose clothing is preferable to tight clothing and bulky jackets. Loose clothes allow easy body movement. Layered clothes can be removed and added as the body heats and cools. Thin leather work gloves are more durable and protective than cloth gloves. The type of footwear used by inspectors depends on personal preference. Typically, tennis shoes, running shoes, hiking boots, and work boots are worn. Flexible footwear has good adhesion on sloped surfaces, fits in narrow footholds, and is lightweight. Stiff footwear is better for standing on small footholds and in webbing slings (anchors and ascenders), and provides better wedge action in footholds. Safety glasses can be worn on the climbing helmet and used during cleaning and testing operations. A helmet liner is useful to wear in cold climates. Kneepads can be worn if warranted.

ADDITIONAL EQUIPMENT

Inspectors who climb must also be ready to clean, measure, test, draw sketches, and take photographs and notes. They carry equipment for these tasks in addition to spare climbing and safety equipment in nylon fanny (waist) or back packs and on their harnesses.

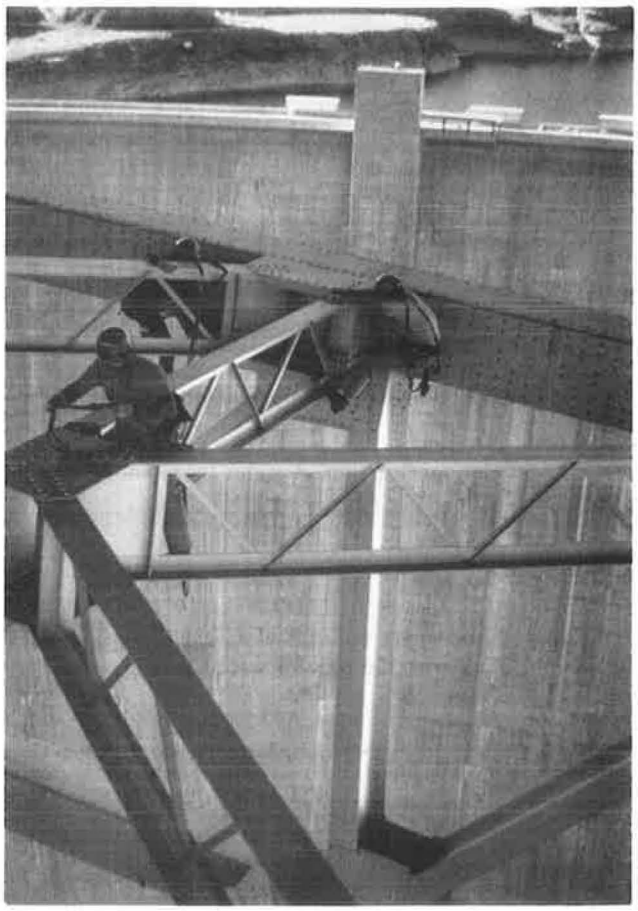

FIGURE 2 Climbing arch bracing.

Some of the measuring tools traditionally used for inspection (calipers, rules, and depth gauges) are cumbersome to use while climbing. In 1987, B&N designed three measuring tools that are adapted for climbing and allow greater flexibility such as one-hand operation and direct readout. These tools include scissor calipers, L-shaped rules, and pit gauges. The tools are used primarily to determine steel component sizes and section loss caused by corrosion.

SUPPORT SYSTEMS

B&N personnel are secured to the bridge at all times while performing their climbing techniques. Each technique has a primary and secondary support system consisting of the climber's body (hands and feet) and equipment.

RESCUE

If a climber should fall while climbing with rope, rescue operations allow the climber to be raised or lowered. The belayer immediately notifies a ground man by way of portable radio. The belayer exits the belay by locking off and securing the sticht plate to prevent any further descent of the climber. The belayer determines if the climber is capable of ascending the rope or if he needs to be raised or lowered. Additional help

or equipment will be obtained by the ground man. The following rescue techniques can be used.

Ascending the Rope

If the climber is not injured and has not fallen a great distance, ascending the rope is the best option. The climber will connect ascenders and a prusik sling to the rope and his harness and begin ascending.

Lowering

It is easier to lower a fallen climber than to raise him as friction and gravity are working with the process. Lowering is not an alternative if any of the following conditions exist: rope is cut, lowering height is greater than the sum of the rope lengths on hand, and there is no suitable location to lower climber to (over water, railroad, power lines, etc.).

Raising

Raising is the slowest and most difficult of the three rescue techniques. Friction, gravity, and stretch of the rope are working against the process. A haul system can be set up by the belayer to aid ascension. The haul system uses pulleys to gain mechanical advantage and prusik slings to prevent the rope from slipping between pulls.

COMMUNICATION

A good communication system is essential in relaying information among the climbing teams, ground man, and authorities. Before the field inspection of a bridge, local law enforcement agencies and emergency medical services are contacted and informed of the location and nature of work. Certain jobs require the use of a cellular phone located in the inspection vehicle. However, other jobs require only ready access to a nearby telephone. The members of each climbing team and the ground man carry portable radios.

When climbing with rope, the belayer and climber must be able to communicate with one another. Communication is usually accomplished by using voice commands in lieu of portable radios. If the area surrounding the climbing team is too noisy to hear voice commands, then hand signals or portable radios are used. If the climber falls and is injured, the belayer notifies the ground man who, in turn, advises the appropriate emergency medical services.

EQUIPMENT MANAGEMENT

Climbing equipment management is a maintenance program for the safety of climbers. Effective management depends on the effort of everyone involved with the equipment including the climbers and the equipment manager. However, the bulk of management lies with the equipment manager. Guidelines inform equipment users of the care, storage, inspection, inventory, coding, and retirement for each piece of equipment.

Duties are split between climbers and the equipment manager. The climbers are responsible for their own equipment during an inspection project and monitor the condition of their equipment daily. They are aware of the possible defects that may occur and know the cause of action to take if a defect is found.

OSHA REGULATIONS

In February 1988, B&N informed OSHA of its bridge inspection program highlighting the climbing approach and requested a clarification or interpretation of the Code of Federal Regulations (CFR) as applied to bridge inspection. OSHA established that the activities of bridge inspection are regulated under the CFR, Title 29, Part 1910. This part of the CFR is the General Industry Standards. Some of the subparts included in Part 1910 are: Subpart D—Walking-Working Surfaces; Subpart F—Powered Platforms, Manlifts, and Vehicle-Mounted Work Platforms; and Subpart I—Personal Protective Equipment. Bridge operations, routine maintenance, service, and inspection are all classified as general industry functions.

B&N met with OSHA officials in April 1988 to present its bridge-climbing procedures. B&N understands that its climbing techniques used for bridge inspection comply with the OSHA Act of 1970. OSHA has acknowledged that the techniques do not fall under the provisions of the CFR, Title 29, Part 1926. This part of the CFR is considered OSHA's Construction Standards. Sections 104–106 of Part 1926 address safety belts, life lines, and lanyards; safety nets; and working over or near water, respectively. Many agencies that perform bridge inspection follow these sections of the Construction Standards.

SUMMARY

Each year many bridges in this country sag, collapse, or otherwise become impassable. Nearly all collapses caused by structural failure could be prevented by thorough inspection procedures and adequate follow-up repair. B&N realizes the importance of a safe, hands-on inspection. Climbing is quicker, safer, and more efficient than time-consuming, costly, traditional methods of inspection. B&N engineers and technicians take the extra effort to perform an untraditional method of inspection. The B&N climbing approach to bridge inspection is unique and effective.

ACKNOWLEDGMENT

The author wishes to express his appreciation to the International Bridge Conference Committee for its permission to use portions of the original paper from the 6th Annual International Bridge Conference, Pittsburgh, Pennsylvania, June 1989.

Publication of this paper sponsored by the Committee on General Structures.

Impact of Turnpike Doubles and Triple 28s on the Rural Interstate Bridge Network

JOSÉ WEISSMANN AND ROB HARRISON

Much truck research undertaken during the 1980s has been directed toward measuring the impact of longer and heavier vehicles on the highway infrastructure. However, bridge costs have been neglected, principally because of the technical difficulties involved in measuring realistic impacts from the available data bases. Recent TRB studies on truck weight limits and Turner vehicles attempt to resolve the issue of bridge costs by including estimates of bridge damage attendant on the operation of various large-truck configurations. At present, these TRB studies constitute the most important sources of information currently available to researchers and policymakers. Yet the assumptions concerning mechanisms for determining bridge deficiencies seem worthy of further investigation, particularly because the TRB findings suggest that productivity benefits substantially overwhelm infrastructure costs. Impact on the rural Interstate bridge system of two long-combination vehicle (LCV) configurations that, although attractive to truckers, were not included in the terms of reference for the TRB studies, is examined. These are double 48-ft trailers (turnpike doubles) and triple 28-ft trailers, both of which use the considerable investment made by the trucking industry in these trailer types. It is estimated that LCV operations on the rural Interstate system result in greater bridge damage than predicted when using the TRB methodology, and that user costs—not reported by the TRB authors—are likely to be extremely high on key rural structures, resulting in cost predictions that could exceed direct agency costs.

During the 1980s, a considerable body of truck research measured the impact of longer and heavier vehicles on the highway infrastructure (*1*). Such truck types are now more commonly termed "long-combination vehicles" (LCVs). Issues investigated have focused primarily on tradeoffs between productivity gains, geometric design, and pavement damage (*2–4*). Truck performance (*5*) and trailer configurations (*6,7*) have received attention as well, leading to useful knowledge regarding the operational implications of LCV units from the trucking industry's perspective. Safety has also been a recurring objective (*8,9*), though the results have frequently been inconclusive and difficult to interpret. Yet bridge damage from LCV trucks has been relatively neglected, in part because of the complex nature of the analysis and paucity of data.

Recent TRB studies have reported on truck weight limit options and issues (*10*), as well as on Turner trucks (*11*), which are configured to lessen pavement damage while increasing gross vehicle mass. In particular, the study on Turner trucks, which includes an estimate of bridge damage attendant on the operation of various larger trucks, represents for researchers and policymakers an important source of information. The mechanism and assumptions made to determine TRB bridge deficiencies seem worthy of further investigation, particularly because the findings suggested that Turner productivity gains overwhelm net infrastructure costs. Notably, these TRB authors did not report user costs incurred during any extensive bridge replacement program—costs that are likely to be extremely high on many structures.

The impact on the rural Interstate bridge system of two LCV configurations that, although favored by truckers, were not part of the terms of reference for the TRB studies, is examined. These are double 48-ft trailers (turnpike doubles) and triple 28-ft trailers, both using the considerable investment made by the trucking industry in these trailer types. In addition, the basic TRB bridge deficiency methodology used to predict bridge failures is broadened and replacement costs are estimated. Finally, some preliminary user cost estimates are associated with the replacement of deficient bridges.

METHODOLOGY

From a U.S. Department of Transportation copy of the latest National Bridge Inventory (NBI) data base (*12*), all Interstate bridges in the system, excluding those located within cities having more than 50,000 inhabitants, were identified. This first-stage exercise produced a data base containing approximately 29,700 structures.

Data from each NBI structural record were next categorized into simple and continuous spans to permit the calculation of bending moments for selected truck types and loads. Load configurations were developed for twin 48-ft and triple 28-ft trailer trucks, on the basis of fully loaded conditions constrained by the uncapped federal bridge formula. A program to predict vehicle moments was then written and applied to all individual rural Interstate structures, with the results for each vehicle configuration compared with the inventory rating on a bridge-by-bridge basis. This rating, originally developed to issue multiple-trip permits, is a more conservative and safer limit (55 percent yield stress) than the operating rating (75 percent yield stress) used in the TRB studies. TRB authors preferred the latter because staff in the bridge divisions in 26 of the 46 states responding to a 1988 survey indicated that they then used operating ratings to post or limit bridge access (*13*). A computer model determined bridge deficiencies. That

Center for Transportation Research, University of Texas at Austin, Austin, Tex. 78712.

is, a bending moments model was run that compared the benchmark standardized rating truck moments for each structure with those induced by the two LCV types—first separately, then operating together. This approach was similar to that reported by the Arizona DOT in 1987 (*14*). Structures that failed to meet the inventory rating load (plus a 5 percent allowance) were identified. In addition, their deck areas were noted to enable a replacement cost estimate to be made from 1989 FHWA unit cost data. Finally, average daily traffic figures for each of the deficient structures were noted and then aggregated to provide an estimate of user cost impacts associated with the state and national replacement programs for such bridges.

SCOPE AND ASSUMPTIONS

General

The impact of operating double 48-ft and triple 28-ft trucks over the continental U.S. Interstate rural bridge network system was investigated under the uncapped (no total vehicle weight limit of 80,000 lb) Federal Bridge Formula (Formula B) limit. The resulting gross loads, axle weights, and dimensions for each LCV type are shown in Figure 1. Although the ability of the current federal bridge formula to protect the infrastructure and permit efficient truck operations has been reviewed in recent research (*15*), the uncapped Formula B is an extension of current legal limits; as such, it remains the best benchmark for this LCV impact study. For each deficient bridge, the deck area and average daily traffic (ADT) were recorded by state, enabling the numbers of deficient bridges to be determined for LCV operations, together with deck surface area and traffic data, first by state, then for the entire national rural bridge network.

Inventory and Operating Ratings

Inventory and operating ratings, originally specified by AASHTO (*16*), are important concepts associated with bending moment models and bridge distress. The inventory rating is defined as the load that produces a stress in the critical bridge element 0.55 times the yield stress (*17*). Generally, the inventory rating is used to issue multiple-trip permits, because the load is designated as what can be used over the design life of a structure without appreciable bridge deterioration.

The operating rating, frequently used to issue single-trip permits and bridge postings, is defined as the load that produces a stress in the critical bridge element 0.75 times the yield stress. As with the previous rating, stresses from the designated vehicle type are compared with the benchmark operating rating figure while a load exceeding the inventory rating—but not the operating rating—will not cause a bridge to collapse; it will shorten the life of the structure by an unknown, and possible significant, amount.

NBI Data Base

Presently, the NBI data base consists of 661,481 records, with each record representing a structure—from culverts to bridges—in the nation's road network. This study addressed the intercity use of LCVs where most LCV ton-miles accrue and ignored the costly process of assimilating them into the urban Interstate networks. This makes the study costs conservative, because urban impacts are likely to be nontrivial. In developing the rural Interstate bridge data base, the basic 661,481 records were reduced to 36,388. In addition, the study disregarded all structures classified as culverts, further reducing the data set to 29,731 bridge structures. For each of the orig-

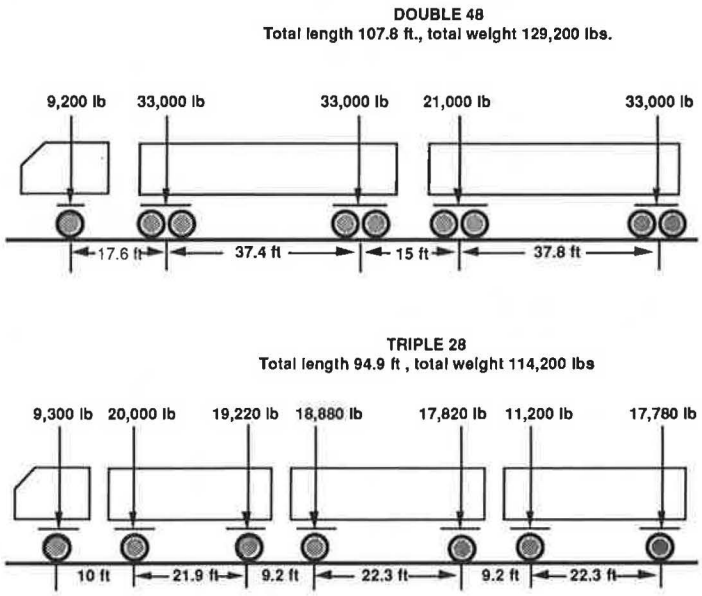

FIGURE 1 Gross loads axle weights and dimensions for double 48-ft and triple 28-ft LCVs.

inal 36,388 structures, selected data were first retrieved from the NBI data base and then sorted by state. Table 1 presents the nationwide distribution of the rural Interstate bridges classified by structure type.

The inventory rating vehicles used by a majority of states for determining operating and inventory ratings are H and HS trucks (*17*). Approximately 80 percent of the Interstate bridge rural subset studied are rated using the HS truck type, while about 11 percent are rated using the H type. For the remainder of the subset, some states (e.g., Kansas and New Jersey) rely on Types 3, 3S2, and 3–3 (*16*) to rate their bridges. Ohio, where all the Interstate rural bridges studied are rated for gross load only, represents a special case. For these bridges, the reported gross inventory rating load was assumed to be distributed over the original design load axle configuration, which turned out to be an HS truck for 96 percent of the structures in the state.

Limitations of the NBI Data Base

The NBI data base is currently the only source of national bridge data available for examining LCV operational policy. Unfortunately, this data base contains transcription errors and inconsistencies in rating procedures between states. Moreover, the NBI, though containing 90 information fields for each bridge on the national network, lacks sufficient engineering detail to determine an accurate analysis of individual bridge capacity. Consequently, several assumptions must be made when studying truck weight and axle configuration impacts. The NBI limits the description of the structural geometry (which directly affects the live-load bending moments calculations) to the number of spans, the structure length, and the length of the maximum span. Such descriptions may be sufficient for modeling a simply supported structure, but they are inadequate with respect to a continuous structure.

TABLE 1 DISTRIBUTION BY STRUCTURE TYPE NATIONWIDE

		Concrete		Steel		Prestress				Bridges+	
State	Concrete	Continuous	Steel	Continuous	Prestress	Continuous	Timber	Culverts	Culverts	Bridges
Alabama	154	113	57	106	7	42	1	205	685	480
Alaska	1		73	23	30		2	2	131	129
Arizona	30	316	9	101	139	9	1	935	1,540	605
Arkansas	137	8	156	24	3			65	393	328
California	387	1,863	152	21	508	264	2	275	3,472	3,197
Colorado	200	131	52	96	54	42	1	105	681	576
Connecticut	7	2	75	6	20			15	125	110
Delaware										
Dist Columbia		2							2	2
Florida	17	21	28	25	573	6		142	812	670
Georgia	144	13	184	106	60	15		170	692	522
Idaho	224	10	18	7	144	1		0	404	404
Illinois	46	93	33	579	140	33		182	1,106	924
Indiana	55	317	190	526	16	18		16	1,138	1,122
Iowa	12	61	2	111	182			81	449	368
Kansas	7	341		189		4	1	118	660	542
Kentucky	88	108	35	117	22	12		76	458	382
Louisiana	374	44	117	74	288		2	198	1,097	899
Maine	2		64	98				26	190	164
Maryland	8	6	109	68	1	3	1	24	220	196
Massachusetts	32	8	293	14	34	6		17	404	387
Michigan	23	19	284	20	108	9		4	467	463
Minnesota	14	35	24	307	243	2		114	739	625
Mississippi	29	105	42	18	290	7	1	140	632	492
Missouri	24	62	31	269	2	29		108	525	417
Montana	56	106	36	88	526	15	1	17	845	828
Nebraska		70	20	35	60	4		45	234	189
Nevada	36	126	16	22	46	4		86	336	250
New Hampshire	38		132	97	12		1	28	308	280
New Jersey	25		338	9	156			64	592	528
New Mexico	15	110	11	74	213	19	2	352	796	444
New York	37	7	700	76	48	10	1	150	1,029	879
North Dakota	11	62	28	119	68	36		46	370	324
North Carolina	32		221	50	94	11		134	542	408
Ohio	33	370	153	1,556	10	1		117	2,240	2,123
Oklahoma	26	142	220	152	10			219	769	550
Oregon	25	333	53	18	94	14	13	0	550	550
Pennsylvania	176	26	116	164	589	5		448	1,524	1,076
Rhode Island	2	2	6	2	6				18	18
South Carolina	193	4	166	23	103			120	609	489
South Dakota		238	4	103	4	19		36	404	368
Tennessee	46	175	11	74	268	87		172	833	661
Texas	573	259	42	267	820	41	1	1,107	3,110	2,003
Utah	24	59	23	48	250	21		82	507	425
Vermont	4		148	91	2			46	291	245
Virginia	124	10	440	106	144			222	1,046	824
Washington	39	171	23	8	116	104		3	464	461
West Virginia	3	7	34	330	14	6		34	428	394
Wisconsin	4	208	12	141	66	103		54	588	534
Wyoming	7	622	15	224	4		4	57	933	876
Totals	3,544	6,785	4,996	6,782	6,587	1,002	35	6,657	36,388	29,731

Two bridges with the following NBI information—one simply supported and the other continuous—can be used as examples:

1. Structure length: 180 ft.
2. Number of spans: 3.
3. Length of maximum span: 80 ft.

Many combinations are possible for the remaining two span lengths for both the continuous and the simply supported bridge, as shown in Figure 2. In the case of the simply supported bridge structure, the modeling approach used calculates the live-load maximum bending moment for the rating vehicle, and the maximum live-load bending moments for both the double and triple LCV configurations using the 80-ft span. Comparing the benchmark moment caused by the rating vehicle with the values from the LCV configurations would then determine bridge deficiency. For such a determination, no assumptions are necessary regarding the bridge geometry as it affects the structural calculations. The critical span of a simply supported bridge is the maximum span, and no interaction exists between adjacent spans of a simply supported structure.

However, because more than half of the bridges in the rural Interstate network are continuous, their analysis requires that some assumptions be made, and questions arise when trying to model this continuous bridge with the NBI available data. For example, is the 80-ft maximum span really the middle span? Are the two remaining spans of the same length? To answer such questions, two assumptions were made: (a) the maximum span is always the middle span; and (b) the remaining spans are calculated by subtracting the maximum span from the overall structure length and dividing the result by the remaining number of spans, as described in the following equation:

$$\text{Secondary span} = \frac{(\text{structure length} - \text{maximum span})}{(n-1)} \quad (1)$$

where n is the number of spans in the structure. In addition, the cross section was assumed to be constant throughout the bridge.

The limitations of the NBI data base make it unsuitable for project-level analysis—for example, for determining what engineering work would correct deficiencies on a specific bridge. However, it is perfectly suitable for network evaluations and, using the previous assumptions, adequate for policy determination of the type sought in this study. Finally, because there is no other comparable national data base, such assumptions must be made for any network analytical modeling.

Structural Models

The calculations performed using NBI data compared the inventory rating bending moments induced on the bridge structure by the rating vehicles, with the bending moments induced by the LCVs under investigation. Inventory rating bending moments are defined as the moments that induce maximum stresses in the bridge superstructure (beams and girders), which are equal to the inventory rating allowable stress as previously defined. Inventory rating bending moments are a combination of the dead- and live-load effects. The type, axle configuration, allowable loading of the rating vehicle, and brief description of the structural geometry are recorded in the NBI data base, making it therefore possible to calculate inventory rating live-load moments for each one of the Interstate bridges, and to compare them with the moments induced by the LCVs under study. The maximum live-load bending moments are calculated by placing the rating vehicles and the LCVs, one at a time, on the position that generates the maximum live load bending moment—an approach similar to that used by White and Minor (*18*).

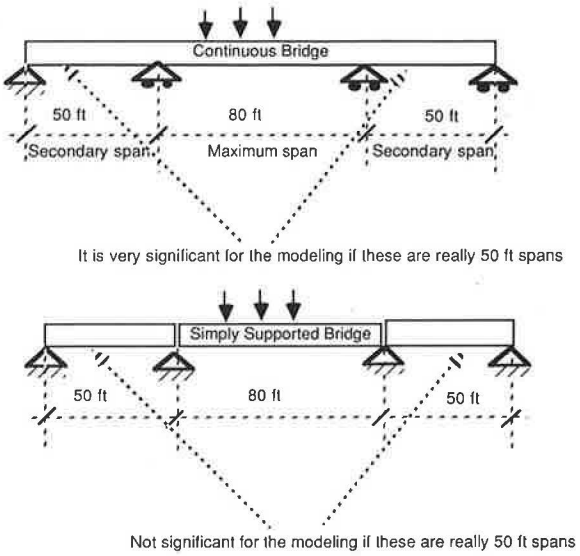

FIGURE 2 Simply supported and continuous bridge calculations as affected by limitations in the NBI data base.

For this study, a bridge was counted as deficient, and thus in need of replacement, if the maximum live-load bending moment, negative or positive, induced by the LCV, exceeded the inventory rating live-load bending moment by 5 percent, a figure reported in the TRB studies. The procedure compared the positive and the negative bending moments, one pair at a time. Now, while the combination of live-load and dead-load moments is usually critical when calculating negative bending moments, the same does not hold for positive moments, where the combination of dead-load and live-load bending moments may affect the search for the bridge cross section having the highest stress. Because dead loads are not recorded on the NBI data base, moment calculations assume that the most critical section for the live load is also the critical section for the combination of dead load and live load.

Deck area and average daily traffic (ADT) were recorded for all bridges screened as deficient. Deficient bridges are reported first by state and then for the nation for double 48s alone, triple 28s alone, and both types together. These data were categorized by two structural types, namely simply supported and continuous bridges. Of the 29,731 bridges identified, 14,569 were classified as continuous structures and 15,162 were classified as simply supported structures. Influence-line diagrams for each structure type were used in the calculations

of the maximum bending moments induced by the rating and LCV configurations under study. Continuous-beam influence line diagrams were used (*19*) to calculate the critical bending moments for the rating vehicles and the LCVs under study. Influence-line diagrams were used to identify the most critical vehicle positions for both negative and positive live-load moments. At the critical positions, where maximum bending moments are induced, the critical bending moments (negative and positive) are calculated using influence-line diagrams. Either negative or positive moment comparisons between rating vehicle live-load bending moments and LCV live-load bending moments will flag a bridge as deficient. The procedures for calculating inventory rating bending moments, LCV bending moments, and deficiencies include the following:

1. Determine if the bridge is continuous or simply supported and obtain the appropriate influence-line diagram.
2. Calculate the maximum bending moments, negative and positive, for continuous bridges, induced by the inventory rating vehicle.
3. Calculate the maximum bending moments, negative and positive, for continuous bridges, induced by the double 48-ft and triple 28-ft LCVs.
4. Flag the bridge as deficient where the LCV live-load moments exceed the inventory rating live-load moments by 5 percent. Record deck area and ADT for each deficient bridge.

A flowchart of the procedure used to perform the screening of structurally deficient bridges nationwide is shown in Figure 3.

All deficient bridges are replaced, not strengthened or rehabilitated (as with the TRB studies). Reasons include the inability to determine appropriate individual bridge corrective strategies from the NBI data, problems of strengthening bridges (like strengthening concrete structures), and the federal requirement that where federal-aid bridges are being strengthened, other features related to functional deficiency must be addressed. The study assumed that all rural Interstate bridges currently met the inventory rating criteria for 80,000-lb trucks. In addition, no allowance was made for grandfathered exemptions, an approach that differed from the TRB study. Many grandfathered configurations are clear LCV types, and logic requires that their impacts be correctly accounted for when determining LCV impacts. Although fatigue costs are not reported, they are likely to be lower than the TRB estimates, because it is assumed that the most conservative of the stress levels (the inventory rating) is used to issue multiple-use permits.

RESULTS

A full summary of the results, by state, is given in Tables 2–4. These cover the number of deficient bridges triggered by triple 28s, double 48s, and both types operating together, respectively. Two categories are reported: (a) the costs of replacing deficient structures, where 1989 FHWA bridge replacement cost data (by state) are adopted; and (b) ADT data for the set of deficient structures. Costs reported are therefore in 1989 prices. The critical costs are those related to the replacement of deficient bridges, including user costs

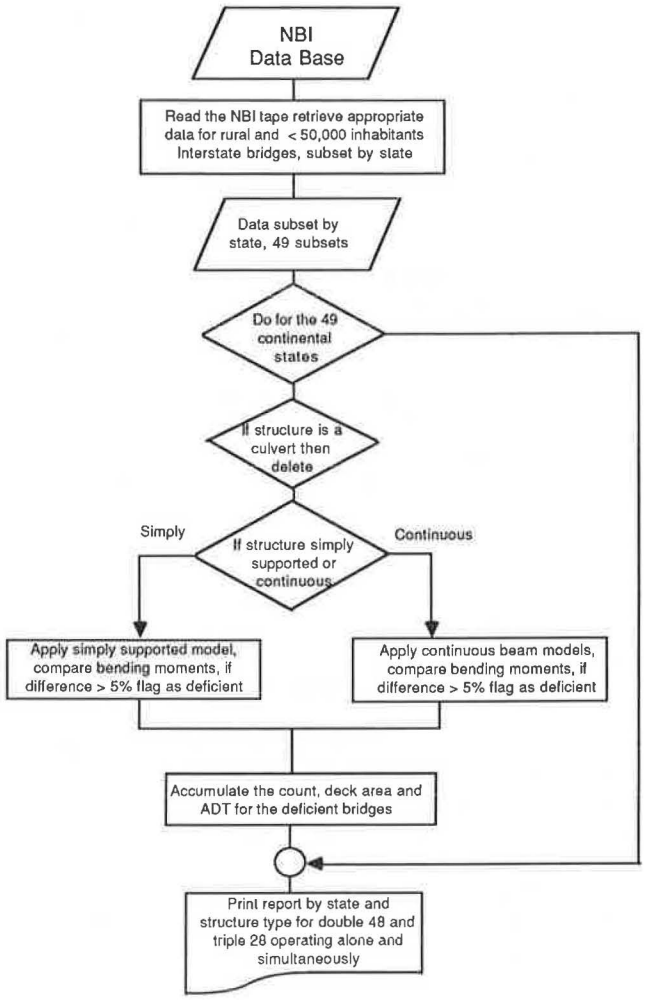

FIGURE 3 Flowchart of the calculations performed when assessing the impacts of LCVs.

attendant on the massive reconstruction program. These are now considered.

Replacement Costs

Replacement costs were developed for each of the two main vehicle categories, and then both operating together. Table 5, which presents results by state, indicates that the operation of triple 28s on the rural Interstate system renders about 2,900 bridges deficient at a replacement cost of $3.9 billion. Double 48s have a much higher impact and render around 6,000 bridges deficient at a cost of $5.8 billion. Finally, both LCV types operating together are predicted to fail around 6,300 structures at an estimated replacement cost of over $6.0 billion. Direct comparisons with other LCV impact results cannot be made because of the different weights and configurations used in the various studies. However, TRB research on heavier trucks constitutes a valuable input for determining the scale of the predicted values on the rural Interstate network. The TRB Turner study nine-axle double has the same axle configuration as the double 48 but is limited to 77 ft in length and around 111,000 lb in mass. The TRB Turner estimates

TABLE 2 SUMMARY OF CALCULATIONS FOR TRIPLE 28s OPERATING ALONE (INVENTORY RATING)

State	Simply Supported Bridges			Continuous Bridges			Continuous and Simply Supported		
	Count	Area	ADT	Count	Area	ADT	Count	Area	ADT
Alabama	6	92	64	4	93	44	10	185	108
Alaska	12	239	51	8	130	27	20	369	78
Arizona	52	335	417	56	589	341	108	924	757
Arkansas	6	100	59	3	304	92	9	404	151
California	264	7,258	10,128	135	7,147	3,942	399	14,405	14,069
Colorado	44	351	230	47	858	284	91	1,208	514
Connecticut	2	10	9	2	106	50	4	116	59
Dist Columbia	0	0	0	0	0	0	0	0	0
Florida	17	950	151	14	1,480	152	31	2,430	302
Georgia	7	181	117	10	596	177	17	777	293
Idaho	30	258	142	1	12	0	31	270	143
Illinois	5	374	22	28	579	213	33	953	235
Indiana	4	34	15	94	1,268	505	98	1,302	519
Iowa	2	9	6	5	134	33	7	143	39
Kansas	3	11	10	276	2,264	1,210	279	2,275	1,221
Kentucky	10	129	78	35	583	442	45	712	520
Louisiana	68	1,894	1,871	15	328	364	83	2,221	2,235
Maine	9	65	38	8	155	87	17	220	125
Maryland	4	73	105	19	540	358	23	613	463
Massachusetts	26	536	1,155	5	251	49	31	787	1,204
Michigan	8	121	83	0	0	0	8	121	83
Minnesota	10	292	315	34	1,415	837	44	1,707	1,152
Mississippi	6	855	100	12	355	105	18	1,209	204
Missouri	6	59	33	82	1,942	705	88	2,000	738
Montana	2	47	5	41	1,255	203	43	1,302	208
Nebraska	8	98	73	11	177	44	19	275	117
Nevada	15	198	40	4	87	8	19	285	48
New Hampshire	13	84	109	53	806	359	66	889	468
New Jersey	96	1,789	3,295	1	24	19	97	1,813	3,315
New Mexico	3	31	10	1	9	6	4	40	15
New York	116	1,880	1,954	21	1,020	373	137	2,900	2,327
North Dakota	2	17	1	48	426	21	50	443	22
North Carolina	32	436	362	16	448	225	48	883	587
Ohio	26	1,003	696	221	2,751	5,622	247	3,754	6,318
Oklahoma	3	28	19	7	117	58	10	145	77
Oregon	20	645	236	18	342	393	38	987	629
Pennsylvania	110	1,222	997	67	1,815	753	177	3,037	1,750
Rhode Island	0	0	0	0	0	0	0	0	0
South Carolina	18	717	112	7	535	72	25	1,252	184
South Dakota	0	0	0	25	244	96	25	244	96
Tennessee	0	0	0	20	501	405	20	501	405
Texas	26	596	243	37	1,651	591	63	2,246	834
Utah	15	139	69	13	162	84	28	302	153
Vermont	6	47	10	8	156	36	14	203	45
Virginia	21	732	786	23	754	415	44	1,486	1,201
Washington	33	445	423	24	484	202	57	929	625
West Virginia	7	74	39	32	849	201	39	924	240
Wisconsin	4	36	71	24	772	212	28	808	283
Wyoming	7	48	27	72	443	165	79	491	192
Totals	1,184	24,537	24,773	1,687	36,955	20,578	2,871	61,493	45,351

Note: Units, Area (sqft) x 1000 and ADT (vehicles) x 1000.

for nine-axle double and seven-axle tractor-semitrailer impacts suggest that 7,000 Interstate and primary bridges would fail the rating criterion (operating) at a replacement cost of $2.8 billion. The TRB 11-axle double has a gross weight of 141,000 lb (near the upper limit for double 48s) but is again limited to 77 ft in length (which severely impacts on bridges), affecting 23,000 Interstate and primary bridges at an estimated cost of over $9 billion. Insofar as it is possible to compare these results, this study would seem to suggest that double-48 and triple-28 operations will have a profound impact on the Interstate bridge, requiring a much larger state replacement program that that indicated by the TRB studies.

Although agency cost considerations have thus far been foremost, any intensive program of Interstate bridge reconstruction will impact on the traveling public in the form of user costs. These costs were not estimated in the TRB document, but the system-wide implications are so great that they deserve to be studied. These implications will be considered next.

User Costs

There were insufficient resources to investigate this issue in detail, but valuable insights into the likely magnitude and impact of these costs can be estimated using only the NBI data. Each bridge record has an ADT, and when determining the characteristics of the deficient bridges, the ADT data recorded on the NBI tape were noted and subsequently aggregated by the vehicle type that rendered the bridge deficient.

The program to replace bridges for triple 28s affected an estimated 45 million vehicles per day. Double 48s affected 85 million vehicles per day, while the two types together affected

TABLE 3 SUMMARY OF CALCULATIONS FOR DOUBLE 48s OPERATING ALONE (INVENTORY RATING)

State	Simply Supported Bridges			Continuous Bridges			Continuous and Simply Supported		
	Count	Area	ADT	Count	Area	ADT	Count	Area	ADT
Alabama	14	845	165	37	453	267	51	1,298	433
Alaska	18	267	58	10	267	72	28	534	130
Arizona	68	403	583	73	682	445	141	1,085	1,028
Arkansas	18	276	183	7	407	127	25	683	310
California	335	8,299	12,687	355	10,820	7,754	690	19,119	20,442
Colorado	74	486	483	89	1,205	479	163	1,691	963
Connecticut	2	5	14	2	106	50	4	111	64
Dist Columbia	0	0	0	0	0	0	0	0	0
Florida	26	1,065	301	27	1,826	203	53	2,892	504
Georgia	13	252	198	31	1,433	462	44	1,686	660
Idaho	74	412	341	5	34	29	79	446	370
Illinois	11	453	61	101	1,104	628	112	1,557	689
Indiana	3	30	38	179	1,727	1,302	182	1,757	1,340
Iowa	5	37	16	32	342	217	37	380	233
Kansas	3	11	10	436	3,323	1,927	439	3,334	1,937
Kentucky	10	129	78	49	742	603	59	871	681
Louisiana	98	2,271	2,634	25	740	931	123	3,011	3,565
Maine	19	118	169	48	580	305	67	698	474
Maryland	5	75	117	28	695	658	33	770	775
Massachusetts	42	616	1,637	9	260	99	51	876	1,736
Michigan	7	108	69	2	12	6	9	120	75
Minnesota	16	388	375	78	2,021	1,680	94	2,409	2,055
Mississippi	15	925	185	17	604	160	32	1,529	345
Missouri	19	128	130	155	2,391	1,206	174	2,519	1,336
Montana	8	141	22	71	1,570	318	79	1,711	340
Nebraska	8	98	73	49	371	282	57	469	355
Nevada	29	456	113	31	233	168	60	690	281
New Hampshire	29	196	207	65	858	531	94	1,054	738
New Jersey	138	3,173	5,232	2	46	62	140	3,219	5,293
New Mexico	4	49	11	48	351	220	52	399	231
New York	157	2,323	2,714	33	1,202	540	190	3,525	3,254
North Dakota	21	148	6	94	662	143	115	810	149
North Carolina	36	444	427	20	459	253	56	902	680
Ohio	41	1,828	1,179	620	6,061	14,556	661	7,888	15,734
Oklahoma	17	73	96	33	477	232	50	549	328
Oregon	30	949	338	105	918	2,070	135	1,867	2,407
Pennsylvania	155	1,624	1,626	100	2,300	1,144	255	3,923	2,769
Rhode Island	0	0	0	1	5	1	1	5	1
South Carolina	35	1,066	328	7	616	60	42	1,682	388
South Dakota	0	0	0	162	995	510	162	995	510
Tennessee	0	0	0	90	1,065	1,904	90	1,065	1,904
Texas	274	2,779	3,258	125	3,562	1,690	399	6,341	4,947
Utah	22	189	87	41	337	163	63	526	250
Vermont	10	97	31	10	286	40	20	383	70
Virginia	39	1,496	1,371	33	953	470	72	2,449	1,841
Washington	58	719	592	72	936	892	130	1,655	1,484
West Virginia	9	96	48	32	849	201	41	945	249
Wisconsin	8	96	160	31	839	271	39	935	431
Wyoming	10	54	43	347	1,485	775	357	1,539	818
Totals	2,033	35,693	38,491	4,017	59,211	47,105	6,050	94,904	85,596

Note: Units, Area (sqft) x 1000 and ADT (vehicles) x 1000.

88 million vehicles. What do such data indicate? A precise answer would require a breakdown of vehicle types (particularly trucks), numbers of vehicles in each category, some measure of daily variation over the week, and time of delay at each structure. Unfortunately, no such data are available from NBI tapes (or from other readily accessible sources), and it would take a dedicated research effort to quantify these effects. In addition, information is needed on the time periods for bridge reconstruction programs. Nevertheless, some assumptions can be made to determine the scale of the impacts.

In attempting to estimate the impacts on traffic affected by the triple 28s and double 48s, whether the traffic data seem reasonable must be considered first. If 88 million vehicles per day are affected, then an average of approximately 14,000 vehicles per day per structure are involved, a figure that does not seem unduly high given the capacity and use of the rural Interstate system. Next, if we assume that half this figure is affected by the capacity constraints imposed by replacement construction activities, then a total of 44 million vehicles per day is predicted to be affected. If we further assume that 5 min are lost per vehicle—decelerating, traveling slowly through or around the construction, and accelerating back to cruising speed—we obtain a total of about 3.7 million hours per day. Now, if only one passenger per vehicle is affected, and their value of time is weighted at $5 per hour, then a total of $18 million per day is lost because of the program. Over a 300-day reconstruction cycle (a figure suggested by records in Texas), a total time delay figure of over $5 billion is thus predicted.

In addition to time costs, vehicle operating costs are affected. Assume that only fuel is affected, and that 0.1 gal is lost per bridge—about 12 cents per vehicle. Then a flow of 44 million vehicles per day produces $5.3 million per day, or $1.6 billion for the 300-day program. Thus, total time

TABLE 4 CALCULATIONS FOR TRIPLE 28s AND DOUBLE 48s OPERATING SIMULTANEOUSLY (INVENTORY RATING)

State	Simply Supported Bridges			Continuous Bridges			Continuous and Simply Supported		
	Count	Area	ADT	Count	Area	ADT	Count	Area	ADT
Alabama	14	845	165	37	453	267	51	1,298	433
Alaska	19	271	59	12	277	75	31	548	134
Arizona	68	403	583	74	692	454	142	1,095	1,037
Arkansas	18	276	183	7	407	127	25	683	310
California	335	8,299	12,687	361	11,017	8,175	696	19,316	20,863
Colorado	75	493	495	94	1,257	508	169	1,750	1,003
Connecticut	4	15	22	2	106	50	6	121	72
Dist Columbia	0	0	0	0	0	0	0	0	0
Florida	26	1,065	301	27	1,826	203	53	2,892	504
Georgia	13	252	198	31	1,433	462	44	1,686	660
Idaho	76	462	349	5	34	29	81	496	378
Illinois	11	453	61	108	1,177	719	119	1,630	780
Indiana	5	42	38	206	1,984	1,440	211	2,026	1,478
Iowa	5	37	16	32	342	217	37	380	233
Kansas	3	11	10	441	3,377	1,966	444	3,388	1,976
Kentucky	10	129	78	52	780	631	62	908	709
Louisiana	100	2,339	2,692	31	803	1,117	131	3,141	3,810
Maine	21	134	180	49	586	311	70	719	490
Maryland	5	75	117	29	778	683	34	854	800
Massachusetts	42	616	1,637	9	260	99	51	876	1,736
Michigan	8	121	83	2	12	6	10	133	89
Minnesota	16	388	375	84	2,073	1,763	100	2,461	2,138
Mississippi	15	925	185	19	617	169	34	1,541	354
Missouri	20	131	131	164	2,466	1,285	184	2,597	1,415
Montana	8	141	22	71	1,570	318	79	1,711	340
Nebraska	8	98	73	51	387	288	59	485	361
Nevada	29	456	113	31	233	168	60	690	281
New Hampshire	29	196	207	75	942	578	104	1,138	785
New Jersey	140	3,215	5,291	2	46	62	142	3,260	5,353
New Mexico	4	49	11	49	359	226	53	408	236
New York	161	2,355	2,760	33	1,202	540	194	3,557	3,300
North Dakota	22	158	6	114	853	152	136	1,010	158
North Carolina	39	481	471	24	495	304	63	975	775
Ohio	42	1,853	1,210	372	6,673	15,702	714	8,527	16,912
Oklahoma	17	73	96	33	477	232	50	549	328
Oregon	30	949	338	107	940	2,113	137	1,889	2,451
Pennsylvania	158	1,657	1,648	103	2,333	1,152	261	3,990	2,799
Rhode Island	0	0	0	1	5	1	1	5	1
South Carolina	35	1,066	328	9	631	86	44	1,697	414
South Dakota	0	0	0	164	1,007	519	164	1,007	519
Tennessee	0	0	0	96	1,132	2,052	96	1,132	2,052
Texas	274	2,779	3,258	125	3,562	1,690	399	6,341	4,947
Utah	22	189	87	50	418	242	72	607	328
Vermont	10	97	31	14	317	57	24	414	87
Virginia	39	1,496	1,371	35	971	504	74	2,467	1,875
Washington	58	719	592	84	1,062	959	142	1,781	1,552
West Virginia	9	96	48	32	849	201	41	945	249
Wisconsin	8	96	160	31	839	271	39	935	431
Wyoming	10	54	43	355	1,546	794	365	1,600	837
Totals	2,061	36,051	38,807	4,237	61,610	49,962	6,298	97,660	88,770

Note: Units, Area (sqft) x 1000 and ADT (vehicles) x 1000.

and fuel costs for triple 28s and double 48s are approximately $7 billion—a substantial impact based on defensible assumptions.

Although the problem of estimating user costs is complex, this large figure suggested that further study was warranted. The financial impacts clearly transcend by a significant (but unknown) amount the agency costs reported for many vehicle configurations in the TRB studies. Concern about the broad assumptions made earlier—and about the significant costs involved—encouraged a more precise examination of the user impacts. Accordingly, the QUEWZ model (*20*), developed at the Texas Transportation Institute for measuring work zone user costs (time and vehicle operating costs) under different traffic scenarios, was selected. This model estimates both vehicle operating costs and passenger time delay costs. Not all bridges were considered, because the traffic levels over many rural Interstate bridges are low enough to enable diversions to one lane per direction without causing congestion. For example, ADT of 15,000 or less did not trigger significant user delay and operating costs when the QUEWZ model was run with a typical bridge work zone traffic strategy. Therefore, the data set was evaluated only for higher ADT levels, specifically bridges exceeding 20,000 ADT, which represent around 18 percent of the rural Interstate population. Because bridge capacity should vary with traffic levels, lane numbers were allocated to various levels of ADT for the purposes of predicting delay and user costs during construction. Two lanes were assigned to the 20,000 ADT level, three lanes to 30,000, and four lanes to the 45,000 category. When dealing with an appropriate traffic management strategy for the 20,000 and 45,000 groups, one and two lanes were closed, respectively. For the three-lane bridge, traffic handling was more complex. After experimenting with various strategies, capacity on the matching bridge was restricted to two lanes, one lane of traffic

TABLE 5 SUMMARY OF DEFICIENT BRIDGES AND REPLACEMENT COSTS FOR VARIOUS TYPES OF LARGE TRUCKS

State		Triple 28 Operating Alone		Double 48 Operating Alone		Triple 28 and Double 48 Operating simultaneously	
	Unit Cost ($/sqft)	Deficient Bridges	Replacement Cost	Deficient Bridges	Replacement Cost	Deficient Bridges	Replacement Cost
Alabama	44	10	8,145	51	57,119	51	57,119
Alaska	117	20	43,143	28	62,495	31	64,079
Arizona	45	108	41,568	141	48,828	142	49,264
Arkansas	47	9	18,988	25	32,094	25	32,094
California	62	399	893,094	690	1,185,374	696	1,197,619
Colorado	48	91	57,999	163	81,155	169	83,999
Connecticut	170	4	19,665	4	18,858	6	20,495
Dist Columbia	164	0	0	0	0	0	0
Florida	53	31	128,809	53	153,256	53	153,256
Georgia	41	17	31,853	44	69,117	44	69,117
Idaho	54	31	14,567	79	24,109	81	26,781
Illinois	50	33	47,673	112	77,845	119	81,501
Indiana	47	98	61,200	182	82,571	211	95,235
Iowa	43	7	6,156	37	16,327	37	16,327
Kansas	38	279	86,448	439	126,693	444	128,729
Kentucky	61	45	43,420	59	53,120	62	55,394
Louisiana	27	83	59,977	123	81,295	131	84,815
Maine	92	17	20,215	67	64,221	70	66,187
Maryland	80	23	49,073	33	61,619	34	68,311
Massachusetts	160	31	125,890	51	140,167	51	140,167
Michigan	69	8	8,331	9	8,311	10	9,177
Minnesota	52	44	88,772	94	125,283	100	127,976
Mississippi	31	18	37,490	32	47,388	34	47,785
Missouri	38	88	76,010	174	95,733	184	98,691
Montana	45	43	58,606	79	77,008	79	77,008
Nebraska	48	19	13,211	57	22,534	59	23,292
Nevada	57	19	16,229	60	39,302	60	39,302
New Hampshire	90	66	80,051	94	94,854	104	102,385
New Jersey	130	97	235,720	140	418,458	142	423,837
New Mexico	50	4	1,988	52	19,972	53	20,399
New York	114	137	330,621	190	401,854	194	405,483
North Dakota	42	50	18,593	115	34,015	136	42,435
North Carolina	42	48	37,106	56	37,900	63	40,958
Ohio	63	247	236,472	661	496,971	714	537,174
Oklahoma	33	10	4,786	50	18,127	50	18,127
Oregon	57	38	56,277	135	106,447	137	107,671
Pennsylvania	107	177	324,970	255	419,812	261	426,893
Rhode Island	79	0	0	1	428	1	428
South Carolina	33	25	41,326	42	55,511	44	56,016
South Dakota	42	25	10,238	162	41,777	164	42,307
Tennessee	36	20	18,044	90	38,330	96	40,760
Texas	33	63	74,127	399	209,240	399	209,240
Utah	42	28	12,667	63	22,077	72	25,482
Vermont	104	14	21,120	20	39,827	24	43,076
Virginia	65	44	96,619	72	159,195	74	160,384
Washington	85	57	78,998	130	140,702	142	151,408
West Virginia	91	39	84,074	41	86,026	41	86,026
Wisconsin	38	28	30,702	39	35,521	39	35,521
Wyoming	41	79	20,127	357	63,089	365	65,605
Totals		2,871	3,871,156	6,050	5,791,958	6,298	5,955,335

Notes: (1) Source for unit cost data, FHWA 1989
(2) Replacement costs in 1,000 dollars.

from the bridge under reconstruction being switched to run counterflow in the closed inside lane. Although this procedure affected users on both bridges, the user costs proved lower than those resulting from three lanes of traffic on one bridge being channeled into one lane.

The predictions for all three ADT categories presented in Table 6 total approximately $6 billion for the bridges exceeding 20,000 ADT. This figure is conservative, because it relates only to a subset of the rural bridge population and uses a truck ADT of 14 percent—lower than most Interstate values. The model also indicates that many high-ADT structures will generate such high user costs that radical planning under construction will be necessary, or their use prohibited to LCVs. This result may, in turn, affect the routing of LCVs and the productivity estimates developed as part of LCV benefits. Further work is underway to assign lane capacities to all failed bridges and to measure the user cost impacts more accurately. However, what preliminary figures clearly indicate is that system costs attendant on the operation of double 48 and triple 28 trucks, configured under uncapped Formula B constraints, of about $12 billion, are very significant, and both replacement and user costs should be compared with predicted productivity gains when attempting to determine the true economic impact.

CONCLUSIONS

Results indicate that LCVs could have a great impact on the Interstate rural bridge network—greater than those estimates obtained using the methodology developed in recent TRB studies. The key assumptions adopted are considered both

TABLE 6 PREDICTED USER COSTS[1] USING QUEWZ MODEL (*20*)

ADT	No. Lanes[2]	No. Deficient Bridges	Cost per Bridge/Day	Total[3] Cost ($ billions)
>20,000 <30,000	2	524	$4,423	0.695296
>30,000 <45,000	3[4]	297	$7,319	0.652123
>45,000	4	363	$39,847	4.339338
Totals		1184		5.686757

[1]Triple 28 and double 48 trucks both permitted to operate on the system.
[2]One lane closed for 2-lane capacity, two lanes for 4-lane capacity.
[3]Cost assumes a 300-day contract cycle per structure.
[4]Construction first rehabilitates two lanes, then the third. Two lanes always open to traffic. When only one lane is open, the matching bridge is opened to diverted traffic and both bridges are reduced to two lane travel.

realistic in terms of the LCV configurations preferred by truckers, and conservative in terms of the inventory rating for bridge fatigue and safety. Furthermore, agency costs are only part of the system impacts; when user costs are included, productivity gains do not necessarily overwhelm total system costs. Although issues related to safety and fatigue costs have not been included in this cost estimate, both are likely to be positive.

Results of this study were compared with a recent American Trucking Association (ATA) document on pavement and bridge damage (*21*). In that document, the authors performed no basic research on the NBI bridge data base, using instead TRB source material. Moreover, the ATA report concentrated only on simply supported structures and did not evaluate continuous bridges. Consequently, its results implied that LCVs were less damaging to the bridge system. The LCV configurations were limited to the uncapped Formula B, but some double-48 rigs are operating at much higher loads, for example up to 146,000 lb on the Florida tollway. Bridge deficiencies are highly sensitive to changes in loadings, and accordingly the LCV configurations were increased to test the magnitude of this change. Increasing the mass of the double 48 in this study to 134,000 lb resulted in an extra 2,000 Interstate structures (33 percent) being rendered deficient. Total replacement and user costs for these bridges were predicted to exceed $17 billion. This sensitivity has profound implications for LCV configurations and weight enforcement strategies. In terms of general policy towards increases in truck size and weight regulations, triple 28s are the least-damaging LCV type, whereas turnpike doubles are significantly more costly, particularly when user impacts are included. Although the implications for LCV user fees, which reflect the highway infrastructure damage, were not considered, they seem an important issue on which to focus additional research.

ACKNOWLEDGMENTS

The authors prepared this paper while engaged as consultants to the Texas Research and Development Foundation (TRDF), Austin, Texas, under contract with the Association of American Railroads (AAR). For technical guidance and assistance, the authors would like to thank Center for Transportation Research faculty at The University of Texas at Austin, as well as members of the bridge division at the Texas State Department of Highways and Public Transportation, and the FHWA. In addition, the 1991 TRB technical session, where this paper was presented, yielded much constructive criticism and identified some technical flaws that have now been addressed.

REFERENCES

1. *Transportation Research Circular 345: Truck Research Profiles*. TRB, National Research Council, Washington, D.C., Jan. 1989.
2. S. R. Godwin, J. R. Morris, H. Cohen, and R. E. Skinner, Jr. Increasing Trucking Productivity within the Constraints of Highway and Bridge Design. *Transportation Quarterly*, Vol. 41, No. 2, 1987, pp. 133–150.
3. *Transportation Research Record 1052*, TRB, National Research Council, Washington, D.C., 1986 (entire issue).
4. *Truck Design and Usage Related to Highway Pavement Performance*. Kentucky Transportation Research Program, Kentucky, 1985.
5. K. N. A. Safwat and C. M. Walton. Expected Performance of Longer Combination Vehicles on Highway Grades. In *Transportation Research Record 1052*, TRB, National Research Council, Washington, D.C., 1986, pp. 63–77.
6. *Special Report 211: Twin Trailer Trucks. Effects on Highways and Highway Safety*. TRB, National Research Council, Washington, D.C., 1986.
7. R. K. Whitford. Limited Trucktrain: A Concept for Energy Conservation and Truck Productivity. In *Transportation Research Record 870*, TRB, National Research Council, Washington, D.C., 1982.
8. K. L. Campbell and L. C. Pettis. *Feasibility Study: Accident Rates of Existing Longer Combination Vehicles*. UMTRI-89-19. University of Michigan Transport Research Institute, Ann Arbor, 1989.
9. B. L. Bowman and J. E. Hummer. *Examination of Truck Accidents on Urban Freeways*. FHWA RD 89-201. FHWA, U.S. Department of Transportation, 1989.
10. *Special Report 225: Truck Weight Limits: Issues and Options*. TRB, National Research Council, Washington, D.C., 1990.
11. *Special Report 227: New Trucks for Greater Productivity and Less Road Wear: An Evaluation of the Turner Proposal*. TRB, National Research Council, Washington, D.C., 1990.
12. *Recording and Coding Guide for the Structure Inventory and Appraisal of the Nation's Bridges*. FHWA, U.S. Department of Transportation, Jan. 1979.
13. F. Moses. *Effects on Bridges of Alternative Truck Configurations and Weights*. Draft Final Report. TRB, National Research Council, Washington, D.C., 1989.

14. R. A. Imbsen and R. A. Schomber. *Simplified Bridge Load Rating Methodology Using the National Bridge Inventory File*. Arizona Department of Transportation, Aug. 1987.
15. R. W. James, J. S. Noel, H. L. Furr, and F. E. Bonilla. Proposed New Truck Weight Limit Formula. *Journal of Structural Engineering, ASCE*, Vol. 112, No. 7, July 1986.
16. *Manual for Maintenance and Inspection for Bridges—1983*. AASHTO, Washington, D.C., 1983.
17. *Standard Specifications for Highway Bridges*, 13th ed. AASHTO, Washington, D.C., 1983.
18. K. R. White and J. Minor. Evaluation of Bridge Overload. *Transportation Engineering Journal, ASCE*, Vol. 1, Jan. 1979.
19. G. Griot and G. H. Lorsch. *Influence Line Tables*. Frederick Ungar Publishing, New York, 1952.
20. J. L. Memmott and C. L. Dudek. *A Model to Calculate the Road User Costs at Work Zones*. Research Report Study 292-1. Texas Transportation Institute, College Station, Tex., 1982 (revised 1985).
21. Sydec, Inc. (with J. Faucett & Associates). *Productivity and Consumer Benefits of Longer Combination Vehicles*. Trucking Research Institute, Alexandria, Va., Jan. 1990.

Any technical errors remaining in this paper are the sole responsibility of the authors.

Publication of this paper sponsored by Committee on General Structures.

Structural Evaluation of the Failure of the Harrison Road Bridge over the Great Miami River

D. R. SCHELLING, C. C. FU, AND V. RAGAVAN

On May 26, 1989, a pile bent and a two-span segment of the temporary bridge that carries Harrison Road over the Great Miami River collapsed. A passenger car fell into the river, causing the drowning of two occupants. Numerous sources confirm that the river, which was in high flood, carried a large amount of debris of various sizes and configurations. According to witnesses' statements, floating debris struck the pile bent, causing it to fail suddenly, bringing with it two sections of the superstructure. A study was commissioned by the National Transportation Safety Board (a) to provide a detailed analysis of the causes and sequence of failure of the structural elements contained within the temporary pile bent and superstructure; (b) to conduct an in-depth review of alternate analyses used to ascertain the causes of failure; (c) to provide recommendations as to the procedural issues which have surfaced due to the failure; and (d) to provide an evaluation of the pile bent with respect to conformance to the AASHTO *Standard Specifications for Highway Bridges*. The results of the study identify various factors that influenced the failure of the pile bent. These include the lack of quantitative guidelines under AASHTO for the determination of frequency and size of floating debris, variances allowed for the design and construction of temporary bridge structures, design procedures for determination of dynamically applied debris forces, and the rating of pile bents under hydrostatic, debris, and line-loading conditions.

In 1987, Hamilton County made a decision to replace an existing 440-ft-long simple-span through-truss with a new bridge over the Great Miami River at Miamitown, Ohio. On May 7, 1987, a consultant firm was commissioned to design the replacement bridge. It was decided to construct a temporary bridge until the new replacement bridge was complete and open.

The contractor submitted a proposal for the construction of both the permanent and temporary bridges on the basis of the consultant's designs and was selected as the successful bidder. Thereupon, the contractor submitted an alternate design for the temporary bridge after award, which is shown in detail in Figure 1. Comparison of the original consultant's design (Figure 2) with the alternate design recommended by the contractor as shown in Figure 1 indicates that the two designs are markedly different in the following respects:

1. The consultant's temporary structure is a three-dimensional frame with bracing positioned to resist lateral loads in two directions. The pier bent designed and constructed by the contractor is a plane frame with bracing positioned to withstand in-plane loads only.

Department of Civil Engineering, University of Maryland, College Park, Md. 20742.

2. The consultant's design exhibited larger members for both the columns and bracing than the contractor's design. Further, the consultant's design had 10 pile bent members as opposed to 4 members provided in the contractor's design. Finally, the consultant's design incorporated a greater amount of lateral bracing than the contractor's design.

3. The consultant's design provided for a much larger pile cap in both section and width than did the contractor's design.

The geometric and structural data that were used in the analysis of the temporary pile bent under the various loads were provided by the National Transportation Safety Board (NTSB) (*1–4*). The basic information relative to the pre- and postfailure conditions is shown in Figures 1 and 2 (*1*).

The actual grade of steel that was used in the construction of the pier bent was uncertain. Values of 36 ksi (i.e., A36 steel) were used for the yield strength in the FHWA, the contractor, and the contractor's consultant analyses. However, metallurgical tests indicate that the grade of steel that was actually used to construct the pile bent was Grade 50. However, because of a potential conflict regarding the value of the yield strength, values of 36 and 50 ksi were both used in the analysis.

Nine locations where the pile sections failed because of the formation of plastic hinges were evident. Table 1 presents the points where failure was indicated in the welds that connected the bracing to the pile members.

STATIC ANALYSIS PROCEDURES

Contained within this section is a definition of the static analysis procedures used to define the critical load conditions and modes of failure of the temporary pile bent. The independent investigation was conducted to assess the causes of failure. The presented analysis, termed the comprehensive analysis, investigated two separate failure modes using a nonlinear three-dimensional finite element analysis.

The objective of the comprehensive analysis is to provide the most appropriate analytical procedures to define most accurately the loading conditions and the manner in which the pile bent failed. In order to meet this objective, the following criteria were used:

1. The most realistic geometric parameters, structural modeling procedures, loading conditions, and material properties were used to replicate the conditions at the time of failure.

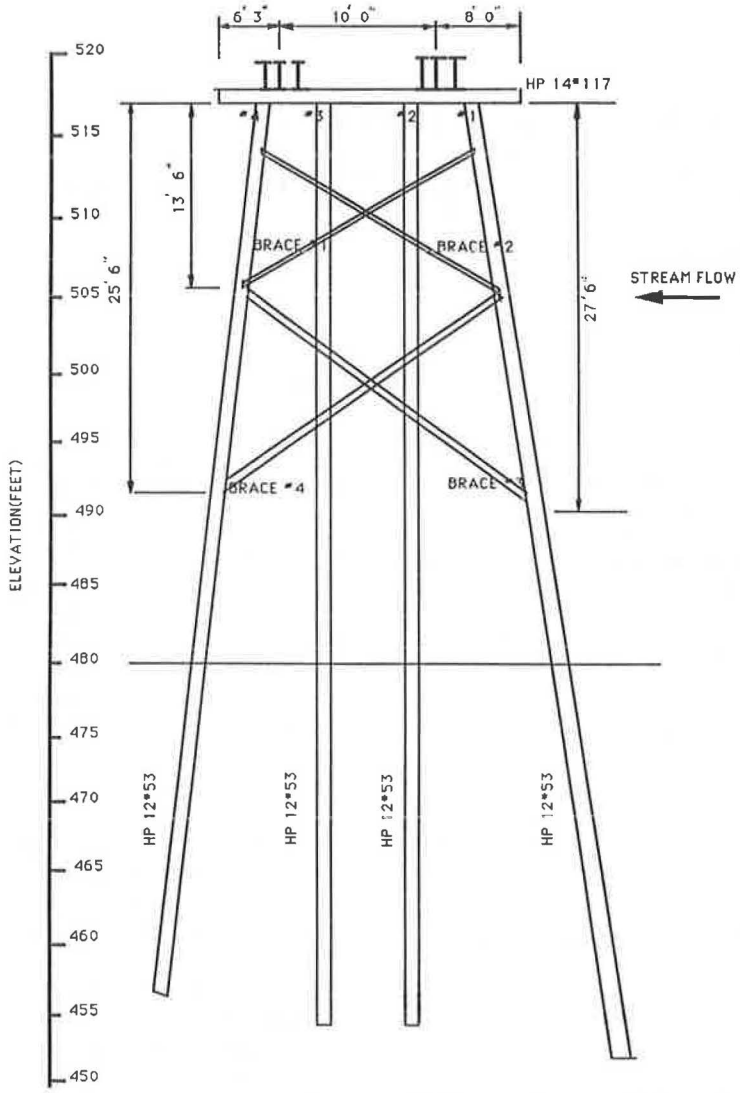

FIGURE 1 Elevation of pile bent (as constructed).

2. The pile bent was analyzed as a system incorporating all influential structural components.

3. The pile bent was investigated with respect to all appropriate and realistic failure modes. These modes were compared to the conditions influencing the bent before and during failure as well as with the postfailure bent configuration as determined by field measurements.

4. Where the prefailure bent parameters, modeling procedures, and postfailure data indicate uncertainty, a range of values was assumed.

Pile Bent Configurations

A series of eight pile bent configurations was subjected to analysis to determine the most probable sequence of failure of the various members and connections contained within the pile bent. Here, a series of three basic configuration types was identified and is defined as follows:

Config ID	*Description*
COR(*I,J*)	The undamaged pier configuration as originally constructed
CPF(*I,J*)	The pile bent at the prefailure condition. Here, various bracing hinges have formed but the damaged pile bent is still capable of sustaining additional load
CCA(*I,J*)	The pile bent is near or at the state of collapse. Here, numerous hinges have formed, large deformations are evident, and bracing connections have failed

For these configurations, the following indices are defined:

Index	*Value*	*Description*
I	1	Modeling with the superstructure included
	2	Modeling with the superstructure not included
J	1	Pier bent with material yield (Fy) of 50 ksi
	2	Pier bent with material yield (Fy) of 36 ksi

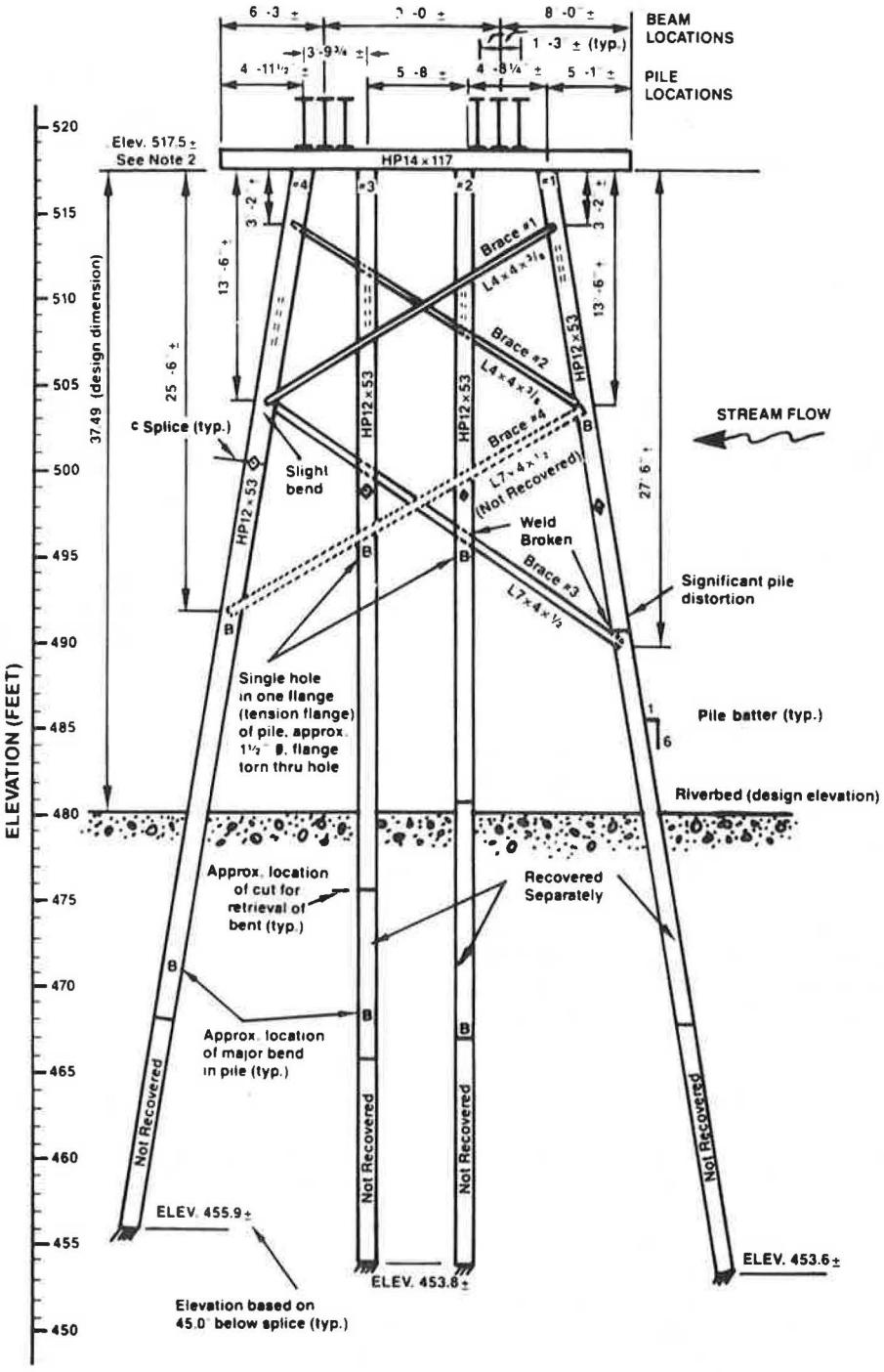

Notes: 1) This drawing based on measurements of salvaged materials.
2) Pier cap elevation based on construction plans.
3) B = Location of bend

FIGURE 2 Elevation of pile bent (postfailure) looking west (east face up).

TABLE 1 POINTS OF FAILURE OF PILE BENT SECTIONS

Pile Number	Brace Number	Hinge Id[a]	Approximate Elevation	Node ID	Comments
1	2	H_{12}	503′	33	Point of application of debris loading
1	3	H_{13}	491′	45	Weld broken
2	3	H_{23}	495′	42	Weld broken; flange containing hole was ruptured
2	–	H_{2G}	468′	50	Approximate fixity point for Pile 2
3	4	H_{34}	495′	43	Flange containing hole was ruptured
3	–	H_{3G}	468′	51	Approximate fixity point for Pile 3
4	1	H_{41}	504′	36	Small bend (*1*)
4	4	H_{44}	491′	48	
4	–	H_{4G}	472′	52	Approximate fixity point of Pile 4

[a]The notation H_{ij} refers to the location of a hinge occurring within the *i*th pile at the *j*th bracing point. When the *j*th bracing point is denoted by G, then the location is at the fixity point of the pile below the midline.

Analysis Components

Two types of analysis were conducted that involve the determination of the lateral load capacity and the sequence of failure from both buckling and elastoplastic-type failures.

First, a stability analysis was performed to determine the capacity and the various column failure modes of the overall structural pier bent system. The results of this analysis were compared with the previously conducted FHWA and the contractor's analyses because they also assumed column-type failure modes. This stability analysis type is often referred to as an eigenvalue buckling or bifurcation analysis. The procedure is conducted by mathematically determining the eigenvalues of the stiffness matrix that represent the critical deformed shapes of the various interconnected structural elements contained within the pile bent system. The load that represents the lower bound of the load capacity from all the various critical member configurations as determined from the eigenvalue analysis is the critical load for the structure.

The second analysis consisted of a determination of capacity and the failure modes of the pile bent caused by the formation of hinges. These occur sequentially throughout the structure as the lateral debris loading is incremented and lead to the overall failure of the bent. The formation of these hinges is characterized as follows (*5–7*)

1. They occur at locations of high moment that exceed the capacity of the section;
2. The hinge itself is caused either by the complete plastification of the section (a plastic hinge) or by buckling of the column element, or by their combination;
3. The formation of a hinge and the moment that initiates its formation may be markedly influenced by the combination of high deformations and axial compressive loadings that occur simultaneously within a member (e.g., P-Delta effects);
4. The formation of any hinge results in the redistribution of moment and forces throughout the entire pile bent. This is caused by the weakening of the structure at the hinge location;
5. A formation of a hinge, in itself, does not indicate overall failure of the bent;
6. When the number of hinges that form within the pile bent exceeds those required for elastic stability, collapse occurs;
7. The formation of hinges generally results in high deformations at various locations throughout the pile bent.
8. The failure of the connections at the juncture of the superstructure and the pile bent could have occurred any time after the formation of the first set of hinges early in the failure sequence. The separation of the superstructure from the pile cap opens the potential for the collapse of the superstructure before the overall failure of the pile bent itself.
9. An elastoplastic analysis is required for the determination of the behavior of the pile bent under the formation of hinges.

A summary of the definition of the column buckling and the elastoplastic mechanism methods used in the comprehensive analysis of the failure of the pier bent are presented in Table 2.

Loadings

The loading components that were applied to the pier bent for analysis of the modes of failure were determined through information supplied by NTSB (*1–4*) and checked by the authors. The components fall into four categories, which are described as follows.

Dead Loading

The dead loads are composed of the pile bent self-weight and that applied to the bent from the superstructure. The value of the dead-load intensities were determined through an evaluation of the various members and components as indicated in the plans compiled by NTSB (*1*).

Live Loading

The live loads were assumed to consist of two cars weighing 12,000 lb positioned directly over Bent 2.

Stream Flow

The loading on the pile bent caused by stream flow is applied as a varying load increasing linearly with depth. A stream velocity of 9 ft/sec was assumed with a full stream force acting on the upstream leg of the bent, 75 percent of the full stream force on the inner legs and no stream force on the downstream leg. The reduction of the force from stream flow on the down-

TABLE 2 DEFINITION OF ANALYSIS COMPONENTS

PIER CONDITION					PURPOSE/METHODOLOGY/ASSUMPTIONS
TITLE (SOURCE)	ANALYSIS ID	F_y (KSI)	PIER CONDITION	L_s	
COMPREHENSIVE ANALYSIS (Authors)	COLUMN BUCKLING FAILURE (CB)	(a)	Original (COR) Prefailure (CPF)	10′	PURPOSE: To determine the global buckling capacities of all the members within the pile bent under various conditions. METHOD: A determination of the eigenvalues of the overall pile bent utilizing 3-D Frame analysis. ASSUMPTIONS: All those inherent within an eigenvalue analysis: 1) Linear elastic material 2) Small deformations 3) Failure occurs by Euler buckling
	ELASTO-PLASTIC FAILURE (EP)	36,50	Original (COR) Prefailure (CPF) Collapse (CCA)	10′	PURPOSE: To determine the capacity and sequence of failure of the pile bent under the incremental application of lateral loads. METHOD: A determination of the loads which will cause full plastification and/or local buckling at various locations throughout the bent utilizing 3-D frame via ANSYS. ASSUMPTIONS: 1) Elasto-plastic material 2) Moment magnification due to large deflection of structure (e.g., P-effects). 3) Moment/rotation values limited by controlling Mp and local buckling. 4) Yield condition is based on the predetermined stress-strain curves based on the unbraced length. 5) The dead, live and stream loads are all staying constant while debris loads increase incrementally. 6) Debris loads must be applied incrementally in order to determine connection failures.

stream pile bent legs is caused by estimated hydrologic shielding effects (*8–10*).

Debris Loading

The debris loading as applied to the pile bent is assumed to be a concentrated force applied upstream at elevation 502 ft. Although a range of values can be assumed including a potentially more severe elevation of 503.5 ft, all values are approximate (FHWA and the contractor assumed an elevation of 499.5 ft) with no elevation being found to be the most accurate. Further, no value of the intensity or exact characterization of the debris loading that caused the failure can be accurately established from field observations. For these reasons, the debris loading is incrementally applied to the pile bent models until failure is indicated and three characterizations of the debris loading are investigated, as follows:

1. The debris loading as applied gradually until failure occurs;
2. The debris loading as applied as a single floating mass that impacts the pile bent and causes sudden failure; and
3. A combination of these loadings.

Loading Spectrum

The loading cases that were used in the comprehensive analysis for determining the causes of failure are presented in Table 3. As indicated in Table 3, a total of 24 case combinations was considered, each requiring over 12 increments of load. Thus, well over 300 individual cases were considered in determining the sequence of failure and the central load combination that caused the failure.

Structural Model

The finite element method was used to determine the response of the pier bent to the loads applied. The definition of the nodes and connectivities (members) that define the modeling of the pier bent is shown in Figure 3. The specific capabilities of the finite element procedures are described as follows:

1. The pier bent is modeled as a three-dimensional frame using prismatic beam elements to represent the members;
2. Geometric nonlinearities caused by large deformations are considered;
3. Material nonlinearity is considered in the form of an elastoplastic idealization; and
4. The elastic buckling analysis uses eigenvalues to determine the critical lateral load intensities.

Pile Fixity

Wet medium sand is assumed to calculate the pile bent fixity locations (*4*). For a wider range of sand material, the fixity location may vary from 7 to 12 ft, and an average embedment distance of 10 ft is assumed.

DYNAMIC ANALYSIS PROCEDURES

The dynamic analysis consists of modeling the pier bent as an equivalent spring system with respect to the application of a lateral load at the water surface (i.e., the Node 33, see Figure 3). Here, the solution of a structurally equivalent one-degree-of-freedom spring mass system is used to represent the impact of a floating mass with the pier bent. Although

TABLE 3 DEFINITION OF ANALYSIS CASES

TITLE (Source)	CASE COMBO	ANALYSIS		LOADING CONDITIONS				PIER MODELS			
		ANALY ID	DESC	LDG ID	DL + LL	SF	DEBRIS	CONFIG ID	F_y KSI	Super Str.	Failure Status
COMPREHENSIVE ANALYSIS	1.1[1]	CB	Buckling	LC1	DL	None	Inc to Failure	COR 1.1	50	With	Pre Failure
	1.2[1]	CB	Buckling	LC1	DL	None	Inc to Failure	COR 2.1	50	W/O	Pre Failure
	1.3[1]	CB	Buckling	LC1	DL	None	Inc to Failure	CPF 2.1	50	W/O	Intermediate
	1.4	CB	Buckling	LC1	DL	None	Inc to Failure	COR 1.2	36	With	Pre Failure
	1.5	CB	Buckling	LC1	DL	None	Inc to Failure	COR 2.2	36	W/O	Pre Failure
	1.6	CB	Buckling	LC1	DL	None	Inc to Failure	CPF 2.2	36	W/O	Intermediate
	1.7[1]	CB	Buckling	LC2	DL+2Cars	Yes	Inc to Failure	COR 1.1	50	With	Pre Failure
	1.8[1]	CB	Buckling	LC2	DL+2Cars	Yes	Inc to Failure	COR 2.1	50	W/O	Pre Failure
	1.9[1]	CB	Buckling	LC2	DL+2Cars	Yes	Inc to Failure	CPF 2.1	50	W/O	Intermediate
	1.10	CB	Buckling	LC2	DL+2Cars	Yes	Inc to Failure	COR 1.2	36	With	Pre Failure
	1.11	CB	Buckling	LC2	DL+2Cars	Yes	Inc to Failure	COR 2.2	36	W/O	Pre Failure
	1.12	CB	Buckling	LC2	DL+2Cars	Yes	Inc to Failure	CPF 2.2	36	W/O	Intermediate
	2.1[1]	EP	Hinges	LC2	DL+2Cars	None	Inc to Failure	COR 1.1	50	With	Pre Failure
	2.2	EP	Hinges	LC2	DL+2Cars	None	Inc to Failure	COR 2.1	50	W/O	Pre Failure
	2.3	EP	Hinges	LC2	DL+2Cars	None	Inc to Failure	CPF 2.1	50	W/O	Intermediate
	2.4[2]	EP	Hinges	LC2	DL+2Cars	None	Inc to Failure	CCA 2.1	50	W/O	Collapse
	2.5	EP	Hinges	LC2	DL+2Cars	None	Inc to Failure	COR 1.2	36	With	Pre Failure
	2.6	EP	Hinges	LC2	DL+2Cars	None	Inc to Failure	COR 2.2	36	W/O	Pre Failure
	2.7	EP	Hinges	LC2	DL+2Cars	None	Inc to Failure	CPF 2.2	36	W/O	Intermediate
	2.8[2]	EP	Hinges	LC2	DL+2Cars	None	Inc to Failure	CCA 2.2	36	W/O	Collapse
	3.1	CB	Buckling	LC3	AASHTO	Yes	AASHTO	COR 2.1	50	W/O	Chk Design
	3.2	CB	Buckling	LC3	AASHTO	Yes	AASHTO	COR 2.2	36	W/O	Chk Design
	3.3	EP	Hinges	LC3	AASHTO	Yes	AASHTO	COR 2.1	50	W/O	Chk Design
	3.4	EP	Hinges	LC3	AASHTO	Yes	AASHTO	COR 2.2	36	W/O	Chk Design

[1] Evaluated but nongoverning.
[2] Governed by CPF analysis; model replaced.

the characterization of such an analysis is approximate, it does yield qualitative results that provide insight into the basic behavior of the pier under impact loading. Both force method and energy method were used to investigate the pile bent under impact. The limiting assumptions of such an analysis are summarized as follows:

1. The mass of the pier, in the force method, is neglected; this assumption tends to overestimate the effect of impact.
2. In the force method, the nonlinear shape of the spring displacement function is assumed to be linear; this assumption overestimates the strength of the pier bent.
3. The hydrodynamic mass, which tends to increase the effect of the impact, is neglected; this assumption tends to underestimate the effect of the impact.
4. Damping effects are neglected; these are felt to be inconsequential.
5. The hydrodynamic force on the mass after impact is neglected. This force could have had a significant effect on increasing the rate of failure of the pier bent.
6. The impact of the mass is assumed to be applied to Node 33 acting in the plane of the pier bent frame throughout the entire time history of failure.

Force Method

A spring-mass system can be represented by the following equation (*11*):

$$\ddot{y} + \lambda^2 y = F(t) \tag{1}$$

where y is the lateral displacement of the floating mass at the debris line (e.g., at Joint 33), $F(t)$ is the force of the water on the debris, and $\lambda^2 = K/M$, where K is the spring constant at the debris line as shown graphically in Figure 4 for the entire range of forces to failure and M is the mass of the floating object.

The assumptions regarding the variables and the boundary conditions for the solution of Equation 1 are as follows:

1. The initial displacement of the mass of the floating debris is given by $y(0) = 0$;
2. The initial velocity of the floating debris is given by $\dot{y}(0) = V_s$, the velocity of the streamflow (9 ft/sec);
3. The mass of the pier bent is neglected;
4. The force of the streamflow is neglected;
5. The density of the floating debris is taken as that of wood, $\rho_w = 0.05$ kg/ft^3;
6. The spring constant, K, will be taken as the initial value of the stiffness of the pier bent, $K = 11.4$ kips/in.;
7. The time of the impact is given by $t = \pi/2\lambda$; and
8. The length of the floating logs as observed is taken as 50 ft (*1*).

From these assumptions, the governing equations of motion are as follows:

$$y = (V_s/\lambda) \sin(\lambda t) \tag{2}$$

$$F = M\ddot{y} \tag{3}$$

where F represents the force of the floating mass on the bent and y is the acceleration of the floating mass. The maximum deformations and accelerations occur for $\lambda t = \pi/2$. Therefore, the maximum force F_m is represented by

$$F_m = M\lambda V_s \tag{4}$$

$$M = F_m^2/(V_s^2 K) = W_l/g \tag{5}$$

where W_1 is the weight of the floating debris, which is idealized as a log.

$$W_1 = F_m^2 g/(V_s^2 K) \tag{6}$$

$$D_1^2 = 4W_1/(\pi L \rho) \tag{7}$$

where D and L represent the diameter and the length, respectively, of the floating log of density ρ.

Energy Method

If the interface forcing function is known, the target structure can be modified mathematically to predict the structural response. Because of lack of information to define a forcing function, energy balance technique is used to estimate structural response.

The impact may be either elastic or plastic. The latter is characterized by the object's remaining in contact with the target subsequent to impact. In elastic impact, it disengages because of the elastic interface restoring force. On the basis of the available information and observation, the debris remains intact with the structure after impact, so the plastic formula is used.

The assumptions for velocity after impact are (a) the duration of the impact is short, and (b) the corresponding spring force is small. Then the velocities of the object and target are given by following equations,

$$V_m = V_s (M_m - eM_e)/(M_m - M_e) \tag{8}$$

$$V_t = V_s M_m (1 + e)/(M_m + M_e) \tag{9}$$

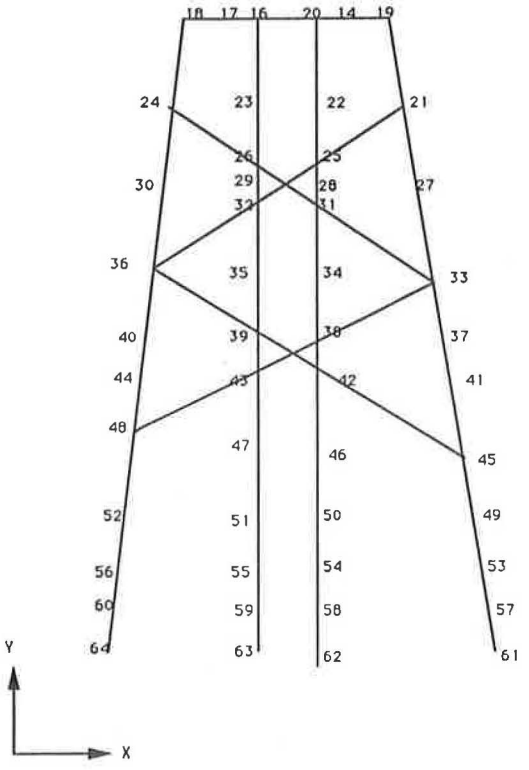

FIGURE 3 Definition of nodes.

The assumption for the required target strain energy capacity for plastic impact are (a) the coefficient of restitution e reduces to zero, and (b) the object and target attain the same velocity. Then the strain energy required is given by

$$E_s = (M_m V_m^2 + M_e V_t^2)/2 \tag{10}$$

From Equations 8 and 9,

$$V_m = V_t = M_m V_s/(M_m + M_e) \tag{11}$$

From Equations 10 and 11,

$$E_s = M_m^2 V_s^2/2(M_m + M_e) \tag{12}$$

Target Effective Mass

For distributed mass element, the effective mass, M_e, during impact varies with the deformed shape of the element during impact. The deflected shape during impact can be approximated by the shape of the first mode, which results in the following expression for M_e:

$$M_e = K/W^2$$

or

$$M_e = K(T_n/2\pi)^2 \tag{13}$$

where the value of K is obtained from the gradient of Figure 1. Finite element modal analysis for bridge substructure was performed to determine the natural frequency of the structure and the effective mass of the target. Then the value of M_e was verified using Equation 13.

Elastic Target Response

$$R_x = KX$$

$$X_m = X_0 + (2E_s/K)^2 \qquad \text{when } X_m < X_e \tag{14a}$$

Elastoplastic Response

$$R_x = KX \qquad \text{when } 0 < X < X_e$$

$$R_x = KX_e = R_m \qquad \text{when } X_e < X < X_m$$

Then

$$X_m = E_s/K(X_e - X_0) + (X_e + X_0)/2 \tag{14b}$$

SUMMARY OF RESULTS

The results of the sequence of failure that most conform to the basic criteria defined before is that given by the elastoplastic failure analysis (see Table 3) that was performed as part of the comprehensive analysis. Here, the lateral debris

loading is applied incrementally, and the effect of each increment is checked for the failure of any component (e.g., piles, connections, and bracing). From this procedure, the following analysis results are obtained as a function of the lateral load intensity:

1. The moments, shears, axle forces, torsion (i.e., the stress resultants), and deformation at each joint;
2. The location of plastic hinges;
3. The failure of any structural component within the pile bent;
4. The level of redistribution of the stress resultants caused by the formation of hinges, along with the failure of any weldment that connects the cross bracing to the pile bent system;
5. The equivalent lateral spring constant of the pile bent at the point of application of the debris loading;
6. The lateral deformations at the beam seat locations; and
7. The value of the intensity of the debris loading when theoretical collapse occurs.

The sequence of the response of Pile Bent 2 to an incrementally applied debris loading is presented in Table 4 for yield strengths of 36 and 50 ksi. The sequence of response represented by the events presented in Table 4 may define the complete load response history of the pile bent. Detailed in Table 4 is a summary of the load levels at which the bracing failed, the sequence and location of the formation of plastic hinges, the deformation at the point of application of the debris and at the top of the pile bent, and, finally, the equivalent stiffness (e.g., the spring constant) of the pier bent system. This spring constant is shown in Figure 4 for the full range of loadings and deformation to failure. From the results of the analysis, the following conclusions can be drawn:

1. The postfailure configuration of the pile bent as documented by NTSB (*1*) conforms to the locations of the hinges predicted by the elastoplastic failure analysis. A summary of the correlation of the hinges from analysis and from field observations is presented in Table 5.
2. The failure of Pile Bent 2 was initiated at a debris loading of about 15 kips for both yield strengths of 36 and 50 ksi by using the elastoplastic method.
3. The intensity of the lateral debris loading required for overall collapse ranged from about 20 to 22.5 kips for a yield strength of 36 ksi and more probable range of values of from 22.5 to 25 kips for a yield strength of 50 ksi.
4. The value of the lateral debris loading at which the connections that attach the superstructure to the pier bent failed and that caused the superstructure to fall off the pier seat is not known from analysis. (Because of the lack of data regarding the size and postfailure disposition of the beam seat connections, a quantitative analysis of the sequence of failure of the superstructure is not possible.) The intensity of the debris loading that caused the failure (falling) of the superstructure ranges from 15,000 to about 25,000 lb.
5. The influence of the superstructure on the overall lateral in-plane stiffness of the pile bent is negligible.
6. The superstructure elements provided a degree of stiffness adequate to prevent out-of-plane torsional movement of the pile bent as well as out-of-plane buckling of Pile (Column) 4.
7. In order to perform the elastoplastic analysis of the pile bent as a system, it is necessary to consider the interacting influence of all members including bracing elements. The alternate buckling analysis assumes that these are secondary non-load-carrying members with lower strength requirements. Examples of such differences as cited by AASHTO (*9,10*) for compression members are given as follows:

		Primary Members		*Secondary Members*	
Item	*AASHTO Ref.*	*Limit*	*Actual*	*Limit*	*Actual*
b/t	10.35.2.3 (Compression)	12	14	16	14
KL/r	10.7.1 (Compression)	120	94	140	137
L/r	10.7.5 (Tension)	200	94	240	137

The 14 actual primary tension members violate the AASHTO primary member requirements.

TABLE 4 PIER BENT STATUS FOR VARIOUS INTENSITIES OF DEBRIS LOADING

Fy (KSI)	DEBRIS LOADING (k)	PIER CONDITION																		LATERAL DEFORMATION			K_{33}
		Hinge Formation Joint List																		Status of Bracing	Config ID	Joint 33 (IN)	Jt. 19 (IN)	Max/Joint (IN/Joint No)	(K/ft)
(1)	(2)	48	64	62	61	43	63	42	58	45	60	59	46	50	54	55	38	56	39	57	(4)	(5)	(6)	(7)	(8)	(9)
50	5.0																				Intact	COR2.1	.620	-0.58		136.8
	7.5																					COR2.1	.850	-0.65		136.8
	10.0																					COR2.1	1.053	-0.80		136.8
	12.5																					COR2.1	1.254	-0.96		136.8
	15.0		X	X	X																	COR2.1	1.497	-1.14	1.82/41	136.8
	17.5	X	X	X	X		X	X														CPF2.1	1.835	-1.40	2.22/41	Variable
	20.0	X	X	X	X	X	X	X	X	X	X											CPF2.1	2.500	-1.91	3.01/45	Variable
	22.5	X	X	X	X	X	X	X	X	X	X	X	X		X							CPF2.1	2.578	-2.72	4.33/45	20.7
	25.0	X	X	X	X	X	X	X	X	X	X	X	X		X							CPF2.1	4.872	-3.70	5.94/45	20.7
	27.5	X	X	X	X	X	X	X	X	X	X	X	X		X	X						CCA2.1	6.258	-4.74	7.66/45	20.7
	30.0	X	X	X	X	X	X	X	X	X	X	X	X		X	X					Failed	Unstable	7.763	-5.88	9.53/45	20.7
36	<15.0																				Intact	COR2.2				136.8
	15.0	X	X	X	X																	COR2.2			1.85/41	
	17.5	X	X	X	X	X	X	X	X	X												CPF2.2			2.31/41	Variable
	20.0	X	X	X	X	X	X	X	X	X	X											CPF2.2			3.29/45	Variable
	22.5	X	X	X	X	X	X	X	X	X	X	X	X	X	X							CPF2.2			4.73/45	20.7
	25.0	X	X	X	X	X	X	X	X	X	X	X	X	X	X							CCA2.2			6.38/45	20.7
	27.5	X	X	X	X	X	X	X	X	X	X	X	X	X	X	X	X					CCA2.2			8.20/45	20.7
	30.0	X	X	X	X	X	X	X	X	X	X	X	X	X	X	X	X	X	X	X	Failed	Unstable			10.73/45	20.7

Notes: a) Values have been used from Fy = 50 case since the overall stiffness for Fy = 36 is almost identical.

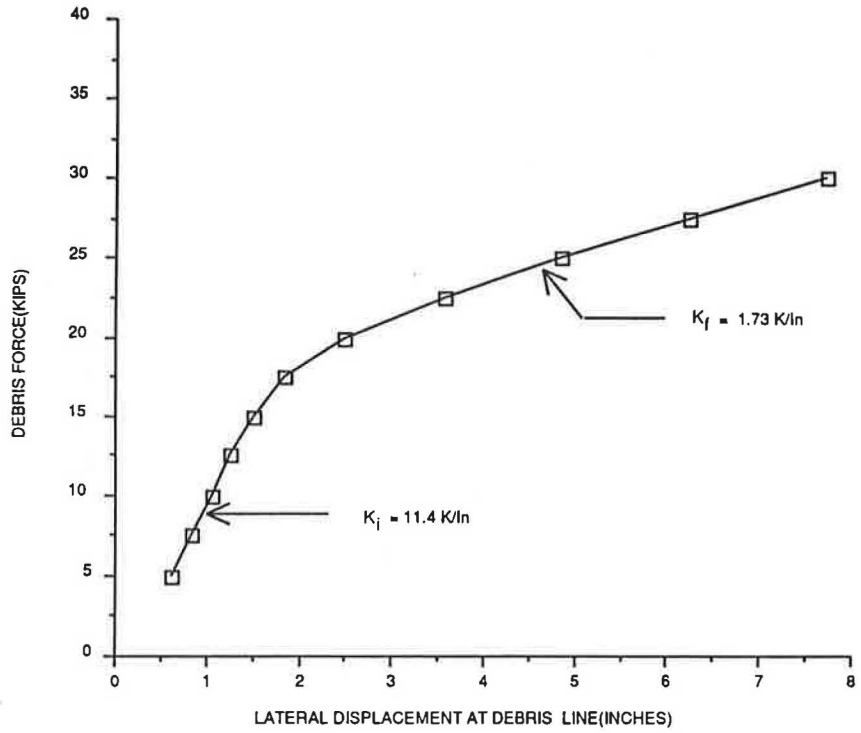

FIGURE 4 Debris force versus displacement for pile bent.

TABLE 5 COMPARISON OF RESULTS OF ANALYSIS AND FIELD OBSERVATION

ID	LOCATION				FIELD OBSERVATION	RESULTS OF ANALYSIS		
	Col. No.	Bracing No.	Node No.	Elevation		Fy (Ksi)	Formation of Hinge	Loading (k)
H_{12}	1	2	33	503′	Hinge with rotation of about 35°	50	None observed	(a)
H_{13}	1	3	45	491′	Severed		Hinge formation	17.5
H_{16}	1	-	61	468′	Member not recovered		Hinge formation	15.0
H_{23}	2	3	42	495′	Hinge location w/ tear & 90° rotation		Hinge formation	17.5
H_{2G}	2	-	62	468′	Severed		Combined plasticized	15.0
H_{2G}	2	-	58	468′	Severed		region for nodes 62 & 58	20.0
H_{34}	3	4	43	495′	Hinge location w/ tear & 90° rotation		Hinge formation	20.0
H_{3G}	3	-	63	468′	Severed		Combined plasticized	17.5
H_{3G}	3	-	59	468′	Severed		region for nodes 63 & 59	22.5
H_{41}	4	1	36	504′	Small bend observed (Ref 12)		None indicated	(b)
H_{44}	4	4	48	491′	Hinge location with 100° rotation		Hinge formation	17.5
H_{4G}	4	-	64	472′	Hinge location with 60° rotation		Combined plasticized	15.0
H_{4G}	4	-	60	472′	Hinge location with 60° rotation		region for nodes 64 & 60	20.0
H_{12}	1	2	33	503′	Hinge with rotation of about 35°	36	None observed	(a)
H_{13}	1	3	45	491′	Severed		Hinge formation	17.5
H_{1G}	1	-	61	468′	Member not recovered		Combined plasticized	15.0
H_{1G}	1	-	57	468′	Member not recovered		region for nodes 61 & 57	30.0
H_{23}	2	3	42	495′	Hinge location w/ tear & 90° rotation		Hinge formation	17.5
H_{2G}	2	-	62	468′	Severed		Combined plasticized	15.0
H_{2G}	2	-	58	468′	Severed		region for nodes 62 & 58	17.5
H_{34}	3	4	43	495′	Hinge location w/ tear & 90° rotation		Hinge formation	17.5
H_{3G}	3	-	63	468′	Severed		Combined plasticized	17.5
H_{3G}	3	-	59	468′	Severed		region for nodes 63 & 59	22.5
H_{41}	4	1	36	504′	Small bend observed (Ref 12)		None indicated	(b)
H_{44}	4	4	48	491′	Hinge location with 100° rotation		Hinge formation	15.0
H_{4G}	4	-	64	472′	Hinge location with 60° rotation		Combined plasticized	15.0
H_{4G}	4	-	60	472′	Hinge location with 60° rotation		region for nodes 64 & 60	20.0

8. When resisting lateral forces, the pier bent actually performs as a frame with the non-pile-bracing members acting as main load-carrying members and not as bracing per se. In such cases, it would be prudent to design the bracing members as primary members because the lateral loads most often govern the design.

9. The holes that exist at Nodes 42 and 43 on one side of the flanges of each column member have caused the increase of stress adjacent to the holes (i.e., stress concentrations or stress raisers). Such increases in stress have resulted in the tensile failure of the flange material from the hole to the outer edge of the flange.

The separation of the material at Nodes 42 and 43 may have caused a low-to-moderate weakening of the pile bent as compared with the results obtained from an analysis of the pile bent with no holes.

10. It has been determined that the pile bent does not meet the strength requirements for even a minimal lateral load intensity caused by waterborne debris.

11. The original design submitted by the consultant may have represented a much more appropriate design, with respect to the capacity to resist lateral loadings such as those caused by floating debris.

The results of a dynamic analysis of the pile bent subjected to a floating mass impacting at the water level are presented in Table 6. These results were generated from the solution of a spring mass system. Here, the weight of the maximum critical log, assumed to be 50 ft in length, along with the corresponding diameter of the log is given for yield strengths of 50 and 36 ksi. The results as summarized in Table 6 lead to the following conclusions:

1. An event characterized by a floating log 50 ft in length and ranging from about 7 to 14 in. in diameter impacting the pile bent at stream flow velocity is capable of providing the lateral impact force required for collapse of the pile bent.
2. If the pile bent were to be rated for an event characterized by the impact of a floating log, the rated log would be 50 ft in length and about 4 in. in diameter.
3. The most probable characterization of the debris that actually struck the pile bent and caused it to fail is a combination of impact and a constant force. A review of the types of debris shown on a video taken at the time of the flood indicates objects exhibiting both large surface areas and mass often interconnected together. A combination of hypothetical combinations of impact and constant force caused by hydrostatic effects is given as follows for a log 50 ft in length and 7 in. in diameter:

ID	*Surface Area*	*K*	V^2 *(ft/sec²)*	*Constant Force (kips)*	*Impact Force (kips)*	*Combined Force (kips)*
1	25	1.375	81	2.8	15.0	17.8
2	64	1.375	81	7.1	15.0	22.1
3	100	1.375	81	11.1	15.0	26.1
4	160	1.375	81	17.8	15.0	32.8

The *K* values originated in Article 3.18.1 (*9*).

Thus, even an object of minimal mass coupled with a surface area of 160 ft² (e.g., a dock about 8 ft deep and 20 ft long) can exert a combined force of over 32 kips, which is in excess of that required for collapse.

An evaluation of the pile bent structure was performed using the 1983 *Standard Specification for Highway Bridges* (*9*). This evaluation involved those provisions that would apply to steel pile bent support structures under the service load design method.

The results from the application of the AASHTO provisions for combined stresses for Column 4 given in Article 10.36 and Equations 10–41 and 10–42 for all applicable load group combinations are presented in Table 7.

A review of the summary indicates that three factors have influenced the performance of the pile bent:

1. Velocity of the stream flow in providing the inertia effects for floating debris;
2. The weakness of the pile to cross frame connections; and
3. The nonconformance of the pile bent design to the AASHTO specification.

Other factors that entered into the structural evaluation are either minor (i.e., depth to fixity, yield strength, and intensity of the dead and live loadings) or are unknown (i.e., the in-

TABLE 6 SUMMARY OF CRITICAL IMPACT CASES

LOAD IMPACT CASE		PIER BENT		LATERAL LOAD				MAX CRITICAL LOG		
ID	Description	Fy (ksi)	K (K/Ft)	Value (K)	F.S.	Time (sec)	Description	Weight (K)	Length (Ft)	Diam (Ft)
	FORCE METHOD:									
DL1.2.1	Rated value for debris loading	50	136.80	8.3	1.8	0.0106	Pre-failure cond.	.200	50	.32
DL1.2.2	Required for connection failure and formation first hinges	50		15.0	1.00	0.0191	Pre-failure cond.	.654	50	.58
DL1.2.3	Most probable upper limit	50		25.0	1.00	0.0319	Upper collapse value	1.816	50	.96
DL1.2.4	Most probable value at failure	50		22.5	1.00	0.0287	Lower collapse value	1.471	50	.87
DL1.2.5	Failure of weld at node 45						Collapse	2.615	50	1.15
DL2.2.1	Rated value for debris loading	36	136.80	8.3	1.8	0.0106	Pre-failure cond.	.200	50	.32
DL2.2.2	Required for connection failure and formation first hinges	36		15.0	1.00	0.0191	Pre-failure cond.	.654	50	.58
DL2.2.3	Most probable upper limit	36		22.5	1.00	0.0207	Upper collapse value	1.471	50	.87
DL2.2.4	Most probable value at failure	36		20.0	1.00	0.0255	Lower collapse value	1.162	50	.77
DL2.2.5	Failure of weld at node 45	36		30.0	1.00	0.0383	Collapse	2.615	50	1.15
	EQUIVALENT ENERGY METHOD:									
DL1.2.2	Required for connection failure and formation first hinges	50	136.80	15.0	1.00	---	Pre-failure cond.	2.46	---	---
DL2.2.2	Required for connection failure and formation first hinges	36	136.80	15.0	1.00	---	Pre-failure cond.	2.46	---	---

TABLE 7 SUMMARY OF RESULTS FOR THE AASHTO CODE CHECK (*9*) ON PILE BENT 2

AASHTO GROUP COMBINATIONS								RESULTS FOR PILE 4 (nodes 48-64)	
GROUP NO.	DL	L+I	SF	W	WL	ICE	% of Allowable Stress	Eq 10-41	Eq 10-42
I	1	1	1	0	0	0	100	Meet	Meet
II	1	0	1	1	0	0	125	Not meet	Not meet
III	1	1	1	.3	1	0	125	Not meet	Meet
IV	1	1	1	0	0	0	125	Meet	Meet
V	1	0	1	1	0	0	140	Meet	Meet
VI	1	1	1	.3	1	0	140	Meet	Meet
VII	1	0	1	0	0	0	133	Meet	Meet
VIII	1	1	1	0	0	1	140	Not meet	Not meet
IX	1	0	1	0	0	1	150	Not meet	Not meet

fluence of the holes in the flanges, the importance of the strength of the connections, and scour).

CONCLUSIONS

The primary causes of failure of the pile bent were the lack of structural capacity under the application of lateral loadings. Various indications were evident within the results developed herein that amply supported this conclusion, as follows.

- Field Survey. The postfailure configuration of the pile bent as determined by an NTSB field survey (*1*) indicated that the failure was caused by a lateral load. Further, a finite element analysis of the pile bent indicated that the level of lateral load required for a failure pattern that was virtually identical to that determined by field observation ranged from 22.5 to 25.0 kips. This correlation verifies that the computer model is predicting the basic behavior of the pile bent correctly.
- Pile Bent Configuration. The pile bent may have been proportioned to resist the vertically applied dead and live loads only. The factors to safety for such loadings were found to be high (3.8), as opposed to the factors of safety resulting from laterally applied loads, which were low, in some cases below 1.0 (i.e., they fell below the specified level of safety). Further, the placement of the lateral structural elements indicated that they were positioned to serve as bracing to strengthen the piles against in-plane buckling rather than to resist lateral forces.
- Code Check. The application of the combined group loadings to the pier bent indicated structural nonconformance to the AASHTO specifications. Specifically, the pile bent failed to meet the AASHTO requirements for Groups II, III, VIII, and IX, each of which contains high lateral load components that include load combinations resulting from stream flow, wind, wind on live loads, and ice. According to AASHTO, "The loading combinations shall be in accordance with Article 3.22" (*9*). Article 3.22 specifies, "Each component of the structure, or the foundation on which it rests, shall be proportional to withstand safely all group combinations of these forces that are applicable to the particular site or type" (Article 3.22) (*9*). Here, no qualifications are stated that limit these requirements for temporary structures.
- Computed Lateral Capacities. The capacity of the pile bent under the application of lateral loadings has been estimated under various criteria summarized as follows:

Criteria	*Lateral Load (kips)*
Nonlinear Analysis	
Rated lateral load capacity (FS = 2.12)	7.1
Lateral load to first yielding	15.0
Lateral load to collapse of superstructure	15.0–25.0
Lateral load to collapse	22.5–25.0
Impact of floating log (L = 50 ft, D = 7–14 in.)	22.5–25.0
Impact of floating log (L = 50 ft, D = 7 in.) plus hydrostatic force (area of 100 ft^2)	22.5–25.0
Standard Linear Frame Analysis for Pile Bent Failing Load Groups:	
II	25.4
III	17.3
VIII	25.0
IX	46.5

Load Group IX represents the maximum lateral load capacity provided by AASHTO. From this summary, the maximum values of the lateral load capacity that would have been provided by the pile bent if it had been proportioned to meet the AASHTO group loading requirements is as follows:

Group No.	*Factor of Safety*	*Failure Criterion*	*Analysis Method*	*Lateral Load Capacity (kips)*
IX	2.12	Eq. 10–41, 10–42 (*5*)	Linear	46.5
IX	1.00	Eq. 10–41, 10–42 (*5*)	Linear	~ 98.6
IX	1.00	Actual collapse	Nonlinear	~148 to ~165

Thus, the following is a comparison of the lateral load capacities of the pile bent as constructed and one that would have met the AASHTO group loadings:

	Lateral Capacity of Bent (kips)	
Failure Criterion	*Meeting AASHTO*	*As Constructed*
Nominal strength (FS = 2.12)	46.5	7.1
Nominal strength (FS = 1.00)	~98.6	15.0
Collapse strength	148–~165	22.5–25.0

Thus, a pile bent that meets the AASHTO group loading requirements is about 6.5 times stronger than that provided by the structure designed by the contractor. Further, the actual lateral load capacity that a pile bent that conforms to AASHTO is about 150 kips as compared to about 25 kips for the contractor's design. Such an increase in the lateral load capacity afforded by a design that would conform to the AASHTO group loadings would almost certainly have prevented failure.

GLOSSARY OF VARIABLES

b = width of flange;
D_1 = diameter of floating log;
e = coefficient of restitution;
E_s = strain energy of system;
$F(t)$ = forcing function during impact;
F_m = maximum force of floating mass;
g = gravity acceleration;
k = equivalent spring stiffness at Joint 33;
L = length of floating log, length of member;
M_e = effective mass of structural system;
M_m = mass of floating debris (object);
t = time of impact, thickness of flange;
T_n = calculated natural period of element;
V_s = velocity of stream flow;
V_m = velocity of floating debris (object);
V_t = target velocity;
W_1 = weight of floating debris;
X_e = yield displacement (at 15-kip debris load);
X_{or} = displacement caused by other load (without debris load);
X_m = maximum combined displacement;
Y = displacement (translation) in X direction;
r = radius of gyration; and
ω, λ = natural frequencies of systems.

REFERENCES

1. R. A. Weber. *Bridge Design and Construction*. Factual Report, National Transportation Safety Board, Washington, D.C., 1989.
2. M. A. McMurtry. *Hydrology and Geology*. Factual Report, National Transportation Safety Board, Washington, D.C., 1989.
3. Collins Engineers. *Underwater Inspection and Soundings of the Temporary Bridge over the Great Miami River at Miamitown, Hamilton County, Ohio*. Exhibit 3-B, Docket No. HY-510-89, National Transportation Safety Board, Washington, D.C., 1989.
4. H. C. Nutting Company. *Report of Geotechnical Investigation, Bridge Replacement on Harrison Pike over the Great Miami River, Miamitown, Ohio, Dated 1987*. National Transportation Safety Board, Washington, D.C., 1989.
5. *Specification for the Design, Fabrication and Erection of Structural Steel for Buildings*, Part II (Plastic Design), American Institute of Steel Construction, Inc., New York, Feb. 12, 1969.
6. A. P. Boresi and O. M. Sidebottom. *Advanced Mechanics of Materials*, 4th ed. John Wiley, New York, 1985.
7. Salmon and Johnson. *Steel Structures, Design and Behavior*. Harper and Row, New York, 1971.
8. *Manual for Maintenance of Bridges*. AASHTO, Washington, D.C., 1983.
9. *Standard Specifications for Highway Bridges*, 13th ed. AASHTO, Washington, D.C., 1983.
10. *Standard Specifications for Highway Bridges*, 14th ed. AASHTO, Washington, D.C., 1989.
11. C. H. Norris, R. J. Hansen, M. J. Holley, Jr., J. M. Biggs, S. Namyet, and J. K. Minami. *Structural Design for Dynamic Loads*. McGraw-Hill, New York, 1959.
12. *Analysis Sheets for the Evaluation of Pile Bent No. 2*. FHWA, U.S. Department of Transportation, 1989.

Publication of this paper sponsored by Committee on General Structures.

Observations of Severe Abutment Backwall Damage

RAY W. JAMES, HEPING ZHANG, AND DAN G. ZOLLINGER

Field studies of highway bridge performance have led to repeated observations of severe cracking and dislocation of the backwalls of reinforced-concrete abutments. The observed distress is correlated with the presence of adjacent reinforced-concrete pavements, and the cause is attributed to the longitudinal growth of the concrete pavements. Field observations are presented and discussed. A finite element model of a representative abutment is used to study the expected stress distributions caused by several hypothesized mechanisms that might contribute to the observed damage. Methods to prevent future damage are discussed.

A field study of the performance of bridge decks, approach slabs, and adjacent pavement surfaces as a part of a study of bridge approach roughness led to numerous observations of severe cracking and often displaced ruptures in abutment backwalls. In extreme cases, the backwall is broken off the abutment and displaced away from the embarkment toward the bridge, usually resting against the adjacent girder ends or bridge deck. The field study included surveys of approximately 117 bridges, and was accomplished with the intention of quantifying the bridge approach roughness. The survey sites were not selected randomly; district engineers in 5 of Texas's 24 districts were first requested to identify sites with a history of required approach roadway maintenance to maintain ride quality. From the responses, a set of 34 bridges was selected for initial inspection and study. In a later phase of the study, a second, randomly selected set of approximately 83 bridges was also examined. Only observations relating to abutment damage are discussed.

DESCRIPTION OF THE OBSERVED BACKWALL DAMAGE

Figure 1 shows a longitudinal section of a representative highway bridge, approach slab, and abutment, typical of current Texas State Department of Highways and Public Transportation (SDHPT) design practice. Most commonly, the approach slab is doweled to the abutment backwall with reinforcing steel. The expansion joint at the end of the girders is usually either an open armored joint or is sealed with a prefabricated neoprene joint seal. In the case of short beams, expansion of the girders is usually provided for with a polymeric bearing pad. Drilled shafts, typically 30 in. in diameter, are commonly used to support the abutment, with shorter and smaller drilled shafts supporting the wingwalls. This relatively deep-drilled shaft foundation has been used for many years to provide durable, stiff, and stable abutment foundations. Figure 2 shows selected design details for a typical abutment used under a two-lane structure.

Figures 3–5 show several examples of observed backwall damage, and represent three observed stages of damage development. The various instances of observed damage are usually remarkably similar. The crack pattern shown in Figure 3, from the lower outside corner of the backwall, is the initial indication of distress in the backwall. This crack increases in length and becomes displaced, until the entire backwall is broken off at its base along the length of the abutment. In advanced stages, considerable spalling occurs, and sometimes embankment fill material is carried out of the displaced fracture.

CORRELATION OF OBSERVED BACKWALL DAMAGE TO CONCRETE PAVEMENTS

Of the 34 sites visited in the initial phase of the field survey, damage to the abutment backwall was observed and noted at 9 sites, all at structures adjacent to reinforced-concrete pavements. At five other structures adjacent to concrete pavements, no mention was made of observed abutment damage. At eight study sites where the adjacent pavement was asphalt concrete, no damage was noted. The objective of the study was to observe approach roughness, not necessarily abutment damage or type of adjacent pavements, so in some early records, the type of adjacent pavement or the absence of abutment damage was not noted. Still, the strong apparent correlation of significant abutment damage with the presence of concrete pavements motivated additional study.

Because the initial study set was obtained by requesting examples of maintenance-intensive sites, the bridges and associated damage are probably not representative of the state's bridges. Because of this question, a more detailed and more random sample of 83 bridges was surveyed. The study bridges were selected by inspecting essentially all bridges on a series of randomly chosen circuitous routes on highways of various types, including farm roads, state highways, U.S. highways, and Interstate highways. Of these 83 bridges, all but 6 were adjacent to asphalt concrete pavements (ACP). Of the 77 bridges adjacent to ACP, damage to the abutment backwall was noted in only two instances. In the case of these two bridges, the observed damage was not similar to that damage shown by Figures 3–5.

The observed damage in one case consisted of cracking and spalling of the top of the wingwall, as shown in Figure 6, apparently caused by unintended contact between the wingwall and the bridge deck. On the opposite side of the deck

Texas Transportation Institute, Texas A&M University, College Station, Tex. 77843–3135.

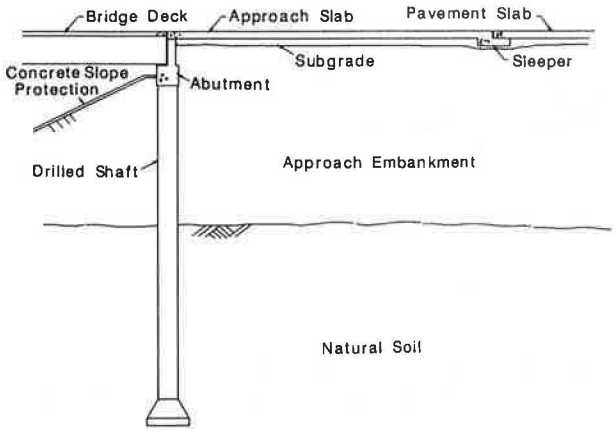

FIGURE 1 Longitudinal section through a typical bridge approach.

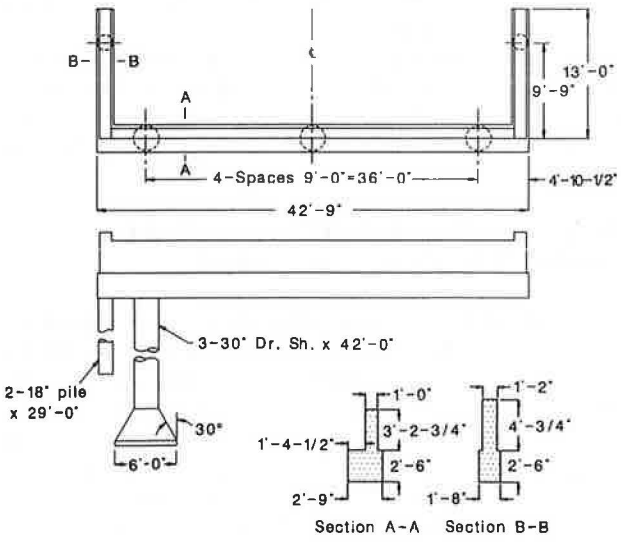

FIGURE 2 Design details for representative reinforced concrete abutment.

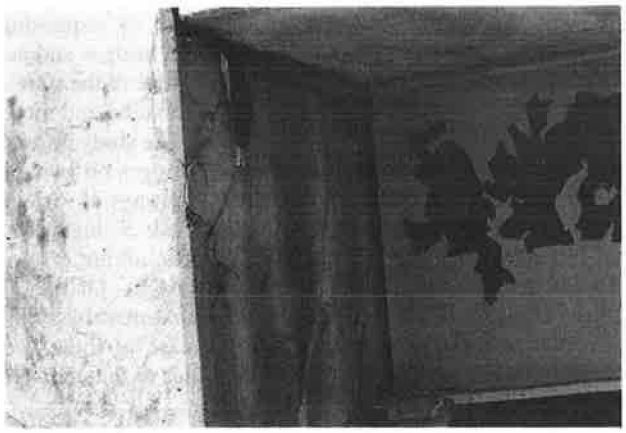

FIGURE 3 Observed damage to abutment backwall, early stage.

FIGURE 4 Observed abutment backwall damage, intermediate stage.

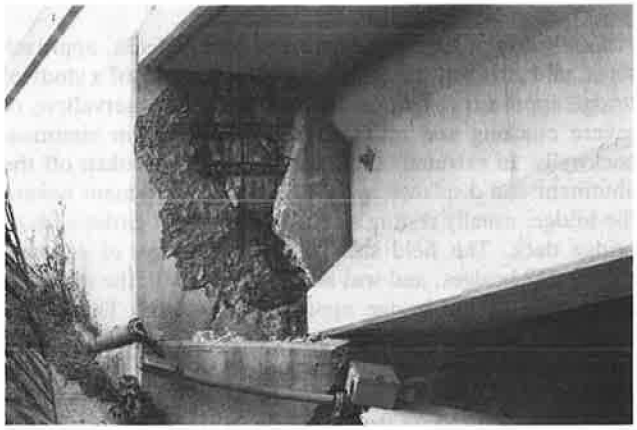

FIGURE 5 Observed abutment backwall damage, advanced stage.

FIGURE 6 Isolated instance of observed damage to abutment backwall adjacent to ACP.

at that abutment, a similar unintended contact pressure has caused cracking and spalling of the edge of the bridge deck. The cause of the bridge or embankment movement resulting in this unintended contact is not known. It may be deduced only that either the embankment is moving toward the bridge, carrying the abutment, or the bridge superstructure is moving toward the embankment. Localized pressure by soil or pavement against the top of the backwall is expected to cause backwall damage before the backwall contacts the girder ends. In the second instance of damage to a backwall at a site adjacent to ACP, the observed damage is generally similar to the first instance, as shown in Figure 7. It is not as clear in this case that the damage is caused by bearing pressure between the wingwall and the deck, as in Figure 6, but a close inspection of the abutment reveals that the damage in this instance is isolated in the wingwall, with the backwall undamaged.

Finally, a third example of distress in a bridge abutment adjacent to ACP was observed in the initial field study. The observed distress in this example took the form of an apparently displaced approach slab, as shown in Figure 8. However, the cause of this displacement is the gross rotation of the abutment as shown in Figure 9. The embankment at this site is underlain by soft soils, and the rotation is attributed to differential settlement. Other evidence of differential settlement is also noted at this site. The mechanism causing the observed distress is therefore different than the mechanism observed at the sites adjacent to reinforced-concrete pavements. No damage was sustained by the backwall in this instance, even though the backwall has been displaced approximately 2 in. toward the approach slab. Design drawings for this structure indicate that the approach slab is not dowelled to the abutment backwall, as is commonly done in other similar structures. Because of this, the relative displacement of backwall and approach slab is not restrained and does not cause distress.

FIGURE 7 Observed damage to abutment wingwall at structure adjacent to ACP: Case 2.

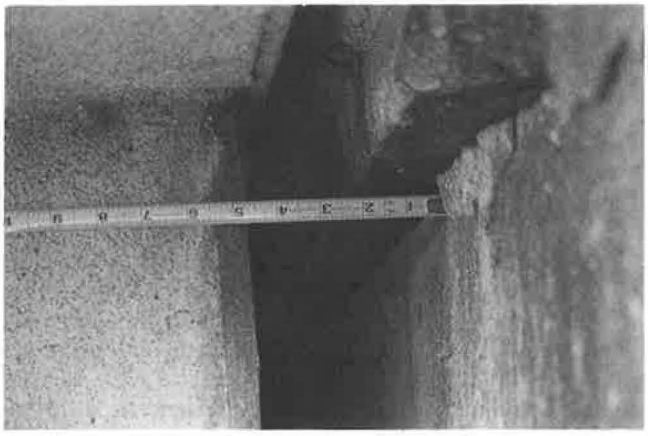

FIGURE 8 Approach slab apparently displaced relative to backwall.

FIGURE 9 Rotated abutment and wingwall.

The six bridges at sites adjacent to reinforced concrete pavements were all on the same section of highway, and of these six, three exhibited significant abutment backwall distress, essentially identical to that shown in Figures 3–5. In summary, three of six abutments next to continuous reinforced-concrete pavements (CRCP) were damaged, whereas none of the 77 bridges next to ACP exhibited similar damage.

OTHER OBSERVATIONS IMPLICATING LONGITUDINAL GROWTH OF CONCRETE PAVEMENTS

In addition to the broken backwalls, other observations indicate longitudinal growth of the CRCP. At some sites where

extensive backwall damage was observed, the shoulders adjacent to the CRCP were paved with a thin layer of hot-mix asphalt concrete. Cracks were observed in the paved shoulder emanating from the edge of the CRCP and propagating out into the paved shoulder at an angle roughly approximating 45 degrees toward the abutment. The points of intersection of these cracks with the edge of the CRCP coincided closely with the known locations of the reinforced-concrete pavement lugs that are designed to anchor the pavement to the subgrade, as shown in the sketch in Figure 10. The presence of these cracks is evidence that the pavement lugs are being pushed through the subgrade, causing soil failure planes whose intersections with the surface are manifested by the observed cracks. Excavations in the shoulder at one such site revealed a large open cavity behind the exposed pavement lug—further evidence that the CRCP is moving toward the abutment in spite of the pavement lugs.

Also, the CRCP exhibits transverse cracks that are more or less randomly spaced except near the approach slab. Near the approach slab, transverse cracks occur only on either side of each pavement lug. These cracks, which precisely locate each of the lugs, are thought to be caused by negative moments above the lugs because of wheel loading, and serve to allow expansion and contraction sufficient to prevent other cracks in the vicinity of the lugs.

MECHANISMS POTENTIALLY CAUSING LONGITUDINAL CRCP MOTION

At least two mechanisms may be identified as potential causes of the longitudinal motion or growth of the CRCP, and the resulting backwall damage. The first of these is a thermal ratcheting mechanism that hypothetically results in a gradual increase in length of the pavement. The second mechanism is a chemical reaction causing dilatational strain in the pavement, and a resulting growth in length. This second mechanism presumably results in a monotonic growth, whereas the first hypothetically results in either an annual cyclic variation in length, or a superposition of an annual cyclic variation and a monotonically increasing growth. These two mechanisms are discussed briefly. More details about the first mechanism are discussed elsewhere (*1*); numerous papers have been published on the topic of chemical reactions in cements and aggregates.

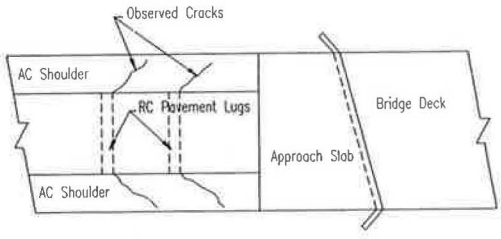

FIGURE 10 Drawing of observed crack patterns in ACP shoulders adjacent to CRCP (plan view).

Thermal Ratcheting Mechanism

The thermal ratcheting mechanism proposed to explain the apparent longitudinal growth of CRCP consists of a thermal expansion of the CRCP during a summer season, followed during the cooler months by a thermal contraction that is restrained by ground friction on the lower surface of the CRCP sufficient to open transverse cracks. These cracks are partially blocked, or propped, with fine soil particles carried from the roadway into the cracks by water. Subsequently, during the next warm season, the pavement again expands, and the next cool season results in another ratchet increment of growth. This mechanism is hypothetically unbounded, and could certainly cause large enough longitudinal growth to close the joints between the pavement and the approach slab, and between the approach slab and deck. This same mechanism may be at work in CRCP blow-ups, and in other phenomena indicative of a significant locked-in longitudinal compressive stress in the pavement.

Chemical Reactions Resulting in Dilatational Strains

A second mechanism that could be a factor in the apparent longitudinal growth of CRCP is a chemical reaction involving the alkali in the cement, and the aggregate. Alkali-silica reactions resulting in large dilatational strains have been reported in the literature (*2*) and are not discussed in detail here. Such reactions may result in extensive deterioration in reinforced concrete, because of resulting large strains in the cementatious matrix. Although evidence of such degradation is not found in the pavements in the present study, the magnitude of the dilatational strains required to account for the observed growth is small compared with the strains that are associated with severe deterioration. As a result, a mild reaction could cause the observed longitudinal growth without significant concrete degradation.

Preliminary results of tests to determine the role played by alkali-aggregate reactions indicate that extensive alkali-silica reactions are not occurring, but some limited reactions are indicated by observed reaction products in accelerated testing. In short, the reactions that may be occurring are not sufficient to cause distress to the pavement, but cannot be ruled out as a cause of longitudinal strains of the magnitude necessary to cause the observed distress to the adjacent abutment backwalls.

FINITE ELEMENT STUDIES OF MECHANISMS POTENTIALLY CAUSING DAMAGE TO ABUTMENTS

Figure 11 shows a finite element model of this abutment structure. It consists of eight-node solid elements modeling the abutment; spring elements, not shown in Figure 11, are used to model the soil-structure interaction. A microcomputer version of the finite element software SAP90 was used in this study. All numerical operations are executed in full 64-bit double precision. Assumed concrete material properties are compressive strength f'_c = 4 ksi, unit weight 140 lb/ft^3, elastic modulus E_c = 36,000 ksi, and Poisson's ratio μ = 0.28.

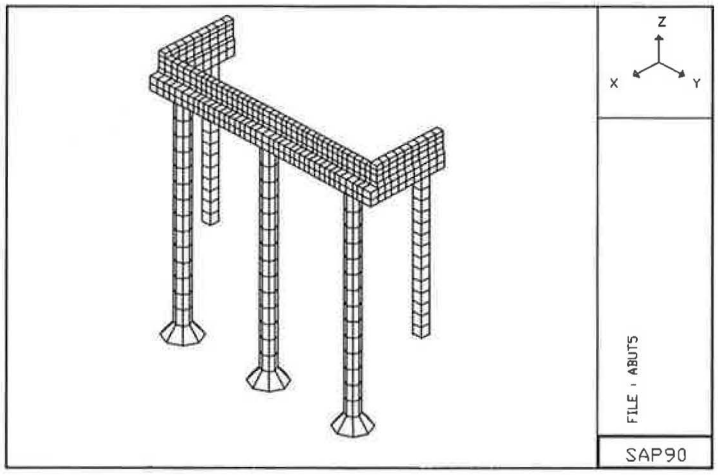

FIGURE 11 Finite element model of bridge abutment.

The soil-structure interaction was simplified by employing a Winkler soil model, as shown in Figure 12. The soil surrounding the shaft is represented by a set of elastic springs. Winkler's assumption states that each spring acts independently. Although this assumption does not exactly describe the soil behavior, it has been demonstrated that solutions of beam-on-foundation problems using Winkler's assumption do not differ appreciably from solutions assuming the soil to be an isotropic, elastic continuum. It is convenient to think of Winkler's model in terms of $P-Y$ curves, also shown in Figure 12. The soil modulus E_s is then taken to be P/Y. Because the $P-Y$ relationship is usually nonlinear, the modulus E_s is not constant, but it may be linearly approximated for small deflections. A linear approximation was used in this study. Terzaghi (*3*) suggested the following formula for stiff clays:

$$k_h = \frac{k_{s1}}{1.5b} \tag{1}$$

where

k_h = coefficient of horizontal subgrade reaction,
k_{s1} = basic value of coefficient of vertical subgrade reaction, and
b = width of pile or drilled shaft.

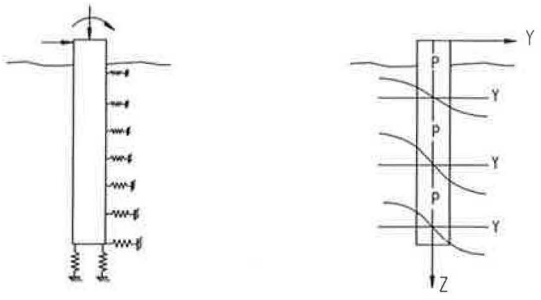

a) Idealization of soil surrounding a shaft b) Set of p-y curves

FIGURE 12 Representation of Winkler soil model and $P-Y$ curves.

Then, the soil modulus $E_s = P/Y$ is given by

$$E_s = k_h b \tag{2}$$

The soil strength data obtained from borings at the site modeled is presented in Table 1. The embankment is approximately 20 to 30 ft deep and consists mainly of clay and sandy clay. Dry densities are approximately 100 lb/ft^3.

Assuming that the coefficient of subgrade reaction does not depend on depth yields the values for k_{s1} presented in Table 2.

The soils surrounding the abutment are modeled as two layers, one representing the embankment fill, and one representing natural undisturbed soil. The E_s values used in the model are presented in Table 3. These values were calculated on the basis of the data in Table 1, assuming the average q_u for fill is 1.5 tons/ft^2 and for natural soil is 2 tons/ft^2, and assuming q_u is about 3 to 5 tons/ft^2 at 42-ft depth. The spring constants for the Winkler springs are obtained from these values for E_s.

The soil's response to the dynamic loads is known to be significantly different from the response to long-term static

TABLE 1 MEASURED VALUES OF SOIL ULTIMATE STRENGTH, q_u

Depth (ft)	Soil Ultimate Strength q_u (tons/ft^2) Boring No.					
	1	2	3	3A	4	5
1	1.25	4				
3	1.5	1.5			2.0	2.0
5	0.75, 1.75	1.5			2.5	1.0
7	1.5	2.0			0.75	1.0, 2.0
9	2.0	2.0		1.5	2.0, 3.0	3.5
11	2.0	2.5		2.75	2.0	3.5
13	1.5	1.5		2.75	1.75	2.25
15	1.0, 2.5	1.5		1.75	1.75	1.5
17	1.5	2.25		2.0	1.75	2.5
19	2.25	1.5		2.25	1.75	2.0
21	2.25	1.5		2.5	1.75	2.0
23	2.5	2.25		3.0		3.0
25				1.75, 4+		4+
27				4+		2.75
29				4+		
31				1.5		

TABLE 2 VALUES OF k_{s1} FOR CALCULATING VALUES OF CLAY SOIL MODULUS E_s

Consistency	q_u (tons/ft²)	k_{s1} (tons/ft³)	Selected k_{s1} (tons/ft³)
Stiff	1–2	50–100	75
Very stiff	2–4	100–200	150
Hard	>4	>200	300

TABLE 3 VALUES OF E_s USED IN MODEL

Subgrade	Filled Layer (tons/ft²)	Natural Layer (tons/ft²)
Horizontal	50	100
Vertical	75	150–300

loads. To model this, the E_s values used for the live load were taken to be twice the values used for static loads. The properties of the soil springs were determined and the finite element model was constructed using these E_s values.

FINITE ELEMENT ANALYSIS

Using the finite element model described earlier, the following loading cases were simulated:

Case 1. Longitudinal Pavement Growth. The end of the approach slab and the top of abutment backwall are assumed to be constrained to move together, so that the abutment backwall is displaced 1 in. toward the bridge deck.

Case 2. Settlement I. The load capacity of one 30-in.-diameter drill shaft on the right side is assumed to be reduced 50 percent (a) dead load only; and (b) live load only (one HS20 truck).

Case 3. Settlement II. Two wingwall piles are assumed to lose all tip resistance.

Case 4. Soil pressure. Soil pressure of 1 kip/ft² is assumed to be uniformly distributed on the inside surfaces of the abutment.

Case 5. Live load only (one HS20 truck).

Case 6. Dead load only.

Case 7. Sensitivity to the soil-structure interaction model when (a) E_s is assumed to be increased 100 percent for Case 1, (b) E_s is assumed to be increased 100 percent for Case 6, and (c) E_s is assumed to be decreased 50 percent for Case 6.

Some simulation results for load Case 1 are presented in Figure 13. In load Case 1, the approach slab is forcing the abutment backwall 1.0 in. forward, and the resulting force between approach slab and abutment backwall is approximately 228 kips. The wingwall is predicted to rotate approximately 0.37 degree. The abutment vertical settlement is about 0.35 in. The anticipated damage for this load case is cracking of the backwall or backwall-wingwall intersection, consistent with the observed damage in the field. Similar results from other load cases are not presented here. Cases 2 and 5 results indicate highest stress concentrations in the top center of the backwall, and in Cases 3 and 4, highest stresses occur at the ends of the backwall. Dead-load stresses in Case 6 are small, as are live-load stresses in Case 5. Accordingly, it may be concluded that the mechanisms modeled in Cases 1, 3, and 4 each acting separately or together could be contributing factors to the damage observed. Because of the other observations implicating pavement growth, and because of the low probability of loss of support under the wingwall piles or the development of high lateral earth pressures on the abutment walls, Case 1 loading is considered the most likely explanation of the observed damage.

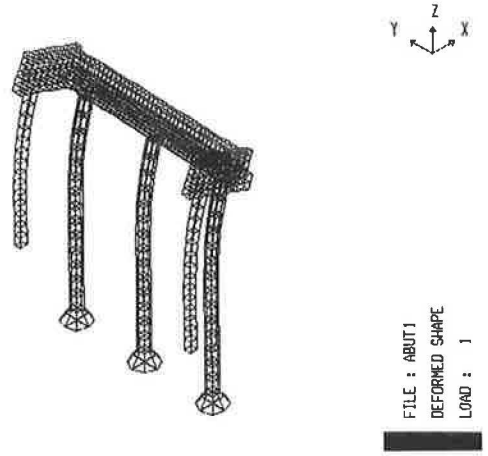

FIGURE 13 Predicted deformed shape for load Case I.

METHODS TO MITIGATE OR ELIMINATE FUTURE DAMAGE TO ABUTMENTS

The reinforced-concrete pavement lugs are intended to anchor the ends of the CRCP. It is apparent that in certain situations, these lugs are not performing their intended function. Two obvious means of mitigating the observed damage are to provide an anchor system that functions reliably or to isolate the CRCP from the approach slab. Strengthening of the abutment backwall sufficiently to resist the thermal expansion of the CRCP is not practical, although it is evident that some redesign of the reinforcement details in the abutment design may be justifiable. The most straightforward way to eliminate future damage to abutments is to provide an isolation, or pressure relief, joint between the end of the CRCP and the approach slab. An isolation joint consisting of a 36-in. gap filled with ACP has been used in other states. Although the presence of such a joint may increase maintenance by requiring periodic planning or grinding, the increased life of the abutments will easily offset small increase in maintenance costs. Other methods to isolate the abutment from the approach slab may also prove practical. Mechanical expansion joints have been proposed and studied. Omitting the dowelled connection between the approach slab and abutment backwall prevents damage to the backwall, but may be undesirable for other reasons.

SUMMARY AND CONCLUSIONS

Field observations of severe damage to abutment backwalls, supported by numerical stress analysis, lead to the conclusion

that the observed damage is caused by longitudinal growth of CRCP, causing longitudinal pressures on the abutment backwalls. Pressure relief joints have not been used at the sites where damage was observed, and are recommended as retrofit solutions at sites where damage has occurred and for prevention at sites where damage has not yet occurred. Whether the longitudinal pavement growth may be attributed to a chemical reaction in the concrete or to a thermal ratcheting mechanism has not yet been determined. This question is still being studied.

Second, it may be concluded that the reinforced-concrete pavement lugs are failing to completely anchor the end of the CRCP, at least at sites where this damage has been observed. A review of the design method for sizing these lugs should be performed as well as a review of several of the failures, to determine whether an improved design method for anchor lugs is warranted.

ACKNOWLEDGMENTS

Much of the work described here was funded by the Texas SDHPT and the FHWA, for which support the authors are appreciative.

REFERENCES

1. R. W. James, H. Zhang, D. G. Zollinger, L. J. Thompson, R. F. Bruner, and D. Xin. *A Study of Bridge Approach Roughness*. Research Report 1213-1F. Texas Transportation Institute, Texas A&M University, College Station, 1990, 113 pp.
2. R. L. Carasquillo and P. G. Snow. Effect of Fly Ash on Alkali-Aggregate Reaction in Concrete. *ACI Materials Journal*, Vol. 84, No. 4, American Concrete Institute, Detroit, Mich., July–Aug. 1987, pp. 299–305.
3. K. Terzhagi. Evaluation of Coefficients of Subgrade Reaction. *Geotechnique—The International Journal of Soil Mechanics*, Vol. 5, No. 4, Institute of Civil Engineers, London, 1955, pp. 297–326.

Publication of this paper sponsored by Committee on General Structures.

Model for Determining the Optimum Rehabilitation Cycle for Concrete Bridge Decks

M. C. VORSTER, T. BAFNA, AND R. E. WEYERS

The optimum rehabilitation cycle for concrete bridge decks is determined by calculating the average annual cost of patching the deck for a number of years and then rehabilitating it to extend life but not enhance the original functional characteristics. The model used to carry out the necessary calculations is based on the fact that every operation performed on the deck gives rise to a stream of future maintenance obligations. It relies on five user-defined inputs and makes specific provisions for the fact that patched areas fail in terms of a deterioration profile different from that exhibited by the original deck. A spreadsheet is developed to perform sensitivity analysis studies using different values for the user-defined inputs. The results are tabulated. It is found that physical life as defined by the deck deterioration profile and economic life as defined by the rehabilitation cycle must be balanced to achieve the best results. The limitations of the model are discussed. The user is cautioned about the use of relatively simple models in a complex environment.

The repair-or-replace decision must be taken at some point in time for every physical asset that deteriorates with age (*1,2*) Concrete bridge decks are no exception. Maintenance personnel are constantly seeking that elusive point in time when the increasing cost of patching a deteriorating deck becomes more expensive than rehabilitating the whole structure.

A solution to the problem is based on work performed under the Strategic Highway Research Program. The approach used is based on methodologies developed for quantifying the economic life of construction equipment (*3,4*). Modifications have been introduced to accommodate the special conditions found in bridge maintenance, and the model that has been developed is unique in this regard.

The average annual cost of patching the deck for a given number of years before rehabilitation and then rehabilitating it is used as the principal value function in the model. This function is defined as follows:

$$Ac_N = \left(\sum_{n=1}^{n=N-1} Pc_{n-1} + Rd_n \right) / N \quad (1)$$

where

Ac_N = Average annual cost of patching the deck for N years and then rehabilitating it,

Pc_{n-1} = Cost of patching the deck in each period before rehabilitation,

Rd_n = Cost of rehabilitating the deck after n periods, and

N = Number of years for which the average annual cost of patching and rehabilitating the deck is to be calculated.

The value of Ac_N varies for assumed values of N; the optimum rehabilitation cycle is defined as the value of N that produces a minimum value for Ac_N.

DEFINITIONS

Replacement and maintenance have been defined as essentially the same process depending on the definition of the operating unit (*5,6*). In this case the operating unit is defined as a single bridge and thus patching and rehabilitating the deck become two alternatives in a spectrum of available bridge maintenance options. The terms are defined as follows:

1. Patching. Patching is the process whereby small localized areas of deterioration in the deck are repaired by removing the deteriorated concrete and replacing it with a substitute material. The objective is to reinstate the surface characteristics of the deck as far as possible. There is no intention of extending the life of the deck in any way and there is no enhancement of the original functional characteristics of the deck.
2. Rehabilitation. Rehabilitation is the process whereby large areas of chloride-contaminated or deteriorated concrete and reinforcing steel are systematically removed from the deck and replaced. The objective is to reinstate the deck to an as-new condition with regard to performance and life by removing chloride-contaminated concrete and arresting corrosion. Enhancing the original functional characteristics of the deck is not intended and the original geometry of the structure remains essentially unchanged.

The main considerations leading to replacement have been classified as excessive maintenance, declining efficiency, inadequacy, and obsolescence (*7*). Patching or rehabilitating all or part of a deck addresses the first two of these factors; the latter two require replacement or reconstruction and thus fall outside the scope of this paper.

Department of Civil Engineering, Virginia Polytechnic Institute and State University, Blacksburg, Va. 24061.

STRUCTURE OF THE MODEL

The model is based on the fact that every operation performed on the deck gives rise to a stream of future maintenance obligations. The amount of maintenance work that must be done in each period depends on the area of the deck, either new or patched, and the portion of this area that will deteriorate and become a candidate for maintenance in the period.

The situation for the original bridge deck may be described as follows:

$$\mathrm{Mo}_N = A \times P(N) \tag{2}$$

where

Mo_N = Maintenance obligation arising from the original deck for the period ending at Year N,
A = Area of the deteriorating deck, and
$P(N)$ = Portion of the original deck that deteriorates in the period ending at Year N and contributes to the stream of future maintenance obligations.

The series $P(1), P(2), \ldots, P(N)$, which describes the deterioration profile for the deck, is defined such that

$$\sum_{n=1}^{n=N} P(n) = 1 \tag{3}$$

The deck deterioration profile plays an important part in determining the maintenance workload and is discussed again later. Figure 1 shows an example of how a stream of future maintenance obligations is generated from an assumed deck and deterioration profile. The fact that patched areas fail in terms of a deterioration profile different from that exhibited by the original deck means that patched areas must be identified and the stream of maintenance obligations arising from the need to repatch a previously patched area must be determined. This is done as follows:

$$\mathrm{Mpx}_n = \mathrm{Apx} \times \mathrm{Ppx}(n) \qquad n = 1, 2, \ldots, N \tag{4}$$

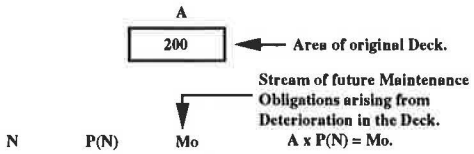

N	P(N)	Mo
5	5%	10
10	10%	20
15	15%	30
20	20%	40
25	25%	40
30	30%	60

FIGURE 1 Maintenance obligations generated by deck. The stream of future obligations is the product of the area and the portion that deteriorates.

where

Mpx_n = Maintenance obligation arising from the need to repatch Patch x in the period ending at Year n,
Apx = Area of Patch x, and
$\mathrm{Ppx}(n)$ = Portion of Patch x that deteriorates in the period ending at Year n.

The series $\mathrm{Ppx}(1), \mathrm{Ppx}(2), \ldots, \mathrm{Ppx}(N)$, which describes the deterioration profile for the patches, is defined such that

$$\sum_{n=1}^{n=N} \mathrm{Ppx}(n) = 1 \tag{5}$$

The patch deterioration profile is different from the deterioration profile for the original deck but is common to all patches of a given type and age. It is discussed again later.

The total maintenance obligation in Period N arising from the need to patch the original deck and repatch the patches is given by

$$\mathrm{Mt}_N = \mathrm{Mo}_N + \mathrm{Mp}_N \tag{6}$$

where

Mt_N = Total maintenance obligation for the period ending in Year N,
Mo_N = Maintenance obligation for the period ending in Year N arising from the original deck (see Equation 2), and
Mp_N = Total maintenance obligation for the period ending in Year N arising from all repatching.

$$\mathrm{Mp}_N = \sum_{n=1}^{n=N} \mathrm{Mpx}_n \tag{7}$$

Figure 2, which expands on Figure 1, shows how Mt_N may be calculated for an assumed deck area, deck deterioration profile, and patch deterioration profile.

The cost of patching the deck in each period before replacement was defined as Pc_{N-1} in Equation 1. This may now be written as

$$\mathrm{Pc}_{N-1} = \mathrm{Mt}_{N-1} \times \mathrm{Cp} \tag{8}$$

where Cp is the unit cost of patching a portion of the deck.

The cost of rehabilitating all or part of the deck was defined as Rd_n in Equation 1. This term may now be written as

$$\mathrm{Rd}_n = \mathrm{Ar} \times \mathrm{Cr}_n \tag{9}$$

where

Ar = Area of deck to be replaced (yd^2),
Cr_n = Unit cost of replacing the deck after n years ($/$\mathrm{yd}^2$).

If Pcr_n is defined as the ratio of the unit cost of patching to the unit cost of rehabilitating and put equal to $\mathrm{Cp}/\mathrm{Cr}_n$ then Equation 1 may be written as follows:

$$\mathrm{Ac}_N = \mathrm{Cr}_N\left(\sum_{n=1}^{n=N-1} \mathrm{Mt}_{n-1} \times \mathrm{Pcr}_n + \mathrm{Ar}\right)/N \tag{10}$$

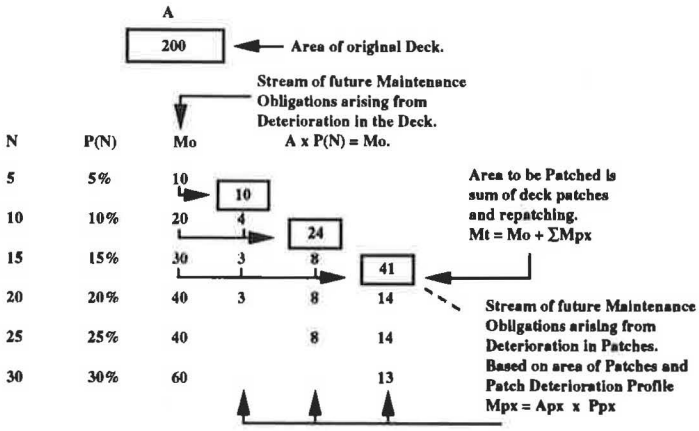

FIGURE 2 Maintenance obligations generated by deck and patches. The stream of future obligations arises from the deck and the need to repatch the patches.

This equation is used to calculate the optimum rehabilitation period in the sensitivity analysis performed later.

USER-DEFINED INPUTS

The model requires a number of user-defined inputs. These are discussed in this section to provide a full understanding of what is needed to use the model

1. Area of Deteriorating Deck, A. This parameter is relatively straightforward with the provision that areas not heavily trafficked or subject to chloride contamination should be eliminated.

2. Area of Deck to be Rehabilitated, Ar. This parameter equals the area of the original deck if a systematic milling hydrodemolition or deck rehabilitation option is selected as the deck replacement strategy. If removal of contaminated concrete and reconstruction to an as-new condition does not cover the full area, then Ar is less than A.

3. Deck Deterioration Profile, $P(N)$. This parameter depends on a number of factors including the original design, quality of the original construction, past and future patterns of chloride contamination, location of the bridge, and traffic patterns. Three possible profiles based on prior research (*8*) are shown in Figure 3 where the ordinate represents the cumulative percentage of the deck that has deteriorated at the end of each 5-year period. The profiles may be classified as follows:

Profile	*Deterioration Commences (years)*	*Deterioration Reaches*	
		30% (years)	*80% (years)*
A	5	15	22
B	5	22	32
C	5	32	47

4. Patch Deterioration Profile, Ppx(N). As with the deck deterioration profile, this parameter depends on the methods and materials used for patching and the quality of workmanship. Little research is available on which to base values for the profiles and three different profiles are shown in Figure

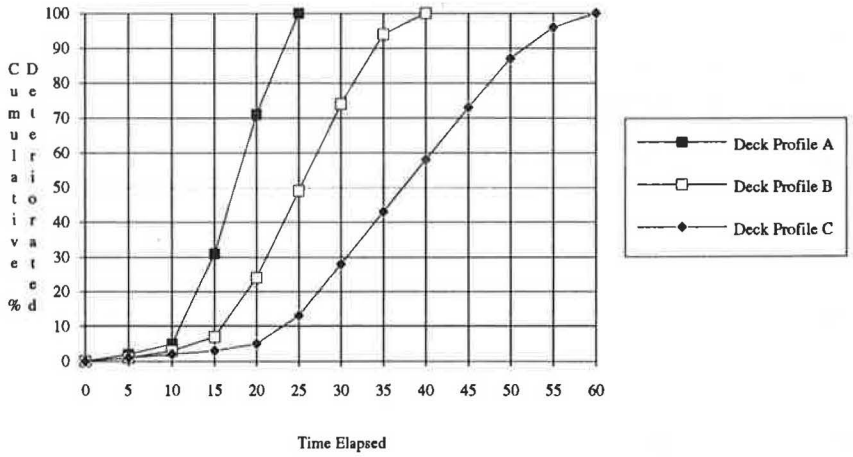

FIGURE 3 Deck deterioration profiles. Cumulative deterioration reaches 30 percent after 15, 22, and 32 years for Profiles A, B, and C, respectively.

4 where the ordinate again represents the cumulative percentage of patched area that needs to be repatched after the end of each 5-year period. The patch profiles may be summarized as follows:

Patch Type	*50% of Patches Deteriorated (years)*	*100% of Patches Deteriorated (years)*
1	3	5
2	4	10
3	13	20

5. Unit Cost Ratio, Pcr. This parameter reflects the ratio of the unit cost of patching to the unit cost of replacing. It is affected by the methods and materials used for patching as well as the cost of removal.

SENSITIVITY ANALYSIS

A spreadsheet was developed to perform the calculations needed to determine the value of Ac_N for various values of N under different conditions. Table 1 presents the nine studies conducted with the corresponding values assumed for the user-defined inputs.

The spreadsheet and graph from Study 5 is given in Figures 5 and 6 as examples of the results obtained. A full set of output graphs is shown in Figures 7–15.

The output graphs indicate how the average annual cost of patching the deck for N years and then replacing it varies with time to produce a minimum point that defines the optimum rehabilitation cycle. The cumulative deterioration profile for the deck is also plotted on the graph and thus it is possible to determine the following three important values from each of the sensitivity analysis studies:

1. The minimum value for the average annual cost, Ac*.
2. The optimum rehabilitation cycle N^*.
3. The cumulative percent deterioration in the deck when the optimum point D* occurs.

These values are presented in Table 2, which forms the basis of the analysis that follows.

ANALYSIS OF RESULTS

1. *Differences in Patch Cost Ratio.* The patch cost ratio (Pcr) for each patch type was varied by 20 percent above and below the median value assumed for each patch type (0.8, 1.0, and 1.2 for Types 1, 2, and 3, respectively.) Table 2 indicates that this choice had no effect on the timing and little effect on the magnitude of the minimum point. The optimum replacement cycle is thus not sensitive to minor variations in the cost of patching at or around the optimum cycle time.

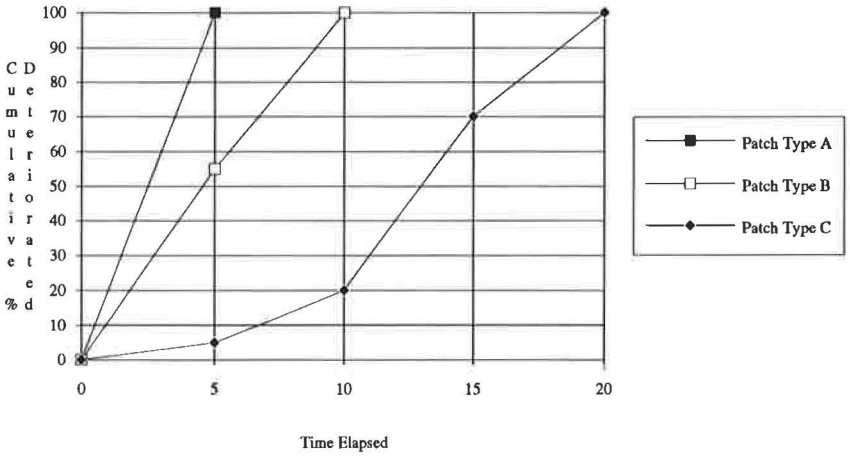

FIGURE 4 Patch deterioration profiles. Cumulative deterioration reaches 100 percent after 5, 10, and 20 years for Patch Types 1, 2, and 3, respectively.

TABLE 1 VALUES ASSUMED FOR USER-DEFINED INPUTS

Study Number	Deck Area (*A*)	Rehabilitated Area (Ar)	Deck Profile *P*(*N*)	Patch Type Ppx(*N*)	Cost Ratio Pcr From	To
1	100	100	A	1	0.64	0.96
2	100	100	A	2	0.80	1.20
3	100	100	A	3	0.96	1.44
4	100	100	B	1	0.64	0.96
5	100	100	B	2	0.80	1.20
6	100	100	B	3	0.96	1.44
7	100	100	C	1	0.64	0.96
8	100	100	C	2	0.80	1.20
9	100	100	C	3	0.96	1.44

User Defined Inputs															
	A		100												
	Ar		100												
	P(N)	N	5	10	15	20	25	30	35	40	45	50	55	60	
		P	1	2	4	17	25	25	20	6					= Deck Profile B
	Ppx(N)	N	5	10	15	20	25	30	35	40	45	50	55	60	
		Ppx	55	45											= Patch Type 2
	Pcr		0.8	1	1.2										

	DECK		PATCHES																
			1	2	3	4	5	6	7	8	9	10	11	12			AcN	AcN	AcN
N		A	Mt 1	Mt 2	Mt 3	Mt 4	Mt 5	Mt 6	Mt 7	Mt 8	Mt 9	Mt 10	Mt 11	Mt 12	Mt	ΣMt			
	P(N)	Mo	Mpx	Mpx	Mpx	Mpx	Mpx	Mpx	Mpx	Mpx	Mpx	Mpx	Mpx	Mpx			Pcr = 0.8	Pcr = 1	Pcr = 1.2
0		100																	
5	1	1	1												1	1	20.0	20.0	20.0
10	2	2	0.55	2.55											2.55	3.55	10.1	10.1	10.1
15	4	4	0.45	1.4025	5.8525										5.8525	9.4025	6.9	6.9	7.0
20	17	17	0	1.1475	3.2189	21.366									21.366	30.769	5.4	5.5	5.6
25	25	25	0	0	2.6336	11.752	39.385								39.385	70.154	5.0	5.2	5.5
30	25	25	0	0	0	9.6149	21.662	56.277							56.277	126.43	5.2	5.7	6.1
35	20	20		0	0	0	17.723	30.952	68.675						68.675	195.11	5.7	6.5	7.2
40	6	6			0	0	0	25.325	37.772	69.096					69.096	264.2	6.4	7.4	8.4
45	0	0				0	0	0	30.904	38.003	68.907				68.907	333.11	6.9	8.1	9.3
50	0	0					0	0	0	31.093	37.899	68.992			68.992	402.1	7.3	8.7	10.0
55	0	0						0	0	0	31.008	37.946	68.954		68.954	471.05	7.7	9.1	10.6
60	0	0							0	0	0	31.046	37.924	68.971	68.971	540.03	7.9	9.5	11.1

FIGURE 5 Analysis of costs for Deck Profile B and Patch Type 2. The optimum rehabilitation cycle is 25 years.

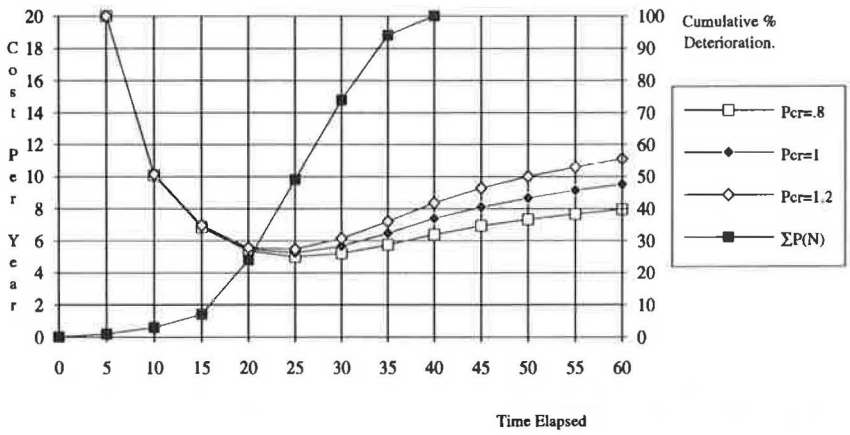

FIGURE 6 Average annual cost and cumulative deterioration profile for deck Profile B and Patch Type 2. The optimum rehabilitation cycle occurs after 25 years when the deck is 49 percent deteriorated.

The graphs do show that relative patch costs are important when the optimum period is exceeded.

2. *Differences in Patch Type.* The three different patch types assumed in the sensitivity analysis studies differed from one another in terms of both their deterioration profiles and their cost ratios, as summarized in the column headings of Table 2. The values obtained indicate that neither Ac* nor N^* changed when the patching type differed for a given deck specification. This result arises from the fact that the three patch types assumed all have the same benefit-to-cost ratio as defined by their deterioration profile [Ppx(N)] and patch cost ratio (Pcr). The results obtained thus illustrate the use of the model to quantify the elusive relationship between service life and cost for various alternative patching methods.

3. *Differences Between Deck Profiles.* The three different deck deterioration profiles assumed produced different values for Ac*, N^*, and D^*. For Profile A, the minimum cost is relatively high (6.2 to 7.3); it occurs at 20 years when deck deterioration has reached 70 percent. This case is clearly infeasible, as the physical life of the deck from a safety and ride

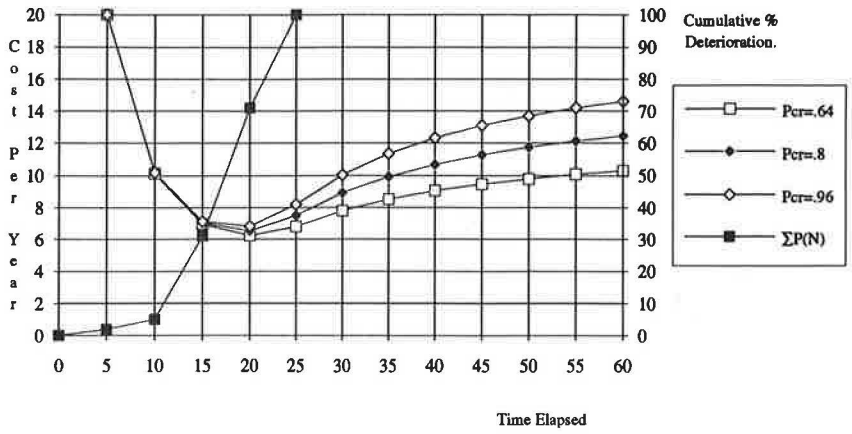

FIGURE 7 Average annual cost and cumulative deterioration profile for Deck Profile A and Patch Type 1. The optimum rehabilitation cycle occurs after 20 years when the deck is 71 percent deteriorated.

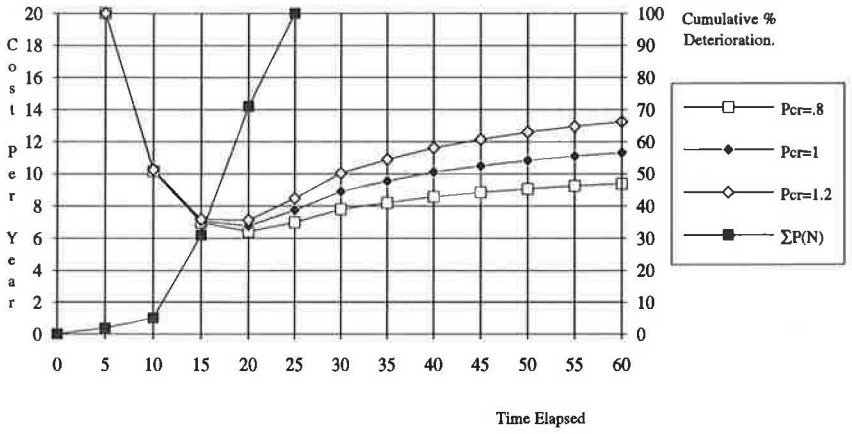

FIGURE 8 Average annual cost and cumulative deterioration profile for Deck Profile A and Patch Type 2. The optimum rehabilitation cycle occurs after 20 years when the deck is 71 percent deteriorated.

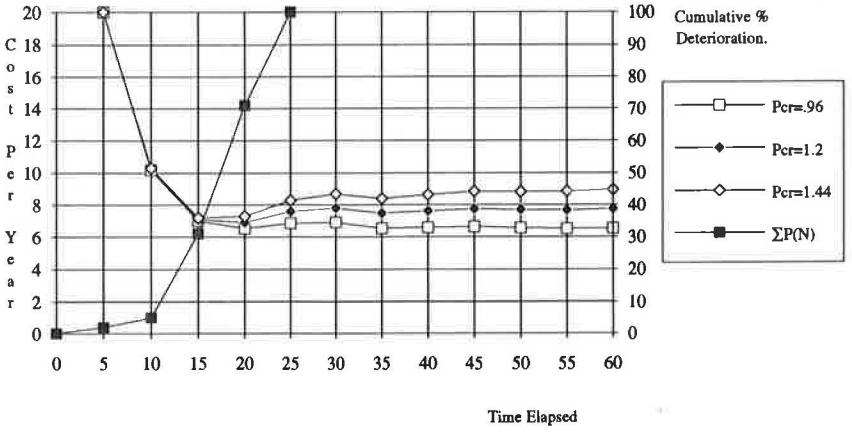

FIGURE 9 Average annual cost and cumulative deterioration profile for Deck Profile A and Patch Type 3. The optimum rehabilitation cycle occurs after 20 years when the deck is 71 percent deteriorated.

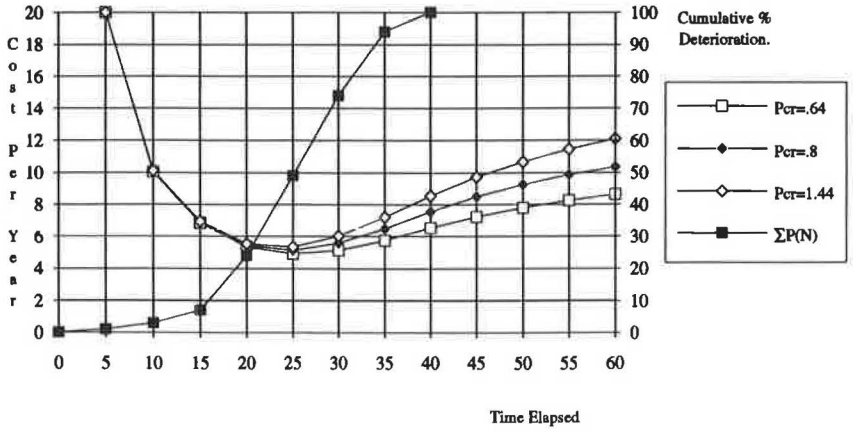

FIGURE 10 Average annual cost and cumulative deterioration profile for Deck Profile B and Patch Type 1. The optimum rehabilitation cycle occurs after 25 years when the deck is 49 percent deteriorated.

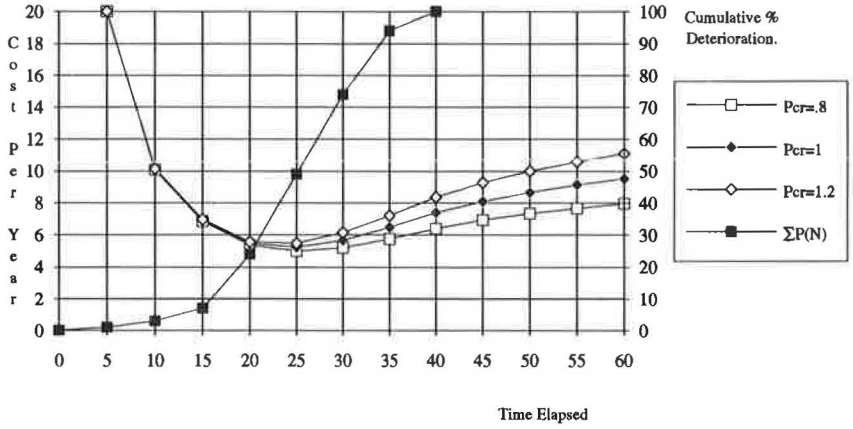

FIGURE 11 Average annual cost and cumulative deterioration profile for Deck Profile B and Patch Type 2. The optimum rehabilitation cycle occurs after 25 years when the deck is 49 percent deteriorated.

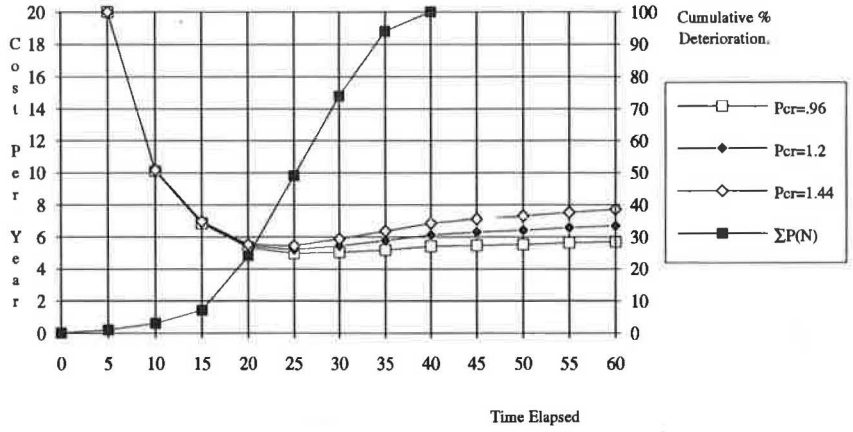

FIGURE 12 Average annual cost and cumulative deterioration profile for Deck Profile B and Patch Type 3. The optimum rehabilitation cycle occurs after 25 years when the deck is 49 percent deteriorated.

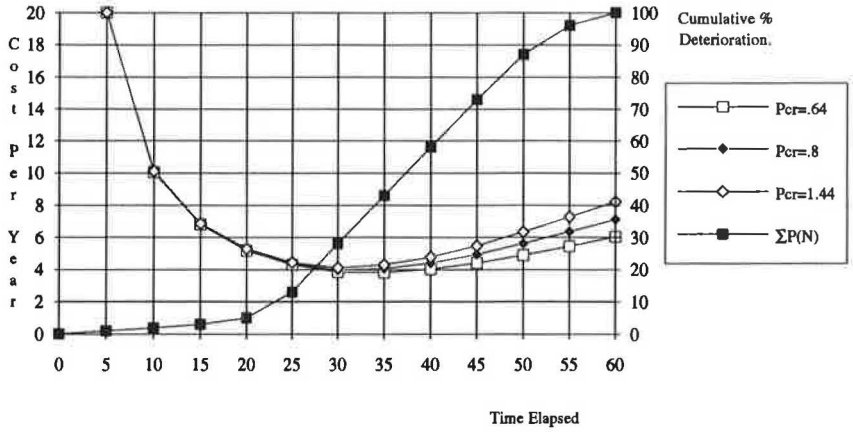

FIGURE 13 Average annual cost and cumulative deterioration profile for Deck Profile C and Patch Type 1. The optimum rehabilitation cycle occurs after 30 years when the deck is 28 percent deteriorated.

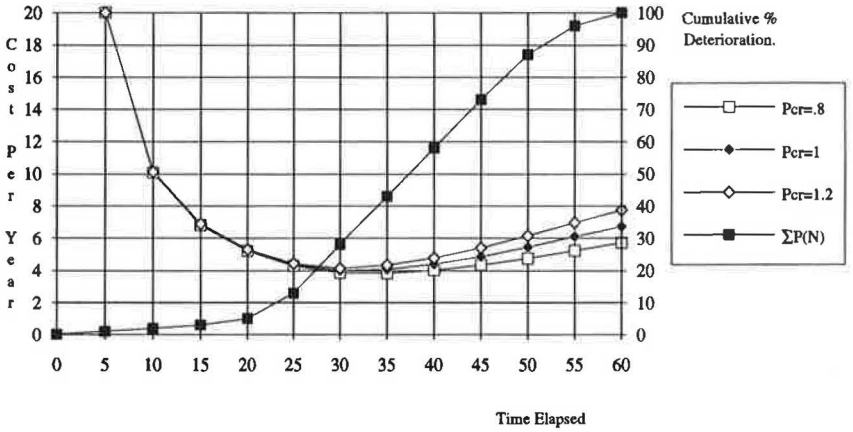

FIGURE 14 Average annual cost and cumulative deterioration profile for Deck Profile C and Patch Type 2. The optimum rehabilitation cycle occurs after 30 years when the deck is 28 percent deteriorated.

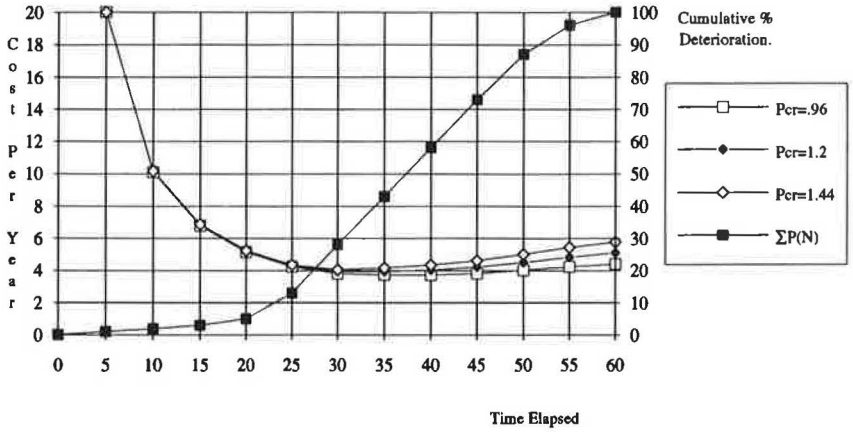

FIGURE 15 Average annual cost and cumulative deterioration profile for Deck Profile C and Patch Type 3. The optimum rehabilitation cycle occurs after 30 years when the deck is 28 percent deteriorated.

TABLE 2 TABULATION OF RESULTS

Deck specification.		Patch Type 1 100% deteriorated in 5 yrs Median cost ratio = .8			Patch Type 2 100% deteriorated in 10 yrs Median cost ratio = 1.0			Patch Type 3 100% deteriorated in 20 yrs Median cost ratio = 1.2		
		Ac*	N* yrs	D*%	Ac*	N* yrs	D*%	Ac*	N* yrs	D*%
Deck profile A	Low Pcr	6.2	20	70	6.4	20	70	6.5	20	70
30% Deterioration in 15 yrs	Med Pcr	6.5	20	70	6.8	20	70	6.9	20	70
	High Pcr	6.8	20	70	7.1	20	70	7.3	20	70
Deck profile B	Low Pcr	4.9	25	50	5.0	25	50	5.0	25	50
30% Deterioration in 22 yrs	Med Pcr	5.1	25	50	5.2	25	50	5.2	25	50
	High Pcr	5.3	25	50	5.5	25	50	5.5	25	50
Deck profile C	Low Pcr	3.8	30	30	3.9	30	30	3.8	30	30
30% Deterioration in 32 yrs	Med Pcr	4	30	30	4.0	30	30	3.9	30	30
	High Pcr	4.1	30	30	4.1	30	30	4.1	30	30

Different deck profiles produce different values for Ac*, N* and D*

quality point of view would have passed by the time deterioration reaches 70 percent. The rehabilitation decisions would thus be driven by physical rather than economic factors, with the period being limited to approximately 15 years, at which time deterioration would have reached or exceeded 30 percent. The resulting cost would be well above the minimum cost.

For Profile B, the minimum cost is lower (4.9 to 5.5) and it occurs at 25 years when deterioration is about 50 percent. Physical life would again govern, with safety and ride quality dictating the rehabilitation decision. In this case, the cycle would be around 23 years at a cost slightly above the economic minimum.

Profile C presents a well-balanced picture. The costs are low (3.8 to 4.1) and the optimum point occurs at 30 years when deterioration is also about 30 percent. This case means that economic and physical life are essentially the same and the two work together to achieve a good result. A rehabilitation cycle of about 30 years would optimize both the physical and the economic aspects of the decision.

CONCLUSIONS

The model presented has been kept simple to develop the concepts and present the methodology. It can be expanded to include many more aspects but apparent quantitative precision in the model should not override the many nonquantifiable factors that affect bridge maintenance decisions. The following factors should be noted:

1. Reduced Ride Quality. No allowance has been made for the fact that the ride quality of a deteriorated or repeatedly patched deck declines. This is a legitimate user cost that could or should be factored into the cost of patching the deck.
2. Functional Obsolescence. No account has been taken of the fact that deck replacement often provides an opportunity to renovate or upgrade the functional aspects of the bridge. This is a complex analysis; suffice to say here that a knowledge of the optimum rehabilitation cycle assists in the timing and quality of the renovate decision.
3. Time Value of Money and Inflation. These factors have been omitted in the model so as not to clutter the computations. Their inclusion is a relatively simple process; the net present value of a stream of future costs can be calculated in the place of arithmetic totals; uniform annuities at the assumed interest rate can replace the average annual cost calculations. The replacement cycle is changed by a small amount, but the concept will not alter. Assumed increases in the cost of future patching and deck replacement can also be included to improve the quality of the answer.

These limitations should be seen in relation to problems associated with defining and quantifying the five user inputs described earlier. Experience leads to a better knowledge of both the inputs and the limitations.

The model has indicated that it is possible to determine the optimum rehabilitation cycle for concrete bridge decks under a set of conditions described by five user-defined inputs. This cycle determines the economic life of the deck, which can be compared with the physical life of the deck as determined by the cumulative deck deterioration profile. Two issues are important:

1. When physical life is less than economic life then costs are high compared with the situation found when physical and economic life are well balanced.
2. This balance can only be achieved when the quality of construction and maintenance on the deck is such that less than 30 percent of the deck requires patching in the first 30 years of its service life.

The relative cost of patching may not affect the situation before the optimum cost point. This conclusion must be tempered by the fact that all the patch types assumed in the sensitivity analysis studies had essentially the same benefit-to-cost ratios as defined by their deterioration profiles and patch cost ratios. This condition changes as the benefit-to-cost ratios change; the value of the model in quantifying these changes should be noted.

Three major points must be stressed:

1. Every operation performed on the deck gives rise to a stream of future maintenance obligations. These obligations cannot be denied and must be met timeously.
2. Quality in the design construction and maintenance of concrete bridge decks is required to balance physical and economic life and to achieve the best results.
3. Bridge maintenance decisions are extremely complex. Models such as the one presented should not limit the bounds of the decision; the results they produce must be seen as guidelines for improved field decisions. Analysis certainly has

a place in the process, but it must complement rather than replace experience.

REFERENCES

1. R. L. Ackoff, E. L. Arnoff, and C. W. Churchman. *Introduction to Operations Research*. John Wiley, New York, 1957, pp. 477–516.
2. B. V. Dean. Replacement Theory. *Publications in Operations Research*, Vol. 5, 1957, pp. 330–362.
3. M. C. Vorster. A Systems Approach to the Management of Construction Equipment. University of Stellenbosch, Stellenbosch, Republic of South Africa, 1981, pp. 10–76.
4. J. L. Riggs. *Economic Decision Models*. McGraw-Hill, New York, 1968, p. 211.
5. R. L. Ackoff and M. N. Sasieni. *Fundamentals of Operations Research*. John Wiley, New York, 1968, pp. 204–229.
6. B. Rapp. *Models for Optimal Investment and Maintenance Decisions*. John Wiley, New York, 1974, p. II–1.
7. H. G. Thuesen and W. J. Fabrycky. *Engineering Economy*, 3rd ed. Prentice-Hall, Englewood Cliffs, N.J., 1964, p. 112.
8. R. E. Weyers, P. D. Cady, and J. M. Hunter. *Cost-Effectiveness of Bridge Repair Details and Procedures, Part 1: Final Report*. Research Project 84-11. Office of Research and Special Studies, Pennsylvania Department of Transportation, Harrisburg, 1987.

Publication of this paper sponsored by Committee on General Structures.

Design Criteria for Right and Skew Slab-and-Girder Bridges

HENDRIK J. MARX, NARBEY KHACHATURIAN, AND WILLIAM L. GAMBLE

Research on skew slab-and-girder bridges has had limited impact on practical bridge design. A literature study indicates that there is no information available that tells a designer exactly how to take into account the effects of skew when designing a slab-and-girder bridge. Thus, research on skew slab-and-girder bridges with the goal of developing design criteria that include the effects of skew is desirable. With this goal in mind, a parametric study is done in which the behavior of simply supported, right and skew slab-and-girder bridges is determined by varying the properties of the structural members and the bridge geometry. The results obtained from linear elastic finite element analyses on 108 bridges are used to develop an accurate, simplified analysis procedure for the maximum bending moments in the girders. Bridges with five precast, prestressed, or steel I-beam girders subjected to two AASHTO HS20–44 standard trucks are considered, but the analysis procedure is suitable for bridges with more than five girders and with more than two traffic lanes. The proposed analysis procedure is based on improved AASHTO wheel load fractions for right bridges, which are modified for skew bridges. It is found that the AASHTO specifications for the distribution of wheel loads in right slab-and-girder bridges are sometimes unsafe and often too conservative.

A slab-and-girder bridge system is a favored structural choice both on economic and on aesthetic grounds. It is so named because it consists of two major structural elements. These are a reinforced-concrete slab that serves as the roadway and distribution medium for concentrated wheel loads, and a number of prefabricated girders that are parallel to traffic and that carry these distributed wheel loads and dead weight to the abutments.

The basic analysis problem is to determine the distribution of wheel loads among the girders to obtain design loads that the engineer can use to proportion the individual girders. This problem has been studied for decades by many researchers using different approaches. However, little research had been done on skew slab-and-girder bridges until the advent of the electronic digital computer, which made extensive numerical solutions possible.

Research on skew slab-and-girder bridges has had limited impact on practical bridge design. A literature survey indicates that there is no information available that tells a designer exactly how to take into account the effects of skew when designing a slab-and-girder bridge. Even the current AASHTO *Standard Specifications for Highway Bridges* (*1*) provides no guidance regarding the effects of skew on the behavior of a bridge.

Previous researchers (*2–4*) were concerned mainly with the development of analytical methods of analysis for skew bridges. Skew bridge behavior has not been thoroughly investigated and results have not been presented in a way that would be helpful to the designer. Thus, research on skew slab-and-girder bridges with the goal of developing design criteria that include the effects of skew is desirable.

H. J. Marx, BKS Inc., P.O. Box 3173, Pretoria 0001, Republic of South Africa. N. Khachaturian and W.L. Gamble, Department of Civil Engineering, University of Illinois at Urbana-Champaign, 205 North Mathews Avenue, Urbana, Ill. 61801.

DESCRIPTION OF THE PROBLEM

With this goal in mind, a parametric study was done by analyzing different simply supported slab-and-girder bridges, using the finite element method of analysis. The data from these analyses were used to determine wheel load distribution characteristics of right and skew bridges, by plotting the maximum girder bending moments that occur against the different parameters defining the geometric layout and structural properties of a bridge.

The changes in bridge behavior that result as a consequence of varying individual parameters were further mulled over and maximum girder bending moments were expressed as functions of certain decisive combined parameters, use of which led to small scatter in girder bending moment results.

An easy-to-use, reliable method of determining maximum girder bending moments in simply supported right and skew slab-and-girder bridges was developed in a form familiar to practicing engineers (*5*, *6*).

The purpose is to present the parameters that control the behavior of a bridge and a proposed simplified method of determining maximum girder bending moments in simply supported right and skew slab-and-girder bridges.

The typical skew bridge shown in Figure 1 consists of a horizontal reinforced-concrete slab of uniform thickness, supported by five identical precast, prestressed concrete girders. The slab edge and girder ends are simply supported at the two parallel skew abutments. The girders are identical, prismatic, and equidistant from each other. The span a, of the bridge, equals the length of the girders and varies from 12.19 to 24.38 m (40 to 80 ft). Only short-span bridges are considered for the reason discussed later. The girder spacing, b, varies from 1.83 to 2.74 m (6 to 9 ft) and the angle of skew, α, defined in Figure 1, varies from 0 to 60 degrees. The slab thicknesses and girder properties used cover the practical ranges for this type of bridge. A total of 108 two-lane slab-and-girder bridges subjected to two AASHTO HS20–44 standard trucks

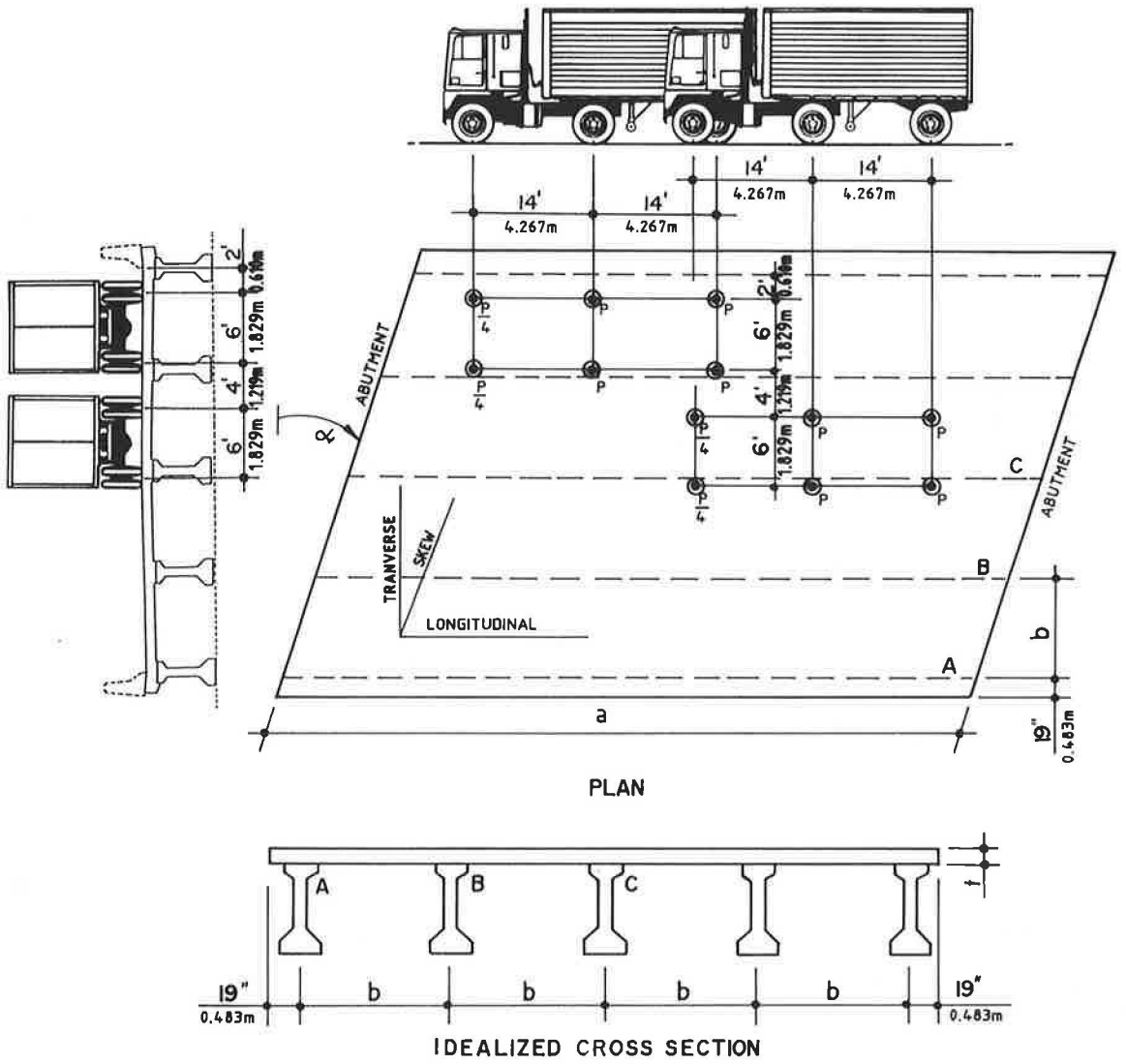

FIGURE 1 Typical bridge considered with AASHTO HS20–44 truck loads.

are analyzed principally to obtain the maximum girder bending moments. The results can also be used for bridges with steel I-beams when a minor modification is made. The following assumptions and limitations, which are justified and discussed in detail by Marx et al. (*6*), are applicable:

1. The material in the slab is homogeneous and isotropic; the slab and girders behave in a linearly elastic manner;
2. Full composite action occurs between the slab and eccentric girders;
3. The stiffening effect of the curbs and parapets is ignored;
4. The girder-slab interaction occurs along a line, that is, the girders have no width;
5. Except for rigid diaphragms at the abutments, no other diaphragms exist;
6. The width of the slab overhangs at the edge girders is 483 mm (19 in.);
7. The faces of the curbs are directly above the edge girders, i.e., no truck wheel can get closer than 0.610 m (2 ft) from an edge girder; and
8. Only I-shaped girders are considered.

It was found (*6*) that girder bending moment results obtained from a five-girder bridge closely and conservatively approximate the results for a bridge with more equidistant girders. Results for five-girder bridges can thus be used for bridges with more girders.

The width of the slab overhangs at the edge girders is not of much importance, but the position of the face of the curb relative to the edge girder has a significant influence on the edge girder bending moments. Illinois and some other states generally have not used span diaphragms in prestressed I-girder bridges for many years.

METHOD OF ANALYSIS USED

The finite element method was used to determine the linearly elastic behavior of a bridge under service loads. The girders were modeled with eccentric Lagrangian-type isoparametric beam elements with the St. Venant girder torsional stiffness taken into account. The bridge deck was modeled with nine-

node Lagrangian-type degenerated isoparametric thin-shell elements.

No closed-form exact solutions exist for skew slab-and-girder bridges with which results could be compared. First it was necessary, therefore, to determine whether the shell elements used to model the deck provided correct results when used in skew configuration. Furthermore, it was necessary to perform a convergence study on a typical bridge to determine to what extent the mesh had to be refined to ensure reliable results. For the purpose of comparing results, the finite element mesh selected was used to analyze certain slab-and-girder bridges for which other solutions existed.

Details on compatibility problems with eccentric beam modeling and on problems encountered with excessive stiffness when a rectangular shell element is distorted into a parallelogram that fits into a skew network have been provided by Marx et al. (*5*, *6*).

INTRODUCTION OF THE PARAMETERS USED

Geometric Parameters

There are three parameters that determine the geometry of the bridge. They are the angle of skew, α, the bridge span, a, and the girder spacing, b. These three parameters have already been defined in Figure 1. Wherever convenient, a fourth dimensionless parameter, the girder spacing to span ratio, b/a, is used.

Structural Parameters

A large number of variables determine the structural properties of a bridge. The large amount of work involved in considering all of these variables in a parametric study would be prohibitive. It is necessary, therefore, to eliminate as many variables as possible without simplifying the structure to such an extent that the structural behavior would be altered. This procedure can be done by ignoring the unimportant variables and by combining others to bring about new ones that control the structural behavior.

The controlling parameters are determined by recognizing the major structural actions in a slab-and-girder bridge, as follows:

1. The slab distributes truck loads over the width of the bridge. To do this, it acts in flexure in the transverse direction, similar to a beam continuous over flexible supports. The transverse flexural rotation of the slab over a girder is resisted by the torsional rigidity of the girder.
2. The eccentric girders act together with the slab to form stiff composite T-section girders that carry the whole load to the abutments in flexure.

It is necessary, therefore, to combine the variables that determine the flexural slab stiffness and those that bring about the flexural composite girder stiffness and the torsional girder stiffness.

Flexural Slab Stiffness D

The flexural slab stiffness per unit width is given by

$$D = \frac{E_s t^3}{12(1 - \mu^2)} \tag{1}$$

where t is the slab thickness, E_s if Young's modulus of elasticity for the slab material, and μ is Poisson's ratio (taken as 0.2 for concrete). The thickness of the slab depends on the girder spacing and is normally between 152 and 254 mm (6 and 10 in.).

Flexural Composite Interior Girder Stiffness, $E_g I_{cg}$

A large number of unimportant structural variables can be eliminated by using the composite girder stiffness as a parameter. The composite moment of inertial of an interior girder, I_{cg}, can easily be determined by using the effective flange width recommendations in the AASHTO *Specifications for Highway Bridges* (*1*) and by transforming the slab concrete to equivalent girder concrete according to their modular ratio. The effect of this approximation is discussed later. E_g is Young's modulus of elasticity for the prefabricated girders, and also for the composite transformed girders.

Torsional Girder Stiffness

The transverse rotation of the slab over a supporting girder is resisted by the torsional rigidity of the girder. In effect, the slab is thereby stiffened in bending in the transverse direction. A stiffer slab distributes truck loads better, so that a more uniform cross distribution of load occurs.

The torsional stiffness of a steel I-beam is small and has negligible influence on the distribution of truck loads to the girders. It can, therefore, be ignored. Precast, prestressed concrete girders have considerably larger torsional stiffness. The influence of girder torsional stiffness becomes gradually larger as the angle of skew increases. However, the effect on the distribution of truck loads to the girders is only about 5 percent. On the other hand, the torsional stiffness of girders of box section, which are not considered in this study, has a significant influence.

Because the behavior of slab-and-girder bridges is so insensitive to girder torsional stiffness, the torsional stiffness is not used as a major parameter in this study. However, it is taken into account. The flexural and torsional properties of the girders used in the analyses are those of actual standard precast, pretensioned, prestressed concrete girders, which are used in practice for spans up to 24.38 m (80 ft).

Although the properties used in the analyses are those for prestressed concrete girders, the results can also be used for steel I-beams by increasing the design girder bending moments by 5 percent.

Dimensionless Stiffness Parameter, H

The behavior of a slab-and-girder bridge depends on the geometry of the bridge as well as on the structural properties

of the bridge members. Newmark (7), on the basis of analyses of bridges using girders having no eccentricity, found that the flexural stiffness of the slab and the flexural stiffness of the girders need not to be considered as two separate parameters. They can be combined to form a new, convenient dimensionless stiffness parameter. Newmark defined the parameter H as the ratio of the longitudinal bending stiffness of an isolated noncomposite girder, E_gI_g, to the transverse bending stiffness of a width of slab equal to the span of the bridge:

$$H = \frac{E_gI_g}{aD} \tag{2}$$

Because D is the flexural stiffness of the slab per unit width, it is necessary to multiply D by some width to make H dimensionless. The span, a, serves this purpose, although a is not the width of the slab effective in the transverse direction. H is simply a convenient dimensionless stiffness parameter. A large H value means that the bridge has large, stiff girders. Newmark (7) found that different bridges with noncomposite girders and the same H and b/a ratios always yield identical influence surfaces for girder bending moments.

A minor modification is necessary to apply H in this study. The moment of inertia of the isolated girders, I_g, should be replaced by the composite moment of inertia, I_{cg}, of an interior girder. The modified H used in this study is then

$$H = \frac{E_gI_{cg}}{aD} \tag{3}$$

The value of H is now a function of the effective flange width, because it depends on the composite girder moment of inertia. The effective flange width is an approximation to take into account the effect of shear lag in the slab, which depends, among other things, on the slab thickness, girder spacing, span, eccentricity of the girders, and loading condition. It is thus obvious that some differences in girder bending moments occur when two bridges with composite girders have the same H and b/a ratios but with different variables determining the H value. However, it is found that these expected differences are less than 2 percent for practical bridges subjected to truck loads, which means that the parameter H is adequate for bridges with composite girders.

Further uncertainties regard the real value of H. What are the real values of E_s and E_g? How much does the effect of slab cracking influence the average flexural stiffness of the slab? Fortunately, it is found that the girder bending moments are not particularly sensitive to moderate variations in H, especially for large values of H.

A particular bridge has only one H value, which is calculated using the flexural stiffness of an interior composite girder. Exterior girder bending moment results are also expressed in terms of this H value, despite the fact that their flexural composite stiffness is different from the interior girders as a result of the difference in effective flange widths. Bridge design manuals indicate that the H value of practical bridges falls between $H = 5$ and $H = 30$.

The value of H depends on both a and b since I_{cg} depends on the effective flange width, which equals the girder spacing, b, in most practical bridges. However, in the parametric study, the values of the parameters are changed one at a time. Thus if b or a is varied, the necessary changes are made to the slab thickness and cross-sectional properties of the prefabricated girders to keep the value of H the same.

Truck-Loading Parameter, P

In this study, the emphasis is on the distribution of truck loads among the girders in the bridge. The HS20–44 standard truck considered is a tractor truck with semitrailer and is in accordance with the AASHTO *Standard Specifications for Highway Bridges* (1). It represents a large number and variety of actual truck types and loadings to which the bridge might be subjected under actual traffic conditions.

Figure 1 shows the locations of the wheel loads and the transverse location of one truck relative to another. Each truck occupies the central portion of a 3.05-m (10-ft)–wide load lane, one truck per lane. These load lanes can be placed anywhere in the entire roadway width of the bridge, which is the clear distance between the faces of the two curbs, to produce maximum moments in whichever girder is considered. This result means that no wheel centroid can act closer than 0.61 m (2 ft) from the face of a curb or edge girder, which is a greatly desired condition (6). As shown in Figure 1, it also means that the minimum transverse distance between the wheel centroids of two trucks in adjacent loading lanes 1.22 m (4 ft).

The AASHTO specifications make provision for the length of the semitrailer to vary such that the rear axle spacing is between 4.27 and 9.14 m (14 and 30 ft). Only simply supported bridges are dealt with, thus the minimum axle spacing of 4.27 m (14 ft) is used to obtain maximum girder bending moments.

Girder bending moment influence lines across the width of the bridge, many of which are reported in previous research (Figures 2 and 3), clearly indicate that the transverse truck spacing should be as small as possible to obtain the maximum moment in any one of the girders. Only the 1.22 m (4 ft) minimum distance between adjacent truck wheel centroids is thus used in the analyses.

Two of the three axles of an HS20–44 standard truck carry the same load. The front axle carries only one-quarter of the load carried by each of the other two axles. The truck loading parameter P is defined as half the load acting on one of the heavy axles of a truck. The total weight of a truck is thus $4.5P$. The value of P should be increased according to the AASHTO provision for impact. The trucks in adjacent loading lanes may travel in the same or in opposite directions. whichever case produces the maximum required effect.

If three or four of the traffic lanes on a bridge are occupied simultaneously, it may result in girder bending moments that are larger than the corresponding moments obtained if only two traffic lanes are loaded. In practice, however, it is unlikely that three or more lanes will be occupied in such a way that all trucks are producing their maximum contribution to the moment in the particular girder under consideration. It is also very unlikely that all of these trucks will be loaded to their maximum capacity. These considerations are recognized in Provision 1.2.9 of the AASHTO specifications, which allow for a reduction in girder design moments obtained from loading conditions in which three or more traffic lanes are loaded.

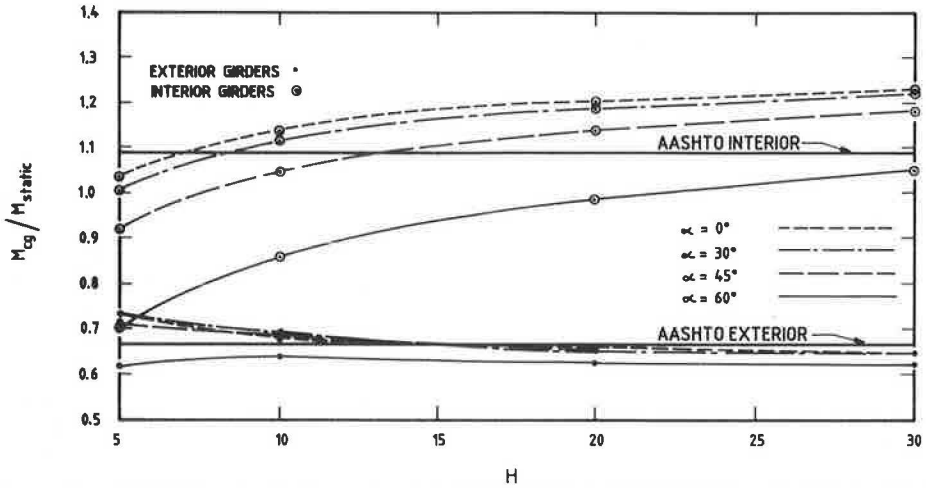

FIGURE 2 Midspan girder bending moment influence lines caused by a point load *P* moving transversely across a right bridge at midspan, *b/a* = 0.05.

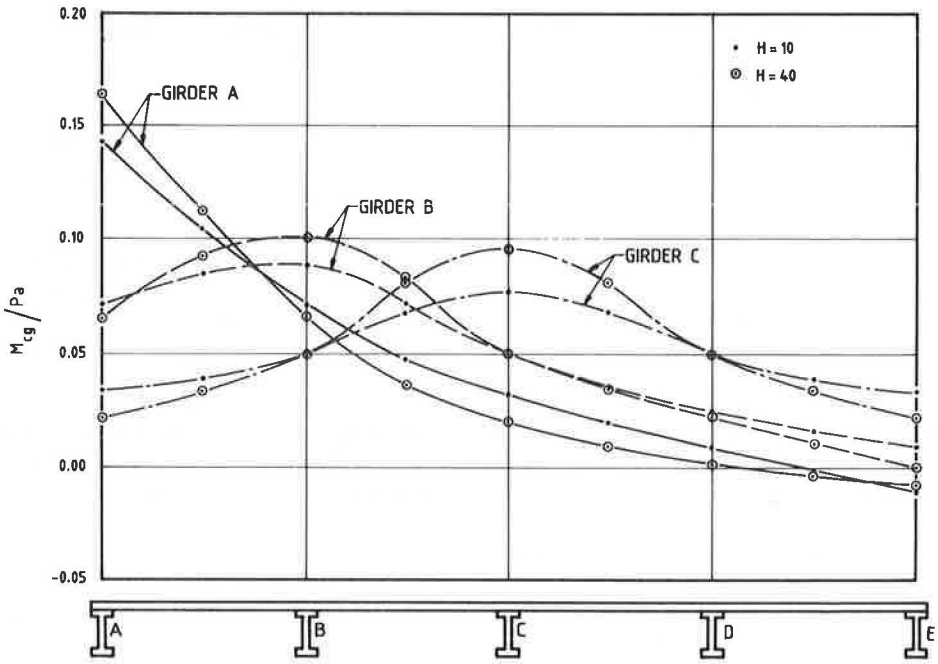

FIGURE 3 Midspan girder bending moment influence lines caused by a point load *P* moving transversely across a right bridge at midspan, *H* = 20.

If the girder moments obtained from load cases in which three or more traffic lanes are loaded are multiplied by their appropriate AASHTO reduction factors, it always results in design moments smaller than those obtained from load cases with two-lane loading. Thus, only two traffic lanes are loaded in this study.

The maximum bending moments in the composite girders, M_{cg}, are obtained from the bending moment envelope diagrams that result when the two trucks are moved progressively along the span. The directions of movement and transverse locations of the trucks, which produce maximum girder bending moments, are determined by trial and error.

The two other types of vehicle loading specified in the AASHTO specifications (*1*) are not of importance for the range of spans considered. These are a lane loading, representing an approximation of a truck train that normally governs for spans longer than 44.8 m (147 ft), and two-axle military loading with axles spaced at 1.22 m (4 ft), which tends to govern in bridges with spans shorter than 11.28 m (37 ft).

BEHAVIOR OF SLAB-AND-GIRDER BRIDGES

Influence of the Vertical Stiffness Ratio, *R*

The behavior of a continuous slab over flexible girders is highly complex. In order to obtain some understanding of this behavior, it is useful, for the purpose of discussion, to degrade the complexity of the structure to something more familiar.

The vertical stiffness at any point along a beam is a function of

$$k_i EI/L^3$$

where

k_i = constant depending on the boundary conditions and the location of the point under consideration,
EI = bending stiffness of the beam, and
L = span of the beam.

The vertical stiffness of an interior composite girder in a slab-and-girder bridge is thus a function of $k_1 E_g I_{cg}/a^3$. Similarly, the vertical stiffness of a section of the slab that is effective in distributing load in the transverse direction is a function of $k_2(k_3 a)D/b^3$, where k_2 is a constant depending on the boundary conditions and $(k_3 a)$ is a fraction of the span, a. The parameters, a, b, and D have been previously defined.

The vertical stiffness ratio, R, is defined as the ratio of the vertical stiffness of an interior composite girder to the vertical stiffness of a section of the slab effective in the transverse direction and is thus proportional to

$$R \propto \frac{\left(\frac{E_g I_{cg}}{a^3}\right)}{\left(\frac{aD}{b^3}\right)} = \left(\frac{E_g I_{cg}}{aD}\right)\left(\frac{b}{a}\right)^3 = H(b/a)^3 \qquad (4)$$

This vertical stiffness ratio, R, which determines the structural behavior of a slab-and-girder bridge, depends on two terms. The first term, which combines the flexural bending stiffness of the interior composite girders and that of the slab, is the flexural stiffness parameter H as previously defined. The second term, which is purely geometric, is the ratio between the girder spacing and span of the bridge.

These two terms have the following effects on the structural behavior. A bridge that has a large H value may either have stiff girders or a highly flexible slab. Consider the theoretical case where a slab-and-girder bridge has an extremely flexible slab. A point load is applied directly above a girder. The particular girder deflects under the load, while the other girders deflect a negligible amount, because the slab is too flexible to transfer any significant loads to them. Thus, the loaded girder has to carry nearly all the load by itself and hardly any load sharing occurs.

On the other hand, a bridge that has a small H value can be thought of as one in which the slab is thick enough to distribute an applied point load, so that all the girders help to carry the load. A small H value thus corresponds to more uniform load distribution across the width of a bridge.

The effect of the second term, the b/a parameter, can be explained as follows. A small b/a ratio corresponds to a long-span bridge with girders at close spacing. The cross section of the bridge does not deform much and the bridge behaves like a single beam in which the load is distributed uniformly over the width. On the other hand, a large b/a ratio corresponds to a bridge with a short span and large girder spacing. The bridge behaves more like a wide slab in which the bending moments caused by a point load are nonuniformly distributed over the width.

Summarizing, a reduction in R caused by a reduction in H or b/a corresponds to an increase in the ability of the slab to distribute the load more uniformly. Because the b/a term is raised to the power three, it is obvious that a small change in its value has a more pronounced effect on the structural behavior than an equivalent change in the H value. The effects of these two terms are now more closely examined.

Effect of Varying the Stiffness Parameter, H

Figure 4 shows a typical graph for the maximum girder bending moment coefficient m_{cg}/M_{static} as a function of the stiffness parameter H for different angles of skew, when the bridge is subjected to two HS20–44 trucks. M_{static} is defined as the maximum static bending moment that results when one row of three wheels (say the left-front, left-middle, and left-rear wheel with loads $P/4$, P, and P, respectively) of one HS20–44 truck moves across a single isolated beam that has the same

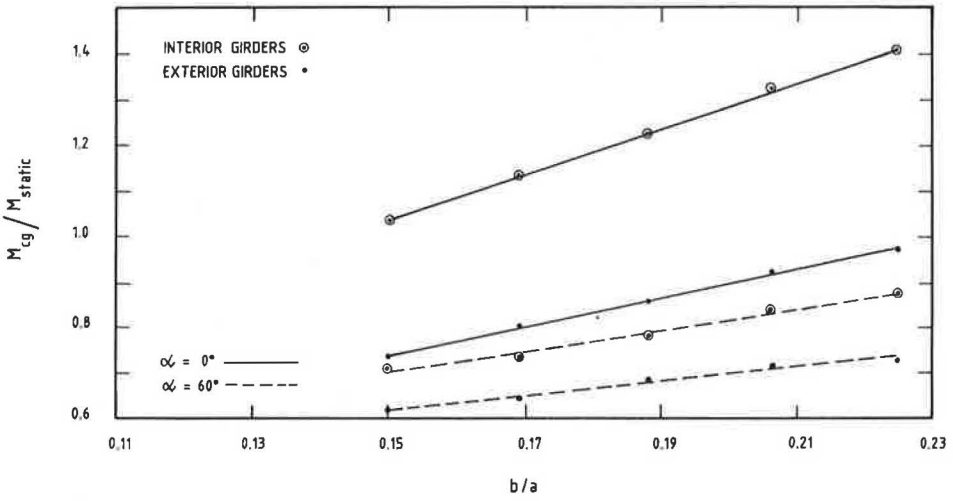

FIGURE 4 Maximum girder bending moment coefficient variation with H, a = 12.19 m (40 ft) and b = 1.83 m (6 ft).

span as the girders in the bridge. In this particular case, the girder spacing and span are 1.83 and 12.19 m (6 and 40 ft), respectively. No distinction is made between the interior girders. Because they are prefabricated, they are usually designed for the same moments, although small differences in maximum moments normally occur. The maximum bending moment in the interior girders always increases as H increases because the ability of the slab to distribute loads decreases.

The girder moments are more sensitive to changes in H when the H value is small. Figure 4 shows that, for $\alpha = 0$, an increase of 50 percent in the H value, from $H = 5$ to $H = 7.5$, results in a 5.8 percent increase in the maximum interior girder bending moment. An increase of 50 percent in the H value from $H = 20$ to $H = 30$ results in only a 2.4 percent increase in moment.

It is fortunate that the girder design moments are insensitive to moderate changes in the H value, because there are many uncertainties surrounding the true value of H. These uncertainties include the effect of cracks in the slab concrete, the true modulus of elasticity of the slab and girder concrete, and the approximation of the effect of shear lag by an effective flange width.

The exterior girder behaves differently. As a rule, an increase in H always results in a small decrease in the maximum exterior girder bending moment. However, it is found that when the angle of skew is 60 degrees, there is, in some cases, a slight increase in the maximum exterior girder moment when H is increased between $H = 5$ and $H \cong 15$, after which the moment decreases again. This is the case for the particular bridge shown in Figure 4. The maximum moment in the exterior girder is highly insensitive to changes in H over the whole range of H considered.

The difference in behavior of the interior and exterior girders can easily be explained with reference to Figure 2. The data were provided by Sithichaikasem (*8*). Figure 2 shows the midspan girder bending moment influence lines for a single point load P moving transversely across a right bridge at midspan. The b/a ratio of the bridge is 0.05. Assume that the girder spacing is 2.44 m (8 ft). To obtain the maximum bending moment in Girder C, Truck 1 is placed in Panel BC and Truck 2 in Panel CD, with the centroids of the nearest wheels 0.61 m (2 ft) away from Girder C on both sides. In Panels BC and CD, the values of the moment influence diagram for Girder C increase when H increases. Thus, the maximum bending moment in Girder C increases.

On the other hand, to obtain the maximum bending moment in the exterior girder, Girder A, the centroid of the nearest longitudinal row of wheels of Truck 1 is placed 0.61 m (2 ft) away from Girder A (face of the curb) according to the AASHTO requirement (*1*). The second row of wheels of Truck 1 falls directly on top of Girder B. All the wheels of Truck 2 fall in Panels BC and CD. The influence line for Girder A indicates that when H increases, only the first row of wheels of Truck 1 causes an increase in bending moment. All the other wheels of Trucks 1 and 2 cause a reduction in moment when H increases. The sum of reductions is slightly more than the moment increase produced by the first line of wheels of Truck 1. Thus, the maximum exterior girder bending moment decreases slightly when H is increased.

Because of the reciprocal law, the shape of a particular girder bending moment influence diagram also represents, to one or other scale, how a point load acting on the girder is distributed to the adjacent girders. Figure 2, also, therefore, demonstrates that a small H value corresponds to a more uniform distribution of load, because the influence lines are flatter for smaller H values.

Summarizing, a larger H value corresponds to a more flexible slab less capable of distributing load. Most of the wheel loads act on the deck in an area supported by the interior girders. Because of the diminished capability of the slab to transfer loads from this area to the edges of the bridge as H increases, the bending moments in the exterior girders decrease at the cost of an increase in moments in the interior girders.

Effect of Varying the Parameter b/a

Figure 5 shows a typical graph for the maximum girder bending moment coefficient M_{cg}/M_{static} as a function of b/a by varying only the girder spacing, b. The bridge is subjected to two HS20–44 trucks. In this particular case, the span is 12.19 m (40 ft) and $H = 5$. Because the span is kept constant, the static bending moment to be distributed remains the same.

Figure 5 shows that as the b/a ratio increases, the maximum girder bending moment coefficients increase approximately linearly for both interior and exterior girders. This linear variation with b/a also holds when skew is introduced.

Figure 3 shows influence lines for girder bending moments at midspan caused by a single point load P moving transversely across the bridge at midspan for $b/a = 0.1$ and 0.2 with $H = 20$. The data were provided by Sithichaikasem (*8*). The influence diagram for a particular girder has a larger peak in the vicinity of the girder for the larger b/a ratio. Because wheel loads are positioned as close as possible to a particular girder to obtain its maximum bending moment, the result is a larger bending moment if b/a is increased.

As b/a is increased, there is a decrease in influence values for wheels located more than approximately one girder spacing away from the girder under consideration. However, because b is increased and the wheels are kept as close as possible to the particular girder, there is a shift in the locations of wheels relative to the influence diagram in the direction of the girder (more wheels in the positive influence area), resulting in higher influence values.

The discussion has concerned a variation in the b/a ratio by changing b. The increase in girder bending moment with b is as a result of the larger slab area that each girder carries (more wheel loads can be applied), as well as the result of the larger b/a ratio, which decreases the ability of the slab to distribute the load in the transverse direction.

Figure 6 shows a typical graph for the maximum girder bending moment coefficient M_{cg}/M_{static} as a function of b/a for different angles of skew. The b/a ratio is now varied by changing only the span, a. The bridge is subjected to two HS20–44 trucks. The girder spacing is 2.74 m (9 ft) and $H = 5$.

Figure 6 shows that the variation in the maximum girder bending moment coefficients is approximately linear when b/a is varied for both right and skew bridges. For a right bridge, the maximum bending moment coefficient increases for the

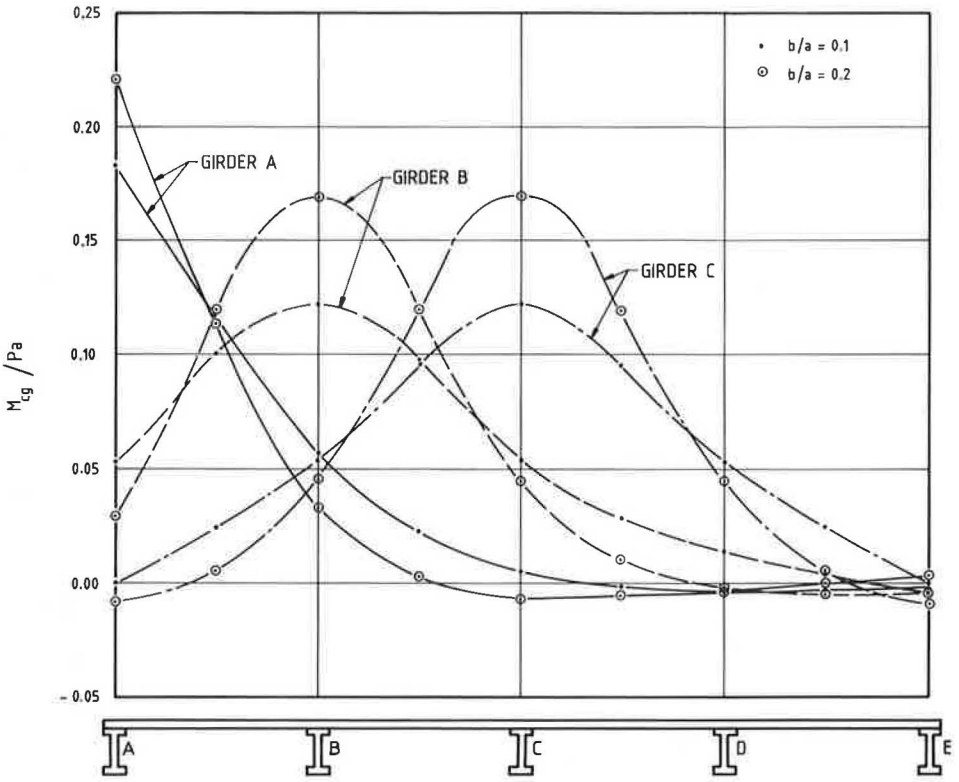

FIGURE 5 Maximum girder bending moment coefficient variation with *b/a* by changing only *b*, *H* = 5 and *a* = 12.19 m (40 ft).

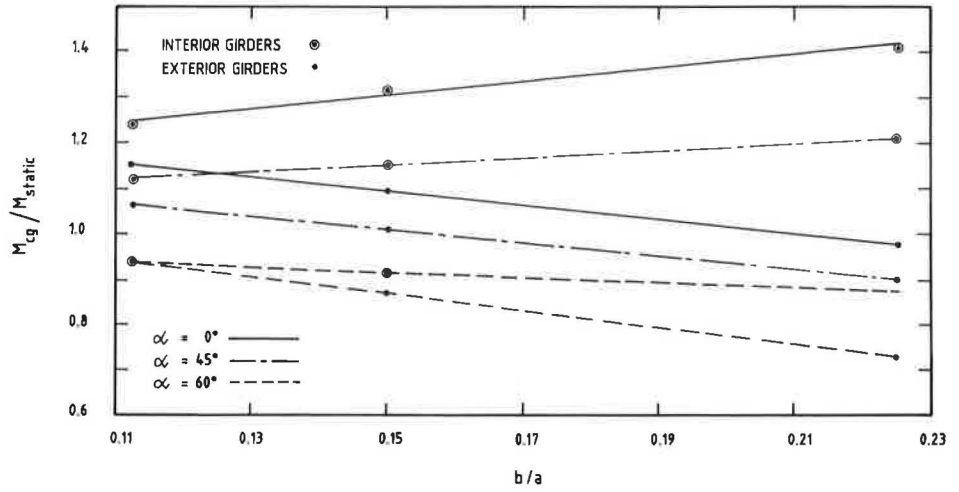

FIGURE 6 Maximum girder bending moment coefficient variation with *b/a* by changing only *a*, *H* = 5 and *b* = 2.74 m (9 ft).

interior girders and decreases for the exterior girders as *b/a* is increased by reducing the span. This behavior is similar to the effect of an increase in *H* as previously discussed.

The variation of the influence lines in Figure 2 caused by an increase in *H* is similar to the variation of the influence lines in Figure 3 caused by an increase in *b/a* ratio. Because *b* is constant in this case, similar effects are obtained because there is no shift in the locations of the wheels relative to the girders, as is the case in Figure 5.

Although the bending moment coefficient for the interior girders of the right bridge in Figure 6 increases with *b/a*, the bending moment is smaller because the static bending moment is smaller when the span is reduced. Figure 6 also shows that the interior girder bending moment coefficient decreases with a decrease in the span for large angles of skew, but this is dealt with in the next section.

The behavior of a slab-and-girder bridge is sensitive to changes in *b* and the *b/a* ratio. The importance of the *b* pa-

rameter and the linear behavior is reflected in the current AASHTO design specifications, because the interior girder bending moments may be calculated using the wheel load fraction $b/5.5$.

Effect of Varying the Angle of Skew α

The influence of the angle of skew on the distribution of wheel loads is the crux of this study. A bridge built on skew alignment always has smaller girder bending moments than its right counterpart with the same span. The larger the angle of skew becomes, the smaller the girder design moments obtained. This holds for all girders in the bridge.

The reduction in bending moments in the girders of skew bridges results as a consequence of the following two effects:

1. With the abutments not perpendicular to the girders, some of the wheels of the trucks are not on the bridge at all or are closer to the supports than in the corresponding right bridge. The total maximum static bending moment to be distributed between the girders is thus reduced.
2. In a short-span bridge with a large angle of skew, there is a tendency for the slab to span in the shortest diagonal direction. The slab transfers part of the load directly to the supports. This slab action decreases the loads that are normally carried by the girders in right bridges. There are corresponding changes in the magnitude of the bending moments in the slab. The effect of skew on the slab moments is not determined in this study.

Figure 7 shows a typical graph for the maximum girder bending moment coefficient M_{cg}/M_{static} as a function of the angle of skew for different H values. The girder spacing is 2.74 m (9 ft) and the span is 12.19 m (40 ft). Figure 7 indicates

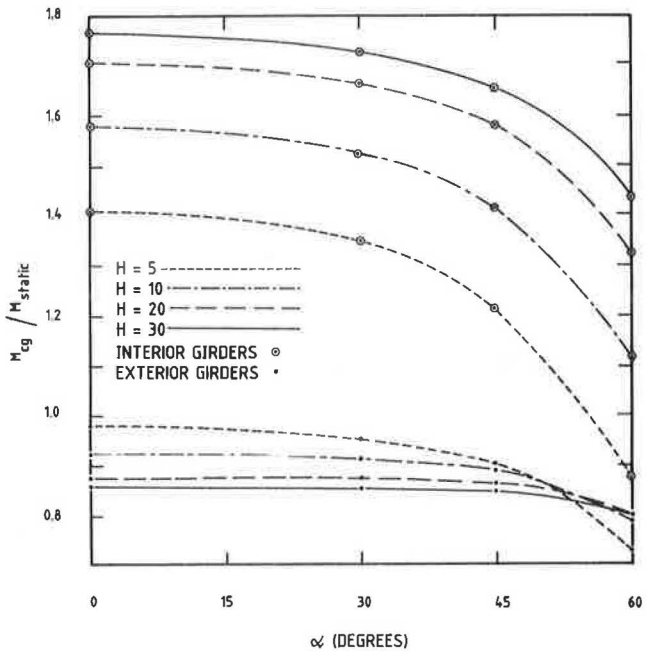

FIGURE 7 Maximum girder bending moment coefficient variation with α, a = 12.19 m (40 ft) and b = 27.74 m (9 ft).

that the exterior girders are highly insensitive to changes in the angle of skew for α between 0 and 45 degrees. The interior girders are also insensitive to changes in α between 0 and 30 degrees. Most of the reduction in girder bending moments occurs for angles of skew larger than 45 degrees. The effect of skew is more pronounced when the H value is small. This result can be explained by the tendency of stiff girders to oppose the action of the slab to span in the shortest diagonal direction. The reduction in girder bending moment because of skew is large for a combination of large angle of skew, large girder spacing, small span, and small H value.

The reduction in maximum interior girder bending moments because of skew is always less than 5 percent for angles of skew up to 30 degrees. When α = 60 degrees, a reduction of as much as 38 percent is possible. The reduction in maximum exterior girder bending moments because of skew is always less than 8 percent for angles of skew up to 45 degrees. When α = 60 degrees, the maximum possible reduction is 25 percent.

Figure 4 shows the typical variation in maximum girder bending moment coefficient with H for different angles of skew. The effect of skewness may only be a reduction in the girder moments, because the shape of the diagrams remains almost the same. This is especially true of the interior girders for which the largest bending moment reductions take place.

Figure 4 also shows that there is a tendency for an edge girder to become the controlling girder in a skew bridge, because the bending moments in the interior girders are reduced much more by skew than those in the exterior girders. This tendency becomes more pronounced for a combination of a large angle of skew, a small H value, a large span, and a small girder spacing. Cohen (*9*) made a similar observation. However, the edge girder controls in only 2 of the 108 bridges analyzed. In these two cases, the maximum exterior girder bending moment is only 0.3 and 1.0 percent larger than the maximum bending moment in the interior girders.

It is possible to avoid the undesired condition of having the controlling moment in an edge girder by keeping the truck wheels at least 0.61 m (2 ft) away from the edge girders. This conclusion is limited to bridges with spans not exceeding 24.38 m (80 ft).

COMPARISON WITH THE AASHTO DESIGN RECOMMENDATIONS FOR RIGHT BRIDGES

Although the actual distribution of load to the girders in a slab-and-girder bridge is highly complex, a fictitious load distribution, which is characterized by the well established concept of a wheel load fraction, can be used to account for the moments in the girders. The current AASHTO *Standard Specifications for Highway Bridges* (*1*) permits the use of wheel load fractions for the design of right slab-and-girder bridges subjected to standard truck loads.

The maximum bending moment coefficients for the interior and exterior girders obtained by using the AASHTO wheel load fractions are also shown in Figure 4 for the particular bridge. The bending moment coefficient for the exterior girders resulting from the wheel load fraction $b/(4 + b/4)$ for steel I-beams is not indicated. This fraction provides design moments that are too large by 30 to 60 percent.

A comparison between the present results for right bridges and the current AASHTO specifications indicates that the AASHTO provisions result in bending moments for the interior girders that are in many cases too small. This is especially so for a combination of a large H value, short span, and small girder spacing. For the range of parameters considered in this study, the AASHTO $b/5.5$ interior girder wheel load fraction is between 12 percent too low and 32 percent too high. Culham (*10*), who analyzed right bridges with intermediate diaphragms, also found that the $b/5.5$ fraction gives interior girder bending moment results that are too small for short spans and too large for large spans.

The current AASHTO provision for exterior girders, which is based on the assumption that the slab acts as if simply supported between adjacent girders, is unconservative in most of the cases considered. It is less safe when H is small and the span is large. The girder spacing does not have any significant effect. For the range of parameters considered in this study, this specified AASHTO method for the exterior girders is up to 23 percent of the unsafe side. However, the AASHTO requirement that edge girders must have at least the same load-carrying capacity as the interior girders governs in these cases. Culham (*10*) also found that this provision for the exterior girders underestimates the load carried by the exterior girders.

The AASHTO specification that requires the same load-carrying capacity for all the girders in the bridge leads to overconservative design of the exterior girders. For bridges with short spans, stiff girders, and large girder spacings, the design bending moments can be more than twice the actual values. However, it is practical to make all girders identical, which would then also allow for a possible future widening of the bridge. This study is based on bridges having identical interior and exterior girders.

SIMPLIFIED ANALYSIS PROCEDURE FOR RIGHT AND SKEW SLAB-AND-GIRDER BRIDGES

General

The comparison between the present girder bending moment results for right bridges and the current AASHTO wheel load fractions indicates that some improvements in the existing analysis method for right bridges are desirable. Furthermore, the need to have some sort of simplified analysis procedure for the girders of skew slab-and-girder bridges exists because the AASHTO specifications provide no design recommendations regarding this matter.

The use of a wheel load fraction to determine girder bending moments is now expanded to cover skew bridges as well. Instead of developing independent expressions for wheel load fractions in skew bridges for each angle of skew, it is more convenient to incorporate the effect of skew by multiplying improved wheel load fractions for right bridges by a skew reduction factor.

The maximum design bending moment for a composite girder can be expressed as

$$M_{cg} = (M_{static})(b/Q)(Z) \tag{5}$$

where

b/Q = wheel load fraction;
Q = a variable that depends on the load distribution capability of the bridge, currently fixed as 1.68 m (5.5 ft) for interior girders according to AASHTO (*1*);
Z = skew reduction factor, defined as the maximum girder bending moment in a skew bridge divided by the maximum girder bending moment that results when the same bridge is made right; and
M_{static} = maximum static bending moment coefficient as defined before.

When $a > 10.06$ m (33 ft), the maximum static bending moment is

$$M_{static} = Pa(1.138/a^2 - 2.667/a + 9/16)$$

with a in meters (6)

or

$$M_{static} = Pa(12.25/a^2 - 8.75/a + 9/16)$$

with a in feet (7)

Because of the lack of torsional stiffness in steel I-beams, it is necessary to increase M_{cg} obtained from Equation 5 by 5 percent if steel I-beams are used as supporting girders.

This simplified analysis method has been developed to obtain the maximum bending moments in the girders. Bakht (*11*) has discussed the case of maximum shear forces in the girders.

Criteria for Interior Girders in Right Bridges

Figure 8 shows Q values for the interior girders in right bridges that should be used in Equation 5. The variable $a/(H)^{1/2}$ used by Newmark (*7*) yields less scatter of wheel load fractions than any other variable used in an attempt to find the best variable. This variable originates from the thought that the bending moments in the girders should depend in some way on the relative deflections of the girders that are proportional to the quantity $a^3/(E_g I_{cg})$. For a particular slab, the quantity a^2/H amounts to the same thing. If $a/(H)^{1/2}$ is used, a convenient linear relationship exists. Two well-defined Q value data bands can be distinguished. One for a group of bridges that has a girder spacing of 1.83 m (6 ft) and one for another group with girder spacing of 2.74 m (9 ft). The two straight lines indicated in Figure 8 as "present" are conservative estimates for Q when b is 1.83 and 2.74 m (6 and 9 ft).

The linearity of the maximum girder bending moments with b when H and a are kept constant (as shown in Figure 5) is recognized and applied to obtain a conservative expression for the Q values of interior girders in right bridges as follows:

$$Q = (0.01538 + b/45.72)[a/(H)^{1/2}] + 1.298 + b/30 \quad \text{(meters)} \tag{8}$$

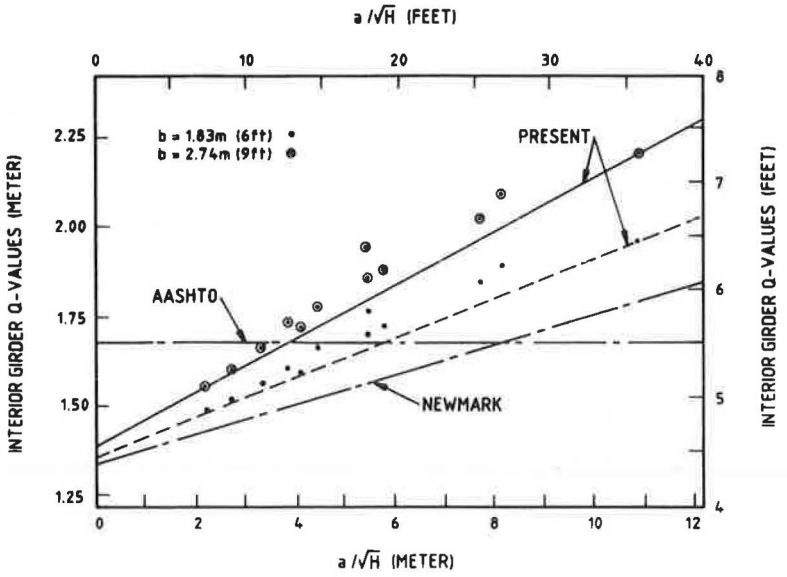

FIGURE 8 Q **values for maximum interior girder bending moments in right bridges.**

or

$$Q = (0.01538 + b/150)[a/(H)]^{1/2}] + 4.26 + b/30 \quad \text{(feet)} \tag{9}$$

The AASHTO wheel load fraction, $b/5.5$, for the interior girders of right bridges is based on research done by Newmark (7) many years ago. The factor $b/5.5$ reflects the linear trend in b, which is observed in the present study, but it does not include directly the effects of H and b/a. This wheel load fraction is an oversimplification of the design equation proposed by Newmark, which includes all relevant parameters and is also indicated in Figure 8. Unlike Newmark's wheel load fractions, which are based on the distribution of load from only one axle of each truck, the current wheel load fractions are obtained directly from the maximum girder bending moments caused by two complete HS20–44 trucks.

Interior girder bending moments for right bridges obtained by using this equation for Q, and thus an improved varying b/Q wheel load factor, are conservative and within 8 percent of the finite element results, whereas, using the fixed AASHTO wheel load fraction, $b/5.5$ results in bending moments between 12 percent too small and 32 percent too large.

Criteria for Exterior Girders in Right Bridges

Figure 9 shows Q values for the exterior girders in right bridges that should be used in Equation 5. These Q values apply only when the minimum distance between the centroids of the edge girder and nearest truck wheels is 0.61 m (2 ft). Figure 9 shows a well-defined functional relationship between Q and $H(b/a)^3$. The quantity $H(b/a)^3$ is proportional to the vertical stiffness ratio, R, which has been discussed previously. The

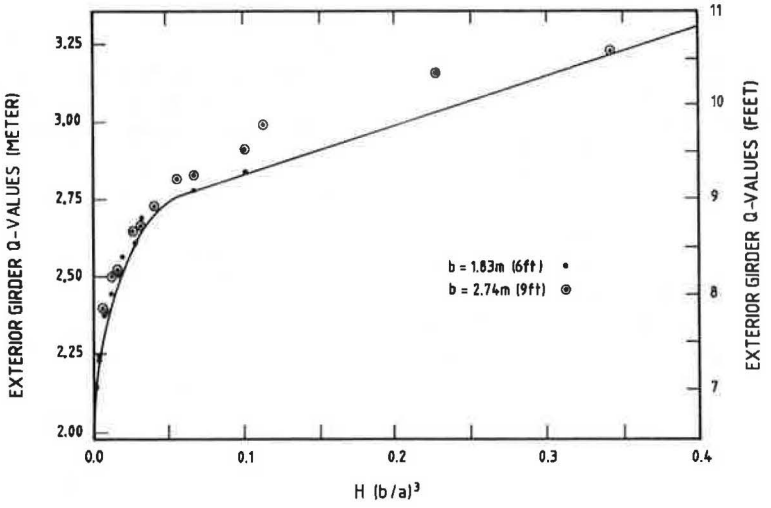

FIGURE 9 Q **values for maximum exterior girder bending moments in right bridges.**

following equations give conservative Q values for exterior girders in right bridges.

For $H(b/a)^3 < 0.0569$,

$$Q = 121.92H(b/a)^3 - 145.69[H(b/a)^3]^{1.1} + 2.042 \quad \text{(m)} \tag{10}$$

or

$$Q = 400H(b/a)^3 - 478[H(b/a)^3]^{1.1} + 6.7 \quad \text{(ft)} \tag{11}$$

For $H(b/a)^3 \geq 0.0569$,

$$Q = 1.597H(b/a)^3 + 2.664 \quad \text{(meters)} \tag{12}$$

or

$$Q = 5.24H(b/a)^3 + 8.74 \quad \text{(feet)} \tag{13}$$

Exterior girder bending moments for right bridges obtained by using these equations for Q and thus an improved varying b/Q wheel load factor are conservative and within 5 percent of the finite element results, whereas, the simply supported slab action AASHTO provision is unconservative in most cases by as much as 23 percent.

Criteria for Girders in Skew Bridges

Before 1985, Chen (*9*) was the only researcher who used his analytical results to develop practical design criteria for skew slab-and-girder bridges. He followed Newmark's (*7*) method for right bridges to determine wheel load fractions for skew bridges by expressing Q values as a function of the variable $a/(H)½$ for a particular angle of skew.

The variable $a/(H)½$ is not a suitable parameter for skew bridges, as Chen's Q values exhibit large scatter, which increases with the angle of skew. At 60 degrees skew, the scatter is as much as 55 percent. As a result of this large scatter in Q values, Chen's conservative design equations do not effectively incorporate the beneficial effect of skew. Furthermore, Chen based his wheel load fractions on the distribution of load from only one axle of each truck and his solution accuracy was seriously impaired by the coarse finite difference network he used.

Recent research on skew slab-and-girder bridges by Bakht (*11*) and Khaleel (*12*) also provides practical analysis criteria for skew bridges.

Figures 10 and 11 show the skew reduction factor Z for interior and exterior girders that should be used in Equation 5. The parameter $b/(aH)$ is the logical choice of variable, because it is found that the reduction caused by skew is large in bridges with large girder spacing, small span, and small H value. See Figures 5, 6, and 7 for verification.

The Z value data points for the exterior girders for $\alpha = 30$ degrees are not indicated in Figure 11. It is obvious from Figure 7 that the reduction is insignificant. The conservative linear equations for Z shown in Figures 10 and 11 are presented in Table 1.

The parameter $b/(aH)$ becomes $bD/(E_gI_{cg})$ when H is substituted. As the bridge span increases, I_{cg} needs to increase drastically to satisfy the deflection limitations. The parameter $b/(aH)$ and thus the effect of skew becomes small for bridges with large spans. This is confirmed by Figure 6 provided by Bakht (*11*). Because the effect of skew is of primary concern

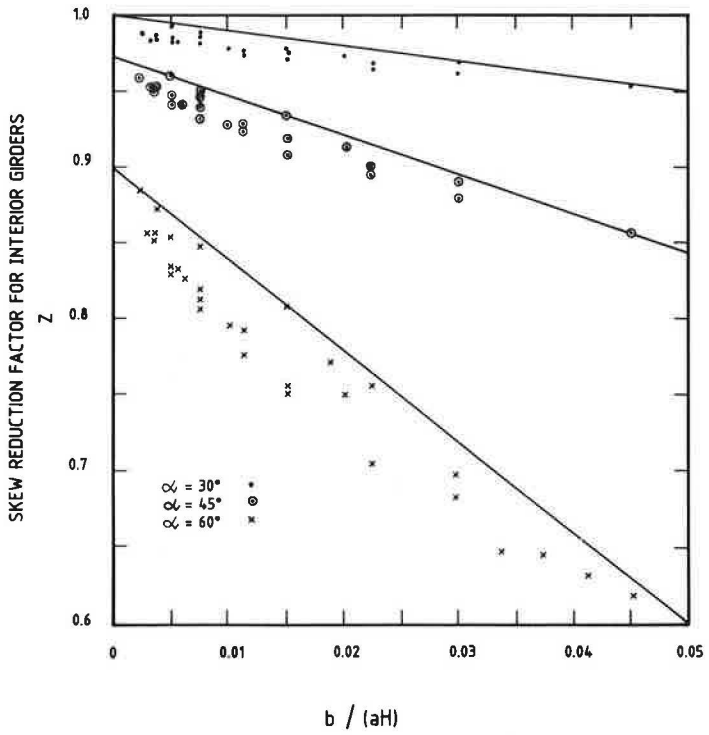

FIGURE 10 Skew reduction factors for maximum interior girder bending moments in skew bridges.

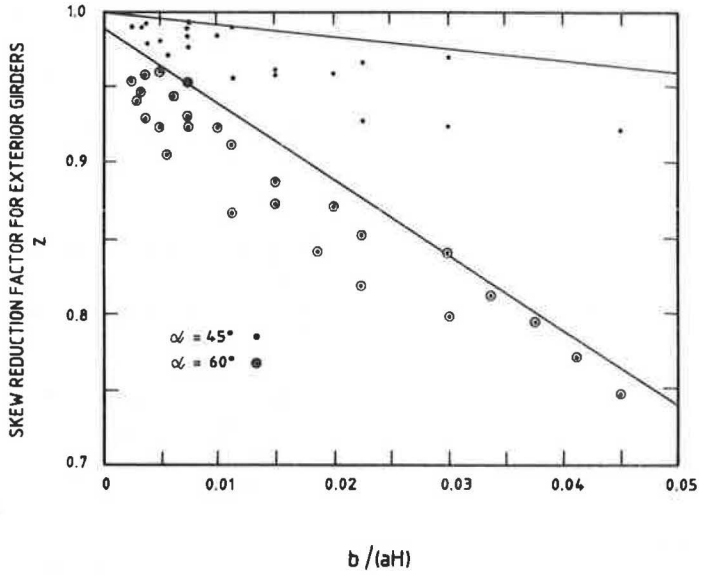

FIGURE 11 Skew reduction factors for maximum exterior girder bending moments in skew bridges.

TABLE 1 SKEW REDUCTION FACTORS, Z, AND MAXIMUM CONSERVATIVE ERRORS

α degrees	INTERIOR GIRDERS		EXTERIOR GIRDERS	
	Z	MAX. % ERROR	Z	MAX. % ERROR
0	1.0	8	1.0	5
30	1.0 - b/(aH)	8	1.0	8
45	.97 - 2.5 b/(aH)	8	1.0 - 0.8 b/(aH)	11
60	.90 - 6.0 b/(aH)	15	.99 - 5.0 b/(aH)	13

in this study, the span of the bridge considered is limited to the range in which the effect of skew is of importance. Therefore, the maximum span considered is 24.38 m (80 ft).

Accuracy of the Simplified Analysis Procedure

The maximum differences between the conservative girder bending moments from Equation 5 and the "correct" bending moments obtained from the finite element analyses are also presented in Table 1. The equations for Z suggested by Marx et al. (*6*) are less conservative, with the result that the error sizes are split in half, but to both sides of the "true" finite element results.

CONCLUSIONS

Proposed Simplified Analysis Method

The proposed simplified analysis procedure can be used to determine the maximum girder bending moments in simply supported right and skew slab-and-girder bridges subjected to AASHTO HS20–44 truck loads. The method uses improved AASHTO wheel load fractions for right bridges, which are modified for skew bridges by using a skew reduction factor. The improved wheel load factor, b/Q, and the skew reduction factor, Z, depend not only on the girder spacing, b, but also on the stiffness parameter, H, and the span, a. The typical bridge considered is shown in Figure 1. The simplified analysis method is based on data obtained from finite element results on bridges with five identical girders subjected to two-lane truck traffic. However, it may be used for bridges with more girders and more load lanes. The accuracy of this method is indicated in Table 1.

Behavior of Slab-and-Girder Bridges

The behavior of slab-and-girder bridges is controlled by the following parameters:

1. Angle of skew, α;
2. Span, a, and girder spacing, b; and
3. Dimensionless stiffness ratio, H, which combines all the structural properties of the bridge members.

The length of the slab overhangs determines the location of the wheels closest to the exterior girders, which has a significant effect on the exterior girders, but a constant value is used in this study.

The effect of skew is a reduction in the girder bending moments. The larger the angle of skew and the ratio $b/(aH)$, the larger the resulting reductions. The maximum interior girder bending moment reduction as a consequence of skew is always less than 5 percent for angles of skew up to 30 degrees, but the reduction is as large as 38 percent when $\alpha = 60$ degrees. The exterior girders are less affected by skew. The maximum exterior girder bending moment reduction is always less than 8 percent for angles of skew up to 45 degrees, but the reduction is as large as 25 percent when $\alpha = 60$ degrees. For all girders, the most significant reductions occur when the angle of skew is more than 45 degrees.

Because the exterior girders are less affected by skew than the interior girders, there is a tendency for the edge girder to become the controlling girder in a skew bridge. This tendency is more pronounced in a bridge with large angle of skew, small H value, large span, and small girder spacing. However, by keeping the faces of the curbs directly above the edge girders, the maximum bending moment always occurs in an interior girder for spans up to 24.38 m (80 ft).

Current AASHTO Wheel Load Factors

For the range of parameters considered in this study, the AASHTO wheel load fraction for interior girders, $b/5.5$, yields results that are between 12 percent too small and 32 percent too large. It is likely that the interior girder bending moments will be underestimated for bridges with a large H value, small span, and small girder spacing. The AASHTO method to determine the maximum exterior girder bending moment by assuming that the slab acts as if simply supported between girders underestimates the actual exterior girder bending moments in most of the bridges considered. It gives bending moments that are up to 23 percent too small. The AASHTO exterior girder wheel load fraction $b/(4 + b/4)$ for steel I-beams yields results that are between 30 and 60 percent too large.

GLOSSARY

The following symbols are used in this paper:

A = identifier for the edge girder, as shown in Figure 1;
a = span of the bridge;
B = identifier for the first interior girder, as shown in Figure 1;
b = girder spacing;
b/a = ratio of the girder spacing to span;
b/Q = wheel load fraction;
C = identifier for the centre girder, as shown in Figure 1;
D = $E_s t^3/12(1 - \mu^2)$ flexural stiffness of the slab per unit width;
E_g = Young's modulus of elasticity for the prefabricated girders;
E_s = Young's modulus of elasticity for the slab;
H = $E_g L_{cg}/aD$ dimensionless stiffness parameter;
I_{cg} = bending moment of inertia of an interior composite girder;
I_g = bending moment of inertia of an isolated prefabricated girder;
M_{cg} = maximum bending moment acting in a composite girder;
M_{static} = maximum static bending moment in an isolated beam subjected to half the load of one AASHTO HS20–44 truck;
P = point load representing half the load of one heavy axle of an AASHTO HS20–44 truck;
Q = variable that depends on the load distribution capability of the bridge;
R = vertical stiffness ratio;
t = slab thickness;
Z = skew reduction factor;
α = angle of skew as defined in Figure 1; and
μ = Poisson's ratio, taken as 0.2 for concrete.

REFERENCES

1. *Standard Specifications for Highway Bridges*, 12th ed. AASHTO, Washington, D.C., 1977.
2. W. C. Gustafson. *Analysis of Eccentrically Stiffened Skewed Plate Structures*. Ph.D. dissertation. Department of Civil Engineering, University of Illinois, Urbana-Champaign, 1986.
3. M. Mehrain. *Finite Element Analysis of Skew Composite Girder Bridges*. Report 67-28. Department of Civil Engineering, University of California, Berkeley, Nov. 1967.
4. G. H. Powell, J. G. Bouwkamp, and I. G. Buckle. *Behavior of Skew Highway Bridges*. Report SESM-69-9. Department of Civil Engineering, University of California, Berkeley, Feb. 1969.
5. H. J. Marx. *Development of Design Criteria for Simply Supported Skew Slab-and-Girder Bridges*. Ph.D. dissertation. Department of Civil Engineering, University of Illinois, Urbana-Champaign, 1985.
6. H. J. Marx, N. Khachaturian, and W. L. Gamble. *Development of Design Criteria for Simply Supported Skew Slab-and-Girder Bridges*. Civil Engineering Studies, Structural Research Series 522; and Illinois Cooperative Highway and Transportation Research Program, Series 210, Jan. 1986.
7. N. M. Newmark and C. P. Siess. *Moments in I-Beam Bridges*. Bulletin Series 336, Engineering Experiment Station, University of Illinois, Urbana-Champaign, 1942.
8. S. Sithichaikasem. *Effects of Diaphragms in Bridges with Prestressed Concrete I-Section Girders*. Civil Engineering Studies, Structural Research Series 383; and Illinois Co-operative Highway Research Program, Series 128; Feb. 1972.
9. T. Y. Chen. *Studies of Slab and Beam Highway Bridges, Part 4. Moments in Simply Supported Skew I-Beam Bridges*. Bulletin 439. Urbana-Champaign, Engineering Experiment Station, University of Illinois, 1954.
10. G. A. Culham and A. Ghali. Distribution of Wheel Loads on Bridge Girders. *Canadian Journal of Civil Engineering*, Vol. 4, No. 1, March 1977.
11. B. Bakht. Analysis of Some Skew Bridges as Right Bridges. *Journal of Structural Engineering*, Vol. 114, No. 10, Oct., 1988, pp. 2307–2322.
12. M. A. Khaleel and R. Y. Itani. Live-Load Moments for Continuous Skew Bridges. *Journal of Structural Engineering*, Vol. 116, No. 9, Sept. 1990, pp. 2361–2373.

Publication of this paper sponsored by Committee on Steel Bridges.

Heat-Straightening of Damaged Structural Steel in Bridges

R. Richard Avent, George M. Fadous, and Randy J. Boudreaux

A 3-year research effort related to the study of heat-straightening repair for damaged steel bridge girders is summarized. Two major areas are emphasized: laboratory behavior of heat-straightened plates and rolled shapes. During the laboratory investigation of flat plates, a number of parameters were studied, including vee angle, depth of vee, heating temperature, plate thickness, and jacking forces. The most important parameters influencing the amount of straightening per heating cycle were vee angle, temperature, and jacking force. The patterns of behavior during the straightening process are plotted to illustrate the effects of each of these parameters. In a similar fashion, a laboratory study of rolled sections was conducted. In addition to the same parameters as those affecting plate behavior, this study showed that cross-section shape affects heat-straightening behavior—a factor heretofore unreported in the literature. It appears that rolled shapes can be grouped into three basic modes of behavior depending on the shape and location of the vee. Results of these tests are plotted showing how the shape of the member can affect the straightening process. Recommendations are given for factors to consider in the heat-straightening repair of bridge girders.

Although instances of heat straightening to repair damaged steel can be traced back nearly 50 years, the method has been more of an art than a science. As a result, highway officials have been hesitant to utilize the procedures. Principal concerns have been related to a vagueness as to the principles behind the procedure, strength reductions both during and after the repair, and limits as to degree of damage that can be repaired. The purpose of this paper is to address these concerns by describing the results of a comprehensive research project on heat-straightening repair of steel bridge girders.

Heat straightening can be used to repair structural steel bridge elements in place, often without shoring. It is an expedient procedure, usually necessitating minor disruptions in traffic. Up to tenfold cost savings are possible as compared with member replacement methods. However, because heat straightening is not well understood by the engineering profession, most repair work of this type is not engineered, but left to a specialized contractor. Because of this lack of knowledge, some engineers have tended to avoid the use of heat-straightening repair. Although engineering research on the subject has progressed in recent years, there has not been a significant amount of information readily available to the profession. This lack of information, combined with a lack of synthesis of available information, had led to speculation and contradictory statements as to various effects associated with the heat-straightening process. It is therefore pertinent to first describe that process.

R. R. Avent and G. M. Fadous, Department of Civil Engineering, Louisiana State University, Baton Rouge, La. 70803. R. J. Boudreaux, Neel-Schaffer, Inc., 666 North St., Suite 203, Jackson, Miss. 39225.

A number of papers have been written that primarily describe basic techniques and successful field applications (*1–9*). The concept is based on use of carefully controlled and applied heat without an active force (although passive restraining forces are often used). The basic element of steel construction is the flat plate. Rolled or built-up members consist of plate elements assembled to obtain an advantageous shape. Thus, vee heat can be considered the fundamental heat pattern associated with heat straightening.

As shown in Figure 1, the heat is applied with a torch to a vee-shaped area, starting at the apex and progressing across the vee in a serpentine motion. The series of sketches in Figure 1 was generated from a comprehensive elastoplastic, thermal, and finite-element analysis (*10*). The amplitudes of movement have been magnified for illustrative purposes and a full-depth vee heat is used. As the apex of the vee is heated, expansion occurs, producing the hump at the apex and a slight downward movement at the free end (Figure 1a). As heating continues, this expansion increases to produce a larger hump and more downward deflection. The cool portion ahead of the torch impedes the longitudinal expansion and also results in a plastic thickening of the material in the heated region. As the torch moves into the lower half of the plate, the hump begins to protrude from both top and bottom, and the downward deflection trend is reversed (Figure 1b). At some point, the plate will return to its original undeformed position, with only the top and bottom bulges plus plate thickening. As the torch nears the open side of the vee, the deflection becomes upward due to the expansion in the torch area (Figure 1c). This process continues until a short time after the torch has been removed and the deflection has reached its maximum upward point. As cooling proceeds, the contraction on the open side of the vee creates downward movement again, until at some point, the plate is again in its original position with a bulge on the top and bottom. The latter stages of cooling produce a final downward deflection along with a slight bulge (Figure 1d). The angle of the vee thus tends to be less than it originally was, because some plastic flow has taken place during the expansion phase and there is little restraint to longitudinal contraction during cooling. The net result is a small but sharp change in the angle of the vee when the process is complete. The hump at top and bottom is quite small compared with the angle change and can be neglected. In addition, a net shortening of the member occurs.

Of course, if the member is already bent, the distortion can be removed by applying the vee heat to oppose the initial deformation, hence the idea of heat straightening. By judi-

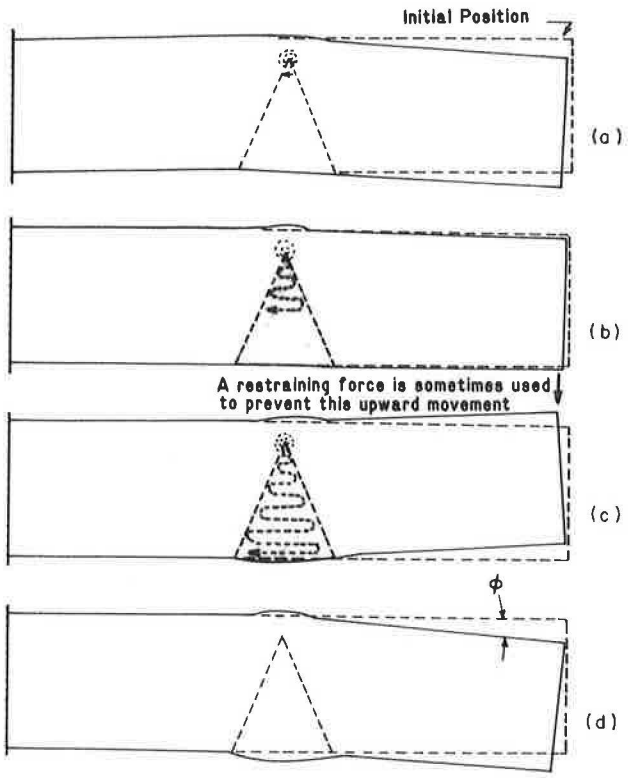

FIGURE 1. Stages of plate deformation as a vee heat is applied to an initially straight plate (deformations are magnified for illustration purposes).

ciously applying vee heat to members, damage to curvature can be removed. Because the net change in curvature after one heating sequence is small, cycles of heating and cooling are often required to correct serious damage. A similar approach can be used on various rolled shapes or built-up members. For large or irregular initial bends, the heating can be done at a number of locations successively along the length of the member. Although simple in principle, the wide variety of structural shapes, damage, and structural configurations likely to be encountered in practice makes it difficult to establish guidelines. In addition, the varied methods of heating and restraining during the repair process complicate the picture even further.

A comprehensive survey of heat-straightening literature has been conducted by Avent (*11*).

In summary, the literature review reveals that additional research is needed to better define the process. Two aspects are of particular importance. First, the basic mechanism of heat straightening is not well understood in that the effects of both external restraints (jacking) and internal restraints (redundancy) have been considered to be of minor concern rather than fundamental to the broad application of the process. Second, because the importance of this parameter has not been identified, there has been little documentation on the behavior of vee-heated plates subjected to varying degrees of constraint and even less on rolled shapes. Third, although a fair amount of research has indicated that most material properties are unaffected by heat straightening, two important aspects have been overlooked: the influence of strain aging on ductility and residual stress distribution. Finally, the research information available has been predicated almost entirely on laboratory studies of simple elements. The reported field investigations were qualitative rather than quantitative and thus could not serve as a building block for future research. Because of these gaps in heat-straightening research, it was indeed true that the artisan practicing the trade was much more important than the engineer. The goal of this paper is to provide a more detailed knowledge base to enable the engineer to assess the need for and direct the application of heat-straightening repairs.

BEHAVIOR OF PLATES SUBJECTED TO HEAT STRAIGHTENING

Although the heat-straightening repair process is relatively simple, it has not been widely used. Two main factors are responsible. First, those who currently use heat straightening practice it as an art form as much as a technique based on engineering principles. These practitioners rely on their experience to guide them through a heat-straightening repair. Second, many engineers believe that any application of heat to steel will permanently weaken it. Because there are no engineering design criteria for using heat straightening, engineers are often hesitant to use it. In recent years, research studies have led to greater understanding of this phenomenon. The purpose in this section is to describe the experimental study of heat straightening as applied to plates.

Vee heats produce small but sharp curves at the vee location. By varying the spacing of the vee heats, a smooth curve of changing radius can be produced. Because damage is usually of varying curvatures, vee heats are the most suitable for structural repairs.

Several detailed studies by Weerth and Nicholson (*13*), Weerth (*12*), and Roeder (*18*) have been conducted on the application of vee heats to plates. These studies have attempted to identify parameters that influence vee heats and to develop predictive models based on these data. The specific findings of these studies will be evaluated in connection with the results of the current investigation.

The actual method of heat straightening is easily learned; however, the handful of practitioners currently using the method rely extensively on their many years of experience to guide them through a repair. An engineer lacking this wealth of experience needs a set of analytical procedures to determine how best to apply the heat-straightening process to a particular repair. These analytical tools, for reasons of economy, should be relatively fast and easy to apply and should allow for such considerations as different vee geometries, temperature ranges, external loadings, and support restraints. At present there are, at one extreme, overly simplistic models (*1,5,15*) that cannot take into account the effect of either temperature variations or internal and external restraint and, at the other extreme, comprehensive computer models (*10,16,14,17,18,12*) based on elastoplastic finite-element or finite strip stress analysis combined with a similar thermal analysis. However, there is not yet an analytical model that offers both practicality and a comprehensive inclusion of all important variables to accurately predict behavior.

This portion of the study is devoted to the development of simple yet efficient procedures for predicting the response of

deformed steel plates during the heat-straightening process. In this section, all parameters are identified and quantified that have an important influence on the heat-straightening process. This phase was accomplished by studying the experimental data available from previous research as well as by conducting an extensive experimental program to provide additional data.

The tests conducted in the experimental program consisted of applying vee heats to straight specimens and measuring the resulting change in geometry. By using straight specimens as opposed to deformed ones, a larger variety and number of tests could be conducted in the least possible time. A total of 255 individual heating cycles were performed during this study. Several supporting frames were used during the course of this study. The specimens were mounted as either cantilevers or simply supported members. All plates were hot-rolled A36 grade steel, and the majority were 1/4 in. × 4 in. × 24 in. The only exceptions to these dimensions were associated with tests on variations in plate thickness and geometry. Plate deformation measurements consisted of measuring the offsets between the plate edge and a reference frame to the nearest 0.001 in.

It has been shown (*18*) that the plastic deformation developed by a vee heat occurs primarily within the vee area. Thus, the acute angle formed between the tangents to the straight portions outside the vee is the angle of plastic rotation, ϕ.

Practically all the existing experimental data on vee-heated plate behavior are found in two studies (*12–14,18*). The basic parameters studied were angle of the vee, ratio of the vee depth to the plate depth, level of external constraining force, and heating temperature. The number of data points was in general relatively small and the variation fairly large. As a result, only general conclusions could be drawn and unanswered questions remained. Therefore, additional experimental data related to these basic parameters were obtained in the current study. In addition, several other variables were evaluated, including plate thickness, plate depth, and heating technique.

The available data on plate behavior include the present study and those of Nicholls and Weerth (*13*), Roeder (*18*). Indicated on plots presented here is the type or source of the data. The data type "current" indicates that only the results of the current study were used, and reference numbers are given for other data. Each parameter is evaluated separately in the following sections.

Vee Angle

Researchers agree that the vee angle is one of the fundamental parameters influencing the plastic rotation of a plate. The data show a fairly linear relationship between plastic rotation and vee angle. For this reason, all data will be plotted with the vee angle as the ordinate and plastic rotation, ϕ, as the abscissa. A first-order least-squares curve fit will also be shown. Plots in succeeding sections show a consistent proportional relationship between these variables.

Of particular interest is the scatter of the experimental results. In both the current study involving 255 plate tests and in Roeder's research (*18*) involving 99 plate tests, a similar level of scatter was observed. In both cases, special efforts were made to control the heating temperature using not only temperature-sensing crayons, but also thermocouples or calibrated contact pyrometers. In spite of such efforts, a significant amount of variation occurred in identical repetitive tests. Surprisingly, the smaller-scale study by Nicholls and Weerth (*13*), which included 21 tests, showed no evidence of random scatter. The consistency of data points was such that smooth curves were produced with no curve fitting necessary. This pattern is even more remarkable when apparently the only temperature control was temperature-sensing crayons. The writers therefore view these data points with some suspicion and have omitted them from most of the comparative studies.

Because a significant level of scatter does exist, the data samples were evaluated. The coefficients of variation for typical cases were on the order of 50 percent. Because the coefficient of variation is quite high, possible causes must be addressed. The most obvious source of the scatter would be the relative degree of control exerted over the parameters of the heating process, in particular, the restraining force and heating temperature. For the available equipment of the current study, the accuracy of measurements could vary by 10 to 15 percent. Similarly, the control of the heating temperature could introduce an error of 10 to 15 percent. A third possible cause is the development of residual stresses. Both Holt (*4*) and Roeder (*18*) suggest that residual stress is not significant in the heat-straightening process. However, a small number of tests conducted as part of this study indicate that very large residual stresses are possible as a result of the heating process. Thus, because of the difficulty in controlling the restraining forces and heating temperatures and the possible development of large residual stresses, a relatively large scatter in the data is not surprising.

Depth of Vee

Past research (*18,12*) has been inconclusive as to the effect of vee depth on plastic rotation. These studies suggest that the relationship is inverse for vee depths greater than two-thirds the plate depth. However, the trend of the experimental data indicates relatively small variations. Indeed, the plate rotations are all approximately the same when using a least-squares curve fit. Therefore, even though it may seem intuitive that increasing the vee depth increases the plastic rotation, there appears to be little justification for such a general statement. Additional research is needed with a larger data base before a conclusive evaluation can be made.

Plate Thickness and Depth

From the results of tests involving different plate thicknesses, it is concluded that plate thickness will not have an important influence on heat straightening. In the current study, the influence of plate depth was investigated in a series of tests with plates of equal thicknesses, vee angles, and zero load ratios. These results showed similar rotation for each case; thus, plate depth under these conditions is not deemed an important factor.

Temperature

One of the most important and yet difficult-to-control parameters of heat straightening is the temperature of the heated metal. Factors affecting the temperature include size of the torch orifice, intensity of the flame, speed of torch movement, and thickness of the plate.

Assuming that adequate control is maintained over the applied temperature, the question arises as to what temperature produces the best results in heat straightening without altering the material properties. Previous investigators differ on the answer. For example, Shanafelt and Horn (*9*) stated that heats above 1200°F on carbon and low-alloy steels will not increase plastic rotation. Rothman and Monroe (*19*) concluded that reheating areas where previous spot heats had been performed will not produce any useful movements. However, the comprehensive testing program by Roeder (*18*) showed that the resulting plastic rotation is directly proportional to the heating temperature up to at least 1600°F. These results were verified in the current research. Plots of vee angle versus angle of plastic rotation for the data from the current study are shown in Figure 2, which indicates that the plastic rotation generally increases linearly with increasing temperature.

The maximum temperature recommended by most researchers is 1200°F for all but the heat-treated high-strength steels. Higher temperatures may result in greater rotation; however, out-of-plane distortion becomes likely and surface damage such as pitting (*18*) will occur at 1400° to 1600°F. Also, temperatures in excess of 1300°F may cause changes in molecular composition (*19*), which could result in changes in material properties after cooling. The limiting temperature of 1200°F allows for several hundred degrees of temperature variation, which was common among experienced practitioners. For the heat-treated constructional alloy steels (F_y = 100 ksi), the heat-straightening process can be used, but temperatures should be limited to 1050°F to ensure that no metallurgical transformations occur (*19*). The conclusion that heat-treated constructional alloy steels can be heat-straightened is contrary to that of Shanafelt and Horn (*9*); however, Roeder (*18*) concurs with this recommendation.

To control the temperature, the speed of the torch movement and the size of the orifice must be adjusted for different thicknesses of material. However, as long as the temperature is maintained at the appropriate level, the contraction effect will be similar. This conclusion was verified by two test series on plates in which the intensity of the torch was varied. In one series, a low-intensity torch was moved slowly to maintain a 1200°F temperature, whereas in the other series a high-intensity torch was moved more quickly while the same temperature was maintained. The rotations in either case were similar.

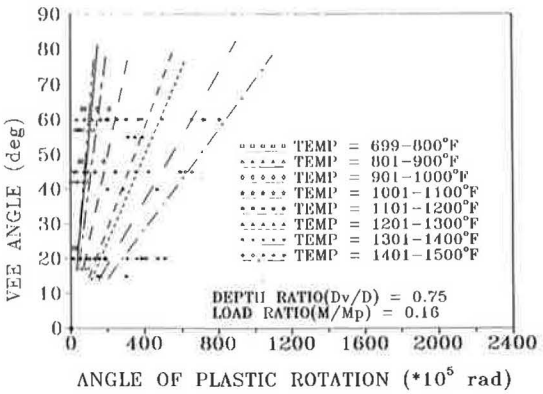

FIGURE 2. Effect of heating temperature on the plastic rotation of a plate subjected to a single heating cycle.

Restraining Forces

The term "restraining forces" can refer to either externally applied forces or internal redundancy. These forces, when properly utilized, can expedite the straightening process. However, if improperly understood, restraining forces can hinder or even prevent straightening. In its simplest terms, the effect of restraining forces can be explained by considering the previous plate element as shown in Figure 1. The basic mechanism of heat straightening is to create plastic flow, causing expansion through the thickness (upsetting) during the heating phase, followed by elastic longitudinal contraction during the cooling phase. This upsetting can be accomplished in two ways. First, as the heat progresses toward the base of the vee, the cool material ahead of the torch prevents complete longitudinal expansion of the heated material, thus forcing upsetting through the thickness. However, as shown in Figure 1b and 1c, some longitudinal expansion occurs because the surrounding cool material does not offer perfect confinement. After cooling, the degree of damage is reduced in proportion to the confinement level from the internal restraints.

A second method of producing the desired upsetting (usually used in conjunction with the vee heat) is to provide a restraining force. The role of the restraining force is to reduce or prevent plate movements associated with longitudinal expansion during the heating phase. For example, if a restraining force is applied as shown in Figure 1c, the upsetting effect will be increased through the flexural constriction of free longitudinal expansion at the open end of the vee. A restraining force is usually applied externally, but sometimes the structure itself provides restraint through internal redundancy.

In essence, a restraining force acts in an identical manner to that of the vee heat concept itself. The material behavior can be viewed as shown in Figure 3. A small element from a plate, when constrained in the x-direction and heated, will expand and flow plastically primarily through the thickness (Figure 3c). Secondary plastic flow will occur in the y-direction. However, this movement will be small in comparison with that of the z-direction, because the plate is much thinner than its y-dimension and offers less restraint to plastic flow. Upon cooling with unrestrained contraction, the final configuration of the element will be smaller in the x-direction and thicker in the z-direction (Figure 3d). The material itself cannot distinguish the cause of the constraint: either cooler adjacent material in the case of the vee heat or an external force in the case of a jacking force. In either case the plastic flow occurs in an identical manner.

In light of this discussion, a set of criteria for constraining forces can be developed. These criteria apply for internal as well as external constraints.

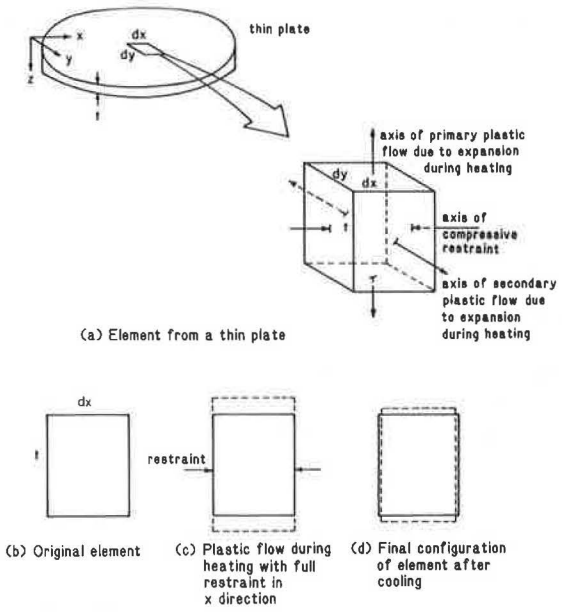

FIGURE 3. Characteristics of plastic flow and restraint during heating straightening.

1. Constraints should be passive during the heating phase; that is, they should be applied before heating and not increased by external means during heating or cooling.
2. Constraints should not prohibit contraction during the cooling phase.
3. Constraints should not produce local buckling of the compression element during the heating phase.
4. Constraints should not produce an unstable structure by either the formation of plastic hinges or member instability during the heat phase.

From a practical viewpoint, these criteria mean that (a) the vee angle should be kept small enough to avoid local buckling, (b) the jacking forces must be applied before heating and be self-relieving as contraction occurs, and (c) the maximum level of any external jacking forces must be based on a structural analysis that includes the reduced strength and stiffness due to the heating effects.

Although practitioners have long recognized the importance of the application of jacking forces during the heat-straightening process, little research has been conducted to quantify its effect. A series of tests designed to evaluate this parameter involved applying a jacking force to a plate such that a moment was created about the strong axis in a direction tending to close the vee. This moment is nondimensionalized for comparison purposes by forming a ratio of the applied moment at the vee to the plastic moment of the cross section, M/M_p. This term is referred to as the load ratio. The tests included load ratios of 0, 0.16, 0.25, and 0.50, with four different vee angles and vees extending over three-fourths the depth of the plate. The results are shown in Figure 4. Roeder (*18*) also studied the effect of load ratio variation, and his results indicated similar behavior. The plots indicate that the variation is generally proportional to the load ratios and that using external loads can greatly expedite the heat-straightening process.

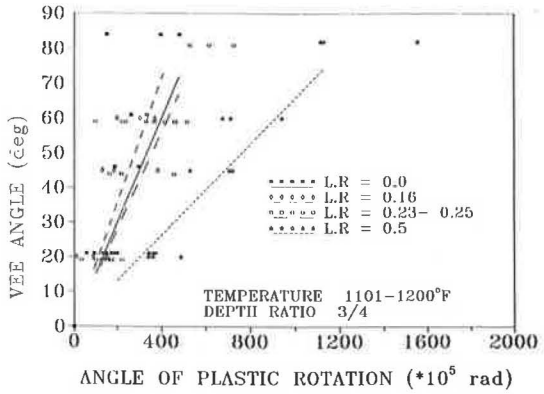

FIGURE 4. Effect of the ratio of bending moment at the vee heat due to restraining force and the plastic moment capacity (L.R.) on the plastic rotation of a plate subjected to a single heating cycle.

A second type of constraint that may exert external forces on a member is axial restraint. A series of tests were conducted using a superimposed axial load on plates for various vee angles. The load created a 20-ksi axial stress or a ratio of actual stress to yield stress of 56 percent. These results are shown in Figure 5 in comparison with the results from the bending load ratios of 0 and 50 percent. The axial load does increase the plastic rotation, but to a lesser extent than the 50 percent bending load ratio.

In summary, the parameters found to have an important influence on the plastic rotations produced by vee heats are vee angle, heating temperature, and external restraining force. The depth of the vee appears to have a small influence in the practical range of greater than 50 percent of the plate width. Likewise, plate thickness and geometry are not important in the range of practicality.

BEHAVIOR OF ROLLED SHAPES SUBJECTED TO HEAT STRAIGHTENING

The basic characteristics of plate behavior have been quantified experimentally. The purpose in this section is to similarly quantify the behavior of rolled shapes subjected to heat

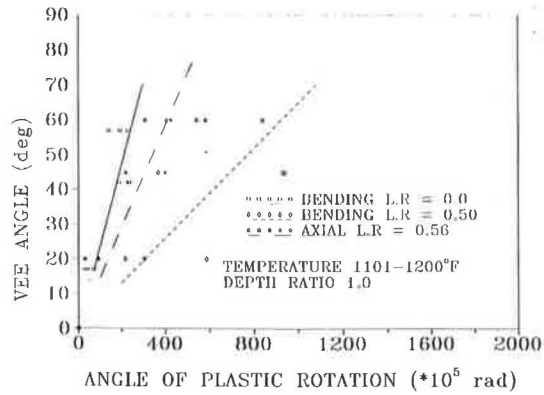

FIGURE 5. Effect of axial restraining forces on the plastic rotation of a plate subjected to a single heating cycle.

straightening. Because rolled shapes are an assemblage of rectangular plate elements, the basic question is how the pattern of assemblage modifies the basic plate behavior during heat straightening. The primary factors to be considered are cross-section configuration, restraining forces, and angle of vee. It is believed that the influence of other factors such as temperature, element thickness, and vee depth is either similar to that of individual plates or has been previously studied and does not warrant additional consideration here.

Very little experimental data are available that provide measurements of the plastic rotation in rolled shapes. Horton (*16*) measured the plastic rotation for a series of 18 wide-flange beams subjected to bending-type restraining forces. In the only other similar study, Roeder (*18*) measured the plastic rotation for eight wide-flange beams subjected to axial restraining forces. This small pool of experimental data was inadequate by itself for the formulation of conclusions on all aspects of behavior. In order to expand this data base, several series of comprehensive experiments were conducted. The laboratory experiments on A36 steel rolled shapes were conducted in a manner quite similar to those for plates. Members were mounted in frames and initial measurements were taken before heating. The primary variables were vee angle and level of restraining force. All specimens were heated at 1200°F. After cooling, the specimens were remeasured. The degree of plastic rotation was computed by comparing the two sets of measurements. Presented here is an evaluation of the significance of these test results. Plots referred to in this discussion will generally include all related data points along with a first-order least-squares curve fit.

Heating Sequence and Pattern

For cross sections consisting of multiple elements, the usual practice is to heat the elements consecutively, although simultaneous heatings are sometimes conducted. Heating sequence refers to the order in which each element is heated. Rolled shapes generally require a vee heat in combination with a rectangular heat. The rectangular heats are necessary because of the perpendicular orientation of plate elements forming the cross section. Thus a pattern of vee and rectangular heats is used for many types of rolled shapes. A set of typical heating patterns for wide flanges, channels, and angles is shown in Figure 6. By using the proper pattern, sweep, camber, and twisting-type movements can be generated. These movements will be referred to as Mode I, II, and III bends, respectively. Through these combinations, a wide variety of damage conditions can be repaired. Although there is general agreement on the use of vee heats, there has been little information on how to optimize heating sequences and patterns combining vee and rectangular heats. Horton is the only researcher to have addressed this subject in even a limited manner. His conclusion was that an effective approach is to perform the vee heat (or heats) first and then the rectanglar heats. This approach was used in all experiments discussed here.

Water-Mist Versus Air Cooling

Another aspect of Horton's study deserves mention here. In most cases he conducted identical experiments, but in one case the beam was allowed to cool by convection to room temperature, and in the another case a water mist was applied. The water-mist application had no significant effect on the amount of plastic rotation that occurred.

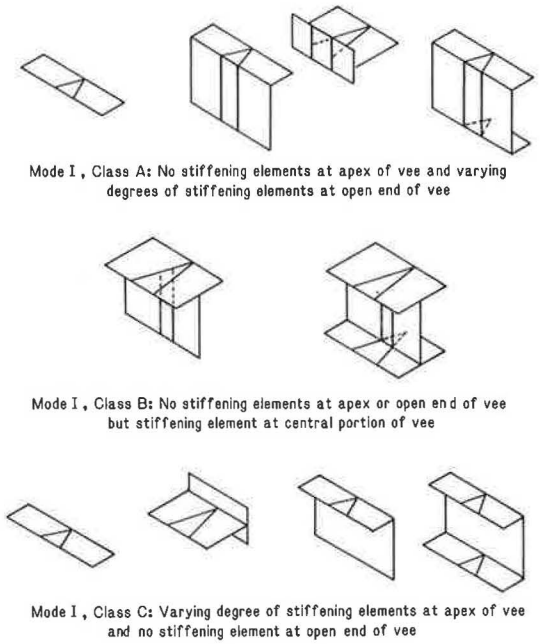

FIGURE 6. Classification of Mode I heating configurations.

Vee Depth

A final aspect of Horton's study was the effect of the vee depth on the Mode I bends. The plastic rotation produced by half-depth vees was significantly smaller than that produced by the full-depth vees, particularly for the most effective heating patterns. The data here are much more conclusive than those discussed previously for partial-depth vee heats in plates. The average value of plastic rotation for 50-degree vee heats for the Mode I case (a) and (d) sequences is 0.00387 rad as compared with the half-depth vee pattern, which produced an average plastic rotation of 0.00253 rad.

Vee Angle

Horton's study indicated that the relationship between plastic rotation and vee angle was fairly linear. The same trend was found in all tests conducted for this study. This behavior will be illustrated in subsequent sections. The accumulation of data suggests that the behavior of rolled shapes is similar to that of plates with respect to vee angle effect.

Restraining Forces

One of the primary factors evaluated in this study was the effect of restraining forces on plastic rotation. This factor has been shown to be of primary importance for plate behavior,

but little data are available for rolled shapes. For example, Horton used a single load ratio, M/M_p, of 16 percent for all cases. To expand the data base, a series of tests were conducted on W 6 × 9 beams for three load ratios: 0, 25, and 50 percent. The results for Mode I bends on wide flange shapes are shown in Figure 7. Also shown for comparison purposes are similar curves for rectangular plates and Horton's results. The plastic rotation is proportional to the load ratio although it does not appear linear. Note, however, that two data points for the 30-degree vee angle and zero load ratio distort that curve. Even though the trend is present, additional data points are needed to more precisely define the relationship between load ratios.

Geometric Effect of Size

A comparison of Horton's data with those of the current study (Figure 7) indicates that the specimen size may be a significant factor. Comparison of Horton's beams (load ratio, 16 percent) with those of the current study (load ratio, 25 percent) indicates that the plastic rotation is inversely proportional to the beam weight (which for these cases roughly translates to wall thicknesses). Three factors may account for this behavior. First, Horton used a different measuring technique for determining plastic rotation. His measurements were limited to a region across the vee of only 8.375 in. The full length of 60 in. was used in this study for measurements. It may be that the short length used by Horton did not capture the full degree of plastic rotation. However, even Horton's data alone (which were obtained in a consistent fashion) indicate the same trend. Second, there is a longer time frame during the heating process in comparison with plates. This time lag to heat separate elements would be proportional to size, allowing previously heated elements more time to cool. Smaller plastic rotations could result from such a scenario. Third, the thicker elements may not have been heated to 1200°F. Horton provides little information on his level of temperature control. As a result, the writers are hesitant to draw firm conclusions from these data. Additional tests are needed to verify this observed trend.

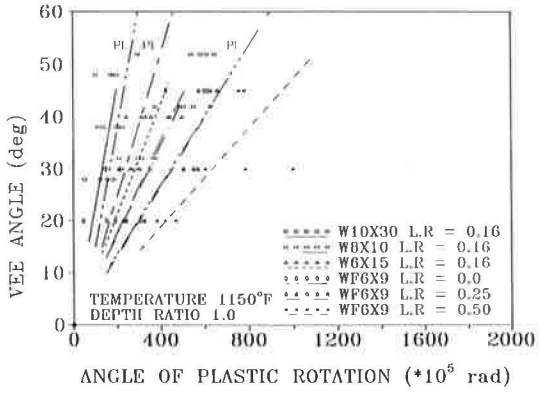

FIGURE 7. Effect of the ratio of bending moment at the vee heat due to restraining force and the plastic moment capacity (load ratio) on the plastic rotation of Mode I wide-flange sections subjected to a single heating cycle.

Geometric Effects of Shape Configuration

This study is the first to determine the plastic rotation for angles and channels in addition to wide flange shapes. As a consequence, the influence of shape factors can be evaluated. Three categories will be considered: Mode I bends (sweep), Mode II bends (chamber), and Mode III bends (twist).

The Mode I bends in general can be classified into several subcategories according to the distribution of material with respect to the vee. This classification is shown in Figure 6. Obviously, the location and size of the stiffening element will influence the member behavior. The magnitude of this influence is shown in Figures 7 and 8 for Mode I, Classes B and A, respectively. Three characteristics are apparent:

1. As the stiffening element to the vee-heated flange varies from the open end toward the apex of the vee, the plastic rotation decreases.
2. For Mode I, Class A, the plastic rotation is proportional to the area of the stiffening element. At this stage only the trends can be noted. Note that no Mode I, Class C tests were conducted.
3. Both Modes I-A and I-B suggest that plastic rotation is larger for these shapes than for similar plates. It appears that the plastic rotation may be proportional to the location of the stiffening element from the vee apex.

The results for Mode II bends of both the channel and wide-flange types are compared in Figure 9. The plastic rotation is significantly smaller for this case in comparison with Mode I. It appears that the stiffening element at the apex offers little significant internal restraint against rotation. The resulting curve fits compare favorably with that those plates.

Mode III bends were also induced by heat straightening. However, only two beams were heated in this fashion, so data are sparse. Enough heating cycles were conducted to obtain a good average value of plastic rotation. For 48 cycles the average plastic rotation of the heated flange alone was 0.00625 rad. Comparing Modes I and III indicates that the behavior is quite similar. Although additional data are needed, it appears that for noncomposite cases, Mode III can be modeled similarly to Mode I. The use of these heating procedures on

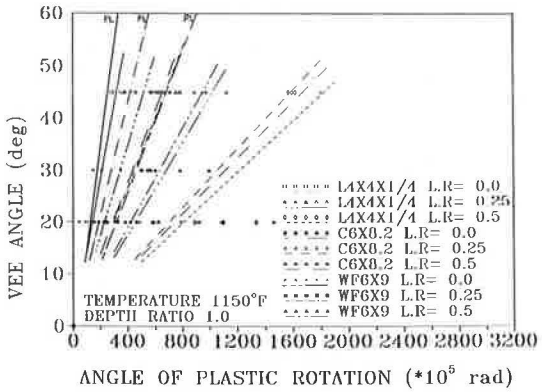

FIGURE 8. Effect of load ratio and cross-section type on the plastic rotation of Mode I, Class A rolled shapes subjected to a single heating cycle.

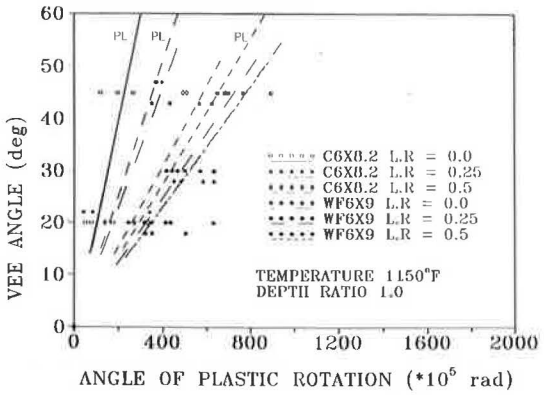

FIGURE 9. Effect of load ratio and cross-section type on the plastic rotation of Mode II rolled shapes subjected to a single heating cycle.

simulated full-scale bridge girders has been reported elsewhere by Avent and Fadous (*20*).

The behavior of rolled shapes was found to be quite complex. In addition to the same factors influencing plate behavior, rolled shapes are influenced by geometric patterns. Additional experimental data are needed to further quantify this behavior.

CONCLUSIONS

Heat straightening as applied to plates and rolled shapes has been studied in detail. The results are summarized as follows:

1. Plates and rolled shapes behave in predictable patterns under cyclic heat straightening. Even though significant scatter exists for specific data points, the average values for a large number of cycles are generally consistent.
2. The primary factors influencing heat straightening are vee angle, temperature, restraining force, and cross-section shape.
3. Movement is proportional to vee angle. However, a vee angle of greater than 45 degrees often leads to bulging of the flange or plate element about its weak axis.
4. Heating temperature should be limited to 1200°F for carbon steel and 1050°F for heat-treated steels.
5. Restraining forces expedite the straightening process without damaging the steel. However, the magnitude of these forces should be known and controlled so as to prevent drifting into the realm of hot mechanical straightening or to cause overstressing under heat.
6. Rolled shapes can be straightened, with the movement per cycle depending on the cross-section shape.

Experimental data suggest that heat straightening of plates and rolled shapes can be quantified for general applications. More research is needed to determine these analytical relationships.

ACKNOWLEDGMENTS

This research was funded through a grant from the Louisiana Transportation Research Center in cooperation with FHWA, U.S. Department of Transportation, and the Louisiana Department of Transportation and Development. Their support is gratefully acknowledged.

REFERENCES

1. How Fire Destroyed and Fire Repaired Air Force Hangers. *Engineering-News Record*, June 18, 1959, pp. 50–53.
2. Flame Buckled this Steel . . . And Flame Straightened It, Part I. *Welding Engineer*, Feb. 1959, p. 43.
3. J. E. Holt. Flame Straightening: A Friend in Need. *Welding Engineer*, Vol. 40, No. 10, Oct. 1955, pp. 44–46; No. 12, Dec., 1955, pp. 30–31.
4. R. E. Holt. Primary Concepts in Flame Bending. *Welding Engineer*, Vol. 56, No. 6, June, 1971, pp. 416–424.
5. R. E. Holt. Flame Straightening Basics. *Welding Engineer*, Vol. 50, No. 9, Sept., 1965, pp. 49–53.
6. Kinks Go Up in Flames. *Engineering New Record*, April 9, 1981, p. 17.
7. E. M. Newman. Repair of Fire Damaged Structural Steel. *Military Engineer*, No. 344, Nov.-Dec., 1959, pp. 448–450.
8. Oxyacetylene Torches Straighten Fire-Warped Steel. *Welding Engineer*, March 1959, pp. 31–34.
9. G. O. Shanafelt and W. G. Horn. *NCHRP Report 271: Guidelines for Evaluation and Repair of Damaged Steel Bridge Members*. Transportation Research Board, National Research Council, Washington, D.C., June 1984.
10. G. S. Gipson and J. C. Ortiz. Toward an Analytical Description of the Heat-Straightening Phenomenon—The Thermal Problem. SECTAM XIII Proceedings.
11. R. R. Avent. Heat-Straightening of Steel: Fact and Fable. *Journal of Structural Engineering*, ASCE, Vol. 115, No. 11, Nov. 1989, pp. 2773–2793.
12. D. E. Weerth. Theoretical and Experimental Analysis of Heat Curved Mild Steel. M.S. thesis, University of Washington, Seattle, 1971.
13. J. I. Nicholls and D. E. Weerth. Investigation of Triangular Heats Applied to Mild Steel Plates. *Engineering Journal*, AISC, Oct., 1972, pp. 137–141.
14. C. W. Roeder. Experimental Study of Heat Induced Deformation. *Journal of Structural Engineering*, ASCE, Vol. 112, No. 10, Oct., 1986, pp. 2247–2262.
15. K. L. Moberg. Damage Assessment and Contraction Straightening of Steel Structures. M.S. thesis, University of Washington, Seattle, 1979.
16. D. L. Horton. Heat Curved Mild Steel Wide Flange Sections: An Experimental and Theoretical Analysis. M.S. thesis, University of Washington, Seattle, 1973.
17. C. W. Roeder. Predictions of Deformations Due to Heat Curving. In *Bridges and Transmission Line Structures*, ASCE, New York, 1987, pp. 101–110.
18. C. W. Roeder. *Use of Thermal Stress for Seismic Damage Repair*. Final Report. University of Washington, Seattle, Oct. 1985.
19. R. L. Rothman and R. E. Monroe. *Effect of Temperature and Strain Upon Ship Steels*. Report 235. Ship Structures Committee, 1973.
20. R. R. Avent and G. M. Fadous. Heat Straightening Prototype Damaged Bridge Girders. *Journal of Structural Engineering*, ASCE, Vol. 115, No. 7, July 1989, pp. 1631–1649.

Publication of this paper sponsored by Committee on Steel Bridges.

Jacking Steel Bridge Superstructures in Washington State

JOHN A. VAN LUND

Lifting steel bridge superstructures in Washington State are described. The use of jacks is an effective means for raising existing plate girder bridges to increase vertical clearance, to remove and replace defective bridge bearings, and to transfer the superstructure dead load from one existing bridge substructure to another. Case studies are presented for two successful jacking operations that involved connecting permanent steel jacking beams to the girders and jacking upward from the substructure. Generally, data on jacking operations do not appear in the technical literature. In one case study presented, data were recorded from jack gauges, and a comparison between calculated and recorded lifting loads is presented that indicates the transverse distribution of loads to the jacks. The total lifting loads recorded exceeded the calculated loads by 22 to 32 percent. Possible reasons for these discrepancies and recommendations for lifting bridge superstructures are given. It is recommended that jacks be sized for at least 1½ times the calculated lifting loads.

During new bridge construction, the lifting of heavy steel superstructure and concrete segments has been accomplished by floating the structural elements to the job site on barges and lifting them from above with long cables or rods and center-pull jacks. Some notable examples of heavy superstructure lifts follow.

EXAMPLES OF HEAVY SUPERSTRUCTURE LIFTS

Fremont Bridge, Willamette River, Portland, Oregon

In March 1973, the steel tied-arch center span, 900-ft (274-m) long, weighing 6,000 tons (5,443 tonnes), was lifted into place 160 ft (49 m) above the Willamette River in Portland, Oregon. Thirty-two 200-ton (181-tonne) center-hole jacks and threaded rods of 4-in. (102-mm) diameter were used. The total time for the lifting operation was 40 hr. It was reported to be the longest and heaviest span lifted in the world (*1*).

Ponte Presidente Costa e Silva, Guanabara Bay, Brazil

The Ponte Presidente Costa e Silva or the Rio Niteroi Bridge over Guanabara Bay connects the cities of Rio de Janeiro and Niteroi, Brazil. The navigation spans consist of parallel steel box girders with two side spans of 656 ft (200 m) and a center span of 984 ft (300 m).

The side spans were divided along the bridge centerline into two equal sections that were barged to the site and lifted 172 ft (52.5 m). Each side span section was 958 ft (292 m) long and weighed 2,480 tons (2,250 tonnes). The two sections were lifted concurrently by ring girders, jacking columns, and twelve 500-ton (450-tonne) jacks. The total load lifted for each side span was 5,815 tons (5,275 tonnes) and was repeated for the other side span. The time for lifting the side span sections was 84 hr. Finally, the 577-ft (176-m) center span, weighing 3,770 tons (3,420 tonnes) was lifted 220 ft (67 m) from the water level by eight 500-ton jacks and was accomplished in 6 days. This lifting operation was reported to be the second-heaviest bridge jacking operation (*2*).

Quebec Railway Bridge, St. Lawrence River, Quebec, Canada

In September 1917, the 640-ft (195-m) suspended span of the Quebec Railway Bridge, weighing 5,400 tons (4,900 tonnes), was successfully lifted into place 150 ft (46 m) above the St. Lawrence River. An earlier attempt failed on September 11, 1916, when the span was dropped after it had been lifted 12 ft (3.7 m) and 11 workers perished. The raising of the span, which took 4 days to complete, was the heaviest bridge jacking operation in the world until the center span of the Fremont Bridge was lifted in 1973 (*3*,*4*).

LIFTING EXISTING BRIDGE SUPERSTRUCTURES

Existing bridge superstructures are lifted for a variety of reasons. Road resurfacing on Interstate highways has reduced the vertical clearances on many of the overhead bridges. Two solutions are possible: cut and lower the roadway below, or raise the bridges. According to Ramey (*5*), raising the bridges to obtain adequate vertical clearance may be more economical.

Bridge superstructures are also raised to rehabilitate and replace bearings on older bridges, or in the case of newer bridges, to replace defective pot bearings (*6*). In Washington State, existing bridge superstructures have been lifted to improve steep approach grades, and to remove and replace bearings. As noted in the Brazilian case study, the dead load of an existing bridge superstructure was lifted from its existing piers and transferred to a new steel-arch supporting system by jacking.

Washington State Department of Transportation, Transportation Building, Olympia, Wash. 98504.

CASE STUDY 1: FRANKLIN FALLS BRIDGE, SR-90, KING COUNTY, WASHINGTON

The Franklin Falls Bridge is located approximately 50 mi (80 km) east of Seattle, Washington, on westbound Interstate 90. This continuous, steel-plate girder bridge has two spans of 350 ft (107 m) each (Figure 1). The four plate girders are 13 ft (4 m) deep and are spaced at 14 ft (4.3 m) centers. Originally built in 1971, the bridge was raised in 1978 during the construction of the Denny Creek Bridge.

The bridge was jacked 20.6 ft (6.3 m) at Pier 1, 17.1 ft (5.2 m) at Pier 2, and 13.6 ft (4.1 m) at Pier 3 to provide additional vertical clearance for avalanches that pass below the bridge. The raising resulted in a 4 percent final grade across the bridge, which was less than the original 5 percent grade.

Jacking

At the end piers or abutments, jacking stiffeners were added 2.25 ft (0.7 m) from the existing girder bearing stiffeners so that the four girders could be jacked concurrently. The total dead load to be lifted at each end pier was 700 tons (636 tonnes). Four 300-ton (272-tonne) jacks, one jack per girder, were used to lift the bridge superstructure at the end piers. The ratio of total jack capacity to total calculated dead load was 1.7.

At the intermediate pier, Pier 2, jacking diaphragms consisting of plate girders 75 in. (1,905 mm) deep were connected with high-strength bolts (ASTM A490) of ⅞-in. (22-mm) diameter to the existing bearing stiffeners in the exterior bays (Figure 2). The total dead load to be jacked was 2,500 tons (2,268 tonnes). Sixteen 300-ton jacks, four jacks per lift point, with a total capacity of 4,800 tons (4,354 tonnes) were used to lift the superstructure. The ratio of total jack capacity to total calculated dead load was 1.9.

Jacking Sequence and Deflection Limitations

The jacking was done in four or more stages as shown in Figures 3a and 3b. When each stage was completed, concrete was placed in 4-ft (1.2-m) lifts and cured before proceeding to the next jacking stage.

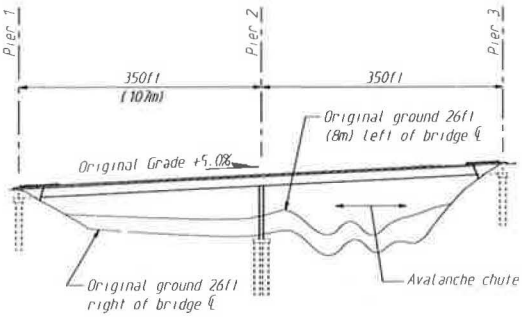

FIGURE 1 Elevation of Franklin Falls Bridge before jacking.

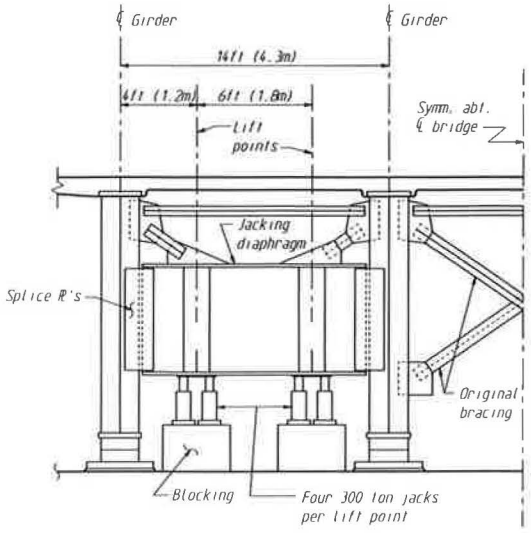

FIGURE 2 Jacking diaphragms at the intermediate pier, Pier 2.

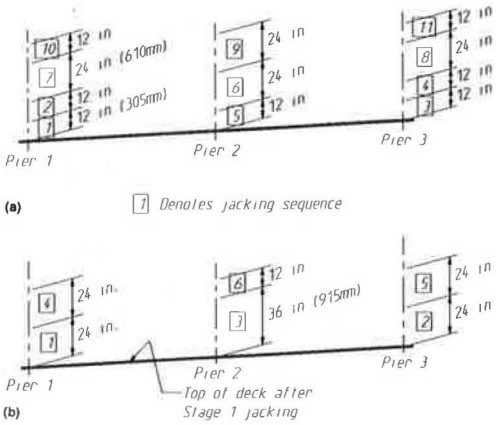

FIGURE 3 Jacking (a) Stage 1, and (b) subsequent stages.

Vertical deflection limits were established to avoid overstressing the concrete deck, steel girders, and crossframes. These were not to be exceeded during any jacking sequence. The relative vertical deflection between any girder at a pier location was ± ¼ in. (6.4 mm). During end pier jacking, the upward deflection between the end piers and intermediate pier, Pier 2, was not to exceed 24 in. (610 mm). When the superstructure was jacked at Pier 2, the deflection was not to exceed 12 in. (305 mm) relative to the end piers. These vertical deflection limits are shown in Figures 4a and 4b.

Bracing

No jacking was permitted when the wind velocity exceeded 25 mph (40 km/hr). To prevent the bridge from shifting or swaying, transverse restrainer struts were connected between the exterior girders and concrete side walls at each end abutment. At Pier 2, vertical cantilever wind-bracing pipes were

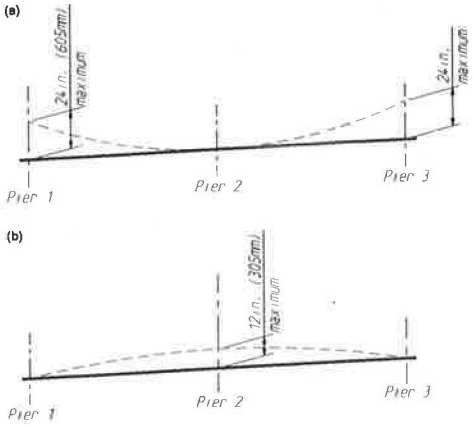

FIGURE 4 Vertical deflection limits for (a) jacking at Piers 1 and 3, and (b) jacking at Pier 2.

attached to the pier top and enclosed by a wind-bracing frame attached to the girders in the center bay.

Eight longitudinal tie rods 2 in. (51 mm) in diameter were connected to the bottom flange of the jacking diaphragms and the concrete deck to ensure that the jacking diaphragms would remain plumb. These were located at each lift point.

CASE STUDY 2: CAPITOL BOULEVARD BRIDGE, SR-5, OLYMPIA, WASHINGTON

The Capitol Boulevard Bridge over Interstate 5 was originally built in 1957 and was reconstructed in 1987–1988 (7). The existing steel-plate girder superstructure was retained, and a new steel-arch supporting system was constructed to replace the existing concrete piers that were removed so that the Interstate below could be widened from four to eight lanes.

One of the most interesting and challenging engineering problems involved the transfer of the existing superstructure dead load to the new arches by jacking.

Bearing Replacement at End Piers 1 and 4

Jacking Sequences 1 and 2

Jacking was done at one location at a time beginning at Pier 1 followed by Pier 4 (Figure 5). Eight 100-ton (91-tonne) hydraulic jacks were used to raise the superstructure at the end piers so that the existing steel slide bearings could be removed and replaced with new ones. As shown in Figure 6, permanent steel jacking beams, W16 × 57 (ASTM A588), were connected to the existing girders with ⅞-in.-diameter high-strength bolts (ASTM A490). Lift points for jacks were located 2.25 ft (0.7 m) from the girders. The hydraulic system used is shown in Figure 7.

The maximum vertical deflection permitted at the end piers was 2.5 in. (64 mm) to prevent overstressing the girders during jacking. In the transverse direction, the relative vertical displacement between adjacent girders was not to exceed ±⅛ in. (±3.2 mm), and the relative vertical deflection of the jacks

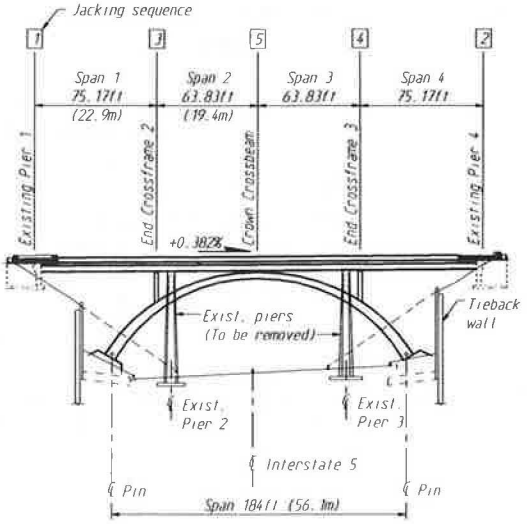

FIGURE 5 Elevation, Capitol Boulevard Bridge.

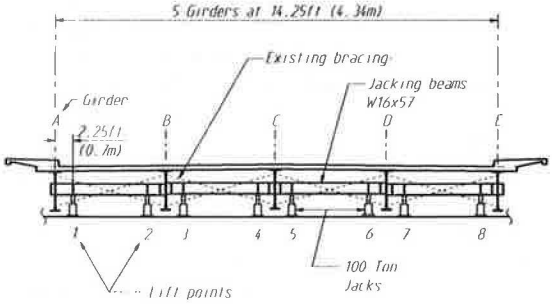

FIGURE 6 Section at end piers.

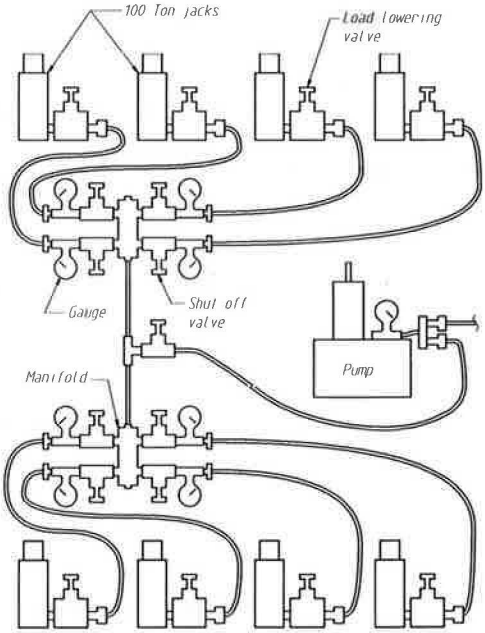

FIGURE 7 Hydraulic jacking system.

on each side of a girder was not to exceed ±⅛ in. (±1.6 mm). These limits on vertical displacement were established so that the original 30-year-old concrete deck, which was to be retained, would not be overstressed.

Calculated Lifting Loads at End Piers

The total lifting load at the end pier was calculated for the original three-span continuous structure shown in Figure 8 by the computer program STRUDL. The noncomposite stiffness of the five steel girders was used because there were no shear connectors and the concrete deck had a joint 1-in. (25-mm) wide over each pier.

The end pier reaction was 300 kips (1,334 kN) for the span dead loads, 20 kips (89 kN) for the concentrated dead load at the centerline of bearings, and 20 kips to lift the system 2.5 in. (63.5 mm). The total calculated lifting load was 340 kips (1,512 kN).

The transverse distribution of the total calculated lifting load to the jacks was determined by applying five equal loads of 68 kips (302 kN) at each girder.

Results of End Pier Jacking

The calculated and recorded lifting loads at each jack are presented in Table 1 and are also expressed as a percent of the total. The total loads recorded were 417.6 kips (1,857 kN) at Pier 1 and 447.8 kips (1,992 kN) at Pier 4, which were 23 and 32 percent greater than those calculated. When expressed as a percentage, the transverse distribution of the total lifting load exhibited good correlation with calculated values for the exterior jacks. However, the actual transverse distribution of the lifting load to the interior jacks was not consistent between Piers 1 and 4 and did not correlate well with the calculated values.

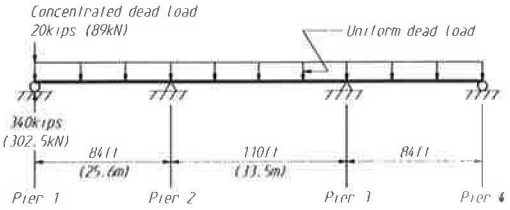

FIGURE 8 Original spans, end pier jacking.

Load Transfer at End Crossframes and Crown Crossbeam

The existing superstructure dead load was transferred to the new steel-arch supporting system by sequential jacking of the superstructure at each end crossframe and crown crossbeam. The existing pier bearings were removed, and the superstructure was lowered on the new bearings at the end crossframes and crown crossbeam. Jacking was done at one location at a time following the sequence shown in Figure 5.

Before jacking, new bearing stiffeners were connected to the existing plate girders, and permanent steel jacking beams (W33 × 118 at the end crossframes and W27 × 84 at the crown crossbeam) were connected to the stiffeners. All field connections were made with ⅞-in.-diameter high-strength bolts (ASTM A325), and all steel was 50-ksi (344-MPa) high-strength steel. A typical connection detail between an exterior girder and a jacking beam is shown in Figure 9.

Jacks, Deflection Limitations, and Blocking

Sixteen 100-ton jacks, two jacks per lift point, were used to raise the superstructure at the end crossframes (Figure 10) and the hydraulic system shown in Figure 7 was doubled.

The vertical deflection criteria for lifting at the end crossframes were the same as those specified for the end pier jacking. However, the total vertical deflection permitted at the crown crossbeam was reduced to 2.0 in. (51 mm). Because of their close proximity to the end crossframes, the existing intermediate piers served as convenient reference points to check both the total and relative deflections of the girders during jacking.

TABLE 1 END PIER JACKING: CALCULATED AND RECORDED LIFTING LOADS

	Lift Points								
Description	1	2	3	4	5	6	7	8	Total
Calculated	81.4	15.7	40.8	32.1	32.1	40.8	15.7	81.4	340.0
Piers 1 & 4	(362)	(70)	(181)	(143)	(143)	(181)	(70)	(362)	(1512)
Percent	24.0	4.6	12.0	9.4	9.4	12.0	4.6	24.0	100.0
Recorded	110.0	25.4	17.0	60.6	55.2	19.0	24.4	106.0	417.6
Pier 1	(489)	(113)	(76)	(270)	(245)	(85)	(108)	(471)	(1857)
Percent	26.3	6.1	4.1	14.5	13.2	4.5	5.9	25.4	100.0
Recorded	98.4	37.5	39.0	42.0	47.4	40.0	41.0	102.5	447.8
Pier 4	(438)	(167)	(173)	(187)	(211)	(178)	(182)	(456)	(1992)
Percent	22.0	8.4	8.7	9.4	10.6	8.9	9.1	22.9	100.0

Loads are in kips (kN)

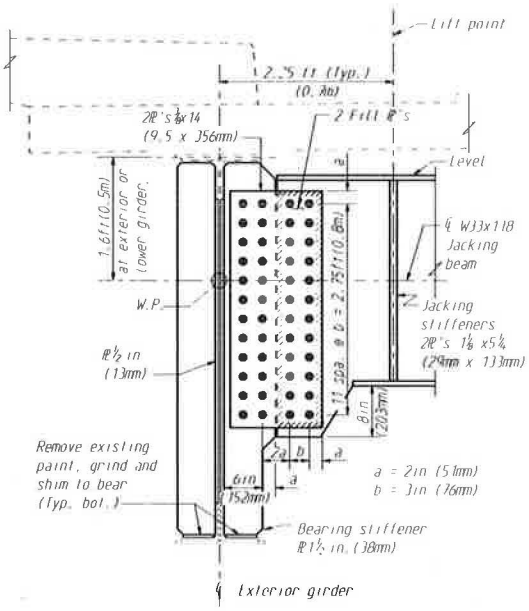

FIGURE 9 Jacking beam to girder connection.

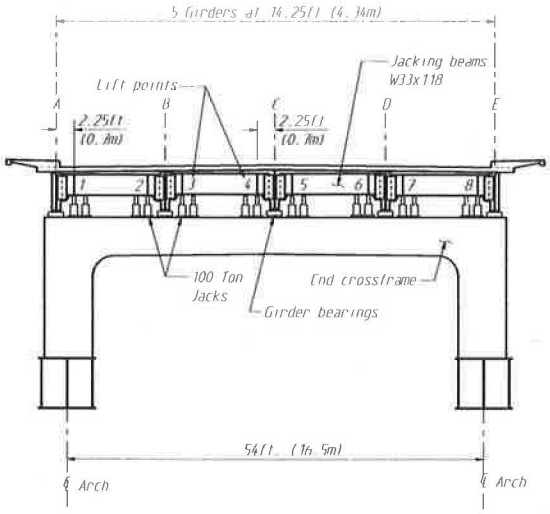

FIGURE 10 End crossframe, jacking beams, and jacks.

During the end crossframe jacking, steel shims were installed as blocking at the existing pier bearings. If a jack should fail, the girders would not be displaced relative to one another by more than the shim thickness of ⅛ in. (5 mm).

Calculated and Recorded Lifting Loads

The existing superstructure had a total dead load of 2,840 kips (12,630 kN). Under final conditions, 2,120 kips (9,430 kN) or 75 percent is transmitted to the arches by the two end crossframes. During jacking, loads greater than these occurred because of the sequence followed.

Computer analyses using STRUDL were performed to determine the magnitude and distribution of the loads and deflections during all jacking sequences. Once the calculated lifting loads were determined, a second analysis was performed to obtain the transverse load distribution to each jack by assuming the total lifting load to be applied as five equal loads at each girder.

Jacking Sequence 3

Figure 11 shows jacking at the first end crossframe. The superstructure was still attached to the opposite existing pier, which prevented the superstructure from moving both longitudinally and transversely. The spaces between the girders and unjacked end crossframe were tightly blocked; this blocking induced a compressive force in the unjacked end crossframe as the arch deflected upwards.

The total calculated load which would lift the superstructure off existing Pier 2 and maintain the original grade was 1,164 kips (5,177 kN). The calculated deflection, which is the sum of the end crossframe deflection, arch deflection, and the upward deflection of the superstructure, varied from 1.3 in. (33 mm) at the exterior girders to 1.6 in. (41 mm) at the middle girder.

The total lifting load, recorded from the jack gauges, was 1,422 kips (6,325 kN), and the measured deflection at liftoff varied from 1.375 in. (35 mm) to 1.625 in. (41 mm). The total recorded lifting load was 22 percent greater than that calculated. The measured deflections were 0.075 in. (2 mm) greater than that calculated at the exterior girders and 0.025 in. (0.6 mm) greater at the middle girder. This provided a good check on the computer analyses.

Jacking Sequence 4

Figure 12 shows jacking at the opposite end crossframe, where the total calculated load that would lift the superstructure off existing Pier 3 was 1,190 kips (5,293 kN). The actual lifting

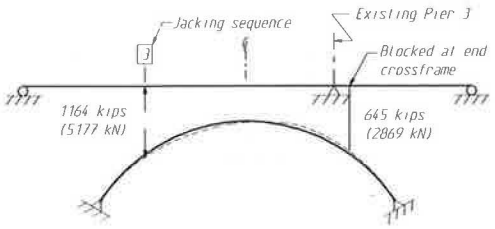

FIGURE 11 Jacking Sequence 3—end crossframe jacking.

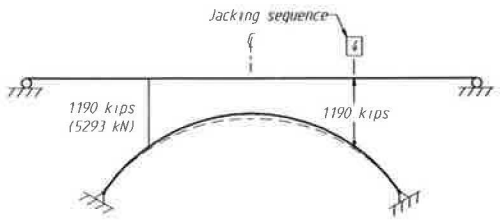

FIGURE 12 Jacking Sequence 4—end crossframe jacking.

load was 1,494.6 kips (6,648 kN) or 26 percent greater than that calculated. The recorded and calculated loads at each jack are presented in Table 2 for Jacking Sequences 3 and 4. Also presented are the percentages of the total at each jack, which exhibit good correlation in predicting the transverse distribution of the total load to the jacks.

Jacking Sequence 5

After completion of the end crossframe jacking, the superstructure at the crown crossbeam was jacked and the bearings installed (Figures 13 and 14). The intent was to induce precompression in each bearing to offset any live load uplift. The total desired precompression was 200 kips (890 kN). The total load recorded was 233.6 kips (1,039 kN) or 17 percent over that desired. A comparison between the recorded and calculated loads at the jacks and the percent of the total at each jack are presented in Table 3.

Final Dead Load Distribution

After completion of the superstructure jacking, the existing deck was resurfaced with a latex concrete wearing course 1½-in. (38-mm) thick. The additional dead load, applied to the superstructure uniformly, was 1.12 kips/ft (16.3 kN/m). The final superstructure dead load distribution to the arches is shown in Figure 15.

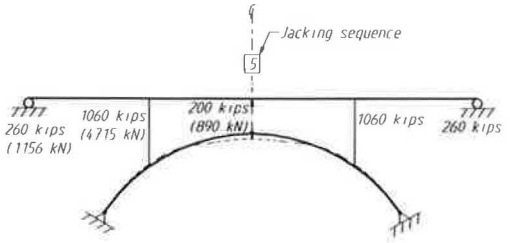

FIGURE 13 Jacking Sequence 5—crown crossbeam jacking.

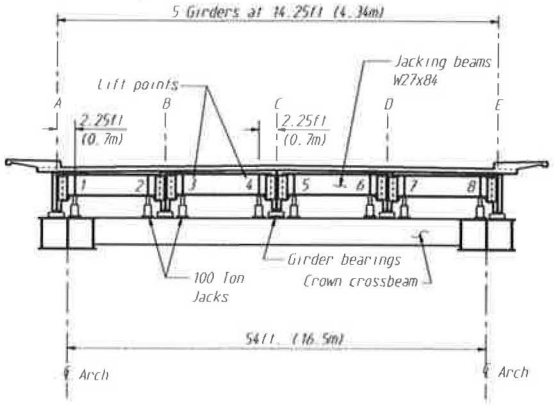

FIGURE 14 Crown crossbeam, jacking beams, and jacks.

Reasons for Higher Lifting Loads

The total loads recorded during the jacking operations were higher than those calculated by 23 percent at Pier 1, 32 percent at Pier 4, and 22 to 26 percent at the end crossframes. There are several possible reasons for these discrepancies:

1. The concrete deck may be thicker than that shown in the original contract plans, which would increase the dead load. The actual dead load is probably within 5 to 6 percent of the calculated dead load on the basis of the calculated and measured deflections.

2. The jacks may not be plumb or loaded concentrically, which may cause the piston to bind or seize up. These internal forces must be overcome to lift the superstructure. They may have caused the jack gauges to record higher lifting loads than those calculated.

3. Frozen bearings and possible composite action of the concrete deck may have contributed to higher lifting loads.

4. The jacks may not have been placed at the same locations that were used for calculating the jack loads. This difference

TABLE 2 END CROSSFRAME JACKING: CALCULATED AND RECORDED LIFTING LOADS

	Lift Points								
Description	1	2	3	4	5	6	7	8	Total
Calculated	273.5	89.6	103.6	115.2	115.2	103.6	89.6	273.5	1164.0
X-Frame 2	(1216)	(399)	(461)	(512)	(512)	(461)	(399)	(1216)	(5176)
Percent	23.5	7.7	8.9	9.9	9.9	8.9	7.7	23.5	100.0
Recorded	348.6	95.6	103.6	165.4	155.6	104.4	101.6	347.2	1422.0
X-Frame 2	(1551)	(425)	(461)	(736)	(692)	(464)	(452)	(1544)	(6325)
Percent	24.5	6.7	7.3	11.6	11.0	7.4	7.1	24.4	100.0
Calculated	279.7	91.6	105.9	117.8	117.8	105.9	91.6	279.7	1190.0
X-Frame 3	(1244)	(407)	(471)	(524)	(524)	(471)	(407)	(1244)	(5292)
Percent	23.5	7.7	8.9	9.9	9.9	8.9	7.7	23.5	100.0
Recorded	352.6	120.6	124.4	142.8	138.2	114.4	119.4	382.2	1494.6
X-Frame 3	(1568)	(536)	(553)	(635)	(615)	(509)	(531)	(1700)	(6647)
Percent	23.6	8.1	8.3	9.5	9.2	7.7	8.0	25.6	100.0

Loads are in kips (kN)

TABLE 3 CROWN CROSSBEAM JACKING: CALCULATED AND RECORDED LIFTING LOADS

	Lift Points								
Description	1	2	3	4	5	6	7	8	Total
Calculated	46.0	18.1	16.1	19.8	19.8	16.1	18.1	46.0	200.0
	(205)	(80)	(72)	(88)	(88)	(72)	(80)	(205)	(890)
Percent	23.0	9.0	8.0	10.0	10.0	8.0	9.0	23.0	100.0
Recorded	37.8	29.0	38.4	29.4	30.6	14.6	10.0	43.8	233.6
	(168)	(129)	(171)	(131)	(136)	(65)	(44)	(195)	(1039)
Percent	16.2	12.4	16.4	12.6	13.1	6.3	4.3	18.7	100.0

Loads are in kips (kN)

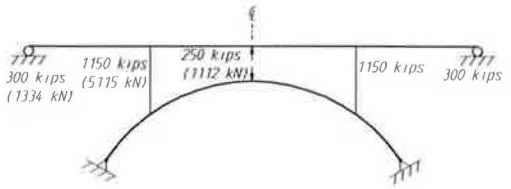

FIGURE 15 Final superstructure dead load distribution.

would cause discrepancies in the transverse distribution of the total lifting loads.

RECOMMENDATIONS FOR LIFTING BRIDGE SUPERSTRUCTURES

Recommendations based on experience at the Washington State Department of Transportation, on guidelines from Orr (*8*), and on the New York State Department of Transportation Standard on Structural Lifting Operations (*9*) are as follows:

1. Calculate the dead load to be lifted. Include the weight of any construction equipment.
2. Locate the lift points and indicate the calculated lifting loads in the contract plans. These should also be shown in the working drawings prepared by the contractor.
3. If jacks are to be used, the cylinder capacity should be from 1½ (*9*) to 2 (*8*) times the calculated lifting load. The manufacturers' name plate and rated capacity should be attached to each jack. The schematic hydraulic layout, including gauges, valves, manifolds, and other equipment, should be shown in the working drawings.
4. If special lift or supporting equipment such as jacking beams or frames are required, they should be properly detailed with particular attention to connection details. Include the type and grade of all materials in the contract and working drawings.
5. So as not to overstress the existing structural members during lifting, indicate the maximum distance to be jacked at each lift point and the maximum relative displacements permitted between adjacent lift points and between adjacent girders. Include any special lift instructions or stage jacking requirements for high lifts.
6. Do not permit traffic on the bridge or the presence of any unnecessary construction personnel near the bridge during lifting. Shim and block as the superstructure is being lifted. In the event of a jack failure, there will be no significant differential settlement and a back-up jack can be quickly installed. Permit traffic on the bridge only after the superstructure has been blocked or shimmed and the load is released from the jacks.
7. Ensure that the superstructure does not move or sway in any direction by establishing maximum permissible deflections and by providing positive restraining systems. This is particularly important for bridges on a steep grade or those located in wind-prone locations.
8. Disconnect any utilities, railings, and traffic barrier cover plates to facilitate lifting.
9. The working drawings, jacking procedures, and calculations should be prepared, stamped, and signed by a professional engineer licensed in the state where the lifting is to take place. This engineer or his designated representative should inspect all aspects of the lifting operation and be present during the lifting.

SUMMARY

1. Two case studies are presented that demonstrate the use of jacks to lift steel bridge superstructures in Washington State.
2. The first case study involves raising the bridge superstructure by as much as 20.6 ft (6.3 m) so that avalanches could pass below without hitting the superstructure.
3. In the second case study, jacking is used as a means to transfer the superstructure dead load from one existing substructure to another. Data were recorded, and a comparison between calculated and measured lifting loads and deflections was presented.
4. Computer analyses are essential in determining the anticipated lifting loads and deflections during jacking. The second case study indicated that the total recorded lifting loads exceeded the calculated loads by 22 to 32 percent.
5. Possible reasons for discrepancies between recorded and calculated lifting loads were given.
6. Recommendations for lifting bridge superstructures were presented.
7. Jacks should be sized for a minimum of 1½ times the calculated lifting loads.

ACKNOWLEDGMENTS

The author wishes to thank the Washington State Department of Transportation (WSDOT) for support in preparing this paper.

The Franklin Falls superstructure lift project was designed by Raymond T. Shaefer, checked by H. Hanson and H. Knoper, and supervised by G. T. Markich, W. B. Horn, and C. S. Gloyd, Office of Bridge and Structures, WSDOT. The field engineer was John L. Vatshell, WSDOT.

The superstructure lift for the Capitol Boulevard Bridge was designed by the author, checked by Y. A. Mhatre and H. L. Coffman, and supervised by U. C. Vasishth, G. T. Markich, and C. S. Gloyd, Office of Bridge and Structures, WSDOT. The field data were provided by Kevin Dayton, District 3, WSDOT.

REFERENCES

1. A. J. Tokola and E. J. Wortman. Erecting the Center Span of the Fremont Bridge. *Civil Engineering, ASCE*, Vol. 43, No. 7, July 1973, pp. 62–65.
2. T. J. Upstone and D. Reily. Construction of the Navigation Spans of the Rio Niteroi Bridge, Brazil. *Proc., Institution of Civil Engineers, Part 1*, Vol. 66, May 1979, pp. 227–246.
3. H. Barker. Quebec Suspended Span Successfully Hung from Cantilevers. *Engineering News-Record*, Vol. 79, No. 13, September 27, 1917, pp. 580–589.
4. D. B. Steinman. *Famous Bridges of the World*. Random House, New York, 1953, pp. 79–80.
5. G. E. Ramey. Lift System for Raising Continuous Concrete Bridges. *Journal of Transportation Engineering, ASCE*, Vol. 109, No. 5, Sept. 1983, pp. 733–746.
6. C. Redfield and C. Seim. Pot Bearing Replacements—Two Case Studies: Cline Avenue Interchange and I-285/I-85 Interchange. *Joint Sealing and Bearing Systems for Concrete Structures*, Vol. 2, SP-94. American Concrete Institute, Detroit, Mich., 1986, pp. 817–823.
7. J. A. Van Lund et al. Steel Arches Used in Bridge Reconstruction over Interstate 5. In *Transportation Research Record 1223*, TRB, National Research Council, Washington, D.C., 1989, pp. 46–53.
8. J. Orr. Planning, Knowledge Keys to Safe Bridge Lifting. *Roads & Bridges*, Vol. 26, No. 4, April 1988, pp. 85–87.
9. Structural Lifting Operations. *Standard Specifications Construction and Materials*, Section 585. New York State Department of Transportation, Jan. 1985, pp. 5-108–5-110.

Publication of this paper sponsored by Committee on Construction of Bridges and Structures.

Alternatives in the Design and Construction of Cable-Stayed Bridges

STEVEN L. KASPAR AND JAMES ROWINGS

Cable-stayed bridges have gained popularity as a design solution for long-span applications in North America. With their advent and implementation, several significant contractual, technical, and personnel-related controversies have evolved that threaten to slow the implementation of this design concept. These problems are reflected in the conflicts and claims currently plaguing the industry. A variety of constructability concepts collected from a unique blend of owners, designers, suppliers, and contractors associated with recent cable-stayed bridge projects are described. The constructability concepts relate to tower design and construction, cantilever deck design and construction, composite deck design and construction, stay-cable configuration and construction, posttensioning component operations, reinforcing steel details, prefabrication operations, stressing operations, grouting operations, closure, and general work sequencing. The concepts provide a starting point for review of designs for efficient and economical construction.

Rapid growth in the application of cable-stayed structures has occurred in North America. Since the end of World War II, the cable-stayed bridge has proven to be the most advantageous and economical long-span bridge solution. These structures represent the highly advanced, long-span bridges using currently available state-of-the-art technology.

Problems have occurred that were not originally anticipated with the advent and implementation of any new technique or procedure. Contractual-, technical-, and personnel-related controversies have evolved. Projects have been completed above budget. Major delays have occurred, forcing late completion. A high number of major claims and litigation frequency exists. In some cases, designers and constructors have been terminated, forcing severe delays and cost overruns.

Recent examples of sophisticated bridge projects illustrate the conflicts plaguing the industry. After terminating the original constructors, the Rhode Island Department of Transportation and the Alabama Highway Department selected new constructors to complete their structures because of differences in the interpretation of the specifications, extended delays, and a conflict over costs (*1*). During the construction of the Sunshine Skyway Bridge in Tampa, Florida, differences of opinion existed about the responsibilities and procedures of the owner, designer, and constructor (*2*). Contract changes and delay damages are being negotiated on the basis of these differences. The West Virginia Department of Highways has received $8 million of claims to date on the construction of the Weirton-Stuebenville Bridge, a $24.1 million structure. In addition, the owner claims the constructor deviated from the accepted erection procedure, thus overstressing several segments (*3*). An increasingly frequent complaint is the constructability of these bridges. The constructor's interpretation of the designer's intent is guesswork (*4*).

The objective is to identify constructability concepts that need to be considered during planning, design, and construction to ensure project success. The theory of constructability will be reviewed along with special considerations in the cable-stayed bridge environment. The ultimate goal is to support reduction of problems on future bridge projects.

S. L. Kaspar, Massman Construction Company, Kansas City, Mo. 64114. J. Rowings, Civil and Construction Engineering Department, Iowa State University, Ames, Iowa 50011.

DESIGN AND CONSTRUCTION OF CABLE-STAYED BRIDGES

The variety of cable-stayed bridges illustrates the ingenious attempts to provide owners with unique design solutions. Modern cable-stayed bridges have used both steel and concrete towers, including single- and double-plane vertical, A-shaped, and double-plane sloping towers. Deck schemes include cast-in-place concrete, precast concrete, orthotropic steel decks, composite decks, and prefabricated steel. Cable configurations include radiating, harp, and fan. Cable systems use high-tensile bars, parallel wires, or steel bars protected by polyethylene or steel pipe (*5,6*).

The design and construction of the superstructure begins with the central towers. Today, concrete is typically used in towers because it is the most economical system (*7*). In areas of strong wind forces, A-shaped towers provide an optimal solution because of their stability (*8*). Inclined or A-shaped towers require temporary ties to prevent collapse during construction (*9*). The towers serve as an anchor for the stay cables. Once the cables are installed and stressed, the towers must provide transverse and longitudinal resistance against the applied cable forces.

Many different deck configurations are used. A fundamental advantage of concrete over steel is that construction can begin as soon as the necessary falsework, formwork, and erection equipment is ready (*10*). Construction operations are not at the mercy of the steel fabricator's delivery schedule. Precast concrete operations can begin as soon as feasible during construction. Proper planning and experienced personnel in the design and development of the precasting facilities ensure better project performance (*11*); however, precast concrete requires a large investment of resources and personnel in the early stages of the project. Cast-in-place concrete construction eliminates potential erection problems caused by improper segment fit-up (M. Miller, personal communication); thus,

erection errors resulting from creep and shrink effects are prevented. On the contrary, composite deck construction offers several advantages over precast and cast-in-place concrete. Construction is simplified because difficult tolerances and match-casting requirements do not exist (*12*). The dead load of a deck configuration using structural steel is less than a similar layout using concrete. Therefore, lower dead loads are induced on the structure's foundation, minimizing substructure requirements (*13*). Each deck configuration needs to be analyzed to attain the best possible design solution.

The main structural elements transferring loads from the deck to the tower are the stay cables. Overall, they can account for 30 percent of the bridge's total cost (*7*). Closely spaced cables allow shallow, slender bridge decks with reduced bending moments. Aerodynamic stability is also increased (*12*). Closer cable spacing permits free cantilevering without the use of temporary guys (*7*). Anchoring the stay cables in the tower is simplified when the configuration permits adequate space between anchors (*8*). Harp-shaped configurations result in standardized tower connection details; in fact, a $400,000 savings is envisaged on the Chesapeake and Delaware Canal Bridge because a harp-shaped configuration will reduce detailing and installation costs (*9*).

Constructability is defined as "the optimum use of construction knowledge and experience in planning, design, procurement, and field operations to achieve overall project objectives" (*14*). An owner can realize potentially large savings as designs are more construction oriented. For example, construction input was used in all phases during the development of a bleached market pulp mill with a savings of approximately 6 percent of construction costs—a 10-to-1 payback of the constructability program's costs. On another project, a 720,000-kW generating station, the plant went into commercial operation 4 months early and $200 million under budget. This saving resulted from experienced construction personnel involvement in the project's development from conceptual stages to completion (*15*).

Additional benefits might be accrued if experienced construction contractors are included in the design process to analyze the construction methods implied in the designs. These constructability reviews should begin as early as the conceptual design stage. Construction personnel can provide innovative ideas about materials, equipment, and methods that will simplify design objectives. Projects designed with this input attract more bidders with lower bid prices because of minimal risk. In some cases, legal entanglements can be avoided because specifications are better defined, designs are more practical, and design errors are corrected early (*16*).

Project planning is the most important function in the life cycle of the project. Construction expertise is required to complement the planning and design functions. Seven major items benefitting project development when construction personnel are involved include (*17*) The following: estimating, scheduling, procurement, constructability, labor, contracting, and organization. Using construction expertise for these activities can improve overall project cost effectiveness.

For constructability to be successful, all members of the design or construction organization must practice this philosophy. Implementation of a constructability program is an intricate task. The most successful constructability programs provide the following (*18*):

1. Clear communication of senior management's commitment and support of constructability.
2. Single-point executive sponsorship of the program.
3. A permanent corporate program and a tailored implementing program within each project.
4. User friendly procedures and methodologies.
5. A corporate data base of lessons learned.
6. Training where necessary.
7. Easy appraisal and feedback.

CABLE-STAYED BRIDGE DEVELOPMENT

The development of a cable-stayed bridge presents its own set of special challenges during conception, design, and construction. These challenges include bridge design requirements, the alternative design process, and balanced cantilever construction.

Bridge Design Requirements

During the design of a cable-stayed bridge structure, the concept selected must meet the owner's established requirements of aesthetics, operability, economics, maintainability, and functionability. Bridge design requires experienced personnel knowledgeable in state-of-the-art techniques and methodologies. Important considerations for a cable-stayed bridge design include (*19,20*):

- A safe and technically sound concept,
- A safe and economical erection method,
- Low maintenance with a long service life,
- An aesthetically pleasing form,
- A low impact on the environment, and
- A design that permits a faster construction time compared to an alternative comprising the same material and manpower input.

Owners want their designers to provide a design scheme that minimizes material costs and exercises adaptable erection requirements. Owners desire flexibility in the final design to allow adequate competition between constructors (*21*). This flexibility will permit constructors to build the structure using methods most acceptable for them. If a project is designed that can use innovative ideas and acceptable standards of construction, the design is more buildable (*16*).

At this time, the United States has fewer than 10 engineering consultants with the capabilities required to design cable-stayed structures (*9*). When cable-stayed technology was first introduced in the United States, design consultants had to rely on European experience. Today, U.S. engineers have learned how to design cable-stayed structures independently (G. Peters, personal communication).

Alternative Design Process

In the United States, an alternate design is required for all bridge projects with an estimated cost over $10 million (*9*). The goals behind this process are to stimulate engineering

creativity and for the owner to obtain financial savings through competitive bidding. Alternate designs may be of different structural types or alternate materials. The theory behind alternate designs permits constructors to bid on the design most suitable for their construction methods and thus save the owner money.

The alternate design concept is not without its faults. First, it virtually doubles the cost of the structure design because two designs are prepared, which doubles the design cost. Second, although the alternative design process theoretically fosters innovation, it creates liability concerns presented by the openness in the contract documents, which permit constructors more flexibility (*22*). Recent trends are for designers to provide schematic erection methods only, with constructors providing structural construction details based on their proposed methods. Liability conflicts result from the changed responsibilities between designers and constructors. Third, the alternative design process can nurture the wrong type of competition. Alternates should focus on the designer's creativity versus material competition (*23*). Instead of promoting a competition regardless of material type, one alternative is typically designed by using concrete while the competing alternative uses steel or a composite scheme. Another fault in this process is that the constructor's alternative is prepared solely to reduce construction costs. It may not meet all of the owners objectives (*21*). For instance, a constructor may sacrifice aesthetics so that concrete forming operations may be simplified. Finally, an alternate design prepared at the constructor's option may not always meet the designer's intent. A constructor-proposed alternative may not satisfy code requirements as conservatively as the designer's alternative. As a result, a conflict arises between the designer and constructor early in the construction process (H. B. McCoy, personal communication).

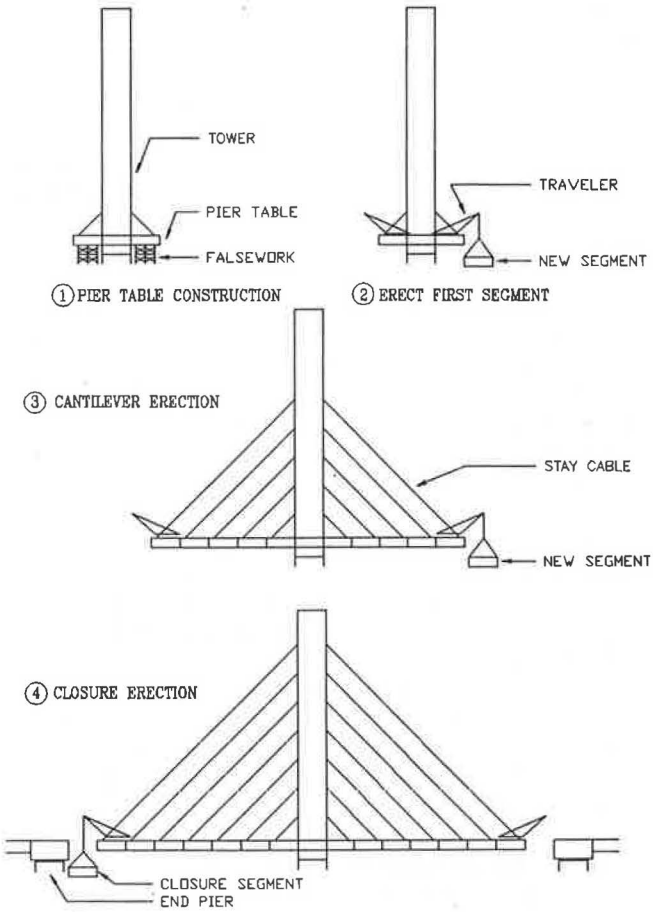

FIGURE 1 Balanced cantilever construction.

Balanced Cantilever Construction

The construction of cable-stayed bridges is made possible with the use of balanced cantilever construction. It is the most common method used in their erection. It permits overhead construction while maintaining traffic below. Expensive, ground-supported falsework is eliminated because the cantilevers are supported from previously completed segments. Construction can proceed over deep valleys, navigable channels, and congested urban areas with little damage done to areas adjacent to the construction site (*22*).

Balanced cantilever construction begins at a permanent center pier or pylon. To begin, the tower deck segments or pier table is constructed on ground-supported or pier-supported falsework. Once complete, a steel truss assembly, called an erection traveler or form traveler, is erected on the completed pier table. Next, a segment is erected on each side of the pier table. In precast or composite deck superstructures, the precast or individual structural members are erected and anchored into place. In cast-in-place construction, the segment is formed and poured in place. Once a segment is placed on each side of the center tower, the travelers are moved outward one segment to erect the next segments. Construction progresses in this way until meeting with the approach spans. Figure 1 shows the balanced cantilever process. As each span cantilevers away from the central tower, the superstructure remains balanced because an equal and opposite force exists on each span.

A critical element in balanced cantilever construction is the preparation and use of the erection sequence. The erection sequence is a step-by-step analysis of the stresses and stress reduction or balancing imposed on the structure. All forces and loads applied to the superstructure are checked against maximum permissible stresses. The final version becomes the constructor's guide to building the superstructure of the bridge. The erection sequence provides a detailed analysis accounting for alignment, applied forces, stay-cable forces, temperature and creep influences, sun contact, construction loads (cranes, forms, travelers, etc.), and erection stages (*8*). The computations are updated at each stage of construction to reflect the changes in the structure's behavior. As the cantilever progresses outward in two directions from the main tower, the entire structural system must be reanalyzed as to how the superstructure will react with the additional applied loads (*22*). Camber curves are generated from these calculations. Permissible plus and minus deviations from the theoretical camber curves are also determined in the erection sequence.

Once the deck superstructure construction begins, an erection sequence analysis helps predict for the constructor the detailed deflection and camber data for each stage. Numerous measurements are taken and compared to the theoretical camber and deflection data in the erection sequence. If measure-

ments are within specified tolerances, the derrick is moved forward to the next segment. If the measurements exceed specified allowable tolerances, stay cable shim calculations, adjustments, and secondary measurements must be repeated until specified tolerances are attained. The erection activities are similar for segments without a cable minus the operations relating to the stay cable. Without the stage-by-stage erection sequence, the constructor would not have adequate information to safely build the deck superstructure.

During the erection of the bridge deck superstructure, the constructor should not deviate from the owner-accepted procedure (*24*). The constructor should show that the requested changes are within the tolerances allowed in the specified erection sequence if a modification is desired. When changes are outside the owner-accepted limit envelope, the constructor prepares an alternate erection sequence. This new sequence must prove to the owner that requested changes meet the intent of the previously accepted guidelines.

Constructability Concepts

Constructability concepts collected from experts in the industry should be considered during project development. With proper analysis and application, greater effectiveness might be possible in the building process. It is hoped that these concepts will provide a review list during the design and construction process and lead to improvements in future cable-stayed bridge projects.

Tower

- Towers constructed from concrete are normally the most economical system (*7*).
- Towers should be constructed from concrete because they are more economical than steel (*8*).
- Towers will normally be made from concrete because the cost of concrete compression members is approximately ⅔ of that of towers made of steel (*25*).
- Basic conditions the tower must satisfy include the following (*7*):
  - —Longitudinal stiffness in regions of cable anchorages;
  - —Lower tower strength to resist forces acting on it (such as cables, wind, braking forces); and
  - —Use concrete strength in cross sections for maximum advantage.
- In the longitudinal direction, the tower should be slender and have a small bending stiffness to avoid large bending moments and reactions by the foundations (*8*).
- Tower bracing above the road deck should be slender and appear light between the thin cables (*8*).
- Temporary tower restraint during construction is difficult and time consuming. On the East Huntington Bridge, temporary forestays and backstays were needed to stabilize the tower during cantilever. It required cables anchored from the tower head to concrete anchorage blocks on the ground. Stressing the cables was difficult because tower head access was limited (*9*).
- Inclined tower construction requires temporary ties to prevent collapse. The towers may need to be cast with an outward chamber for dead load deflection caused by the inclination (*26*).
- Towers providing live- or dead-end cable anchorages should be readily accessible for cable installation, stressing, and grouting. This includes providing sufficient space for personnel and equipment necessary to complete these activities. If tower prestressing exists, the same access criteria is required (*26*).
- Loads induced on the tower by temporary crane tie-ins need to be checked so allowable stresses are not exceeded (*26*).

Cantilevered Deck

- Avoid pierhead segments considerably heavier than the next segments as they require additional and expensive lifting equipment (*19*).
- Pierhead segments need to be the minimum length required for the installation of one traveler (*19*).
- The pier table and cantilever need to support reactions from form travelers, erection gantries, and self-weight (*19*).
- Bottom-of-deck cable blister forming is difficult and expensive. Moreover, access needs to be provided for forming, cable stressing, and later cable adjustments (*19*).
- Details and computations of the cast-in-place concrete-forming system should be submitted to the engineer. This includes maximum loadings and stresses created because of equipment and concrete; deflections during placement, temporary supports, and tie-downs to stabilize cantilevers; and a detailed step-by-step procedure for placement, stressing, and form advancement (*24*).
- Because of applied cable forces, the longitudinal thrust in the deck increases toward the centerline of the towers. Therefore, additional prestressing is not required to resist deck tensile forces. At span ends, the cable thrust is lower and bending moments are higher, requiring deck prestress to resist applied loads (*8*).
- Deck prestress is not normally required except at the center of the main span unless it is needed for cantilevering (*9*).
- When deck prestress is needed, continuous longitudinal strands should be used from anchor to anchor versus prestress bars coupled at each segment joint (*26*).
- Camber will be monitored at each stage of construction. The constructor should submit a survey plan depicting proper erection to the final grades and cambers shown on the plans (*24*).
- Recommended erection tolerance from the predicted alignment is ± 1 in. (*24*).
- The constructor should prepare a table of elevations and alignments at each stage of construction including the following points (*24*):
  - —A benchmark point from which all other measurements will be taken.
  - —All four corners and center line at segment faces of top slab of pier segments to establish grade and crown.
  - —Two points on longitudinal center line of each pier segment, one on each edge, to establish alignment.
  - —One point on the longitudinal center line and at least one corner of each segment along every joint between cast-

in-place segments to establish elevations and alignment at every stage of erection.

—During construction, it is recommended that the engineer establish a separate, independent measuring system from the one used by the constructor.

This system of checks and balances ensures proper geometry control (*27*).

Composite Deck

- On composite structures, the concrete deck carries the compressive forces of the stay cables. The steel sections should be small to avoid creep problems (*8*).
- The overriding concern is to keep the tensile stresses in the concrete roadway slab as small as possible (*25*).
- Economy is attained through ease of construction. Long production runs of repetitive modular elements ensure erection speed and less risk for the constructor (*12*).
- Integral composite action is achieved by placing concrete strips around lapping rebar and shear connectors (*12*).
- Careful detailing is required between the composite deck and structural steel interface. Proper overlap of protruding rebar from the deck between shear studs on the steel flange is necessary for ease of construction (*12*).
- In order to minimize the effects from creep and shrinkage between the precast panels and steel deck, they should be stored for at least 60 days before erection (*28*).

Stay-Cable Configuration

- The configuration of cables and their connections to the deck and tower are significant factors in the overall costs of cable-stayed bridges (*12*).
- It is better to anchor cables at both the tower and girder ends vis-à-vis running a continuous cable from the girder through the tower to the opposite girder (*8*).
- Continuous cables over saddles are not preferred by the FHWA because they lack accessibility for inspection, they are difficult to replace, and two stays are involved in the event of an accident instead of one (*9*).
- Closely spaced cables eliminate temporary-support cables and allow free cantilevering during construction. Furthermore, they create smaller bending moments and thus smaller girder beams (*8*).
- Standardized cable configurations and geometry at the tower simplify installation and construction operations (J. Sutter, personal communication).
- A harp-shaped cable configuration results in a standardized connection detail. All cables enter the tower at the same angle (*9*).
- Harp-shaped cable configurations permit the construction of the deck before completion of the tower (*9*).
- Harp-shaped configurations require more cable steel, induce more compression forces in the deck, and produce bending moments in a longer tower section (*8*).
- In fan-shaped configurations, all cables are anchored at the top of the tower, resulting in a large force concentration at one spot. Furthermore, it is difficult to anchor all the cables in one small area (*8*).
- The semi-fan configuration moves the tower cable anchorages over a relative length of the tower head (*8*).
- Cable anchorages at the tower and deck should be recessed rather than external to simplify formwork details (*26*).

Stay Cables

- Cable-stayed bridges should be designed such that the loss of an individual cable would not result in significant structural damage to the bridge (*29*).
- Cable designs should allow replacement of any stay (*29*).
- Acceptance testing of stay cables requires sophisticated test equipment, technical expertise, and a long lead time to perform the tests. Tests are typically performed in Europe and can be expensive (*26*).
- Fatigue testing is usually required on three representative samples of the complete system. Failure of one component is cause for rejection of the complete system (*9*).
- Testing should be performed at the earliest possible time during construction to enable modifications and corrections of unforeseen complications.
- All cable items requiring testing should be clearly stated in the contract specifications.
- To simplify construction, the permanent design should use the permanent stay cable during cantilever erection. The use of temporary support cables should be avoided (J. Sutter, personal communication).
- Wrapping black polyethylene (PE) tubing with white Tedlar tape is now required by FHWA. It reduces the maximum temperature of the stay from 65°C to 38°C (*9*).
- The only problems occurring to date involving the use of PE tubes resulted from excessive pressure during cable grouting and mishandling of the stays (*9*).
- Bar stays are not accepted by the FHWA because (*9*)

—Couplers act as stress raisers that reduce the fatigue resistance.

—The bars have a lower ultimate tensile strength.

—Assembly errors are possible with incomplete attachment of the bars to the couplers.

Posttensioning Components

- All posttensioning materials will be tested by the engineer (*24*).
- Contract specifications should clearly define storage requirements and corrosion protection of all posttensioning components.
- The constructor should provide a warehouse attendant during construction to ensure proper management of posttensioning materials.
- Posttensioning duct alignments should be fully dimensioned through each segment. This process is done by quoting offsets vertically and laterally from known control lines or surfaces at regular intervals of no more than 2 to 3 ft where small radii and reverse curves occur (*11*).
- In anchorage zones, allow for the largest commercially available anchorage likely to be used with the tendons con-

cerned. Then, if the constructor elects to use a smaller anchorage, it can easily be accommodated with only a minor change to the very localized detail (*11*).

- Specify a sequence for posttensioning of all tendons and bars (*11*).
- During concreting, a stiffening mandrel should be provided inside the empty duct to maintain geometry and protection of the empty duct.
- Prestressing tendons should be designed for maximum permissible eccentricities (*19*).
- Prestressing tendons should be taken full length through the structure where they can be easily stopped. Furthermore, they should not be prematurely stopped and started where the additional anchorage and stressing costs outweigh the length of tendons saved (*19*).

Reinforcing Steel

- Moreton (*11*) has made the following suggestions regarding the integration of rebar with other bridge components:
  - —Ensure that all reinforcing bar cages can be assembled easily from simple bar shapes, avoiding as much as possible closed loops and multiple bends.
  - —Ensure that reinforcing bar bending diagrams are shown in full in the plans adjacent to the component to which they apply or on the next sheets.
  - —Ensure that reinforcing bar lengths and bends are according to normally accepted industry practice, amply allowing for bending tolerances.
  - —Ensure that reinforcing bars will fit inside the concrete dimensions, recognizing that there are construction tolerances (in the specifications) on concrete thickness and covers. Do not forget that a ribbed reinforcing bar is physically larger than its nominal diameter.
  - —Ensure that all reinforcing bars are bent to avoid posttensioning ducts.
  - —Clearly state on the plans that if a conflict exists between the posttensioning duct and the rebar, the duct alignment takes precedence over the location of the rebar. The rebar will be relocated at the direction of the engineer.

Prefabrication

- All segments or major structural elements should be clearly marked after casting (*24*).
- A usual rejection rate for precast segments should not exceed 0.5 percent (*11*).
- Gee (*19*) has made the following comments regarding prefabrication:
  - —To justify precast operations, sufficient repetition and quantity must exist for the investment of special forms and equipment.
  - —If prefabricating of elements is used, cast-in-place concrete must be minimized.
  - —Prefabrication or precasting can proceed while foundation or substructure work is progressing. However, the costs incurred for fabrication, transportation, and erection of large, heavy units must be cheaper than the subsequent time savings.
  - —In water applications, suitable dock facilities must exist for transportation of segments.
  - —Precast elements and operations must consider road transportation load requirements.
  - —Delivery of precast elements should be to the most economical and accessible location.
  - —Benefits from precasting cannot be suppressed while workers wait for cast-in-place concrete activities.
- Moreton (*11*) suggests the following recommendations for improvement:
  - —Organize the plans for the convenience of the contractor who has to fabricate and erect the components.
  - —Exhibit details in full, either on or next to the sheet showing the component, and to a large scale.
  - —Exhibit the assumed ages of segments at the time of erection and all material properties assumed in the design.

Stressing

- Stressing of stays is easier when performed from the tower head (*9*).
- All strands of tendons of more than four 0.5-in.-diameter or 0.6-in.-diameter strands should be stressed simultaneously with a multistrand jack (*24*).
- Monostrand jacks are not normally permitted to stress cables because the subsequent force transfer to adjacent strands is unknown.
- Within 30 days of stressing operations, all jacks should be calibrated with a specific gauge and load calibration curves. Recalibration should be at six-month intervals. Jacks and gauges should not be interchangeable (*24*).
- Jacks should provide a means of visually examining and measuring elongation movement during stressing (*24*).
- The constructor should provide records of all stressing operations including gauge pressures and tendon elongations at each stage for review and approval. Tails should not be cut off until stressing records have been approved (*24*).
- Stay-cable force adjustments are a time-consuming task that should be minimized in any way possible (*30*).
- Final cable stressing and adjustments on the Dame Point Bridge required from 4 to 5 weeks (*9*).
- Cable adjustments are performed in the early morning such that temperature differential influences are minimized.

Grouting

- The design and subsequent testing of the grout mix may require a substantial amount of time. Allow adequate time for design, testing, and approval.
- Grouting operations are more economical if several tendons or cables are grouted simultaneously rather than a few at a time.
- It is recommended that grouting be delayed until the entire span is stressed (*24*).
- Cable grouting should be done in lifts to avoid excessive hydrostatic pressure, which can cause cracking of PE pipe (*30*).
- Within 15 days after ducts are grouted, all blockouts for anchorages should be grouted or filled with nonshrink grout, a special mortar, or another protection system (*24*).

• Cable grouting should be done in the early morning so that the grout temperature differential is minimized (*9*).

Closures

• Before construction of closures, cantilevers should be locked to prevent movement or rotation of one cantilever in relation to the other cantilever or end-pier girder (*24*).

• Before closures, stay-cable adjustments may be required to locate cantilevers in the correct position.

• Casting the end-pier girder away from the cantilever several months before connection minimizes creep and shrinkage effects (*30*).

Additional Concepts

• For steel members, a practical welding procedure or sequence of procedures should exist that enables all welds to be completed and inspected without delays (*20*).

• Design structural steel connections such that one member uses a standard-sized hole whereas the other member uses a slotted hole.

• Sufficient access should be provided for all structural steel erection and connections (*19*).

• Alternate concrete mix designs with higher strengths may permit faster turnaround for forming and stripping operations (*31*).

• Delivery times for specialized posttensioning material and equipment should be accounted for in the project schedule.

• Blockout design requirements for posttensioning and stay-cable systems include formwork, cable installation and equipment, rebar installation, stressing, grouting, pourbacks, scaffolding, and inserts for temporary work platforms (*26*).

CONCLUSIONS

The design and construction of a cable-stayed bridge have the potential for technical challenge and economical success in the 1990s. Building a cable-stayed structure represents state-of-the-art bridge technology with theoretical potential for magnificent spans. However, the North American cable-stayed bridge market has experienced continuous problems during its development. Constructability concepts have been collected and presented to focus attention on the problem areas. Constructors with losses from past projects will either increase their future bids or decide not to bid on future projects. Should this happen, more expensive alternatives, such as steel truss bridges or suspension bridges, may be built. These concepts should be examined to determine if they are appropriate on the basis of local economics and project requirements.

REFERENCES

1. H. Lass, S. Setzer, and P. Green. Two Bridge Projects Restart After DOTs Change Contractors. *Engineering News-Record* 223.1, July 6, 1989, pp. 7–8.
2. A. Soast. Skyway Bridge Boasts a Record and Innovations. *Engineering News-Record*, Sept. 1986, pp. 23–25.
3. State Fumes Over Late Bridge. *Engineering News-Record*, Vol. 223, No. 1, July 6, 1989, p. 8.
4. A. F. Gee. Constructability of Bridges—A Construction Engineer's View. *Concrete International*, Vol. 11, No. 5, May 1989, pp. 48–52.
5. W. Podolny and J. B. Scalzi. *Construction and Design of Cable-Stayed Bridges*, 2nd ed. John Wiley, New York, 1986.
6. M. S. Troitsky. *Cable-Stayed Bridges. An Approach to Modern Bridge Design*. Van Nostrand–Reinhold, New York, 1988.
7. *VSL Stay Cables for Cable-Stayed Bridges*. VSL International, Ltd., Jan. 1984.
8. F. Leonhardt. Cable-Stayed Bridges with Prestressed Concrete. *PCI Journal*, Vol. 32, No. 5, Sept.–Oct. 1987, pp. 52–80.
9. G. W. Hughes and W. K. Wheeler. *Cable-Stayed Bridges, Report on Study Tour of North America, 23 Nov.–11 Dec. 1988*. Roads and Traffic Authority, New South Wales, Feb. 1989.
10. C. J. Pankow. The Builder's Function in Advancing the Techniques of Concrete Construction. *Concrete International*, Vol. 9, No. 10, Oct. 1987, pp. 23–27.
11. A. J. Moreton. Segmental Bridge Construction in Florida—A Review and Perspective. *PCI Journal*, Vol. 34, No. 3, May-June 1989, pp. 36–77.
12. P. R. Taylor. Composite Cable-Stayed Bridges. The Concept with the Competitive Edge. *Engineering Journal of the American Institute of Steel Construction*, Vol. 24, No. 4, 1987, pp. 157–163.
13. A. Grant. Design and Construction of the East Huntington Bridge. *PCI Journal*, Vol. 32, No. 6, Nov.-Dec. 1987, pp. 20–29.
14. *Constructability Concepts File*. Publication 3-3. Construction Industry Institute, Austin, Tex., Aug. 1987.
15. *Constructability, A Primer*. Publication 3-1. Construction Industry Institute, Austin, Tex., July 1986.
16. Can Your Design Be Built? *Civil Engineering, ASCE*, Vol. 56, No. 1 Jan. 1986, pp. 49–51.
17. S. Harlin. Early Construction Input Improves Efficiency for Project Engineering. *Pulp & Paper*, Vol. 62, No. 9, Sept. 1988, pp. 16–118.
18. *Guidelines for Implementing a Constructability Program*. Publication 3-2. Construction Industry Institute, Austin, Tex., July 1987.
19. A. F. Gee. Bridge Winners and Losers (Rapid Evaluation of Bridge Designs and Construction Methods). *The Structural Engineer*, Vol. 65a, No. 4, Apr. 1987, pp. 141–145.
20. R. Heinen. Who Should Design Bridges? *Civil Engineering, ASCE*, Vol. 55, No. 1, July 1985, pp. 63–66.
21. R. Tappin. Bridges—Design for Construction. *Civil Engineering* (London), Jan.-Feb. 1988, pp. 10–11, 13–14.
22. J. A. Murillo. Modern Bridge Construction and Engineering Services. *TR News*, No. 142, May–June 1989, pp. 7–11, 32.
23. R. Robison. Cable Stays Catch On. *Civil Engineering, ASCE*, Vol. 56, No. 1, June 1986, pp. 58–61.
24. *Design and Construction Specifications for Segmental Concrete Bridges*. Final Report, Post-Tensioning Institute, Feb. 1988.
25. W. Zellner, S. Reiner, and H. Svensson. Recent Trends in the Design and Construction of Cable-Stayed Bridges. *Proc., 12th Congress*, International Association for Bridge and Structural Engineers, Sept. 3–7, 1984, pp. 279–284.
26. S. L. Kaspar. *Constructability and the Cable-Stayed Bridge*. Technical Report. Iowa State University, Ames, Oct. 1989.
27. J. M. Muller and J. M. Barker. Design of the Lynn Cove Viaduct. *PCI Journal*, Vol. 30, No. 5, Sept.–Oct. 1985, pp. 38–53.
28. P. Taylor, J. E. Torrejon, and K. Manniche. Use of Concrete in the Annacis Bridge Main Span. Paper SP93-31. *Proc., International Conference on Concrete in Transportation*, 1986, pp. 695–720.
29. Ad Hoc Committee on Cable-Stayed Bridges. *Recommendations for Stay Cable Design & Testing*. Post-Tensioning Institute, Jan. 1986.
30. M.-C. Tang. Construction of East Huntington Bridge. *PCI Journal*, Vol. 32, No. 6, Nov.–Dec. 1987, pp. 32–48.
31. R. L. Nickerson. Building Bridges Faster. *Civil Engineering, ASCE*, Vol. 58, No. 1, Jan. 1988, pp. 59–62.

Publication of this paper sponsored by Committee on Concrete Bridges.

Cost Comparison of AASHTO Type IV and Modified Type IV Bridge Beams with 54- and 63-in. Bulb-Tees

SHERRELL HELM

Standard AASHO precast, prestressed concrete beams are widely used throughout the United States. The standard sections were developed in the 1950s taking into account the casting and handling techniques and the concrete mix design technology of the 1950s. In 1982, in a survey of bridges throughout the United States by the FHWA, it was determined that the AASHTO shapes were less efficient and less cost-effective than the bulb-tee shapes. Cost comparisons of an actual project are presented that was originally designed using Type IV and Type IV modified beams but was redesigned and constructed using 54- and 63-in. bulb-tee beams. The replacement of AASHTO beams with bulb-tee beams was permitted on a one-for-one replacement basis; therefore, the cost analysis reflects the cost differences of the beams in exactly the same load-span conditions. Comparative designs are shown and cost analyses of the designs are summarized, indicating total estimated cost savings of the bulb-tee solution over the standard AASHTO beam design.

The information generated in the past few years concerning the efficiency of precast, prestressed bulb-tee bridge beams has produced a keen interest on the part of many producers and designers throughout the United States.

Recently, major projects have been constructed using bulb-tee bridge beams in applications formerly reserved for standard precast, prestressed AASHTO beams. Such projects, for the first time, permit a comparison of bridge costs between the standard AASHTO shapes and the bulb-tee beams. The Interstate spur I-565 from I-65 west to Huntsville, Alabama, is one such project. Other recent major projects that use bulb-tee beams are located in the states of Illinois, Missouri, and Oklahoma.

A review of the development of the precast, prestressed concrete bridge industry reveals that bulb-tee shapes have been in existence for some time and have been used rather routinely in isolated parts of the country. For example, the states of Washington and Colorado each have standard bulb-tee shapes (see Figure 1). There are several reasons for the lack of widespread use, until recently, of the bulb-tee beam shapes.

One of the primary reasons bulb-tees have not been used more extensively to date is that the AASHTO standard bridge beams are widely and successfully used throughout the United States.

Southern Prestressed, Inc., P.O. Box 2338, Pensacola, Fla. 32513. Current affiliation: Precast Technical Assistance Corporation, 1300 Dunmire St., Suite B, Pensacola, Fla. 32504.

Standardization of the AASHTO shapes, which occurred in the late 1950s, made possible the investment by the industry in forms, casting facilities, and equipment conducive to the production of AASHTO standard beams and has contributed to their successful use and the lack of interest in searching for a better solution.

At the time the AASHTO standards were developed, the standard sections of the precast, prestressed concrete industry had to be configured and designed in such a way that they could be produced economically and of high quality by using the equipment, casting procedures, and concrete mix design technology available.

Although it was certainly possible in the 1950s to design a more efficient beam configuration than the AASHTO standard beams, from a production standpoint it has not always been entirely feasible to manufacture the more efficient shapes.

In February 1982, FHWA published a final report entitled *Optimized Sections for Major Prestressed Concrete Bridge Girders* (*1*). In the conclusion of that report, the first two statements are as follows:

1. "In all states surveyed, except California, the most economical bridges for spans for approximately 70 to 130 feet are constructed with pretensioned bridge girders."
2. "When compared with other sections, AASHTO standard bridge girders are not the most structurally efficient or cost-effective for spans of 80 to 140 feet."

Item 9 of the report's conclusion states:

> For girders with 6-in.-thick webs, most cost-effective sections are modified bulb-tees. For spans of 80 to 120 feet, modified bulb-tees have 17 percent less in-place cost of girder and deck compared to AASHTO girders. . . . (*1*)

Rabbat and Russell (*2*) stated, "Modified bulb-tees are recommended for use as national standards." They also noted that there is a continuing search within the industry to develop new, more efficient products to compete in the construction market. Second, among the precast prestressed concrete bridge producers, there has been a need in many sections of the country for an efficient bridge beam that has span capabilities in excess of 100 ft.

The information that Rabbat and Russell presented indicated that the bulb-tee would address both of these points for the bridge producers of the precast, prestressed concrete industry.

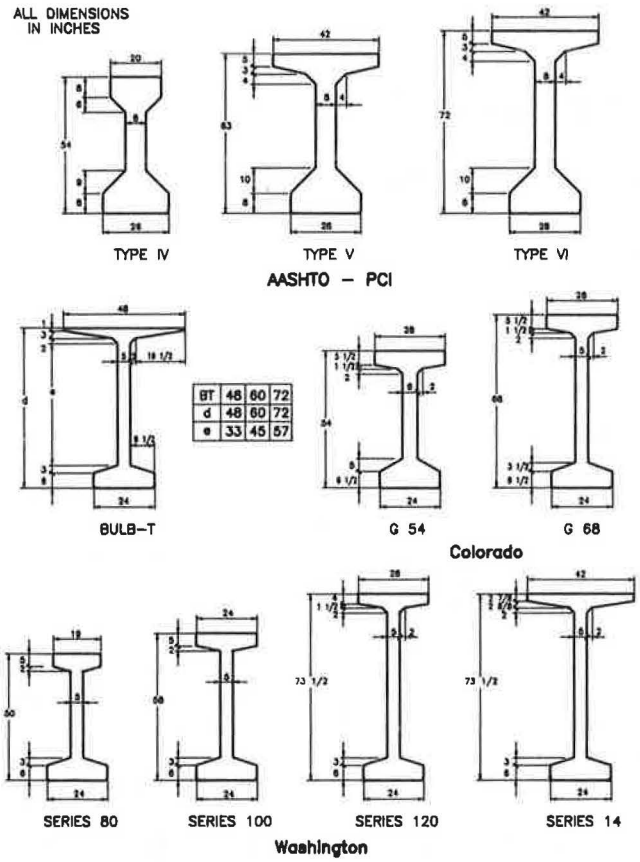

FIGURE 1 Existing girders analyzed (2).

PROMOTION ON THE LOCAL LEVEL

By late 1983, the Gulf South Prestressed Concrete Association (GSPCA) representing prestressed concrete producers in Alabama, Louisiana, and Mississippi retained a consulting engineer to research and propose to the Association a bulb-tee bridge girder that, first, would have span capabilities of up to 150 ft and second, would provide a more efficient beam than the AASHTO Type IV and Modified IV beams.

By late 1984, the GSPCA had in-hand design information and drawings of some detail for the bulb-tee to present to the state highway departments and departments of transportation in the Gulf South area (see Figure 2).

In January 1985, the GSPCA made a presentation of the information on a proposed new bulb-tee section to the Alabama Highway Department (see Figure 3). The bulb-tee design information was reviewed with considerable interest by a number of the department's engineers during the presentation.

In July 1986, the PCI Bridge Committee issued a three-sheet summary of their recommended bulb-tee sections that agreed with the GSPCA section configurations (see Figure 4).

Because of the interest of the Alabama Highway Department and the encouragement of the FHWA representatives in Montgomery, the first opportunity to use the bulb-tee sections on a major project in Alabama surfaced in mid-1988.

THE MADISON COUNTY PROJECT OVERVIEW

The construction of a major Interstate system spur (I-565) off I-65 to the city of Huntsville, some 23 mi to the east, was designed using standard AASHTO Type IV and Modified Type IV beams. An alternate approach permitting a redesign on a one-for-one replacement basis of the AASHTO girders with 54- and 63-in.-deep bulb-tee girders was included in the bidding instructions. The alternative, therefore, permitted the contractors and material suppliers the option of bidding either the standard AASHTO shapes, as shown on the bid drawings, or substituting bulb-tees as an alternative. There was also a stipulation in the bid package that the contractor was responsible for the redesign and preparation of the revised record drawings that replaced the drawings of the AASHTO girders. In addition to revised beam details showing bulb-tees instead of AASHTO shapes, the precast supplier was required to provide revised pier cap elevations for the contractor and for the state to supplement their record drawings. No allowance for foundation, pier, or deck redesign was considered

FIGURE 2 The Gulf South Prestressed Concrete Association.

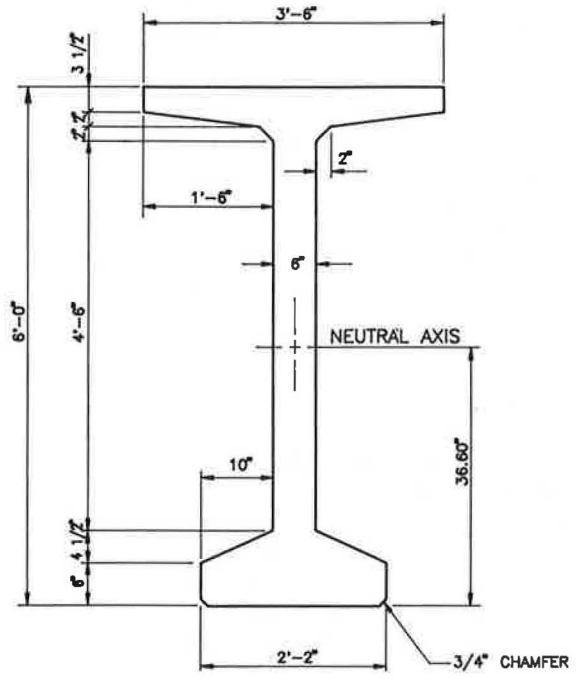

FIGURE 3 72-in. bulb-tee section.

by this alternative. Because the bulb-tee alternative provided a lighter superstructure, the piers and foundations were more than adequate. The wider top-flange configuration of the bulb-tee should also be considered in the design of the bridge deck. The project schedule, however, would not allow time for deck, foundation, and pier redesign.

The last 2.4 mi of the Madison County project contained 168,000 linear ft of bridge girders on both elevated main-line highway and interchange ramps, and was let in six separate contracts.

As designed, there were 88,034 linear ft of AASHTO Type IV girders, 73,119 linear ft of Modified AASHTO Type IV girders and 7,051 linear ft of AASHTO Type III girders.

In all, there were 1,729 beams totaling 168,203 linear ft (see Figure 5).

Because there was a complete design of the standard AASHTO beams and the complete design for comparable bulb-tee shapes had to be produced, the result was an excellent comparison of the two-beam configurations. As stated previously, however, only the girder design changed. The effect of any savings that could have been achieved by redesigning the deck or substructure is not part of the comparison.

THE REDESIGN COMPARISONS

The 54-in. bulb-tee was substituted for the standard AASHTO Type IV beam.

Figure 6 shows the side-by-side comparison of the two beams. Note that there is an approximate 19¾ percent weight reduction with a corresponding 14 percent increase in the section modulus with respect to the top of the beam. The combination of these two factors has a significant effect on the prestressing required for a beam of any given span.

In order to achieve spans of up to about 120 ft, the Alabama Highway Department has used a Modified Type IV beam that is a standard AASHTO Type IV beam with the top flange

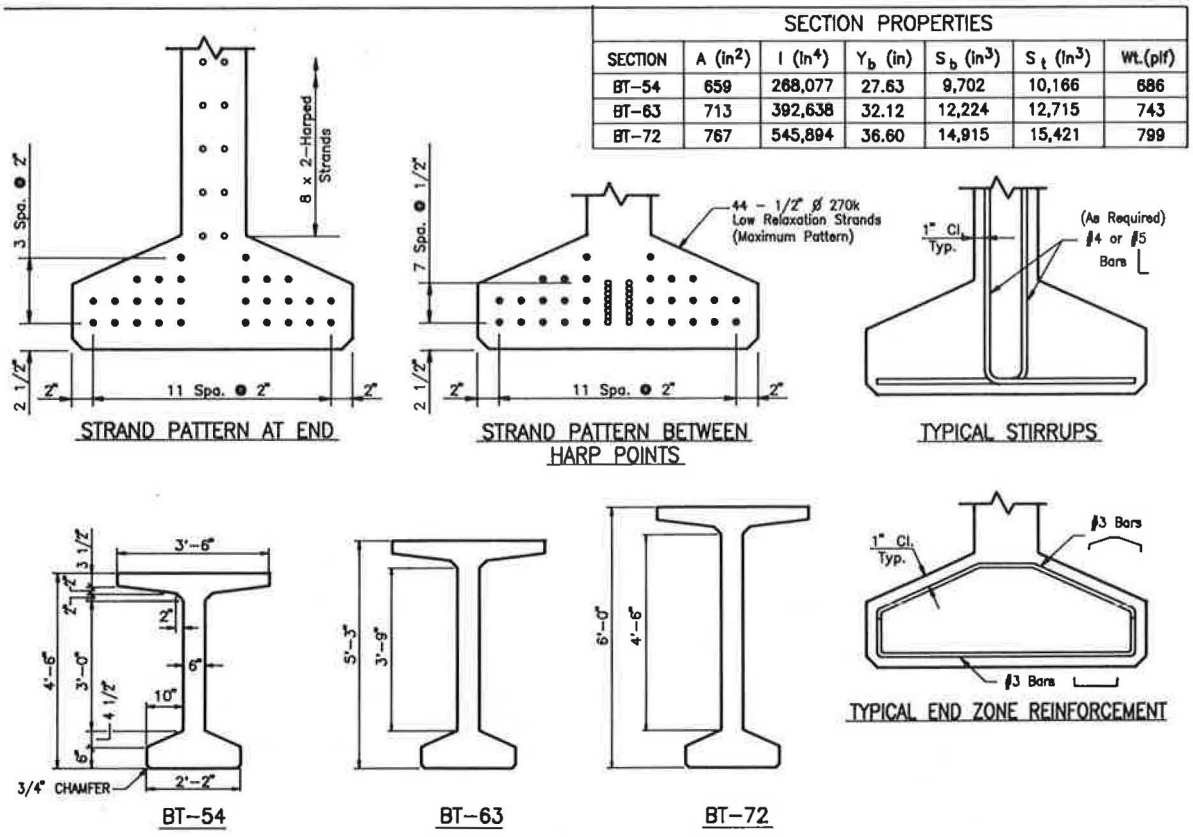

FIGURE 4 Bulb-T sections recommended by PCI Bridge Committee.

BRIDGE BEAM QUANTITIES

AASHTO TYPE III	AASHTO TYPE IV	AASHTO TYPE IV (MODIFIED)	JOB TOTALS
7,050 L.F.	88,034 L.F.	73,119 L.F.	168,203 L.F.
96 PCS.	954 PCS.	679 PCS.	1,729 PCS.
1,015 C.Y.	17,862 C.Y.	17,095 C.Y.	35,972 C.Y.

FIGURE 5 Madison County, Alabama I-565, summary of six projects.

extended 6 in. resulting in a beam of 60 in. in depth. Figure 7 shows the comparison between the modified Type IV and the 63-in. bulb-tee. The weight reduction in this case is 21½ percent and the section modulus with respect to the top of the beam increase is about 6½ percent.

The most typical length of the 54-in. bulb-tee was estimated to be between 95 and 100 ft on the Madison County project. In a 95-ft 54-in. bulb-tee, there is a concrete savings of 3.2 yd/beam over the Type IV beam and a corresponding 12,350-lb weight reduction.

For the 63-in. bulb-tee, the most typical beam length was between 105 and 110 ft. For a 107-ft 6-in. beam, there is a savings of 5.4 yd of concrete when compared with the Modified Type IV beam, and a corresponding 21,940-lb weight reduction/beam.

Strand reductions in the bulb-tees were significant, in every case, when compared with the standard AASHTO shapes they replaced.

The type of strand was also changed from stress-relieved to low-relaxation strand in the redesign, resulting in additional savings in strand. In cases in which the ultimate strength of the girders controlled the design, little benefit was realized from the use of low-relaxation strand. For stress-controlled designs, savings are estimated to average about 5 to 7 percent strand reductions. The increased section modulus of the bulb-tee shapes and the reduced weight are the major factors affecting the required number of strands and whether or not draping of strands is required.

The reduction in the number of strands required in the 54-in. bulb-tee over the Type IV beam ranged up to replacement of 44½-in.-diam 270-kip strands in the Type IV beam with 32½-in.-diam special low-relaxation strands in the bulb-tee.

Figure 8 shows one of the more dramatic comparisons. The 98-ft span AASHTO Type IV beams had 40½-in.-diam 270K stress-relieved strands (area = 6.12 in.^{2}) with eight of the strands draped or harped. The 54-in. bulb-tee had 28½-in. special low-relaxation strands (area = 4.676 in.^{2}) a reduction in area of prestressing steel of 1.44 in.^{2} or 23½ percent. It is significant that the draped-strand condition was eliminated, thus resulting in a reduction in labor and production time.

An average decrease in stranding of nine strands (0.943 in.^{2}) for 54-in. bulb-tees or a 14 percent reduction in strand area was estimated.

Figure 9 shows a Modified Type IV with 46½-in.-diam 270-kip stress-relieved strand (area = 7.038 in.^{2}), 10 of which are draped. The 63-in. bulb-tee beam that replaced it has 33½-in.-diam special low-relaxation strand (area = 5.511 in.^{2}). The difference is 1.527 in.^{2} of prestressing steel or a savings of 21.7 percent; also the drape was not required in the bulb-tee beam, which again results in a measurable reduction in production labor.

The average strand reduction is estimated to be about 11 strands in the 63-in. bulb-tee, 1.193 in.^{2}/beam, or about 17

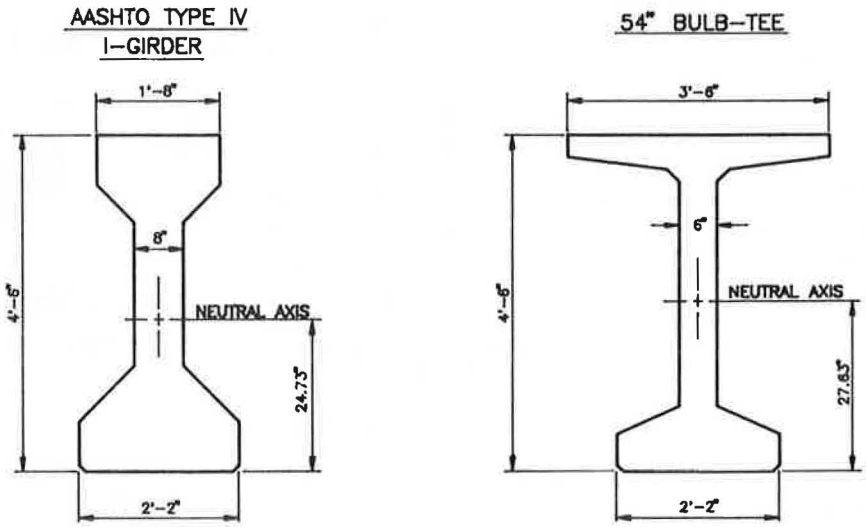

SECTION PROPERTIES

TYPE	AREA (in^2)	WT. (lb/ft)	I_x (in^4)	Y_b (in)	S_b (in^3)	S_t (in^3)
TYPE IV	789	822	260,730	24.73	10,543	8,908
54" BT	659	686	268,045	27.63	9,701	10,165

APPROXIMATE SPAN RANGE OF 70–100 FEET – HS20 LOADING

FIGURE 6 Bridge girder comparison (Type IV versus 54-in. bulb-T).

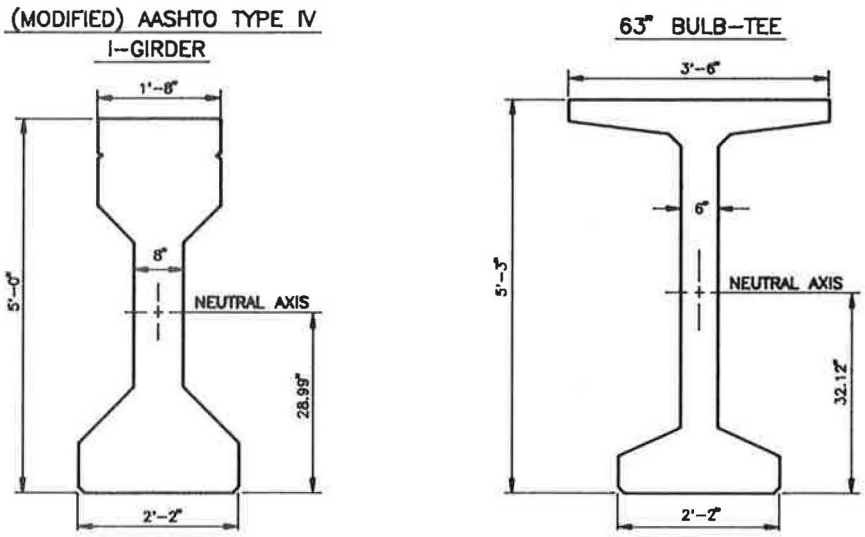

SECTION PROPERTIES

TYPE	AREA (in^2)	WT. (lb/ft)	I_x (in^4)	Y_b (in)	S_b (in^3)	S_t (in^3)
TYPE IV MOD	909	947	369,500	28.99	12,746	11,916
63" BT	713	743	392,509	32.12	12,220	12,711

APPROXIMATE SPAN RANGE OF 100–120 FEET – HS20 LOADING

FIGURE 7 Bridge girder comparison (modified Type IV versus 63-in. bulb-T).

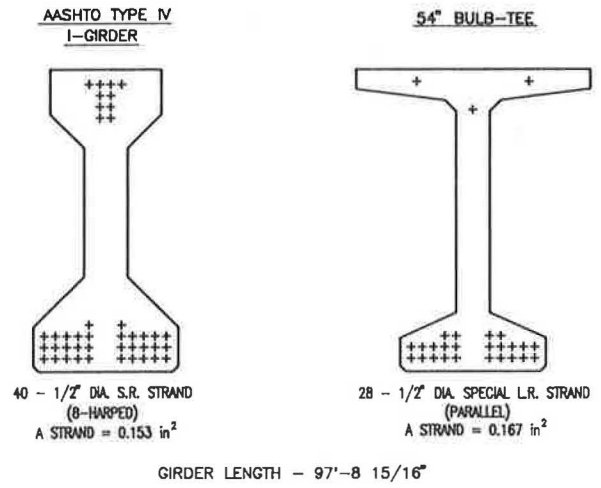

FIGURE 8 Typical strand patterns (40½-in.-diam SR and 28½-in.-diam special LR).

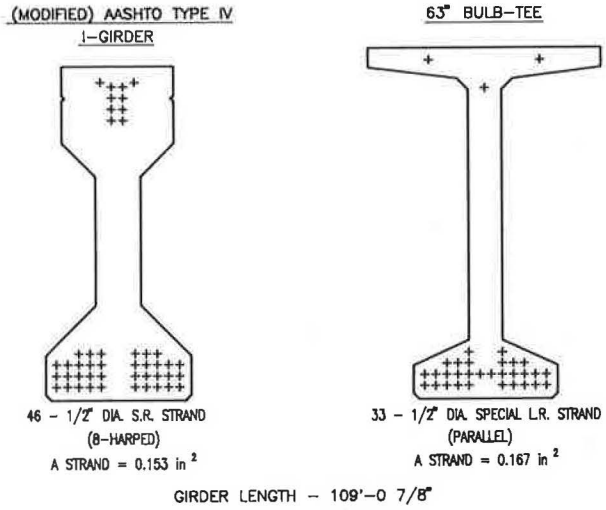

FIGURE 9 Typical strand patterns (46½-in.-diam SR and 33½-in.-diam special LR).

percent less prestressing steel. Again, the draped strands were eliminated in many of the girder designs. In designs in which draped strands were eliminated, strands were sheathed at the girder ends to control end stresses of the girders. No adverse effects were encountered when the draped-strand designs were replaced with parallel stranding; however, strands were used in or near the upper flange as shown in Figures 8 and 9.

Typically, there was little difference in the amount of stirrups and other reinforcement between the AASHTO beams and the bulb-tees.

The materials reductions on the project were quite significant and bear out the projections made by Rabbat and Russell (*2*). The materials savings achieved by the use of bulb-tees on the Madison County, Alabama, project are summarized as follows:

- *54-in. Bulb-Tees versus AASHTO Type IV*

Strand: 3.096 lb/ft of beam × 88,034 ft = 272,553 lb
Concrete: 0.0335 yd^3/ft × 88,034 ft = 2,940 yd^3

- *63-in. Bulb-Tees versus Modified Type IV*

Strand: 4.136 lb/ft of beam × 73,119 ft = 302,420 lb
Concrete: 0.0504 yd^3/ft × 73,119 ft = 3,685 yd^3

The total savings of prestressing strand for the entire project was 574,973 lb and the concrete savings was 6,625 yd^3.

The estimated cost differences as summarized in the following paragraphs are based on the average reduction in stranding of nine strands in the 54-in. bulb-tees and an 11-strand reduction in the 63-in. bulb-tees when compared with their AASHTO beam counterpart. The material cost differences are well defined on the basis of reductions of concrete and prestressing steel. The labor cost reductions are based on conservative estimates of the labor required to place those materials in a typical casting operation.

A summary of estimated cost differences follows.

	AASHTO Type IV	*54-in. Bulb-Tee*
Strand:	42½-in.-diam 270-kip SR	33½-in. special LR
Cost/foot of beam	$8.33	$6.26
Estimated labor for stranding	0.91	0.72
Material and labor	$9.24	$6.98
Concrete:	0.2029 yd³/ft	0.1695 yd³/ft
Cost in place/ft @ $76/yd³	$15.42	$12.88
Total cost/ft (strand and concrete)	$24.66	$19.86
Cost difference:	$4.80/ft of beam	
	Modified AASHTO Type IV	*63-in. Bulb-Tee*
Strand:	44½-in.-diam 270-kip SR	33½-in.-diam special LR
Cost/ft of beam	$8.72	$6.84
Estimated labor for stranding	0.95	0.72
	$9.67	$7.56
Concrete:	0.2338 yd³/ft	0.1834 yd³/ft
Cost in place/ft	$17.77	$13.95
Total cost/ft.: (strand and concrete)	$27.44	$21.51
Cost difference:	$5.93/ft of beam	

On the basis of these estimated cost differences, the total cost savings achieved by using the bulb-tee alternate on the Madison County, Alabama, project are as follows:

- 54-in. bulb-tees:

$4.80/ft. of beam × 88,034 Linear ft = $422,563.

- 63-in. bulb-tees:

$5.93 per foot of beam × 73,119 Linear ft = $433,596.

Thus the project total is $856,159.

Because of variations in material and labor costs and production methods, the actual savings realized from the use of the PCI bulb-tee bridge beams vary from location to location and from plant to plant. However, the savings are measurable and significant and the present day prestress concrete producer is capable of producing the bulb-tee shape with little or no more difficulty than he produces the standard AASHTO shapes.

CONCLUSIONS

The increased efficiency and cost savings predicted by the referenced study are verified by the experience with the bulb-tee section.

It was possible for engineers to design a more efficient shape in the 1950s when the standard AASHTO shapes were established but production methods and equipment and concrete mix design technology of the day had to be taken into account.

For today's technology, the bulb-tee is a viable product for the average precast, prestressed concrete bridge producer. For producers to make the switch from the AASHTO standard shapes to the bulb-tee may require great effort. The initial cost of new forms is not easy to overcome on small jobs. A common national standard should be adopted by the individual states. Where precast, prestressed concrete producers cross state lines, the cost savings are lost on form cost and relearning of details when each state has its own version of the bulb-tee.

REFERENCES

1. *Optimized Sections for Major Prestressed Concrete Bridge Girders*. Final Report FHWA/RD-82/005. FHWA, U.S. Department of Transportation, Feb. 1982, pp. 76–78.
2. B. G. Rabbat and H. G. Russell. Optimized Sections for Precast Prestressed Bridge Girders. *PCI Journal*, Vol. 27, No. 4, July-Aug. 1982, pp. 88–104.

Publication of this paper sponsored by Committee on Concrete Bridges.

Analytical Investigation of Slab Bridges with Integral Wall Abutments

H. J. DAGHER, M. ELGAALY, AND J. KANKAM

The design of a single-span bridge with integral wall abutments is simple when the bridge has no skew. For skewed bridges, the design is complicated by higher shears and moments that develop near the obtuse angle. The finite element method can be used to compute these moments and shears; however, it is time consuming for everyday design unless specialized pre- and postprocessors are available. A linear elastic finite element analysis was used to investigate the effects of dead loads, AASHTO live loads, and earth pressures on 20 different bridges with spans ranging from 15 to 60 ft and skew angles varying from 0 to 60 degrees. The results of the study have been used to produce charts that are adequate for design purposes. These charts relate the moments, shears, and deflections in a skew bridge to those in a 1-ft-wide plane frame taken along the longitudinal center line of the skew bridge. Work to refine and verify the results obtained to date through laboratory model testing and nonlinear finite element analysis is ongoing.

The slab bridges considered in this study are rigidly connected to supporting wall abutments. A recent nationwide survey conducted by the authors indicated that 22 states had a total of 11,500 bridges of this type, both skew and straight, either already existing or projected for the future (*1*). Two major reasons for building such bridges are the reduction of positive moments and the elimination of bridge deck expansion joints, thus reducing construction and maintenance costs. Conventional bridge bearing devices often become ineffective and are susceptible to deterioration from roadway runoff through open or leaking deck joints.

Many investigations have been conducted on the behavior of skew slabs under load. However, most of this work relates to skew slabs that are supported on columns, beams, or on nonintegral supports.

Bakht (*2*) proposed that skew slab-on-girder bridges having $(s \tan(\alpha)/L) < 0.05$ could be analyzed as equivalent right bridges, where s, L, and α are the girder spacing, bridge span, and skew angle, respectively. Cheung et al. (*3*) presented a general finite element program that could be used to evaluate bending moments and support reactions in complex modern bridges of any shape. Clark (*4*) suggested a method of preventing punching shear when a concentrated load is near a free edge of a reinforced-concrete slab.

Cope et al. (*5–13*) outlined a nonlinear method for analyzing slab bridges; the method was considered to be expensive and was therefore recommended only for assessment of more approximate design methods or for analysis of complicated one-off structures. They also observed from laboratory tests on five 1:5-scale, reinforced-concrete, column-supported skew slabs that shear failure was always initiated in the free-edge zone and that increasing skew angle considerably decreased the shear capacity of a slab. The presence of vertical bonded reinforcement at the free edge produced considerable enhancement to the overall shear capacity of a slab. Also, slabs with the main reinforcement parallel to the free edges were found to possess better load distribution properties than those with the main reinforcement perpendicular to supports and were therefore less likely to undergo punching shear failure when subjected to heavy concentrated loading. They also found that predicted shear forces from thick- and thin-plate analyses of slabs were broadly in agreement except in the edge zones (with widths of about two slab thicknesses for a 45-degree skew slab) were thick-plate theories indicated much higher shear stresses. They recommended that when the design of bridge slabs is based on the results of thin-plate theory, reactions provide a better guide to the distribution of shear forces in obtuse corner regions than do values of shear forces predicted from derivatives of moments.

Mahmoudzadeh et al. (*14*) conducted parametric studies of 54 reinforced-concrete, multispan, slab bridges with a finite element program called GENDEK-5 to assess the effects of skew on support reactions and internal bending moments. They observed that

1. Maximum positive and negative slab moments were governed by AASHTO alternate loading and HS20 truck loads, respectively, except that the alternate loading governed both moments at 60-degree skews;
2. Longitudinal bending moments were significantly reduced with increasing skew angle;
3. The alternate loading was the controlling factor for abutment total reactions;

Rusch and Hergenroder (*15*) published 174 contour charts of influence surfaces for bending moments and torsional moments in skew slabs. The charts were based on tests on models and cover skew angles of 30, 45, and 60 degrees.

Greimann et al. (*16*) summarized the findings of a survey of the highway departments of all 50 states to obtain information on the design and performance of skewed bridges with integral abutments. They concluded that there was a lack of theoretical and experimental research in this area, with the result that most states designed integral abutments on skewed bridges on the basis of empirical experience without adequate theoretical analysis.

Considerable research work has been conducted on the finite element analysis of reinforced concrete (*17,18*). In ad-

Civil Engineering Department, Boardman Hall, University of Maine, Orono, Maine 04469.

dition, many methods are available for the design and analysis of reinforced-concrete slabs. These methods include elastic theory, limit analysis theory, and modifications of the elastic and limit analysis theories as in the American Concrete Institute code. The design procedure is based on work by Wood (*19*) and Hillerborg (*20*). Considerable information on the behavior of reinforced-concrete slabs may be found in textbooks solely dedicated to RC slabs, such as those by Wood (*21*), Park and Gamble (*22*), and Cope and Clark (*23*).

LINEAR AND NONLINEAR ANALYSIS

Typically, design moments and shears in reinforced-concrete structures are obtained by conducting a linear elastic analysis of the structure using factored loads. The resulting moments and shears are then compared with the nominal ultimate capacity of a member.

Although this practice does not predict the actual moment and shear distributions at the limit state, it leads to conservative designs. This effect is because reinforced-concrete structures normally have enough ductility so that some redistribution of moments and shears is possible if the ultimate capacity is reached at one point. This has been recognized by the American Concrete Institute's building code, which has provisions for redistribution of moments at the supports of continuous flexural members.

The ability of reinforced concrete to redistribute moments is used in yield line analysis of slabs, which is commonly used for slab design in Scandinavian countries. When a portion of a slab reaches its ultimate capacity, the reinforcement will yield, and this portion of the slab will act as a plastic hinge that will hold a constant moment. When additional load is applied on the slab, the plastic hinge rotates and additional moment is transferred to adjacent sections that have not yet yielded.

The results presented are based on a linear elastic analysis using a University of Maine mainframe version of the SAP finite element program (*24*). The recommendations given are therefore conservative, and are being refined using nonlinear analysis and laboratory testing.

OBJECTIVE OF THIS STUDY

Integral skewed slab bridges are characterized by high moments and shears in the vicinity of the obtuse corners. This effect is shown in Figure 1 by the distribution of shear in the slab near the wall for a bridge with a 70-ft span and a 20-degree skew angle, subjected to self-weight. (The shear forces near the obtuse corners do not vanish because they are calculated using the membrane stresses at the center of the corner wall element adjacent to the slab.) Cracking near the obtuse corner of an integral skew slab bridge with these dimensions has been observed recently in Maine (*1*). Figure 2 shows the magnitudes of design moments at the obtuse and acute corners in an 84-ft-span bridge with a skew angle of 45 degrees. The irregularity of the curves in Figure 2 results from the definition of the design moments, which are different from the bending moments obtained directly from a finite element analysis. As described later, the design moments are obtained by combining the flexural and torsional moments from a finite element analysis.

The magnitude of flexural and shearing stresses in these bridges can be obtained using finite element analysis. However, the finite element analysis is time consuming for everyday design. There is therefore a need for simplified methods of determining design moments and shears. The objective of this study was to produce such design aids.

FINITE ELEMENT MODELING

The finite element models of the structure are composed of the following elements, available in the SAP Program (*24*):

1. Thin-plate elements with four nodes per element and five degrees of freedom per node were used in the walls and

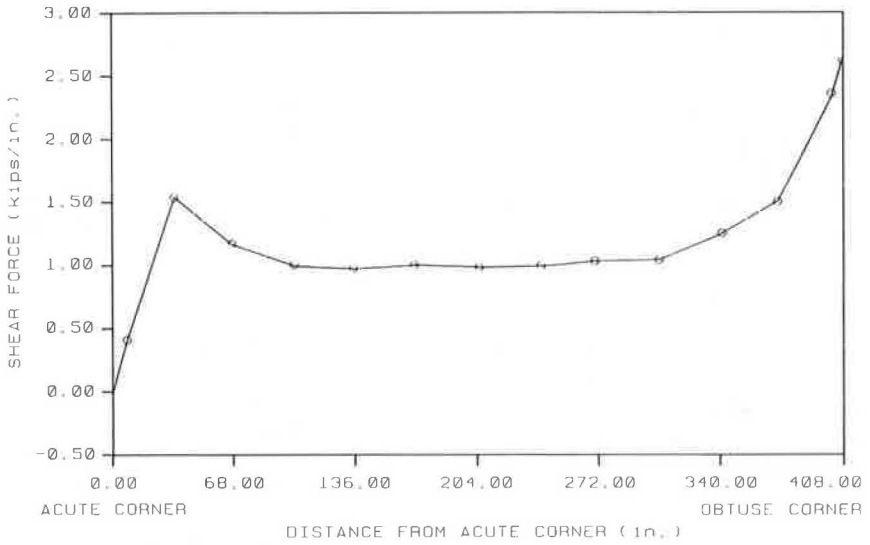

FIGURE 1 Typical shear force distribution in a skew slab at a support caused by self-weight.

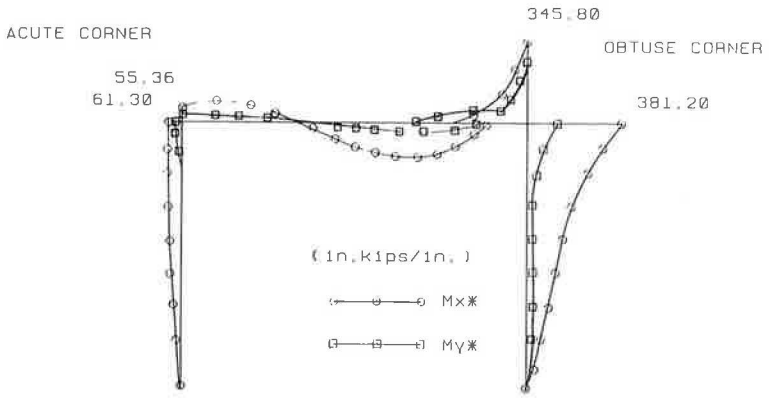

FIGURE 2 Typical distribution of design moments near the free edge of a skewed-slab bridge caused by self-weight.

skew slab. They were restrained against in-plane rotation (drilling) when the elements intersecting at the node were in the same plane.

2. Boundary elements were used to restrain the drilling degrees of freedom in plate elements when these were not in the direction of a global coordinate axis. Boundary elements were also used to obtain the reactive moments and forces at the base of the walls.

At the strength limit state, the moment of inertia of the walls was taken to be that of the gross cross section; the value for the slab was taken as half that of the gross cross section of the slab. This procedure reflects common design practice and is based on the assumption that flexural cracking of the slab requires the use of the cracked moment of inertia, whereas the walls are subjected to compressive dead and live loads that will reduce cracking. These assumptions are in line with the ACI318-89 (*25*), Section R.8.6.1.

An example of a finite element mesh used for the analysis is shown in Figure 3. A graded, finer mesh was used near the edges of the slab to better depict the high rate of change of moments and shears at these locations.

PREPROCESSOR

A special preprocessor was developed for rigid-frame skew slab bridgers that were to be analyzed with the SAP Finite Element Program (*1*). With the preprocessor, the user interactively specifies the overall dimensions, material properties, and loading conditions of the bridge. The preprocessor generates the numbers and coordinates of the nodes of the structure, the numbers and connectivities of the plate elements, the properties of the boundary elements, and other necessary data in the format required by SAP.

The preprocessor also generates AASHTO loadings automatically. For the AASHTO truck loadings for example, HS25 trucks are automatically moved across the bridge and the resulting nodal loads are automatically calculated.

CONVERGENCE STUDIES

Convergence studies were carried out using three models with 325, 665, and 1,000 plate elements.

For the structure shown in Figure 4, maximum vertical displacements caused by the self-weight of the structure (at point *P*), as well as maximum design moments (at point *E*), are plotted in Figure 5 for the three different models. Values for the models with 325 and 665 plate elements are expressed as percentages of corresponding values for the model with 1,000 elements.

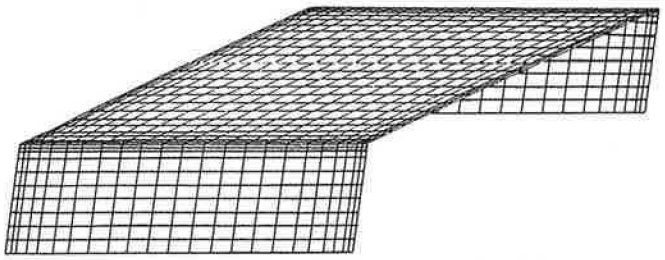

FIGURE 3 Typical finite element mesh of 1,000 elements used for rigid-frame skewed-slab bridge.

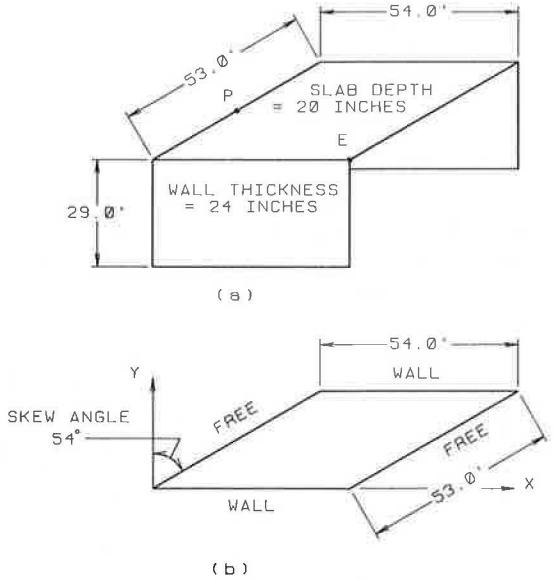

FIGURE 4 Structure used in convergence studies: (a) the whole frame, and (b) top view of slab.

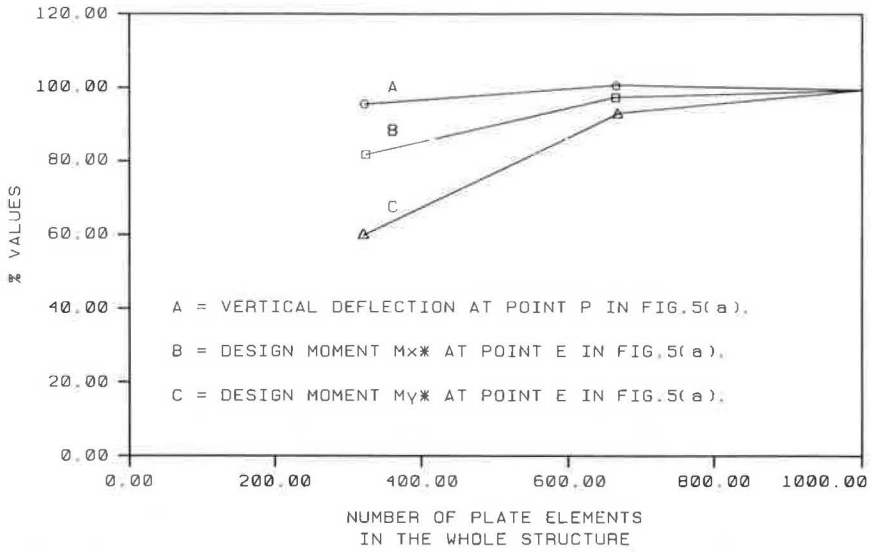

FIGURE 5 Convergence studies.

Increasing the number of elements from 325 to 665 results in an improvement of 16 percent (for Mx*) and 36 percent (for My*) in the moments and 5 percent in the displacements. An improvement of less than 10 percent on the moments, and less than 4 percent in the displacements is achieved by refining the model from 665 to 1,000 elements. The 1,000-element model was adopted for use in the parametric studies.

POSTPROCESSOR

A postprocessor was developed to convert the results of the finite element analysis into design moments, to plot moment envelopes for any longitudinal or transverse section, to plot shear envelope for the slab at the supports, and to record the maximum vertical displacement in the slab.

PARAMETRIC STUDY

In the parametric study, 20 different bridges were analyzed for 15 loading conditions each. The finite element analyses were significantly expedited by using the specialized pre- and postprocessors. In fact, routine analysis and design of skew slab bridges can be efficiently carried out on a personal computer should the appropriate finite element software and the specialized pre- and postprocessors be available. If this is the case, the design method proposed may serve for preliminary design.

Using the preprocessor, 2 min were required to prepare the SAP data file for each analysis. The actual time taken by the SAP program for each 1,000-element analysis was fewer than 200 sec on the University of Maine's IBM 3090 Model 200I Computer. However, because of time sharing with other jobs, the total time taken to get the results of the analysis was about 9 min.

For each analysis, a number of equilibrium checks were conducted, such as comparing the reactive forces at the base of the walls with the sum of the applied loads. The results of the parametric studies have been embodied in the design curves that are described elsewhere.

Geometries of Bridges

Based partly on AASHTO requirements for minimum lane width (*26*), ACI 343R-88 requirements for minimum depth of bridge slabs (*27*), and results of the nationwide survey, the following ranges of parameters were used in the parametric studies, which were expedited with the pre- and postprocessors:

- Skew angles 0, 15, 30, 45, and 60 degrees;
- Width at supports 30, 31, 35, 43, and 60 ft;
- Normal span 15, 30, 45, and 60 ft;
- Slab thickness 15, 18, 26, and 36 in.;
- Wall thickness 18, 21, 30, and 40 in.; and
- Wall height 20 ft.

Each value of the width of support listed previously corresponds to one skew angle only, so that a two-lane bridge with a 30-ft transverse width is always obtained. The edge beam had a width of 22 in. and a height of 36 in. above the slab. However, it was conservatively judged to be nonstructural, and its weight was applied as a line load. This decision was based on the fact that, in practice, the edge beam is often cast only after the slab has been cast and cured for some time and the supporting formwork has been removed.

Loading Conditions

The loading conditions used for the parametric studies were composed of the following (Figure 6):

1. Self-weight including a 825-lb/ft edge beam;
2. AASHTO HS25 lane loads;
3. AASHTO HS25 truck loads;

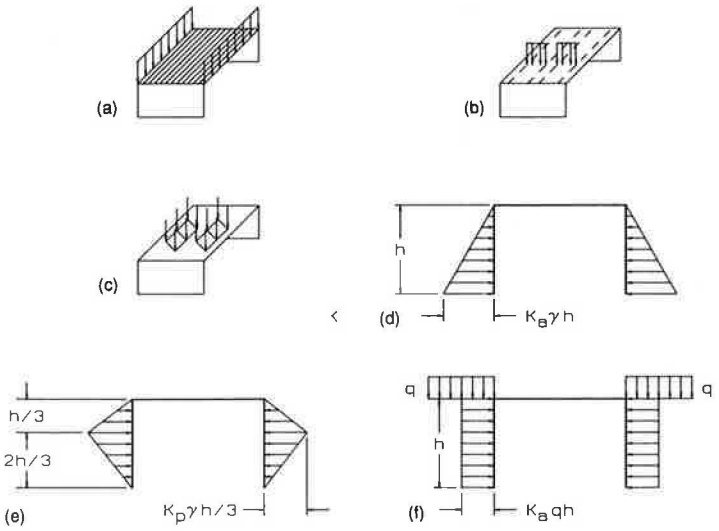

FIGURE 6 Loading conditions used in parametric studies: (a) self-weight including 825-lb/ft edge beam, (b) AASHTO HS25 lane loads for typical two lanes, (c) AASHTO HS25 truck loads for typical two lanes, (d) active earth pressure, (e) passive earth pressure, and (f) surcharge.

4. A triangular earth pressure distribution with a generic maximum value of 100 lb/ft² at the base of the walls and a value of zero at the top of the walls;

5. A passive earth pressure with a generic value of 100 lb/ft² at a depth of one-third the wall height, which linearly varies to zero at the top and bottom of the walls. This distribution is based on results of field measurements reported by Elgaaly et al. (*28*);

6. Uniform earth pressure with a generic value of 100 lb/ft² to represent the effect of surcharge; and

7. A uniform load of 100 lb/ft² on the slab (not shown in Figure 6).

For the AASHTO truck loads, one HS25 truck was used per design lane. The trucks were placed on the bridge at 10 successive locations, starting from one wall and extending to the other. For the lane loadings, the line loads were placed at the center of the slab and then near the wall. Results obtained from these analyses were used to plot an envelope of maximum live load moments for the bridge. For the range of spans considered, the AASHTO truck load condition controls the live load stresses.

For each combination of bridge and type of load, a corresponding two-dimensional frame analysis was carried out, the frame chosen being a 1-ft-wide strip taken along the longitudinal center line of the bridge. Live load analysis for the frame was based on Paragraph 3.24.3.2 of the AASHTO Standard Specifications (*26*).

Results of the parametric studies for 20 different bridges and their corresponding frames were used to produce the design curves whose description follows.

DESIGN CURVES

The design curves allow conversion of the results from a plane frame analysis to values that apply for a skew slab bridge with integral slab abutments. The frame analysis must be conducted following the guidelines in AASHTO, Paragraph 3.24.3.2 (*26*), using a 1-ft-wide longitudinal strip taken along the skew span of the bridge. The design curves allow the calculation of moments, shears, and deflections at selected points in the skew slab bridge (see Figure 7).

Range of Design Curves

The design curves were produced for skew angles ranging from 0 to 60 degrees, and for aspect ratios varying from 0.5 to 2.0. The skew angle is defined as the amount by which the angle at the acute corner of the plan view of the slab is less than 90 degrees. The aspect ratio is defined as the ratio

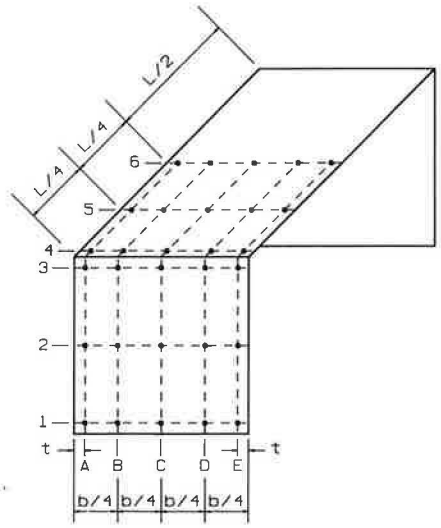

FIGURE 7 Reference points for design curves.

L/W, where L is the skew span of the bridge and W is the width of the slab along a support. The wall thicknesses used in the studies were always 3 or 4 in. greater than the corresponding slab thicknesses.

Initially, the parametric studies included analyses with the base of the wall both fixed and free. Figure 8 shows typical details for pinned and fixed wall bases. Results indicated that the restraint condition at the base of the wall does not, for most practical purposes, influence the distribution of stresses in the slab. The two-dimensional rigid frame analysis, which still needs to be conducted before the proposed charts are used, can take into account any restraint condition at the base of the wall. The design charts will simply distribute the moments thus obtained across the width of the bridge.

Assumed Steel Orientation in Design Curves

The design curves assume that the steel reinforcement will be placed parallel and perpendicular to the center line of the bridge (Figure 9). The 90-degree orientation between the longitudinal and transverse reinforcements results in the least amount of steel required. However, it will result in slightly higher fabrication costs because the transverse bars will not all be of the same length.

Design Moments for Flexure and Torsion

Figure 10 shows the directions of the coordinate axes and notation for moments. The bending moments Mx and My and the torsional moments Mxy produced by the finite element analysis are converted into the design moments Mx* and My* according to the following equations (*19*):

$$Mx^* = Mx \pm |Mxy|$$
$$My^* = My \pm |Mxy|$$

where

Mx* = design moment for reinforcement in the slab parallel to the skew span (Figure 9) and for vertical reinforcement in the wall, and

My* = design moment for reinforcement in the slab perpendicular to the skew span (Figure 9) and for horizontal reinforcement in the wall.

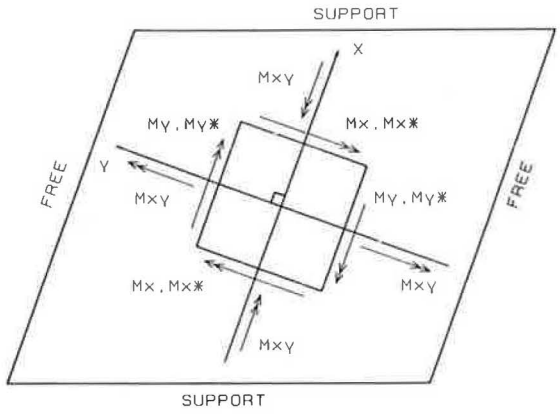

FIGURE 10 Plan view of the slab showing directions of coordinate axes and notation for positive moments.

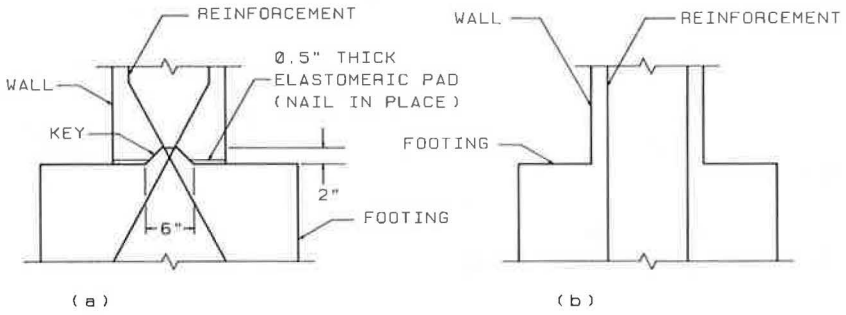

FIGURE 8 Typical details at the bottom of the abutment wall: (a) pinned base, and (b) fixed base.

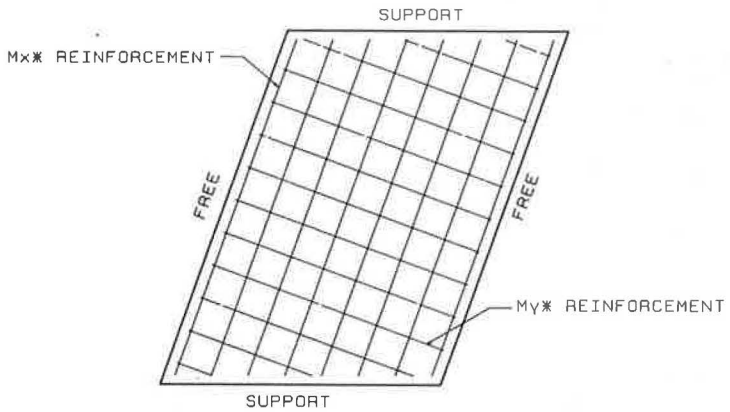

FIGURE 9 Design moments on plan view of slab.

The term "design moments" refers to equivalent bending moments for which reinforcement can be specified to account for both the flexural and torsional moments obtained from the finite element analysis. This concept, which is widely used in Great Britain and Europe, was originally developed by Hillerborg (*20*) and further extended by Wood (*19*); it is being further investigated.

Because of the assumptions in thin-plate theory that form the basis for the finite element analysis and the inaccuracies related to mesh size, certain limitations apply to the interpretation of the twisting moments, which are high and which do not go to zero at the free edges as they are supposed to do according to Kirchhoff boundary conditions. The design moments Mx* and My*, which include these twisting moments, consequently become artificially high near the free edges of the slab, and have therefore been discarded in this region.

In the design curves, moments near the obtuse or acute corners have been taken at a distance t from the free edge of the slab (t = slab thickness). For example, in Figure 11, the ratio Mx*/Mxp is given at point *E*4, which is at distance t from the free edge of the slab. For zero skew and an aspect ratio of 0.5, Figure 11 yields Mx*/Mxp = 1.8 for self-weight plus edge beam weight. If the edge beam did not exist, this ratio would have been equal to one for zero skew.

The design curves allow the calculation of design moments at 30 selected locations covering one-half of the bridge, as shown in Figure 7. For example, moments may be computed at point *A*2, located at the intersection of Longitudinal Line *A* and Transverse Line 2 shown in Figure 7. Line *A* is a longitudinal line parallel to the center line of the bridge and located at a distance equal to the slab thickness t from the free edge. For self-weight and AASHTO live load, Line 2 goes through the midheight of the wall; for each pressure, it goes through the point of maximum positive moment in the wall.

For a given point and type of load, the design curves yield the ratios Mx*/Mxp and My*/Mxp of the design moments in the slab to those in the corresponding plane frame for different aspect ratios and skew angles, where Mxp is the bending moment at the corresponding point in the two-dimensional frame. For points *A*2, *B*2, *C*2, *D*2, and *E*2, for instance, the corresponding point in the two-dimensional frame taken along the longitudinal center line would be *C*2; whereas for points *A*4, *B*4, *C*4, *D*4 and *E*4, the corresponding point would be *C*4.

Figures 11 and 12 show typical moment design curves for point *E*4 under self-weight plus edge beam. A complete set of design curves was provided by Dagher et al. (*1*).

Design for Shear

Figures 13 and 14 show typical shear design curves for point *E*4 under self-weight plus edge beam weight and for point *D*4 under AASHTO live loads, respectively. The curves yield the ratios Vs/Vp for different aspect ratios and skew angles, where Vs is the shearing force (force per unit width) at the reference point in the skew slab; and Vp is the shearing force at the corresponding point in the two-dimensional frame.

A typical curve of Vs/Vp is shown in Figure 15. As stated earlier, the full design guide (*1*) does not yield moment and shear ratios within distance t from the free edge, because of concerns about the accuracy of the model in these regions. For self-weight plus edge beam, Figure 14 shows design curves for the maximum values of Vs/Vp that occur between point *E*4 and the free edge near the obtuse corner. Whether these should be used in design rather than the values at point *E*4 is a matter that requires further research.

Maximum Vertical Displacement

Figures 16 and 17 show typical displacement design curves. The curves give the ratios Ds/Dp for different aspect ratios and skew angles, where Ds is the maximum vertical displacement in the slab and Dp is the maximum vertical displacement in the corresponding two-dimensional frame.

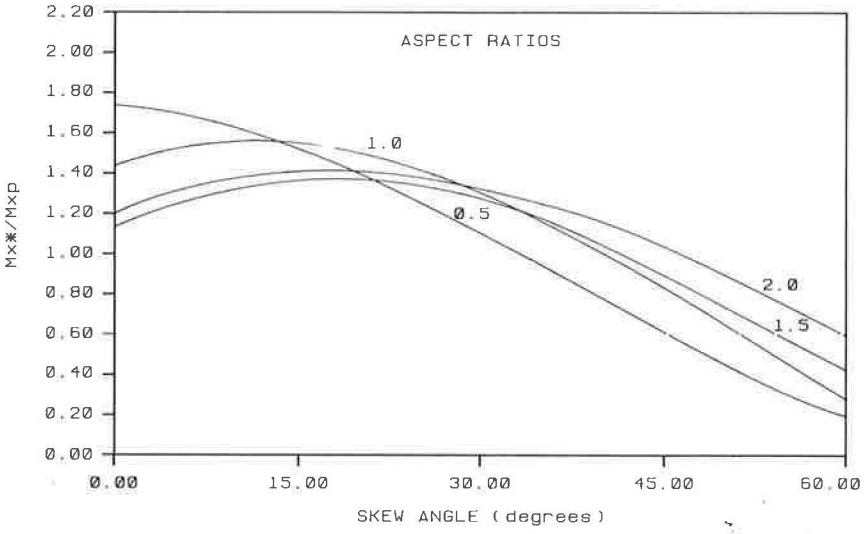

FIGURE 11 Pinned-base bridges under self-weight plus edge beam weight—curves for Mx*/Mxp at Point *E*4.

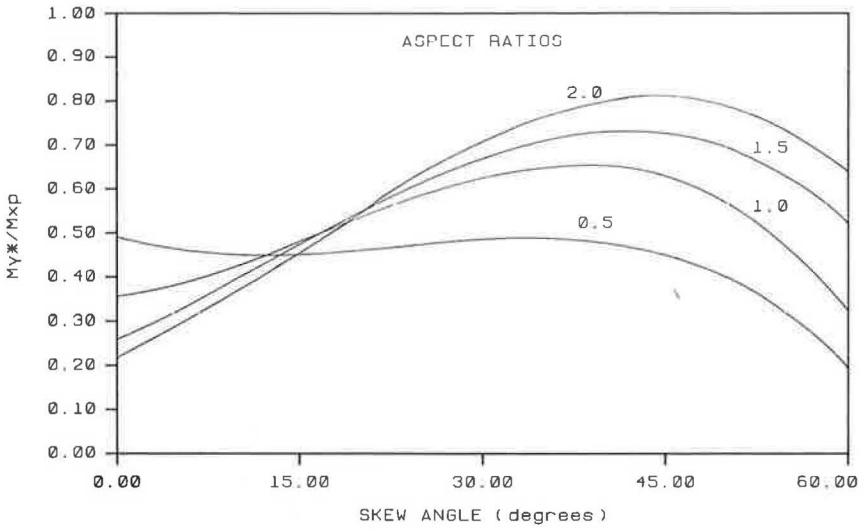

FIGURE 12 Pinned-base bridges under self-weight plus edge beam weight—curves for My*/Mxp for Point *E*4.

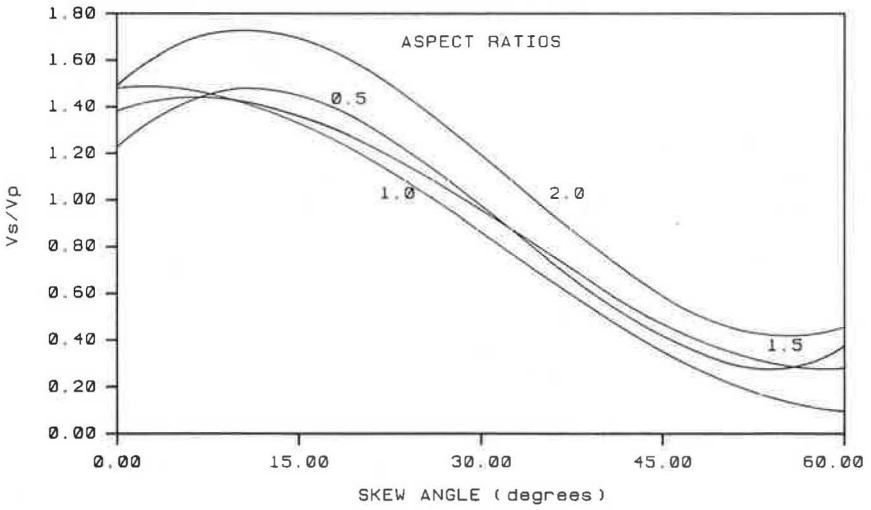

FIGURE 13 Pinned-base bridges under self-weight plus edge beam weight—curves for Vs/Vp at Point *E*4.

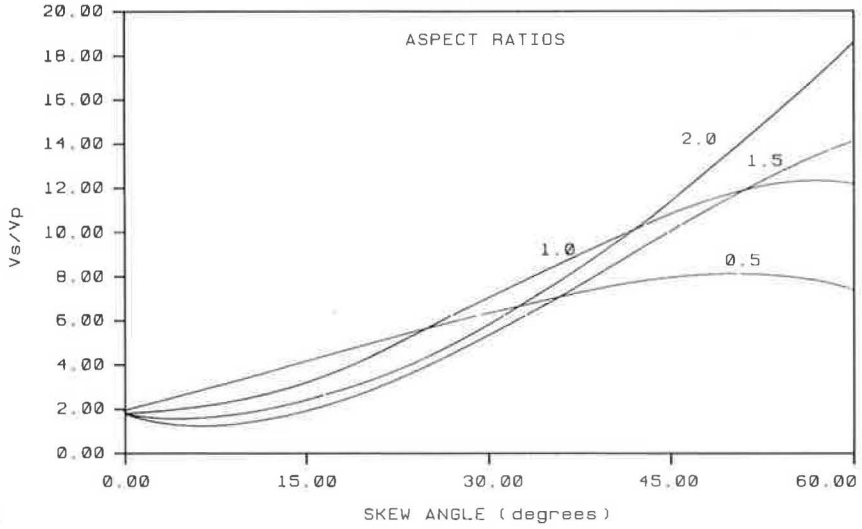

FIGURE 14 Pinned-base bridges under self-weight plus edge beam weight—curves for Vs/Vp between Point *E*4 and the free edge.

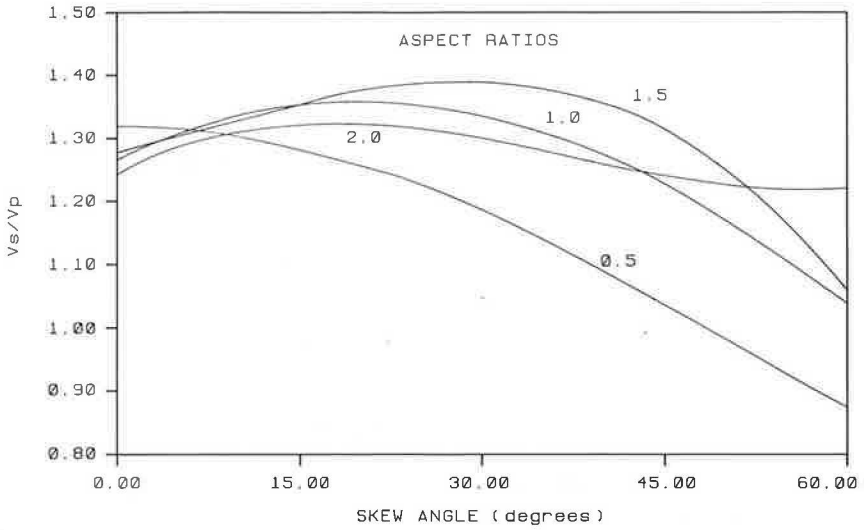

FIGURE 15 Pinned-base bridges under live load—curves for Vs/Vp at Point *D*4.

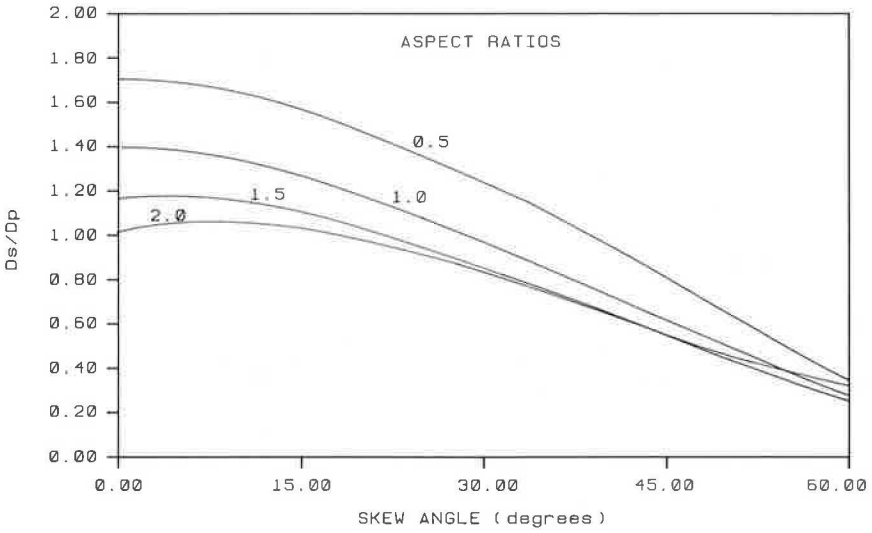

FIGURE 16 Pinned-base bridges under self-weight plus edge beam weight—curves for Ds/Dp.

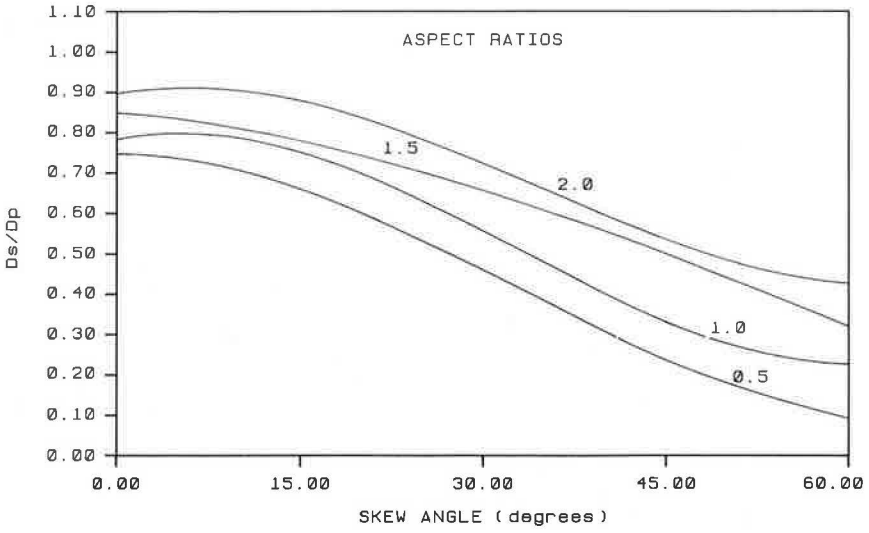

FIGURE 17 Pinned-base bridges under live load—curves for Ds/Dp.

EXAMPLE ON USE OF DESIGN CURVES

The following example illustrates the use of the design curves. A bridge may begin with the following properties:

- Skew span = 73.6 ft,
- Width along support = 34 ft, and
- Skew angle = 20 degrees.

It is then required to find the design moments at point *E*4 in the slab caused by self-weight and the weight of the edge beam.

The solution consists of the following steps:

- Step 1. Extract the equivalent 1-ft-wide two-dimensional frame for the bridge following the guidelines in AASHTO, Paragraph 3.24.3.2 (*26*).
- Step 2. Conduct a two-dimensional frame analysis for the load under consideration. For the given problem, this procedure results in a negative moment (Mxp) of 146.83 ft-kips/ft width in the slab near the wall.
- Step 3. Using a skew angle of 20 degrees and an aspect ratio of 73.6/34 = 2.2, obtain the design ratios from the uniformly distributed load design curves for point *E*4; i.e., Mx*/Mxp = 1.38 and My*/Mxp = 0.552.
- Step 4. Multiply the moments obtained in Step 2 by the design ratios in Step 3 to obtain the design moments:

Mx* = 1.38 × 146.83 = 202.9 ft-kips/ft
My* = 0.552 × 146.83 = 81.05 ft-kips/ft

In order to review the accuracy of the design curves, the predicted values of Mx* and My* were compared with the corresponding values obtained directly from a three-dimensional finite element analysis:

Mx* (from finite element analysis) = 215.1 ft-kips/ft
My* (from finite element analysis) = 81.89 ft-kips/ft

The discrepancy between predicted and computed values of Mx* is only 5.7 percent, whereas the discrepancy for My* is only 1.0 percent.

CONCLUSIONS

1. Integral reinforced-concrete skew slab bridges have relatively high shears and moments near the obtuse corner of the slab.
2. The literature reviewed did not reveal any previous theoretical or experimental research directly related to this problem.
3. The current design practice of providing for the transverse reinforcement with temperature and shrinkage reinforcement (AASHTO, Paragraph 8.20) or distribution reinforcement (AASHTO, Paragraph 3.24.10.2) may be inadequate.
4. A plane frame analysis of a skew slab bridge conducted following the guidelines in AASHTO, Paragraph 3.24.3.2, and using the skew span of the bridge can underpredict values of shear and moment near the obtuse corners. The magnitude of the resulting error depends on the skew angle and the aspect ratio of the bridge.
5. The degree of fixity at the base of the wall does not, for most practical situations, affect the distribution of shear and moments in the slab.
6. The research reported is still in progress and the published results are preliminary, based on linear finite element analyses. Laboratory testing of scale models and nonlinear analyses are underway to verify and refine the results presented herein.

ACKNOWLEDGMENTS

This investigation was sponsored by the Maine Department of Transportation. The assistance and helpful comments of Stephen Abott, Warren Foster, Brian Pickard, Leon Taylor, and John Buxton of the Maine Department of Transportation are greatly appreciated.

REFERENCES

1. H. J. Dagher, M. Elgaaly, J. Kankam, and L. Comstock. *Skew Slab Bridges with Integral Slab Abutments*: Vols. 1–6. Civil Engineering Department, University of Maine, Orono, Feb. 1991.
2. B. Bakht. Analysis of Some Skew Bridges as Right Bridges. *Journal of Structural Engineering, ASCE*, Vol. 114, No. 10, 1988, pp. 2307–2322.
3. Y. K. Cheung, I. P. King, and O. C. Zienkiewicz. Slab Bridges with Arbitrary Shape and Support Conditions: A General Method of Analysis Based on Finite Elements. *Proc., Institute of Civil Engineers*, Vol. 40, 1968, pp. 9–36.
4. L. A. Clark. Punching Shear Near the Free Edges of Slabs. *Concrete*, Aug. 1984, pp. 15–17.
5. R. J. Cope and P. V. Rao. Non-Linear Finite Element Analysis of Concrete Slab Structures. In *Proc., Institute of Civil Engineers*, Part 2, Marshalltown, South Africa, 1977, pp. 159–179.
6. R. J. Cope, P. V. Rao, and K. R. Edwards. Non-Linear Finite Element Analysis Techniques for Concrete Slabs. In *Proc., International Conference on Numerical Methods for Non-Linear Problems*, Swansea, Wales, 1980, pp. 445–456.
7. R. J. Cope and P. V. Rao. A Two-Stage Procedure for the Non-Linear Analysis of Slab Bridges. In *Proc., Institute of Civil Engineers*, Part 2, Vol. 75, Marshalltown, South Africa, Dec. 1983, pp. 671–688.
8. R. J. Cope and P. V. Rao. Moment Distribution in Skewed Slab Bridges. In *Proc., Institute of Civil Engineers*, Part 2, Vol. 75, Marshalltown, South Africa, Sept. 1983, pp. 419–451.
9. R. J. Cope and P. V. Rao. Shear Force in Edge Zones of Concrete Slabs. *The Structural Engineer*, Vol. 62A, No. 3, Mar. 1984, pp. 87–92.
10. R. J. Cope. Material Modelling of Real Reinforced Concrete Slabs. In *Proc., International Conference on Computer-Aided Analysis and Design of Structures*, Part I, Split, Yugoslavia, Sept. 1984, pp. 85–117.
11. R. J. Cope. Flexural Shear Failure of Reinforced Concrete Slab Bridges. In *Proc., Institute Civil Engineers*, Part 2, Vol. 79, Sept. 1985, pp. 559–583.
12. R. J. Cope and L. A. Clark. *Concrete Slabs: Analysis and Design*. Elsevier, London and New York, 1989.
13. R. J. Cope, P. V. Rao, and K. R. Edwards. *Shear in Skew Reinforced Concrete Slab Bridges*. Department of Civil Engineering, University of Liverpool, England, Oct. 1983.
14. M. Mahmoudzadeh, R. E. Davis, and F. M. Semans. *Modification of Slab Design Standards for Effects of Skew*. FHWA, U.S. Department of Transportation, 1984.
15. H. Rusch and A. Hergenroder. *Influence Surfaces of Moments in Skew Slabs*. Werner-Verlag, Dusseldorf, Germany, 1969.

16. L. F. Greimann, A. M. Wolde-Tinsae, and P. S. Yang. Skewed Bridges with Integral Abutments. In *Transportation Research Record 903*, TRB, National Research Council, Washington, D.C., 1983.
17. *Finite Element Analysis of Reinforced Concrete*. Task Committee on Finite Element Analysis of Reinforced Concrete Structures, ASCE, New York, 1982.
18. Finite Element Analysis of Reinforced Concrete Structures. Proc., Joint Seminar, Japan Society of the Promotion of Science and the National Science Foundation, C. Meyer and H. Okamura, eds., ASCE, New York, 1985, 685 pp.
19. R. H. Wood. The Reinforcement of Slabs in Accordance with a Predetermined Field of Moments. *Concrete*, Feb. 1968, pp. 69–76.
20. A. Hillerborg. Reinforcement of Slabs and Shells Designed According to the Theory of Elasticity. *Betong 1953*, pp. 101–109.
21. R. H. Wood. *Plastic Analysis and Design of Slab and Plates*. Thames and Hudson, London, 1961, 344 pp.
22. R. Park and W. L. Gamble. *Reinforced Concrete Slabs*. John Wiley, New York, 1980, 618 pp.
23. R. J. Cope and L. A. Clark. *Concrete Slabs: Analysis and Design*. Elsevier Applied Science, London and New York, 1984, 502 pp.
24. K. J. Bathe, E. L. Wilson, and F. E. Peterson. *SAP4: Structural Analysis Program for Static and Dynamic Response of Linear Systems*. University of California, Berkeley, 1964.
25. *Building Code Requirements for Reinforced Concrete*. ACI 318-89. American Concrete Institute, Detroit, Mich., 1989.
26. *Standard Specifications for Highway Bridges*, 13th ed. AASHTO, Washington, D.C., 1983.
27. *Analysis and Design of Reinforced Concrete Bridge Structures*. ACI 343R-88. American Concrete Institute, Detroit, Mich., 1988.
28. M. Elgaaly, T. Sandford, and C. Colby. *Monitoring the Forks Bridge to June 6, 1990*. Maine Department of Transportation, Augusta, Dec., 1990.

Publication of this paper sponsored by Committee on Concrete Bridges.

Information Needs for the Proper Application of Hydrologic Regional Regression Equations

JOHN OWEN HURD

Regional regression equations are used by many state and local agencies to estimate flood characteristics used in the design of drainage structures. The regression equations are preferred by many users because of their relative accuracy, simplicity (i.e., ease of application), and replicability. However, the experience of the Ohio Department of Transportation indicates that some problems do exist in applying the equations. The problems are in part caused by the disparity in background of report writers and users and in part to limitations of the equations. The experience of ODOT is used to demonstrate some of the potential misapplications of regional regression equations, and some of the information that has been given to designers to clarify the application of the equations is presented.

There are numerous methods of estimating flood characteristics (such as flood peaks and hydrographs) to be used in the design of drainage facilities for ungauged drainage basins. These include the rational method (*1*), SCS method (*2*), index flood method (*3*), regional regression equations (*4*), and so on. Regional regression equations are used by many state and local transportation agencies to estimate flood characteristics used in the design of drainage structures. The most commonly used equations are those used to estimate flood peaks. These equations generally relate flood characteristics to certain drainage basin characteristics, climatic variables, and channel characteristics. The equations are developed by using multiple-regression analyses to relate flood characteristics determined from flood records at gauged sites to the basin characteristics of these sites. There has been much deliberation over the correct means of developing the flood characteristics from the gauged streamflow data (*5*). However, for the purpose of this discussion it is assumed that the methods used to determine the flood characteristics at the gauged site are accurate.

The regression equations are preferred by many users because of their relative accuracy, simplicity (i.e., ease of application), and replicability. The regional equations may more accurately estimate flood characteristics within their range of use because they are developed from flood data for a specific region, whereas methods based on a larger broader base of flood data may be less accurate. Flood peak estimates for 25- and 100-year recurrence intervals using current Ohio equations (*6*) provide the same accuracy as log-Pearson Type III estimates from station records of 7 and 9 years, respectively. Most regional regression equations are easy to use. They represent flood characteristics as simple log-linear functions of a few easily determined drainage basin parameters such as drainage area, main channel slope, and average annual precipitation. Generally, little subjective judgment is required by the user in determining values for these parameters. Flood characteristics estimated by use of the equations are usually insensitive to small errors in parameter estimation. Therefore, nearly all practitioners will arrive at the same results by using the equations to estimate flood characteristics at a selected ungauged site.

Ohio Department of Transportation, 25 South Front Street, Columbus, Ohio 43215.

THE PROBLEM

It appears that a problem could not exist if this method is so accurate, easy to use, and gives such consistent results. However, the experience of the Ohio Department of Transportation (ODOT) indicates that problems do exist in applying the equations. Part of the reason for these problems involves the individuals performing the design of drainage facilities for various governmental agencies or private consultants. These individuals are rarely hydrologists and their knowledge of the statistical methods used in development of the regional regression equations is often limited at best. This lack may be true even in large agencies and consulting firms. In some instances, drainage designers are not registered engineers, but technicians with limited educational background in the theory behind the hydraulic design methods they are using. In other instances, individuals doing drainage design are not specialists, but general highway designers performing drainage design, structural design, highway design, and so on. The limitation may be especially common within small agencies or consulting firms. These people are not normally afforded the time to become familiar with the intricacies and background of all the design methods being used.

Another reason for the problems involves the limitations of the equations. The equations are generally accurate only within the specific geographic area for which they were developed. Their use is further limited to the particular type of basins from which data used in their development were gathered (e.g., natural unregulated rural basins). The application of the equations should be limited to sites with basin characteristics within the ranges of the basin characteristics in the original data set used to develop the equations.

Even then the equations may give biased estimates of flood characteristics for basins with certain basin features. In Ohio, use of the rural flood peak equations for steep basins with main channel orientation aligned with prevailing storm move-

ment (*7*) and basins with a large percentage of strip-mined area (*6*) have been identified as giving biased estimates by observation of residuals between gauging station flood peak estimates and those obtained from regression equations. This situation normally occurs when there are insufficient data available to statistically quantify the effect of that particular characteristic for which flood estimates are biased.

The methods used to develop the regional regression equations and the limitations of the equations are usually thoroughly discussed in the research reports providing the equations. The reports are generally well written, but they are written as research reports for those familiar with the practice of hydrology and not as users manuals for the practicing drainage designer. Because of the disparity between the backgrounds of the report writers and those of the report users, there may often be errors in application of regional regression equations in spite of the report quality. One reason may be that designers are not reading the reports in detail. This is not recommended but is understandable because the equations are generally so easy to apply.

In the following section, the experience of ODOT is used to demonstrate some of the potential misapplications of regional regression equations, and some of the information that has been given to designers to clarify the application of the equations will be presented.

ODOT EXPERIENCE

ODOT has used regional regression equations to estimate rural flood peaks for more than 20 years. ODOT also currently uses regional regression equations to estimate urban flood peak discharges, urban flood hydrographs associated with flood peaks, urban basin lag times, and urban flood volumes associated with flood peaks for small streams. At the time of this report, equations were being developed to estimate rural flood hydrographs associated with flood peaks, rural basin lag times, rural flood volumes associated with flood peaks, and rural and urban flood volume, duration, and frequency relations for small streams. During this time, many misapplications of the equations have occurred and many questions from drainage designers have been received. The following subsections categorize the misapplications and questions.

Determination of Geographic Region

It should be relatively simple for the designer to determine the geographic region in which the ungauged drainage area of interest is located. This is not always the case. The first regional regression equation used by ODOT to estimate flood peak discharges for rural basins (*8*) was

$$Q_{2.33} = 50CA^{0.8}Sl^{0.298} \quad (1)$$

where

$Q_{2.33}$ = mean annual flood, ft³/sec;
A = drainage area, mi²;
Sl = main channel slope, ft/mi, and
C = a regional constant ranging from 0.3 to 1.7.

The 5- through 100-year rural peak discharges were determined by multiplying $Q_{2.33}$ by factors that were a function of recurrence interval and drainage area. This equation was used for the entire state of Ohio.

The factor C was used to eliminate geographic bias in flood estimates from the statewide equation. It was delineated by soil association boundaries of the Soil Conservation Service (SCS). Because these boundaries were not precisely defined on the maps available to drainage designers and did not coincide with drainage basin boundaries, the designers were often left with a difficult subjective decision to make about which value of the coefficient to use. Because of the wide range in C values, a large difference in flood peak estimates could result. The most common difficulty was differentiating between $C = 1.0$ or 1.6. Because practitioners generally use a conservative approach, a 60 percent overestimate in flood peaks often resulted.

Equation 1 has since been replaced twice with updated regional regression equations (*6,9*). In each case, the regional boundaries were defined by drainage basin divides in place of soil association areas. Region boundaries may cross the main channel of a large well-gauged stream, but the location is clearly noted as either just upstream or downstream of a major tributary. Analyses were performed during development of these equations to determine whether any soil parameter had a significant effect on flood peaks. No soil parameters were determined to have a significant effect. Designers no longer had any problem determining which equations to use. They have only to follow the watercourse for the basin of interest down to a major stream if the drainage basin happens to be near a regional boundary.

Determination of Equation Suitability

The designer must also determine whether the regional regression equation is suitable for the drainage basin being analyzed. It may not be as simple as it would seem to confirm that the basin is, for example, rural, unregulated, and within the equation parameter limits.

As previously stated, ODOT currently uses regional regression equations to estimate flood peak discharges from both rural and urban basins (*10*). The urban peak equations are

$$Q_T = \mathrm{RC} \cdot A^a \mathrm{Sl}^b \mathrm{El}^c (13 - \mathrm{BDF})^d \quad (2)$$

where

Q_T = T year peak discharge, ft³/sec;
RC, a, b, c, and d = regression constants,
A = drainage area, mi²;
Sl = main channel slope, ft/mi;
El = basin elevation index, 1,000s of feet; and
BDF = a basin development factor ranging from 0 (little or no development) to 12 (fully developed).

The rural peak equations are of the form

$$Q_T = \mathrm{RCA}^a \mathrm{Sl}^b (\mathrm{St} + 1)^c \quad (3)$$

where St is the percentage of the area in storage and the other terms are as defined for Equation 2.

Many drainage basins in Ohio are partially developed. Hence, these basins fall into a neutral category in which the effects of the development on stream flow may not be significant. For those areas with slight urban development (BDF < 5), it is recommended that both the rural and urban methods be considered (*10*). The designer must then decide which estimate to use. This decision is complicated by the fact that in some cases use of the rural equations provides larger flood peak estimates than use of the urban equations. On the basis of the results of studies demonstrating the effect of location of detention facilities on flood peaks from urbanized areas, it appears reasonable to assume that development in the lower one-third of a basin could reduce flood peaks compared with natural conditions, whereas development in the upper one-third would increase the peaks substantially (*11–13*). Thus designers have been offered the following guidelines for estimating peak discharges using both urban and rural flood peak equations. If development is in only the lower one-third of the basin, use of the lesser peak discharge is recommended; if the development is only in the upper one-third of the basin, use of the greater peak discharge is recommended; if the development is in the middle or spread throughout, use of the average is recommended.

Once it is determined that the basin is rural, the rural equations may still not be applicable to the particular unregulated basin even if its characteristics are within the range of parameter limits. More information about the basin may be required to determine if the regional regression equations can be used to predict flood peaks (or other characteristics) for the basin. In Ohio, for example, basin characteristics of the 275 gaged basins used to develop the final regional regression equations for rural flood peaks were determined from U.S. Geological Survey (USGS) 7.5-min (1 in. = 2,000 ft) topographic quadrangle maps. Furthermore, the main channel from the basin mouth to the divide was defined from the contours on these maps.

In order to confidently use the regional regression equations, the designer should be able to determine the value of each independent parameter by the same means and with the same ease as was done for the gauged sites during equation development. In the particular case of Ohio's flood peak equations, if a basin boundary cannot be defined without precise mapping or a definite channel does not exist (e.g., sheet flow areas), other discharge estimation methods should be considered. A rule of thumb ODOT provides to designers using the Ohio rural flood peak regression equations is the following: "If all the information needed for the equation cannot be confidently obtained from a USGS 1 in. = 2,000 ft map, another method should be considered." ODOT recommends the use of the rational method for determining flood peaks for drainage areas of small sheet flow type.

The suitability of the regression equation may still not be verified. The values of parameters obtained should fall within the range of those parameters at the gauged sites used to develop the equations. This is not always as simple to verify as it may seem. A particular basin may have characteristics each of which has a value within the range of the basin characteristic of the original data set. However, the point formed by these values may be outside the range of points in multiple-dimensional space for the data set used in equation development.

Consider Equation 3 used by ODOT to estimate rural flood peaks. For the data sets used to develop the equations, drainage area and main channel slope are highly correlated. In general, as drainage area decreases, main channel slope increases. Thus, a large basin with a steep channel slope may lie outside the two-dimensional space of the original data set even though each characteristic may have a value within the range of that particular variable. Figure 1 shows an exaggerated illustration of this concept.

If the regional regression equations involve only one or two basin characteristics, it can easily be determined if the basin of interest has characteristics within the multiple-dimensional space either directly or graphically. However, most current regional regression equations contain three or more basin characteristics. The urban peak equations used by ODOT have four variables. Manually solving this problem for three or more variables is virtually impossible. However, with high-powered desktop computers available, simple programs can be developed to determine whether the basin of interest lies with the multiple-dimensional space of the original data set. Currently, the USGS Water Resources Division, Ohio Office, is developing such a microcomputer program for the rural peak equations used by ODOT.

Application of the Equations

After it is determined that the regional regression equations are applicable to the ungauged site being studied and which particular regional regression equation should be used, the appropriate equation must be applied properly.

As has been previously discussed, the designer should be able to obtain values of basin characteristic parameters by the same methods used for the data in development of the regional regression equations. For some parameters, it may be imperative to obtain the parameter value in the same way, whereas for others it may not. For example, Equation 3 is examined in more detail.

Although the designer should be able to delineate the drainage area boundary on a 1 in. = 2,000 ft topographic map, the drainage area may be determined from a topographic map of a different scale. The scale of a map should not significantly affect the accuracy of the determination, nor should a different scale than 1 in. = 2,000 ft cause constant over- or underestimation of the value. However, use of a less accurate map may increase the variability of the drainage area estimate and is not recommended.

The same cannot be said for determination of main channel slope, which is defined as "the difference in elevation at points

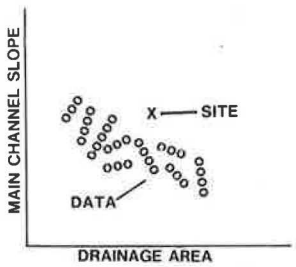

FIGURE 1 Illustrative plot of basin characteristics outside the multidimensional space of the data.

10 and 85 percent of the distance along the main channel from the specified location on the channel to the topographic divide, divided by the distance between the points" (*6*). Figure 2 shows how a sinuous drainage basin channel might be plotted on different scale maps. Although the 10 and 85 percent elevations would remain relatively the same regardless of the map scale, the length of the channel would probably increase as the scale of the map becomes larger. Thus, the main channel slope would decrease. If the regression equations were developed using values of main channel slope determined from 1 in. = 2,000 ft scale map, use of larger scale maps by the designer would consistently underestimate the main channel slope, which would result in consistently underestimated flood peaks. The converse would be true if a smaller scale were used. A not uncommon error in main channel slope estimate of 20 percent results in a 4 to 13 percent error in flood estimates for the usual 0.2 to 0.6 range in main channel slope exponent. ODOT has recommended that designers use 1 in. = 2,000 ft topographic maps to estimate main channel slope.

Storage is defined for Equation 3 as "the percentage of the contributing drainage area occupied by lakes, ponds, and swamps as explicitly shown on USGS 7.5-min (1 in. = 2,000 ft scale) topographic quadrangle maps" (*6*). The equation does not apply to drainage basins where reservoirs provide enough storage to cause the basin to be considered regulated because such basins were not included in the regression analyses (*6*). The parameter involves only surface area and no consideration is given to whether the pond or swamp is full or empty, if any freeboard exists, or what total number of acre-feet of storage is provided. The definition of storage provided by Webber and Bartlett (*9*) was not as clear regarding how storage was determined. Several designers had underestimated this parameter using the equations from that report because field checks indicated that the ponds in the area were "generally full at the time of the field check and appeared to provide little storage capacity." Failure to take full account of storage will consistently overestimate flood peaks. Ignoring a 2 percent storage value in the current equations (*6*) for rural peaks results in a 38 to 49 percent overestimate. To avoid this problem, the current report clearly defined storage exactly as it was determined for the gauged sites used in the multiple regression analyses.

The fact that all information required for using Equation 3 can or should be obtained from 1 in. = 2,000 ft scale top maps does not excuse the designer from verifying that the information on the topographic map is accurate and current.

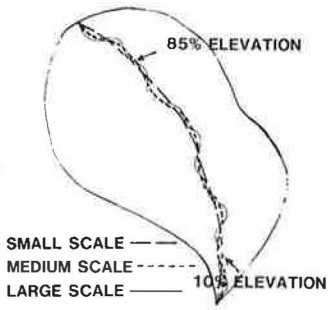

FIGURE 2 Main channel plotted on different scale maps.

Verification may include a combination of field checks, review of recent aerial photographs, consultation with local officials, etc. Thorough field inspection is recommended for urban basins. To apply Equation 2 for urban areas, the designer must do a field check to determine the basin development factor (BDF), and must use local sewer and street maps to verify the actual drainage area.

Extrapolation of the regional regression equations beyond the limits of the original data used to develop the equations is not recommended. However, there are times when the drainage basin being studied has one parameter with a value just outside the recommended range and no other method of flood estimation appears more reasonable. The designer must evaluate whether or not this extrapolation may produce an over- or underestimate of the flood characteristic. Normally, if the values of the other parameters are well within the ranges of the original data set, slight extrapolation may be reasonable unless computation of the flood characteristic is unusually oversensitive to small changes in the value of the extrapolated parameter.

Before development of regression Equation 3, the equations used for one geographic region in Ohio were as follows (*9*):

$$Q_2 = 42.6A^{0.802}\mathrm{SI}^{0.225} \tag{4}$$

$$Q_{100} = 52.6A^{0.857}\mathrm{SI}^{0.619} \tag{5}$$

with all symbols as defined for previous equations. Q_5 through Q_{50} were similar with the power of slope increasing proportionally and the regression constant and the power of area increasing only slightly. The increase in peak discharge estimates from Q_2 through Q_{100} is more commonly the result of a comparable increase in the regression constants with the exponents of the parameters changing much less. However, in this particular regression analysis the increase from Q_2 through Q_{100} is reflected more in the unusually large increase in the power of slope, which apparently compensates for the lack of change in the regression constant. These equations were carefully checked for bias with regard to slope, but none was observed. Although the increase in exponent for main channel slope was unusual, the sensitivity of flood peak estimates to relative changes in main channel slope was not considered excessive. Therefore, no effort was made to change the form of the variable in the equation to reduce sensitivity. Both Equation 3 and all other regional regression equations from the earlier work (*8*,*9*) have increasing regression constants as recurrence interval increases, whereas changes in the slope exponents are much smaller and the exponent may increase slightly or decrease as the recurrence interval increases.

The particular region for which Equations 4 and 5 were developed has very steep watersheds. It is not usual to find ungauged drainage basins that have main-channel slopes outside the range of those in the original data set. Extrapolating Equation 4 to steeper slopes would appear reasonable because the value of Q_2 is somewhat insensitive to an increase in slope. However, extrapolation of Equation 5 for steeper slopes may overestimate Q_{100} because the value of that flood peak appears unusually sensitive to any increase in slope. Any flood characteristics computed by equations such as Equation 5 through extrapolation of slopes should be checked by an independent method.

Where the ungauged basin has a particular basin characteristic for which the regional regression equations are known to give biased estimates, subjective adjustment of the estimated flood characteristics may be required. For example, flood peaks estimated by use of the current regional regression equations may need to be increased for steep drainage basins oriented within 20 degrees of the prevailing storm movement (*7*), whereas peak estimates for basins with a larger percentage of strip mine areas may need to be decreased (*6*). In each case, the magnitude of the adjustment may be estimated comparing the presumed biased estimates with estimates based on methods that are either less sensitive to the particular basin characteristic causing the bias or which take into account the effect of that characteristic.

Equations relating flood peaks to channel shape (geometry) characteristics have been developed for Ohio (*14,15*). They are not as accurate as the basin characteristic equations with regard to the regression statistics. However, they provide a means to check flood peak estimates computed by questionable application of the basin characteristic equations. They were developed at ODOT's request to provide an independent method of flood peak estimation for watersheds where the more conventional basin characteristic equations are known to produce biased estimates. The channel-shape equations should be used to help quantify an adjustment to the flood estimates computed by use of the basin characteristic equation.

RECOMMENDATIONS

On the basis of ODOT experience with the use of the regional regression equations to estimate flood characteristics for ungauged watersheds, the following recommendations are presented.

1. Where possible, watershed divides should be used for regional regression equation boundaries.
2. The methods used to determine the value of each parameter during development of the regional regression equations should be clearly defined in research reports.
3. Users of regional regression equations should be advised if the values of parameters must be determined by the same means as those used for the original data set.
4. Microcomputer programs should be developed to determine whether selected ungauged sites have parameter values within the multidimensional space of the original data set used to develop the regional regression equations.
5. Short courses should be held for users of the equations as part of the implementation process for any new reports.
6. Independent methods of estimating flood characteristics should be developed to be used as check methods in which use of the regional regression equations produces questionable results.
7. Research should be conducted to quantify the effects on flood characteristics of main-channel orientation, strip-mined areas, and other basin characteristics that affect the accuracy of flood characteristic estimates.

ACKNOWLEDGMENTS

This paper was funded by the Ohio Department of Transportation.

Sincere appreciation is given to James M. Sherwood and other personnel of the Water Resources Division, Ohio Office, U.S. Geological Survey, for their critical review of this paper.

REFERENCES

1. Design and Construction of Sanitary and Storm Sewers. *Manual and Report on Engineering Practice 37*, ASCE, New York, 1970.
2. *Urban Hydrology for Small Watersheds*. Technical Release 55; Soil Conservation Service, U.S. Department of Agriculture, Washington, D.C., 1975.
3. T. Dalrymple. *Flood Frequency Analyses*, Water Supply Paper 1543-A. U.S. Geological Survey, 1960.
4. F. D. Masch. *Hydrology*. FHWA-IP-84-15 (HEC 19). FHWA, U.S. Department of Transportation, 1984.
5. V. P. Singh. Hydrologic Frequency Modeling. *Proc., International Symposium of Flood Frequency and Risk Analysis*, D. Reidel Publishing; 1987.
6. G. F. Koltun and J. W. Roberts. *Techniques for Estimating Flood-Peak Discharges of Rural Unregulated Streams in Ohio*. Water Resources Investigations Report 89-4126, U.S. Geological Survey, 1989.
7. J. O. Hurd. Effect of Main Channel Orientation on Flood Peaks for Streams in Ohio. In *Transportation Research Record 1073*; TRB, National Security Council, Washington, D.C., 1986.
8. W. P. Cross and R. I. Mayo. *Floods in Ohio Magnitude and Frequency*. Bulletin 43. Ohio Department of Natural Resources, Columbus, 1969.
9. E. E. Webber and W. P. Bartlett, Jr. *Floods in Ohio Magnitude and Frequency*. Bulletin 45. Ohio Department of Natural Resources, Columbus, 1977.
10. J. M. Sherwood. *Estimating Peak Discharges, Flood Volumes, and Hydrograph Shapes of Small Ungaged Urban Streams in Ohio*. Water Resources Investigations Report 86-4197. U.S. Geological Survey, 1987.
11. R. H. McCuen. A Regional Approach to Urban Stormwater Detention. *Geophysical Research Letters*, Vol. 1, No. 7, 1974.
12. D. C. Curtis and R. H. McCuen. Design Efficiency of Stormwater Detention Basins. *Journal of the Water Resources Planning and Management Division, ASCE*, May 1977.
13. A. C. Flores, A. M. Bedient, and L. W. Mays. Method for Optimizing Size and Location of Urban Detention Storage. *Proc., International Symposium on Urban Hydrology, Hydraulics, and Sediment Control*, 1982.
14. E. E. Webber and J. W. Roberts. Floodflow Characteristics Related to Channel Geometry in Ohio. Open File Report 81-1105. U.S. Geological Survey, 1981.
15. D. K. Roth. Estimation of Flood Peaks from Channel Characteristics in Ohio. Water Resources Investigations Report 85-4175. U.S. Geological Survey, 1985.

The findings and opinions expressed herein are those of the author and do not constitute a standard or specification.

Publication of this paper sponsored by Committee on Hydrology, Hydraulics, and Water Quality.

Identifying Stream Gauges to Operate for Regional Information

GARY D. TASKER

The problem of identifying at which sites to collect future streamflow data is formulated as a mathematical program to optimize regional information subject to a budget constraint. An approximate solution is obtained using a step-backward technique that identifies gauging station sites, either existing or new, and whether to discontinue or not start data collection if the budget is exceeded. The method allows a network manager to design a nearly optimal streamflow data network for collecting regional information. The method is illustrated by a network of stream gauges in Illinois.

How to determine which gauging stations (old or new) to operate, given a limited budget, to minimize the errors, or uncertainty, in estimated design flows at ungauged sites is addressed. The benefit of estimating design flows with less uncertainty is that it decreases the probability of overestimating or underestimating the size of bridge or culvert openings. In this manner, optimizing the stream gauging network for regional information can reduce costs of highway design and maintenance. The approach to solving the problem is to define the objective, formulate the problem as a mathematical program, and find an approximate solution.

The technique is based on the regional regression method of estimating design flows, such as the 50-year peak flow, from physiographic characteristics, such as drainage area, channel slope, soil type, and land use; and meteorological variables, such as mean annual precipitation and 2-year, 24-hr rainfall intensity. The regional regression model is a multivariable regression model that can be written, after suitable transformations, in the linear form:

$$\mathbf{Y} = \mathbf{X}\boldsymbol{\beta} + \mathbf{e}$$

where

- $\mathbf{Y}$ = $(n \times 1)$ vector of flow characteristic at n sites,
- $\mathbf{X}$ = $(n \times p)$ matrix of $(p - 1)$ basin characteristics at the n sites augmented by a column of 1s,
- $\boldsymbol{\beta}$ = $(p \times 1)$ vector of regression parameters to be estimated, and
- $\mathbf{e}$ = $(n \times 1)$ vector of random errors.

The dependent variable is a flow characteristic, such as the logarithm of the 50-year flood (commonly used in the design of bridges and culverts), that is derived from a sample of observed flows, such as the logarithms of observed annual peak discharges at each site.

U.S. Geological Survey, 430 National Center, Reston, Va. 22092.

Hydrologists have used ordinary least squares (OLS) methods to estimate $\boldsymbol{\beta}$. The OLS estimates are appropriate and statistically efficient when the at-site flow estimates are equally reliable, the natural variability is the same at each site, and observed concurrent flows at every pair of sites are independent. In practice, hydrologic data sets are not so homogeneous.

A more appropriate estimator of $\boldsymbol{\beta}$ is the generalized least squares (GLS) estimator,

$$\boldsymbol{\beta} = (\mathbf{X}^T\boldsymbol{\Lambda}^{-1}\mathbf{X})^{-1}\mathbf{X}^T\boldsymbol{\Lambda}^{-1}\mathbf{Y}$$

in which it is assumed that the errors have zero mean $E[\mathbf{e}] = 0$, and covariance matrix $E[\mathbf{e}\mathbf{e}^T] = \boldsymbol{\Lambda}$. The matrix $\boldsymbol{\Lambda}$ is a weighting matrix that accounts for unequal record lengths used for computing flow characteristics and for cross correlations between flow characteristics at different sites.

The operational difficulty with the GLS estimator of $\boldsymbol{\beta}$ is that $\boldsymbol{\Lambda}$ is unknown and must be estimated from the data. Stedinger and Tasker (*1*) proposed that $\boldsymbol{\Lambda}$ be estimated as

$$\boldsymbol{\Lambda} = \gamma^2\mathbf{I} + \mathbf{W}$$

where γ^2 is an estimate of the model error variance and $\mathbf{W}$ is an $(n \times n)$ matrix of sampling covariance. The model error variance (γ^2) is the portion of total error variance that is because of an imperfect model; it is not a function of the sample data. Model error occurs because many of the factors that explain variations in $\mathbf{Y}$ are unknown or imperfectly specified. Estimation of γ^2 is made by an interactive search technique outlined in Tasker and Stedinger (*2*). The sampling error variance $(\mathbf{W})$ is the error variance caused by estimating the regression coefficients $(\boldsymbol{\beta})$ with limited data in both the temporal and spatial dimensions.

The critical feature of this GLS technique is that it allows the covariance matrix $\boldsymbol{\Lambda}$ to be expressed in terms of record length at each gauge in the network. For the interested reader, the elements of the $\boldsymbol{\Lambda}$ matrix are given in Tasker and Stedinger (*2*, p. 363). For the problem at hand, it is enough to note that the values of the diagonal elements of the $\boldsymbol{\Lambda}$ matrix change as the record length associated with any gauging station change, and that the value of the off-diagonal element associated with any pair of stations is a function of the relative location of the sites. These changes reflect the decrease in variance of the response variable $(\mathbf{Y})$ as the record length increases, and the redundant information collected from cross-correlated annual peaks. Record length may refer to current record length or record length at the end of a planning horizon. Thus $\boldsymbol{\Lambda}$ may be calculated for different sets of record-length combinations that reflect different future data collection strategies.

DEFINITION OF OBJECTIVE

The first step in solving the problem at hand is to define the objective to be minimized. Let $\theta(\mathbf{x})$ represent the true streamflow statistic at a site with basin characteristics described by the column vector $\mathbf{x}$. The precision with which the regression estimate at the site ($\mathbf{x}\hat{\beta}$) approximates $\theta(\mathbf{x})$ can be described by the mean square error of prediction (MSE) at an ungauged site with basin characteristics $\mathbf{x}$

$$\mathrm{MSE}(\mathbf{x}) = \gamma^2 + \mathbf{x}^T(\mathbf{X}^T\mathbf{\Lambda}^{-1}\mathbf{X})^{-1}\mathbf{x}$$

The regional statistical information contained in the regression model for the site is proportional to the reciprocal of MSE($\mathbf{x}$) (*3*).

Generally, interest lies in the average MSE over a representative set of basin characteristics rather than the MSE for a particular $\mathbf{x}$ as in the previous equation. Let that representative set be described by a set of vectors $\mathbf{x}_1, \ldots, \mathbf{x}_m$. Then the average MSE criterion would be

$$Z = \gamma^2 + m^{-1} \sum_{i=1}^{m} \mathrm{MSE}(\mathbf{x}_i)$$

Because γ^2 is not a function of how long gauges are operated, the first term on the right side of this equation may be ignored in the objective function Z.

Consider how to identify a feasible gauging strategy that minimizes Z. This analysis assumes that a gauging network already exists and is providing some data on which to base the design. Let $j = 1, \ldots, m_e$ index the existing stations of which the available record lengths are n_j. To this basic set can be added additional new gauging stations indexed by $j = m_e + 1, \ldots, m_e + m_a$, budgets permitting. The goal will be to identify some set, indexed by k, of these $m_e + m_a$ stations to continue to operate over the planning horizon (some 5 to 20 years). If the planning horizon is too short, it would seldom be advantageous to add a new gauge because it would not have an opportunity to accumulate a useful record. Thus, too short a time horizon will lead to myopic strategies that are suboptimal in the long run.

In designing an optimal data collection strategy, it must be recognized that some gauging stations will continue to be operated because of specific data needs, such as managing outflows from a reservoir or monitoring long-term trends. Other sites, perhaps, must be eliminated, such as a site that will be flooded by a new dam and can no longer be operated as a gauging station. Both of these types of gauging stations are termed "nondiscretionary" because the decision to continue or discontinue operation is made outside of this analysis. Of the $m_e + m_a$ gauging sites, let F equal the set of discretionary sites that one can choose to operate or not. The problem then is to find the feasible subset (S_k) of F that minimizes Z, subject to a budget limit (B) on discretionary gauging. Recall that $\mathbf{X}$ is the set of basin characteristics corresponding to both the existing gauging station and any additional gauging station sites specified by S_k, and $\mathbf{\Lambda}$ is the GLS weighting matrix pertaining to this set of gauging stations and record lengths that will pertain at end of the planning period. Fundamentally, the optimization of Z poses a large nonlinear integer programming problem. Because the number of subsets of F that are within the gauging budget can be large, a direct attack on the problem is not attractive. However, an approximate solution may be obtained using a step-backward approach (*4*). The step-backward approach starts by considering all possible gauges as being part of the network and incrementally dropping the least valuable stations until the remaining set is within the discretionary data collection budget constraint.

APPLICATION OF NETWORK ANALYSIS

In order to illustrate the network analysis procedure, a network of 85 gauges in Illinois was selected for analysis. The flow and basin characteristics for these sites were taken in a regional analysis of flood characteristics conducted by the U.S. Geological Survey in cooperation with the Illinois Department of Transportation (*4*). At some of these stations, much more data than annual peak flows are collected, but for this analysis only the annual peak flow regional information is considered. Thirty-six of the stations were selected as stations that must be continued, and two stations were selected as stations that cannot be continued. These 38 stations are classified as nondiscretionary (stations for which the choice of continuing or discontinuing operation was made before the analysis). The remaining 47 stations, along with 15 potentially new stations, are considered discretionary. The approximate locations of all these sites are shown in Figure 1, and flow and basin characteristics are presented in Table 1. The selection and classification of these gauges as discretionary or nondiscretionary were made for illustrative purposes and do not necessarily reflect the true classification of the gauges.

The first task in analysis of this network was to run a GLS regression of the 50-year peak discharge on basin characteristics using the methods described by Tasker and Stedinger (*2*). The final regression was

$$\begin{aligned}\log Q50 = {} & 2.1763 + 0.7538(\log \mathrm{AREA}) \\ & + 0.4767(\log \mathrm{SLOPE}) \\ & + 0.6791[\log (I24{,}2 - 2.5)]\end{aligned}$$

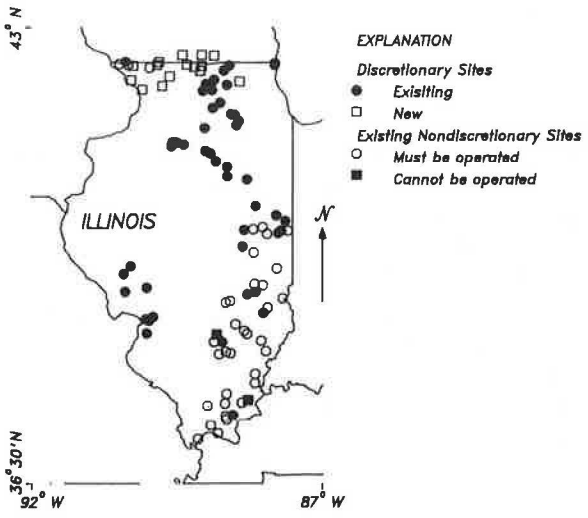

FIGURE 1 Location of gauging stations used in study.

TABLE 1 DATA USED IN REGRESSION

Station Number	AREA	SLOPE	I24,2	50-Yr Peak	Station Number	AREA	SLOPE	I24,2	50-Yr Peak
3336100	1.0	21.0	2.9	310.	5438300	0.8	87.3	2.8	254.
3336500	35.0	6.9	3.0	5100.	5438390	88.1	8.3	2.8	4140.
3336900	134.0	5.5	3.0	6610.	5438500	538.0	4.6	2.8	13400.
3337500	68.0	2.6	3.0	3510.	5438850	1.7	28.7	2.9	422.
3338000	340.0	3.0	3.0	9430.	5439000	77.7	2.7	2.9	2840.
3338100	2.2	15.8	3.0	758.	5439500	387.0	2.3	2.8	9720.
3338500	958.0	3.1	3.0	30500.	5439550	1.7	53.8	2.8	570.
3338800	1.3	33.2	3.0	1300.	5440000	1099.0	4.1	2.8	21600.
3339000	1290.0	3.2	3.0	36800.	5440500	117.0	6.3	2.9	8000.
3341700	1.1	44.3	3.1	588.	5551700	70.2	5.6	2.8	2030.
3341900	0.0	52.8	3.2	62.	5551800	0.4	87.1	2.9	541.
3343400	186.0	3.0	3.1	7110.	5551900	32.6	8.8	2.8	1640.
3344000	919.0	1.5	3.1	24200.	5551930	21.1	10.0	2.8	735.
3344250	0.1	10.5	3.2	75.	5554000	186.0	5.4	2.9	5940.
3344425	0.1	97.1	3.2	137.	5554500	579.0	1.1	3.0	14400.
3344500	7.6	15.7	3.2	3820.	5554600	0.2	60.7	3.0	186.
3345500	1516.0	1.6	3.2	46600.	5555000	1084.0	1.3	3.0	21900.
3346000	318.0	4.3	3.2	26100.	5555300	1251.0	1.4	3.0	36100.
3378000	228.0	2.8	3.3	6400.	5555400	0.1	50.4	3.0	292.
3378635	240.0	5.3	3.2	11000.	5555775	0.4	24.5	2.9	130.
3378650	1.6	19.6	3.3	806.	5556500	196.0	6.1	3.0	13000.
3378900	745.0	2.7	3.3	29600.	5557000	86.7	9.0	3.0	11100.
3378980	0.4	73.6	3.2	502.	5557100	0.3	97.1	3.0	396.
3379500	1131.0	2.0	3.3	49100.	5557500	99.0	12.7	3.0	8200.
3379650	1.6	36.1	3.3	1350.	5586350	1.8	53.9	3.4	1750.
3380300	0.1	98.7	3.4	119.	5586500	2.3	24.3	3.4	982.
3380350	208.0	2.8	3.3	19100.	5586850	0.0	63.4	3.4	48.
3380400	1.1	36.1	3.4	728.	5587000	868.0	2.3	3.4	36600.
3380450	0.4	87.6	3.4	352.	5587850	0.4	42.5	3.4	675.
3380475	97.2	4.1	3.4	9360.	5587900	212.0	5.1	3.4	9660.
3380500	464.0	1.9	3.4	29700.	5588000	36.7	7.9	3.5	8410.
3381500	3102.0	1.2	3.3	39100.	5589500	22.6	11.1	3.5	7280.
3381600	0.2	89.8	3.3	352.	5590000	12.4	17.2	3.0	1480.
3382025	0.5	75.5	3.5	516.	5590400	109.0	2.5	3.1	3720.
3382100	147.0	4.3	3.5	5860.					
3382170	13.3	12.2	3.4	2500.	--POSSIBLE NEW STATIONS----------				
3382510	8.5	25.5	3.4	704.	990001	0.9	157.9	3.0	
3382520	1.1	28.3	3.4	772.	990002	247.0	10.9	3.0	
3384450	42.9	16.2	3.5	15800.	990003	230.0	6.6	3.0	
3385000	19.1	21.4	3.5	7780.	990004	3340.0	0.7	2.8	
3385500	1.0	145.2	3.5	1690.	990005	202.0	2.7	2.8	
3612000	244.0	2.7	3.5	11700.	990006	1034.0	2.3	2.9	
3612200	0.3	141.0	3.5	460.	990007	1.3	40.9	3.0	
3614000	2.0	23.9	3.6	887.	990008	1326.0	1.6	3.0	
4087300	1.5	34.3	2.7	357.	990009	2.0	29.4	3.0	
4087400	5.0	21.7	2.6	939.	990010	523.0	3.2	2.9	
5414820	39.6	18.9	3.0	14500.	990011	0.5	97.1	2.9	
5415000	125.0	11.3	3.0	17100.	990012	2550.0	0.9	2.9	
5415500	20.1	37.3	3.0	12400.	990013	6363.0	0.8	2.7	
5418750	1.9	35.2	3.0	700.	990014	2.2	40.3	2.8	
5438250	85.1	5.7	2.8	4360.	990015	14.4	7.4	2.7	

where Q50 is the 50-year peak discharge, AREA is the basin's drainage area, SLOPE is the average basin slope, and I24,2 is the 2-year, 24-hr rainfall intensity.

Next, the step-backward search procedure was run for two cases. In the first case, only 47 existing stations were considered as discretionary gauges. Recall that 38 of the 85 stations were not discretionary because they were selected as stations that must be continued or could not be continued. In the second case, 15 new stations were added to the set of discretionary stations. The two stations identified as stations that could not be continued are forced to be the first stations to be dropped by the step-backward search by giving them a relatively large cost. All stations were given a relative cost of 1 except for these two stations, which were given a cost of 1,000.

The results of the analysis for Cases 1 and 2 are presented in Tables 2 and 3, respectively. Figure 2 shows that, in this example, operating new stations provides a greater marginal decrease in the objective function (increase in regional information) than does operating only existing stations. The most effective stations to operate for the planning horizon can be determined by reading from the bottom to the top of Tables 2 and 3. That is, the last station listed for a given case is the best to operate, the next to last is the next best to operate, and so on.

CONCLUSIONS

The step-backward search method was presented as a procedure for the problem of deciding which gauging stations to operate in the future (including possible new stations) to minimize the sampling error in a regional hydrologic regression. The step-backward search method can be used to identify a feasible network design that is probably near the optimal; the method also gives the network manager a management tool that can (a) identify a nearly optimal gauging plan or network design, (b) provide insight into how much regional information is lost or gained by decisions to reduce or increase the operating budget, and (c) evaluate any proposed network design by comparing it with a nearly efficient design at the same budget level.

TABLE 2 COMPUTER RESULTS FOR CASE 1 IN WHICH NO NEW STATIONS ARE CONSIDERED AND FOR WHICH THE PLANNING HORIZON IS 20 YEARS

Step	Discontinued stations	Average sampling error	Relative Cost	Number of stations available for regression analysis
0	NONE	0.00223	2083.	85
1	3382520	0.00223	1083.	85
2	3380300	0.00223	83.	85
3	3345500	0.00223	82.	85
4	5555300	0.00223	81.	85
5	5590000	0.00223	80.	85
6	5587000	0.00223	79.	85
7	5554500	0.00223	78.	85
8	5557000	0.00223	77.	85
9	5556500	0.00223	76.	85
10	5557500	0.00223	75.	85
11	3338500	0.00223	74.	85
12	5415000	0.00223	73.	85
13	5555000	0.00223	72.	85
14	5554000	0.00223	71.	85
15	3380350	0.00223	70.	85
16	3336500	0.00223	69.	85
17	5590400	0.00223	68.	85
18	5440500	0.00223	67.	85
19	5588000	0.00223	66.	85
20	5589500	0.00223	65.	85
21	5439000	0.00223	64.	85
22	5439500	0.00223	63.	85
23	3338800	0.00223	62.	85
24	5438500	0.00223	61.	85
25	5440000	0.00223	60.	85
26	5586500	0.00223	59.	85
27	5438850	0.00223	58.	85
28	5587900	0.00223	57.	85
29	3338100	0.00224	56.	85
30	5555400	0.00224	55.	85
31	5551800	0.00224	54.	85
32	3336100	0.00225	53.	85
33	5557100	0.00225	52.	85
34	5551700	0.00226	51.	85
35	3384450	0.00226	50.	85
36	3344425	0.00226	49.	85
37	5438250	0.00227	48.	85
38	5551900	0.00227	47.	85
39	5587850	0.00228	46.	85
40	5554600	0.00229	45.	85
41	5438390	0.00230	44.	85
42	5586350	0.00232	43.	85
43	5551930	0.00233	42.	85
44	5586850	0.00234	41.	85
45	5555775	0.00236	40.	85
46	3344250	0.00238	39.	85
47	5438300	0.00239	38.	85
48	5439550	0.00241	37.	85
49	4087400	0.00247	36.	85

The following stations are not eligible to be discontinued:

3336900	3337500	3338000	3339000	3341700	3341900	3343400	3344000
3378000	3378635	3378650	3378900	3378980	3379500	3379650	3380400
3380500	3381500	3381600	3382025	3382100	3382170	3382510	3385000
3612200	3614000	4087300	5414820	5415500	5418750	3344500	3346000
3380450	3380475	3385500	3612000				

TABLE 3 COMPUTER RESULTS FOR CASE 2 IN WHICH 15 NEW STATIONS (NUMBERS BEGINNING WITH 9900) ARE CONSIDERED AS DISCRETIONARY SITES AND FOR WHICH THE PLANNING HORIZON IS 20 YEARS

Step	Discontinued stations	Average sampling error	Relative Cost	Number of stations available for regression analysis
0	NONE	0.00188	2098.	100
1	3380300	0.00188	1098.	100
2	3382520	0.00188	98.	100
3	5555300	0.00188	97.	100
4	3345500	0.00188	96.	100
5	5590000	0.00188	95.	100
6	5554500	0.00188	94.	100
7	990011	0.00190	93.	99
8	5557000	0.00190	92.	99
9	3338500	0.00190	91.	99
10	5556500	0.00190	90.	99
11	5557500	0.00190	89.	99
12	5554000	0.00190	88.	99
13	5555000	0.00190	87.	99
14	5587000	0.00189	86.	99
15	5415000	0.00189	85.	99
16	3336500	0.00189	84.	99
17	5440500	0.00189	83.	99
18	5439500	0.00189	82.	99
19	5439000	0.00189	81.	99
20	5590400	0.00189	80.	99
21	3380350	0.00189	79.	99
22	5438500	0.00189	78.	99
23	5440000	0.00189	77.	99
24	3338800	0.00190	76.	99
25	5588000	0.00189	75.	99
26	5589500	0.00189	74.	99
27	990008	0.00190	73.	98
28	5438850	0.00190	72.	98
29	5551700	0.00190	71.	98
30	5551900	0.00190	70.	98
31	5586500	0.00191	69.	98
32	990006	0.00191	68.	97
33	990003	0.00192	67.	96
34	3338100	0.00193	66.	96
35	5438250	0.00193	65.	96
36	3336100	0.00193	64.	96
37	5557100	0.00194	63.	96
38	5587900	0.00194	62.	96
39	5551800	0.00194	61.	96
40	990010	0.00195	60.	95
41	990014	0.00197	59.	94
42	990009	0.00199	58.	93
43	990007	0.00201	57.	92
44	5438390	0.00201	56.	92
45	3384450	0.00201	55.	92
46	5551930	0.00202	54.	92
47	5555400	0.00202	53.	92
48	990002	0.00204	52.	91
49	3344425	0.00205	51.	91
50	990012	0.00206	50.	90
51	990005	0.00208	49.	89
52	5587850	0.00209	48.	89
53	5554600	0.00210	47.	89
54	5586350	0.00211	46.	89
55	5555775	0.00212	45.	89
56	990004	0.00215	44.	88
57	5439550	0.00216	43.	88
58	5438300	0.00217	42.	88
59	5586850	0.00219	41.	88
60	990001	0.00224	40.	87
61	3344250	0.00226	39.	87
62	990013	0.00233	38.	86
63	990015	0.00241	37.	85
64	4087400	0.00247	36.	85

The following stations are not eligible to be discontinued:

3336900	3337500	3338000	3339000	3341700	3341900	3343400	3344000
3378000	3378635	3378650	3378900	3378980	3379500	3379650	3380400
3380500	3381500	3381600	3382025	3382100	3382170	3382510	3385000
3612200	3614000	4087300	5414820	5415500	5418750	3344500	3346000
3380450	3380475	3385500	3612000				

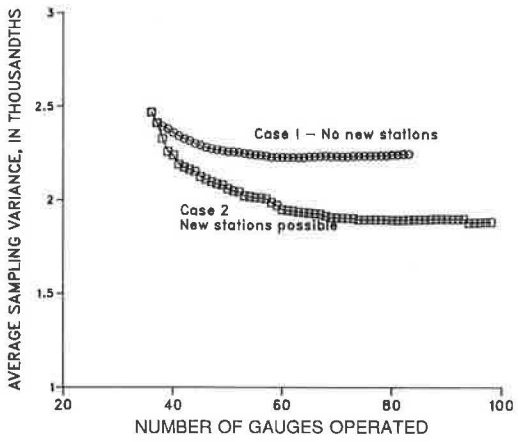

FIGURE 2 Results of network analysis.

REFERENCES

1. J. R. Stedinger and G. D. Tasker. Regional Hydrologic Analysis I. Ordinary, Weighted, and Generalized Least Squares Compared. *Water Resources Research*, Vol. 21, No. 9 1985, pp. I421–I432.
2. G. D. Tasker and J. R. Stedinger. An Operational GLS Model for Hydrologic Regression: *Journal of Hydrology*, Vol. III, 1989, pp. 361–375.
3. R. A. Fisher. *The Design of Experiments*. Oliver and Boyd, London, 1949.
4. G. W. Curtis. Technique for Estimating Flood-Peak Discharges and Frequencies on Rural Streams: Water Resources Investigations Report 87-4207, U.S. Geological Survey, 1987, 79 pp.

Publication of this paper sponsored by Committee on Hydrology, Hydraulics, and Water Quality.

Velocity Profiles and Scour Depth Measurements Around Bridge Piers

VINCENZA C. SANTORO, PIERRE Y. JULIEN, EVERETT V. RICHARDSON, AND STEVEN R. ABT

Local scour around a model of the Schoharie bridge pier was experimentally investigated in the laboratory. The tests simply focused on the effects of the angle of attack and flow velocity on the maximum depth of scour. Clear-water scour conditions prevailed, that is, the shear stress at the bottom in the upstream flow is always less than the critical value for beginning of sediment motion. The experimental results indicate that the effect of the angle of attack is related to the undisturbed flow Froude number. In particular, the ratio of the measured scour depths for skewed and aligned piers decreases with increasing Froude numbers. Velocity is found to have an important influence on scour depth.

The 1987 bridge failure on the Schoharie Creek in New York State claimed 10 lives and required considerable effort to rebuild the structure. The bridge collapse has been attributed to the scouring action of the flow around its piers. The risk of bridge failure because of pier scour and the design of appropriate countermeasures remain serious concerns for thousands of bridges in the United States and abroad. The past 50 years of research provides basic understanding of the physical mechanism of local scour; nevertheless, the quantitative dependence of the scour depth on the scouring parameters justifies further investigations because existing scour equations are not yet fully reliable.

A series of experiments was conducted at Colorado State University using a laboratory model of one of the Schoharie Creek bridge piers. The main objective was to investigate pier scour under the effects of two variables: angle of attack and mean flow velocity. Two sets of runs were completed, one with the pier aligned with the flow and one with the pier angled at 10 degrees with respect to the main flow direction. Within each set of runs the upstream velocity was maintained below the critical conditions of motion of the bed material, thus clear-water scour conditions prevailed during the experiments. Scour depth, change in water surface elevation, time-averaged point velocity, and maximum velocity fluctuations were measured along six cross sections near the pier.

EXPERIMENTAL SETUP AND PROCEDURE

The experiments were conducted in a 61- × 2.4- × 1.2-m recirculating laboratory flume at the Engineering Research Center. A large-scale (1:15) model of the Schoharie Creek bridge pier is shown in Figure 1. The footing has a rectangular shape, wider and longer than the pier itself, which is well rounded on both ends. Metal pieces fix the model pier to the flume sidewalls. Pea-size gravel (D_{50} = 3.3 mm) covers the flume bed up to the top of the foundation footing. Rails on the top of each flume sidewall support a motorized carriage holding a point gauge, a depth measuring device, and the current meter probe used for velocity measurements. In the first three tests, the pier was aligned with the flow; in the remaining three tests, the pier was skewed at an angle α of 10 degrees between the pier axis and the main flow direction. The discharge and slope were controlled to maintain average velocities of 0.3, 0.6, and 0.9 m/sec while keeping the flow depth constant at y_1 = 0.3 m for each run. The test conditions are presented in Table 1. The downstream conditions were controlled by a tail gate. With the study reach located 30 m upstream of the tailgate, steady uniform flow conditions prevailed in the study reach without the pier. Each run was allowed sufficient time, at least 8 hr, to simulate conditions approaching the maximum expected scour.

Reference nets in Figures 2 and 3 indicate the location of each measuring vertical. In the case of the aligned pier, measurements were taken on only half the flow field after the symmetry in velocity profiles on each side of the pier was checked. At least five velocity measurements were taken on each vertical, except where deposits significantly reduced the flow depth. When the erosive action allowed it, measurements were also taken below the zero reference (the elevation of the undisturbed bed).

Velocity measurements were taken using a Marsh-McBirney 2D electromagnetic current meter. Average values and maximum fluctuations of the two velocity components parallel and perpendicular (in a plane parallel to the bottom of the flume) to the main flow direction were recorded. The current meter was connected to an HP 3468 Multimeter connected to an HP 82162A thermal printer and to an HP 71 calculator in an IL loop. Over a period of 30 sec, 57 measurements were read, stored, and averaged for each probe position and each flow direction. Changes in the bed elevation and water surface elevation profiles were also compiled from these measurements by Santoro (*1*).

RESULTS

Flow Patterns Around the Pier

The downstream velocity distribution was obtained from the measurements at each cross section and at planes parallel to

V. C. Santoro, Department of Civil Engineering, Istituto di Idraulica Idrologia e Gestione delle Acque, Universita di Catania, Via le A. Doria 6, 95125 Catania, Italy. P. Y. Julien, E. V. Richardson, and S. R. Abt, Engineering Research Center, Colorado State University, Fort Collins, Colo. 80523.

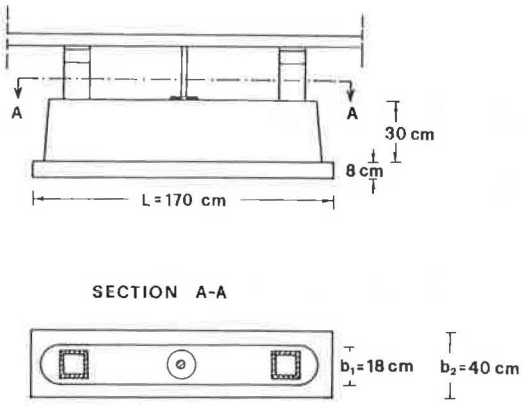

FIGURE 1 Geometric characteristics of the Schoharie bridge pier model.

TABLE 1 SUMMARY OF TEST CONDITIONS

Run number	Upstream flow depth y_1 [m]	Upstream flow velocity V [m/s]	Discharge Q [m^3/s]	Slope S [%]	Froude number Fr	Pier Angle α
1	0.3	0.3	0.223	0.014	0.176	0°
2	0.3	0.6	0.447	0.055	0.352	0°
3	0.3	0.9	0.670	0.123	0.529	0°
4	0.3	0.3	0.223	0.014	0.176	10°
5	0.3	0.6	0.447	0.055	0.352	10°
6	0.3	0.9	0.670	0.123	0.529	10°

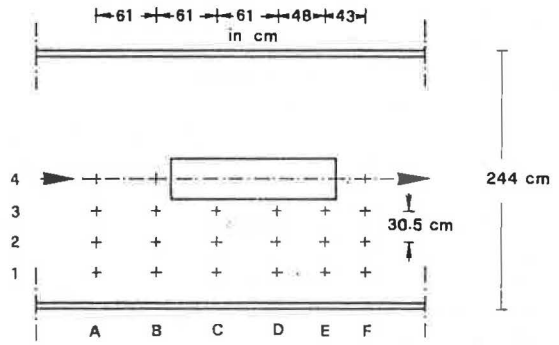

FIGURE 2 Reference net for aligned pier (α = 0 degrees).

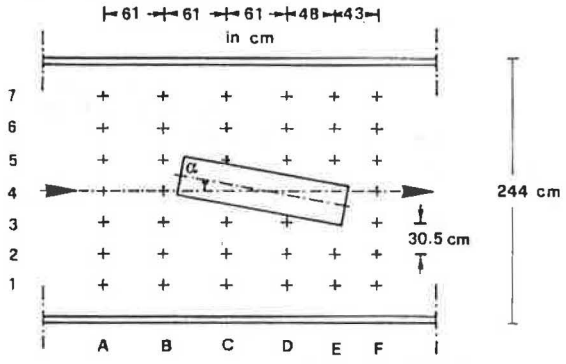

FIGURE 3 Reference net for angled pier (α = 10 degrees).

the flume bed. The flow is slowed down in the central area upstream of the pier; this effect is accentuated for the angled pier. Figure 4 shows the results of the measured velocity distribution at Cross Section C from Run 4 for the angled pier. The velocity is maximum on the side the pier is skewed toward, and the maximum velocity is found at an elevation ranging between 0.4 and 0.7 of the undisturbed flow depth y_1. The ratio of the maximum measured velocity to the undisturbed flow velocity is 1.4 for the aligned pier and 1.6 for the angled pier.

Lower velocity is measured in the wake of the pier, and asymmetric profiles result for the angled pier. Figure 5 shows a plan view of the dimensionless velocity distribution in a section parallel to the bottom of the flume set at an elevation corresponding to 0.4 of the undisturbed flow depth y_1. The overall flow pattern is described well in that maximum velocities are found on the narrow sides of the skewed pier. However, the number of verticals precludes any detailed analysis of the flow near the pier and along the sidewalls. Discharge measurements from the orifice inserted in the recirculating pipeline compared favorably with the calculated discharge from the integration of the velocity distribution over the cross section.

Total Scour Around the Pier

The total scour around the pier combines the effects of two conditions: contraction scour caused by the higher velocity in the reduced cross-sectional area near the pier, and local scour caused by the horseshoe vortex around the base of the pier. Qualitative and comparative information can be drawn from the photographs and measurements of the flume bed surface at the end of each run.

Under low flow velocities, the extent of scour is relatively limited downstream of the pier. Only the front part of the pier was exposed. At higher velocities (Figure 6), the scour hole extended alongside the entire pier and a deposition area formed downstream of the pier. The scour pattern of the skewed pier is highly asymmetrical with the maximum scour localized on the side toward which the pier is skewed (Figure 7). The areas of deposition downstream of the pier were more accentuated. Table 2 presents the geometric characteristics of the scour hole in the different runs. The side slope of the scour hole is steeper for the aligned pier than for the skewed pier.

Contraction Scour

The presence of the pier contracted 7.3 percent of the channel width at the pier level and 16 percent at the footing level. The measurements suggest that at least part of the erosion alongside the pier was caused by contraction scour. Measured contraction scour depths were compared with the depths predicted by Laursen's equation (*2*), which computes the contraction scour depth y_c as the difference between the flow depth y_2 in the contracted reach and the upstream flow depth y_1:

$$y_c = y_2 - y_1 \quad (1)$$

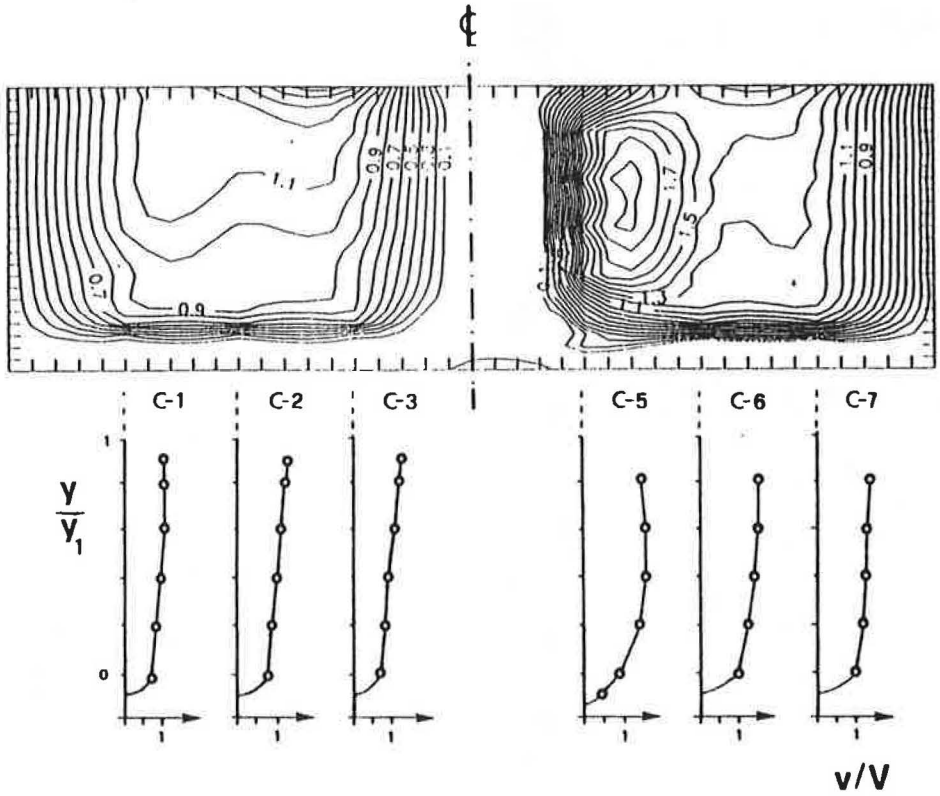

FIGURE 4 Dimensionless velocity distribution v/V, Run 4 (Section C, V = 0.3 m/sec, and α = 10 degrees).

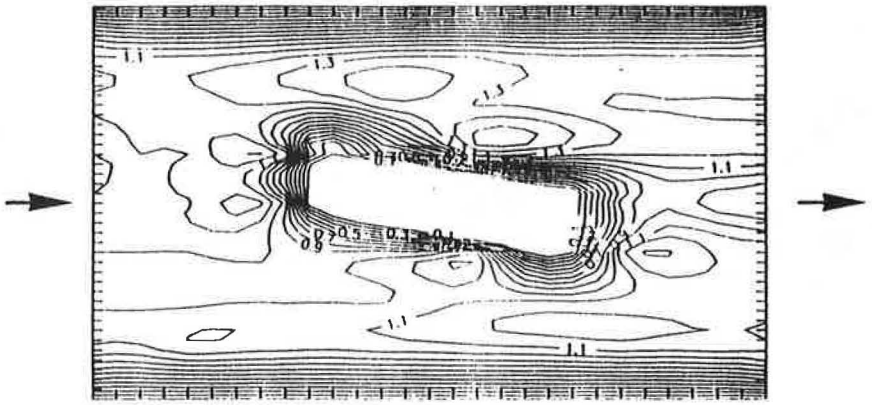

FIGURE 5 Plan view of the dimensionless velocity distribution v/V at a depth y = $0.4y_1$, Run 4 (V = 0.3 m/sec, α = 10 degrees).

where y_2 is given by

$$\frac{y_2}{y_1} = \left(\frac{W_1}{W_2}\right)^A \left(\frac{n_2}{n_1}\right)^B \tag{2}$$

in which W is the channel width, n is Manning's coefficient, A and B are two exponents whose values are tabulated as a function of the mode of transport of the bed material in the contracted reach, and the subscripts 1 and 2 refer to the undisturbed and contracted reach, respectively. Assuming $n_1 = n_2$ while the width ratio is based on the pier width, a constant value of y_c = 0.035 m is obtained for all test conditions. This result is compared with the measurements in Figure 8.

Maximum Local Scour Depths

The deepest scour always occurred right in front of the pier where contraction scour was not yet present. This finding means that the maximum scour depth is not significantly influenced by the contraction scour. It was then possible to

FIGURE 6 Scour alongside the aligned pier (Run 3).

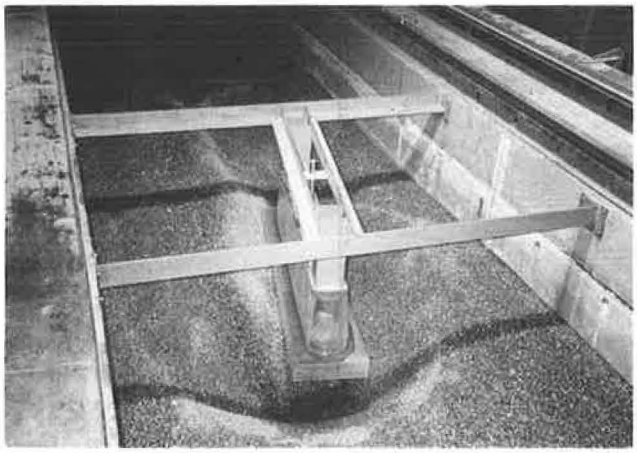

FIGURE 7 Scour around the skewed pier (Run 6).

compare the measured local scour depths y_{sm} with the maximum calculated scour depth y_{sc} from the following equations.

- CSU equation (*3*):

$$\frac{y_{sc}}{y_1} = 2.0\left(\frac{b}{y_1}\right)^{0.65} \mathrm{Fr}^{0.43} \tag{3}$$

TABLE 2 GEOMETRIC CHARACTERISTICS OF THE SCOUR HOLE

Run number	Upstream flow velocity V [m/s]	Pier angle α	Scour depth y_s [m]	Scour width [m]	Side slope
1	0.3	0°	0.076	0.152	1.00
2	0.6	0°	0.158	0.274	0.87
3	0.9	0°	0.305	0.457	0.75
4	0.3	10°	0.122	0.213	0.88
5	0.6	10°	0.241	0.357	0.75
6	0.9	10°	0.427	0.518	0.61

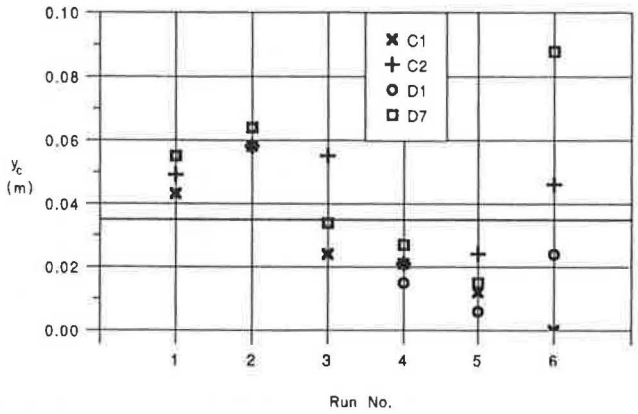

FIGURE 8 Computed and measured contraction scour depths.

- Laursen equation (*2*):

$$\frac{b}{y_1} = 5.5\,\frac{y_{sc}}{y_1}\left[\frac{\left(\dfrac{y_{sc}}{11.5y_1} + 1\right)^{7/6}}{(\tau_0/\tau_c)^{1/2}} - 1\right] \tag{4}$$

- Froehlich equation (*4*):

$$\frac{y_{sc}}{b} = 0.32\phi\left(\frac{b^1}{b}\right)^{0.62}\left(\frac{y_1}{b}\right)^{0.46}\mathrm{Fr}^{0.20}\left(\frac{b}{D_{50}}\right)^{0.08} + 1 \tag{5}$$

where

y_1 = upstream flow depth,
b = pier width,
Fr = Froude number,
τ_0 = bed shear stress,
τ_c = critical bed shear stress,
b^1 = projected pier width normal to the flow direction,
D_{50} = mean sediment size, and
ϕ = pier shape factor (ϕ = 1 for a round-nosed pier).

Because the complex pier geometry provides both the pier width and the footing as possible values for b, calculations of scour depth using both values are considered separately. Figures 9 and 10 show the results.

It is concluded from the experimental results shown in Figures 9 and 10 that the pier width, rather than the foundation

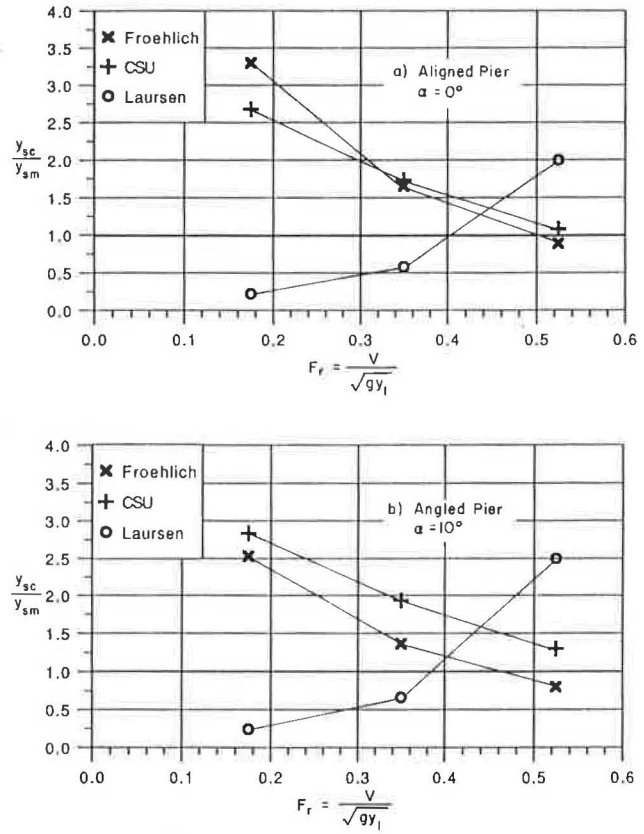

FIGURE 9 Ratio of computed to measured scour depths using b = pier width.

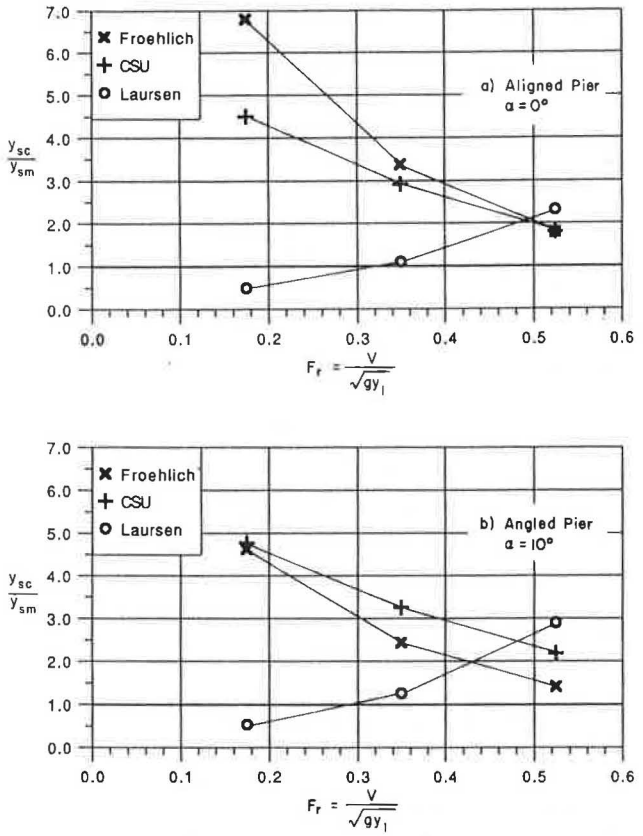

FIGURE 10 Ratio of computed to measured scour depths using b = footing width.

width, is more appropriate for calculating local pier scour. In general, these equations tend to overestimate the scour depth, with the exception of Laursen's equation, which underestimates the scour depth at low Froude numbers.

Influence of the Pier Angle

These experiments allow direct comparison between the scour depth $y_{s10°}$ when the pier is angled at 10 degrees, and pier scour of an aligned pier $y_{s0°}$, the other parameters being equal. The ratio $y_s^* = y_{s10°}/y_{s0°}$ between corresponding scour depths separates the effect of the pier angle α in the case of these experiments. Figure 11 shows the values of y_s^* from laboratory measurements obtained from the three scour depth equations. In Figure 11, pier orientation seems correlated to the Froude number, decreasing when the Froude number increases. The possibility of a dependence of the angle correction coefficient on the flow velocity (or Froude number) is not unreasonable. The strength of the vortices depends on both the upstream velocity and the projected pier width perpendicular to the flow direction (which is affected by the pier angle). The influence of the angle of attack might be related to the flow average velocity in the sense that as the Froude number increases (here velocity and Froude number are used interchangeably because the depth remains constant) and the inclination of the pier increases, the scour depth cannot increase indefinitely but must approach an ultimate limit.

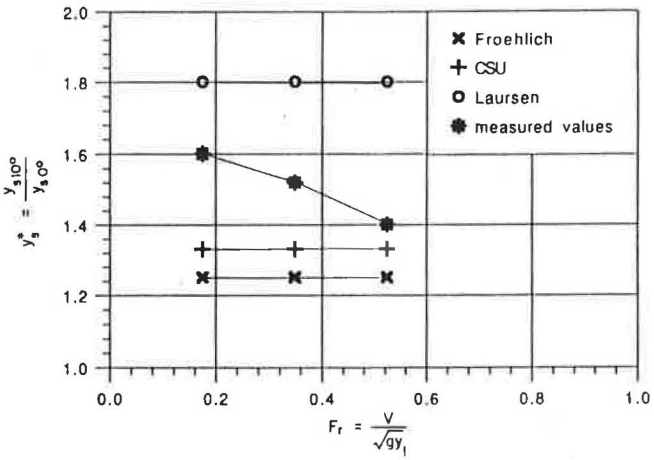

FIGURE 11 Effect of pier alignment on pier scour.

Maximum Velocities

Some riprap design methods are based on velocity measurements. Typically, a representative riprap size or stone weight can be determined from an average velocity, bottom velocity, or reference velocity. For instance, the Isbash formula relates the riprap stone weight to the sixth power of the velocity. It is then clear that riprap design is highly sensitive to velocity measurements.

In the particular case of riprap design around piers, the velocity increases because of both the contraction effect and the turbulence. Maximum and minimum instantaneous velocities were measured at each point to provide an indication of the maximum velocity fluctuations normally expected around bridge piers. The measurements indicate that the maximum ratio of the maximum point velocity v_{max} to the average undisturbed velocity V decreases with increasing velocity. The maximum measured ratio is as high as 1.8, and it is registered during Run 4.

Possible Armoring Effect

Two samples of the bed material from the surface of the front part of the scour hole were taken and analyzed after the tests. The sieve analyses before and after Run 3 indicate that the amount of particles smaller than approximately 2 mm on the scour hole surface had significantly diminished, whereas all the particles smaller than 0.5 mm had been totally washed out. However, the tests results do not indicate significant armoring effects.

Comparison with Prototype Scour Depth

At a linear scale of 1:15, the Froude number analogy yields a velocity scale 1:3.87. The prototype conditions for which field data were available (*5*) are closely modeled in Run 3. The measured scour depth in the experiments scaled to 4.57 m of scour depth at the prototype scale, which compares to the field-measured scour depth of 4.27 m.

CONCLUSIONS

The following considerations can be drawn from these laboratory experiments on velocity and scour depth measurements around a model of the Schoharie bridge pier:

1. The time-averaged point velocity distribution in cross and plan sections exhibits two areas of increased velocities alongside the pier. The recorded values were as high as 1.6 times the mean upstream approach velocity.
2. With the initial bed surface at the same elevation as the top of the footing, scour depth calculations based on pier width are more appropriate than those based on the footing width.
3. The measured local scour depths are in reasonable agreement with the local scour depths calculated from three scour equations. All equations perform better at higher values of the Froude number (Fr > 0.3).
4. The ratio y_s^* of the angled pier scour depth $y_{s(10°)}$ to the aligned pier scour depth $y_{s(0°)}$ decreases with increasing Froude number as shown in Figure 11. Although few experiments are considered, the detected trend is nevertheless significant.
5. The ratio of the maximum velocity fluctuations to the mean undisturbed upstream velocity decreases as the mean flow velocity increases. Values as high as 1.8 times the mean approach velocity were measured around the angled pier.
6. From the measurements reported at the prototype scale of 1:15, the run with an aligned pier and the maximum velocity (3.48 m/sec) gave a scour depth at the prototype scale of 4.57 m, which compares well with the field-measured scour depth of 4.27 m.

NOTATION

b = pier width,
b^1 = projected width of the pier in perpendicular direction to the main flow,
D_{50} = mean sediment size,
Fr = Froude number,
L = length of the pier,
n = Manning roughness coefficient,
Q = total discharge,
V = mean approach flow velocity,
y_1 = upstream flow depth,
y_2 = flow depth in the contracted reach,
y_c = contraction scour,
y_s = maximum depth of scour below mean bed level,
y_{sc} = calculated local scour depth,
y_{sm} = measured local scour depth,
$y_{s10°}$ = scour depth at an angle α = 10 degrees,
$y_{s0°}$ = scour depth at an angle α = 0 degrees,
y_s^* = ratio $y_{s10°}/y_{s0°}$,
W = width of the channel,
α = angle of attack of the flow,
ϕ = pier shape factor (ϕ = 1 for round-nosed piers),
τ_0 = bed shear stress, and
τ_c = critical shear stress.

REFERENCES

1. V. C. Santoro. *Experimental Study on Scour and Velocity Field around Bridge Piers*. M. S. thesis, Colorado State University, Fort Collins, July 1989.
2. E. M. Laursen. *Predicting Scour at Bridge Piers and Abutments*. General Report 3, University of Arizona, Tucson, 1980.
3. E. V. Richardson, D. Simons, and P. Y. Julien. *Highways in the River Environment*. FHWA-HI-90.016. FHWA, U.S. Department of Transportation, 1990.
4. D. C. Froehlich. *Local Scour at Bridge Piers from Onsite Measurements*. Water Resources Division, U.S. Geological Survey, 1987.
5. E. V. Richardson, J. F. Ruff, and T. E. Brisbane. Schoharie Creek Bridge Model Study. *Proc., ASCE, Hydraulic Division Specification Conference*, Colorado Springs, Colo., Aug. 1988.

Publication of this paper sponsored by Committee on Hydrology, Hydraulics, and Water Quality.

A Temporal, Spatial Pier Scour Model

PEGGY A. JOHNSON AND RICHARD H. MCCUEN

Civil engineers are faced with problems involving all aspects of aging infrastructure. One area in critical need of attention is the design, monitoring, and maintenance of bridge piers where local pier scour is a concern. The scour depth at a particular time during the design life of a bridge is a function of the flow-duration characteristics of storms that occurred before the time of interest. Current scour models and equations provide a single-valued estimate of the ultimate scour depth for a design discharge; the engineer does not have a time-dependent estimate of the scour depth. The objective of this study was to develop a conceptual, time-dependent pier scour model and a methodology to assess the risk of bridge failure because of pier scour over the life of the bridge. The time-dependent pier scour model was formulated and calibrated with laboratory data and observations as well as field observations. The time dependency enables the engineer to estimate the scour depth at any time during the life of the bridge.

Civil engineers are faced with problems involving all aspects of aging infrastructure—from monitoring and maintenance to replacement and design. One area in critical need of attention is the design and protection of bridge piers where local scour is a concern.

Current literature contains many equations and models for predicting the depth of scour that can be expected around a bridge pier. Most of these models provide a single maximum value for the scour depth rather than the scour depth as a function of time. There are two significant problems with this. First, these models are time invariant in that they cannot estimate the number of years that will be required to scour to the computed depth; thus, the time-invariant models do not suggest the safe design life associated with the predicted scour depth. Second, at a bridge where the current scour depth has been measured, the existing models do not enable the engineer to estimate the future progress of scour.

The goals of this study were (a) to formulate a model that could account for the temporal and spatial variation of scour at a bridge pier, and (b) to use the model to determine the effect of pier geometry, channel bed materials, and hydrologic characteristics on pier scour.

BRIDGE PIER SCOUR

Scour is the erosive action of water in excavating and carrying away material from the channel bed (*1*). An obstruction, such as a bridge, interferes with the flow of the stream, which changes the flow patterns at the obstruction. This results in a deepening of the scour hole around the bridge pier beyond the level that would naturally occur from degradation and general scour. This is commonly referred to as "local scour."

Department of Civil Engineering, University of Maryland, College Park, Md. 20742.

The flow pattern around the bridge pier is complex. As the streamflow approaches the pier, an adverse pressure gradient caused by the pier drives a portion of the approach flow downward just ahead of the pier. This downflow is thought by some researchers to be the main cause of local scour around bridge piers (*2*). According to Chiew (*2*), the rate of erosion of the scour hole is directly associated with the magnitude of the downflow, which is directly related to the velocity of the approaching river flow. The jet of water in the downflow can be used to represent the strength of the vortex. The downflow is an integral part of the vortex that forms in the scour hole. Although the vortex significantly contributes to the erosion, the vortex flow pattern is highly correlated with the downflow; therefore, for the purpose of estimating the depth of scour, a significant correlation between downflow scour and vortex scour is assumed in the scour model. Because the downflow can be described in terms of a measurable quantity, velocity, this description was chosen as the best alternative to modeling the vortex.

The many parameters that affect bridge pier scour may be classified as streamflow characteristics, such as velocity and flow depth; bed material characteristics, such as the sediment size and distribution; and bridge pier characteristics, such as the width, shape, and length of the pier. Although the model uses these parameters as input, these parameters are defined elsewhere (*3–5*).

TEMPORAL PIER SCOUR MODEL

A conceptual, time-dependent pier scour model was developed to assess the effect of various hydrologic conditions and other parameters on pier scour. The model determines the temporal development of a scour hole just upstream of a bridge pier. The functional forms used to represent the processes were selected so that the model would reflect relationships suggested by laboratory observations and measurements in the literature (*2,3,6–9*).

The purpose of developing a time-dependent model was to provide a method of assessing the effects of changes in parameters—such as pier width, flow velocity, and riprap size—on the scouring process as storms of various flow velocities and durations move past a bridge pier. Such a conceptually based model can be used for either project evaluation (analysis) or design (synthesis).

Model Components

The model consists of three main components, which estimate (a) the downflow velocity, (b) the termination velocity (anal-

ogous to a velocity of incipient motion for a channel bed), and (c) the erosion rate and scour depth. A brief description of each component follows. Further detail is provided by Johnson (*10*).

Downward Velocity

The maximum downward velocity is a function of the approach velocity, pier size, and flow depth. An increase in the velocity, pier size, or flow depth would result in an increase in the maximum downward velocity (V_{dmax}). However, on the basis of experimental observation, V_{dmax} probably does not exceed one to two times the approach velocity. Therefore, V_{dmax} may be expressed as an exponential function

$$V_{dmax} = C_1 V_0[1 - \exp(-C_2 bY)] \quad (1)$$

where

C_1 and C_2 = numerical constants,
V_0 = approach velocity,
b = pier width, and
Y = approach flow depth.

The form of Equation 1 was selected because it defines a curve exhibiting the trend suggested by results from laboratory studies.

The maximum downward velocity occurs at some depth beneath the level of the original bed elevation. From this depth to the bottom of the scour hole, the downward velocity gradually decreases from V_{dmax}. The downward velocity at any depth below the location of V_{dmax} within the hole is then some portion of V_{dmax}

$$V_d = KV_{dmax} \quad (2)$$

where V_d is the downward velocity at some depth and K is a function of the scour depth. Using Melville's (*7*) data, the decrease in velocity toward the bottom of the hole can be approximated with a logistic function. The following expression for K provides a rational structure and incorporates variables that are expected to affect the relationship between V_d and V_{dmax}:

$$K = 1 - \frac{1}{1 + \exp(-C_3 D - C_4 b)} \quad (3)$$

where

C_3 = shape parameter,
C_4 = location parameter, and
D = depth of scour.

Using D equal to the current depth of the scour hole enables the value of K at the base of the hole to be computed. Equation 3 assumes that the downward velocity occurs at the level of the original bed elevation, then decreases with depth in the hole. The velocity at the base of the hole for any depth D may then be found by substituting Equation 3 into Equation 2.

Termination Velocity

The downward velocity eventually decreases to a value that is no longer capable of causing erosion in the hole. The velocity at which this occurs is termed the "termination velocity" and is derived using a summation of the primary resisting and erosive forces. At incipient motion of the particles at the bottom of the scour hole,

$$F_r = F_e \quad (4)$$

where F_r is the resisting force caused by the weight of the sediment and F_e is the erosive force caused by the impinging jet of the water in the downward flow just upstream of the pier. The shear stress caused by the impinging jet, as shown in Figure 1, is modeled with the momentum equation

$$\tau = \{(\rho V_d^2 \cos\phi)^2 + [\rho V_d^2(1 - \sin\phi)]^2\}^{0.5}$$
$$\tau = \rho V_d^2 (2)^{1/2}(1 - \sin\phi)^{0.5} \quad (5)$$

where

V_d = downward velocity at the base of the hole,
ρ = density of water, and
ϕ = angle of repose (as shown in Figure 1).

At incipient motion, the termination velocity, V_t (here, V_t is actually the initiation velocity) may be substituted for V_d in Equation 5.

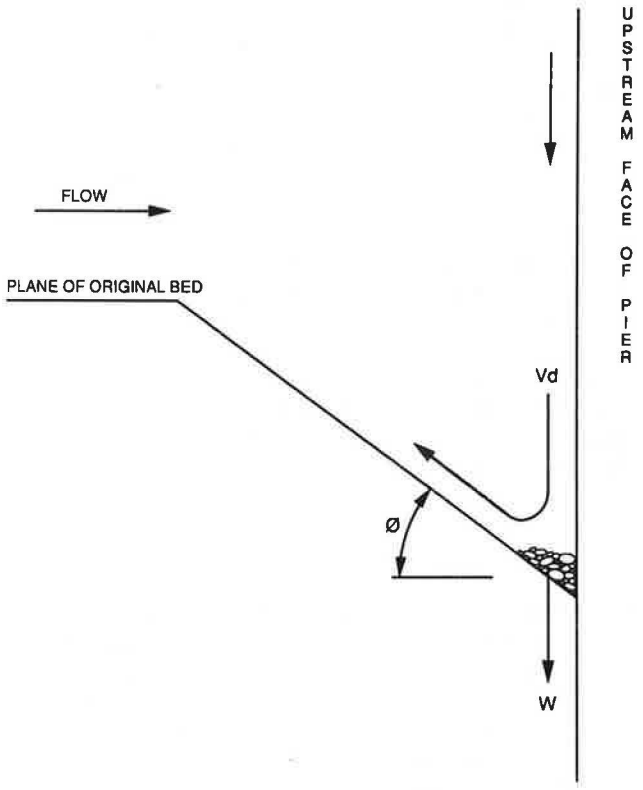

FIGURE 1 Impinging jet at the base of a pier in the scour hole.

Assuming that the particles are spherical with a cross-sectional or projected area of $\pi d^2/4$ (d is the sediment diameter), the weight component along the slope is

$$W = \rho_s g\left[\frac{4}{3}\pi\left(\frac{d}{2}\right)^3\right] \sin \phi \tag{6}$$

where ρ_s is the density of the sediment. Equations 5 and 6 may be substituted into Equation 4 to obtain

$$\frac{1}{6}\rho_s g\pi d^3(\sin \phi) = \frac{1}{4}\pi d^2 \rho V_t^2 (2)^{1/2}(1 - \sin \phi)^{0.5} \tag{7}$$

Solving for the termination velocity in the hole yields

$$V_{tu}^2 = \frac{2\rho_s g d \sin \phi}{3\rho(2)^{1/2}(1 - \sin \phi)^{1/2}} \tag{8}$$

where V_{tu} is the unadjusted termination velocity. Equation 8 is valid only for uniform sediments and is similar to White's (*11*) derivation for the threshold condition on a channel bed. Equation 8 must be modified to account for turbulence and circulation factors through the use of a numerical coefficient.

For nonuniform sediments, the termination velocity is also a function of the sediment gradation ($G = d_{84}/d_{50}$), particularly at low velocities. As G increases, the effective termination velocity increases, the erosion rate decreases, and the scour depth decreases. The following equation was developed to represent the termination velocity for uniform and nonuniform sediments:

$$V_t = C_6\left[\frac{2\rho_s g d G \sin \phi}{3\rho(2)^{1/2}(1 - \sin \phi)^{1/2}}\right]^{1/2} + C_7 G \exp(-C_5 V_0) \tag{9}$$

where C_6 reflects other factors involved in initiating particle motion, such as the circulation in the hole; and C_5 and C_7 are fitting coefficients.

Erosion Rate

The erosion rate is directly associated with the downward velocity. Erosion rate equations commonly involve the difference between a value of shear stress or velocity and a critical shear stress or critical velocity (*12–14*). Therefore, the following functional form was selected for estimating erosion rates:

$$\frac{\Delta D}{\Delta t} = C_8(V_d - V_t) \tag{10}$$

where

D = scour depth (m),
t = time required to scour depth D (sec), and
C_8 = numerical coefficient.

The downflow velocity (V_d) decreases according to Equation 2 until it reaches the termination velocity (V_t). For clear-water conditions, scour ceases when the erosion rate becomes zero. For live bed scour, scour ceases when the erosion rate equals the rate of sediment transport into the scour hole. Equation 10 may be used to determine the scour depth for a given time increment. The final scour depth is taken as the equilibrium or maximum depth.

Model Calibration

Data obtained from laboratory studies by Melville (*7*) and Chiew (*2*) were used to calibrate the model. The coefficients for Equations 1, 3, 4, and 10 were fit simultaneously using a nonlinear least squares method. Initial estimates of the coefficients, which are required for operating the nonlinear least squares program, were obtained from the literature where possible. An angle of repose of 30 degrees was assumed for the calibration, because this value is typical for the rounded sands found in a river setting. The specific gravity of the sediment was assumed to be 2.65. The optimization procedure resulted in the following coefficients, which are presented in Table 1: from Equation 1, $C_1 = 0.8$ and $C_2 = 134$; from Equation 3, $C_3 = 63$ and $C_4 = 1.05$; from Equation 9, $C_5 = 31.2$, $C_6 = 2$ for live-bed conditions and 0.65 for clear-water conditions, and $C_7 = 1.0$; and from Equation 10, $C_8 = 0.000015$.

For the overall data set, the resulting set of coefficients yielded a correlation coefficient of approximately 0.80 and a standard error–to–standard deviation ratio of about 0.62.

Calibration for Field Scale

On the basis of the model calibrated for laboratory conditions, a model appropriate for field use was fit. The numerical coefficients were adjusted to represent larger piers, flow depths, and flow velocities at actual bridge sites. Those coefficients associated with sediment size were not adjusted because the sediments used in the laboratory experiments were not unlike those that are expected in a river environment.

The coefficients were adjusted by assuming average pier sizes, flow depths, and velocities for field conditions, then scaling the coefficients accordingly. Many pier widths are in the range of 1 to 3 m; thus an average pier width of 2 m was assumed. Dividing this average width by the average width used in the laboratory (0.04 m) results in a laboratory-to-prototype ratio of 1:62. Then, assuming that pier Froude

TABLE 1 NUMERICAL COEFFICIENTS FOR LABORATORY AND FIELD SCOUR MODELS

C_i	Units	Laboratory	Field
1 (Eq. 1)		0.8	0.8
2 (Eq. 1)	m_2^{-1}	134.0	0.2
3 (Eq. 3)	m^{-1}	63.0	1.02
4 (Eq. 3)	m^{-1}	1.05	1.05
5 (Eq. 9)	$(m/s)^{-1}$	31.2	3.95
6 (Eq. 9)		2.0	2.0
7 (Eq. 9)	m/s	1.0	1.0
8 (Eq. 10)		0.000015	0.000015

numbers for laboratory and field conditions are similar results in a velocity scaling ratio of $1:(62)^{1/2}$. The scaling ratio for flow depth was obtained in a similar manner. An average flow depth of 2 m was assumed. Dividing the average laboratory flow depth of 0.2 m by 2 m results in a scaling ratio of 1:10. The resulting numerical coefficients for the field model are presented in Table 1.

The set of coefficients determined by the method described here may be used as default values. A more accurate set of coefficients may be determined by scaling the values for the particular bridge site, rather than scaling for a typical or average bridge; however, the default values will provide an estimate of the progression of the scour hole around the bridge pier.

After the field model was tested and satisfactory results obtained, components were added to the model to determine the effects of the shape of the pier nose and the angle of attack of the approach flow to the pier.

Pier Geometry

The geometry of the pier is important in determining the depth of scour. The wider the pier, the greater the resulting scour depth. Other aspects of the pier geometry, such as the shape of the nose of the pier and the angle at which the pier is situated with respect to the direction of the approach flow, also significantly affect the depth of scour. The pier width may be multiplied by two factors, K_1 and K_2, reflecting these factors, to obtain an effective pier width

$$b_e = K_1 K_2 b \tag{11}$$

The angle of attack and nose shape factors were added to the computer program using information from tables and figures provided by Tison (*15*), Laursen and Toch (*16*), Chabert and Engeldinger (*17*), and Laursen (*18*).

ASSUMPTIONS AND LIMITATIONS OF THE MODEL

In developing a time-dependent model, a number of assumptions were made. One of the most important assumptions is that loose refill material deposited in the scour hole as the flood recedes is instantaneously blown out of the hole when the next flood flow occurs.

The model described herein is classified as being time dependent. It has been observed frequently during laboratory experiments using sands and gravels that the scour hole forms in a short period of time. This observation may lead one to believe that pier scour is relatively independent of time. In the field, however, the scouring process may be time dependent for several reasons. The first is that the peak flood discharge of a single storm event may not be maintained long enough to scour to a maximum depth; therefore, it would take more than one such storm to scour to the maximum depth. Second, the sediments around the bridge piers will be subject to many different flood discharges; some will have an insignificant effect on the scouring process, and others will erode the hole to a new depth.

These varying flow-duration conditions have not been tested in a laboratory setting. The time dependency, even in cohesionless sediments, can be seen in bridge failures like that at the Schoharie Creek bridge. Although the piers were placed on glacial till (a nearly nonerodible geologic formation), the base of the scour hole was only as wide as the excavation. The scour hole developed in the cohesionless riprap and backfill placed in the excavation. Flood records show that the largest storm in the history of the bridge (76,500 ft^3/sec, a 100-year storm) occurred in 1955. The bridge failed 32 years later when a 50-year flood (64,900 ft^3/sec) occurred. Because the bridge did not fail during the larger storm, it must be concluded that the peak discharge was not sustained long enough to permit the hole to scour to the depth required for failure and therefore that there exists a time dependency.

The third assumption of the model, inherent in the time-dependency assumption, is that the model accounts only for cohesionless sediments, that is, sand and gravel. These are the sediments typically found in the excavation pits around the piers as backfill and riprap. The model does not account for situations where piles are driven into cohesive soils where there is no excavation.

The conceptual model considers only local scour around the piers. Perhaps a greater concern in some cases, and certainly an integral part of the scour process, is channel degradation. Over the course of a single storm and certainly over the life of a bridge, the bed elevation of the channel may change: either degradation or aggradation may occur. In some cases, degradation may be a more critical problem than local scour, exposing the pier to failure conditions. The assumption made here, however, is either that degradation does not occur or that the process of degradation can be treated separately from local scour.

STORM GENERATION

To assess the long-term progression of scour at a bridge pier, time-dependent hydrologic input must be used with the scour model. For this purpose, a storm-generation model was developed to simulate realistic flow sequences. The model can then be simulated for the design life of a bridge (e.g., 50 years) to evaluate the effect of individual design parameters (e.g., riprap size).

The model to generate flood flows consists of two parts (*10*). First, the number of storms above a threshold discharge (q_b) that will occur in a year (i.e., a partial duration series) is determined. Second, the storm magnitude for each of the storms in the partial duration series is generated.

The number of storms above the threshold discharge may be generated using a Poisson process. The Poisson parameter is estimated using the mean number of storms above q_b. The magnitudes of the storms (q) in the partial-duration series may be represented by the exponential distribution

$$q = -\beta \ln(U) + q_b \tag{12}$$

where

β = exponential parameter,
U = random uniform number between 0 and 1, and
q_b = base level or threshold discharge.

Although this single-parameter distribution is not easily fitted to a given set of data, it is a relatively simple distribution with a closed-form solution, making it easily adaptable in a simulation model.

The parameter of the exponential distribution is estimated by the mean of the discharge data. However, the fit of the distribution may be improved by optimizing the parameter. More information regarding the simulation of storm series was provided by Todorovic (*19*), Cunnane (*20*), North (*21*), Cruise and Arora (*22*), and Johnson (*10*).

EXAMPLE APPLICATION

As an example of simulating bridge pier scour over a period of years, the scour depth was computed and accumulated over a 75-year period. The 75-year simulations were performed under the assumptions of a 275-km^2 watershed, a pier 2.5 m wide and 6 m long, and a sediment size of 10 mm with a gradation of 18 (i.e., $d_{84}/d_{50} = 18$). The angle of attack of the approach flow to the pier was 5 degrees. For the storm simulator, the partial duration series threshold was 33 m^3/sec, the exponential parameter was 25, and the Poisson parameter was 3. The individual storms were assumed to be 24 hr in duration, distributed in a triangular hydrograph.

Figure 2 shows the increase in the mean scour depth with time. The scour depth increased rapidly during the first 15 years as storm waters removed the initial volume of material; however, the scour depth during this time remained low, less than about 1.7 m. At 20 years, the scour depth had increased to a value greater than 1.9 m, but the rate of increase in the scour depth had decreased. By 75 years, the scour depth had nearly reached a limiting value greater than 2.9 m.

RECOMMENDATIONS

To improve the model presented here, or any pier scour model, further research into the scour process is necessary. The vortex mechanism at the base of the pier must be examined. It is a complex process; thus, research must be undertaken that will focus on characterizing the vortex strength rather than attempting to derive a theoretical model. Characterizing the strength will provide a usable expression for the vortex strength in terms of shear stress or velocity that is a function of both the pier and flow characteristics.

The understanding and modeling of scour would also be enhanced by field data. Although some field data exist, they have been collected at various times during flooding (some during the flood recession, some several days later, etc.), using different equipment different criteria for determining where the bottom of the hole is. Research must be aimed at developing methods of monitoring scour around piers, including equipment that can withstand the turbulence in the vicinity of the pier and determine the depth to the actual bottom of the scour hole.

Most scour research deals only with sand and gravel as the sediment at the base of the pier. This is reasonable for many bridge pier situations, particularly those where the footing excavation was filled with alluvial backfill and riprap. At other bridges, the piers may rest directly on pilings that have been driven into the channel bottom. In these cases, the sediment is usually not cohesionless sand and gravel. Instead, the channel sediment may consist of cohesive soil, compacted sediments, cemented sediments, or a combination of these. The scour process will occur at a much slower rate in these sedi-

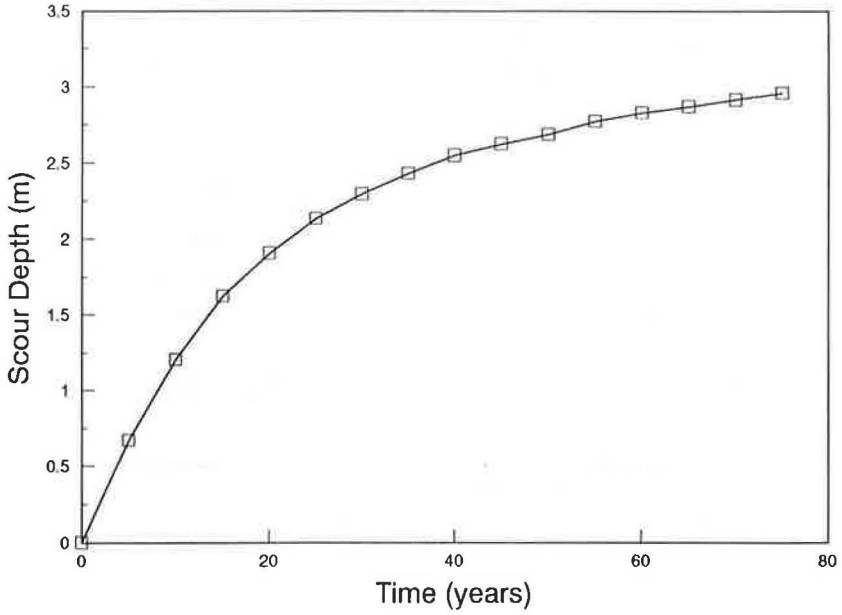

FIGURE 2 Scour depth as a function of time.

ments than in sand and gravel. Therefore, these models may provide a magnitude for the ultimate scour depth that can only be reached given an unreasonably long period of time. The time rate of scour must be studied for these cases.

DISCUSSION AND CONCLUSIONS

The purpose of this study was to develop a conceptual, time-dependent pier scour model. A time-dependent pier scour model was considered necessary for several reasons. First, bridge failures, such as the Schoharie Creek bridge, indicate that the magnitude, duration, and frequency of the flood flows determine the depth to which the scour hole develops during any one flood event. The peak flow rate may not be sustained for an adequate period of time to develop the scour hole to an ultimate depth; therefore, a number of storms may be required to scour the hole to its maximum depth. Second, the development of the time-dependent pier scour model provides a basis from which the probability of failure can be estimated over the design life of the bridge.

Input Requirements of the Model

The pier scour and risk-of-failure model developed here requires information that is generally available or that is routinely obtained for most bridge sites. The model requires the pier characteristics (pier width, shape, and length) and sediment characteristics (mean sediment size, sediment gradation, and friction velocity).

In addition to the pier and sediment characteristics, hydrologic data are required. If data from a gauged station nearby are available, a partial-duration series may be developed. If the design site is at an ungauged location, it is possible to develop a partial-duration series by estimating the appropriate parameter. Assuming an exponential distribution for the partial-duration series, only the exponential parameter and the mean number of storms, which is required for simulating the number of storms using a Poisson process, are required to simulate the hydrology.

Implications

The model developed here yields an estimate of the depth of scour for a period of time, such as the design life. Besides being used to estimate scour depth, the model may be used to determine the effects of various scour control improvements. In particular, riprap is commonly placed around the pier and within the excavation area of the pier to control scour. The model can be used to determine whether the riprap is of adequate size to remain within the excavation area over an extended period of time. This would simply entail entering the desired riprap size as the mean particle size (d_{50}) and determining the scour depth over the desired number of years on the basis of expected hydrologic conditions. If the scour depth is excessive or greater than some allowable value, then the particle size should be increased and the test rerun until an acceptable solution is found.

When designing a bridge pier, the engineer can use the model to evaluate various design alternatives as a function of parameters such as the size, shape, and depth of the pier. Having a better understanding of the effects of the various parameters on scour will enable the engineer to design safer piers.

The effect of changes in the upstream watershed on the scour depth may also be determined using the pier scour model. Upstream changes often affect the stream discharge; reflecting these changes in the hydrologic simulation will enable the engineer to determine the effect of the changes on the scour depth.

If a measured discharge record is used at a site, the history of the scour progression at a bridge site may also be simulated using this model. Estimates of the temporal variation of scour history may be desired for different reasons, including model calibration when measurements of the scour depth are made or legal cases involving bridge failure. Rather than a flood series simulation, the measured flood discharge record can be used. In this way, the temporal variation of scour for the historic record of discharges would be estimated. This may be important if measurements of scour have not been taken in the past, but the current scour depth estimation is desired for reasons of safety or recordkeeping.

The various components of the model may be easily modified as new developments are made through further research. As information is collected on erosion rates of compacted and cohesive channel materials, the erosion rate component can be modified to reflect these findings. The model will then provide a time-dependent scour estimate for a variety of materials.

REFERENCES

1. G. R. Hopkins, R. W. Vance, and B. Kasraie. *Scour Around Bridge Piers.* Report FHWA-RD-79-103. FHWA, U.S. Department of Transportation, 1980, 131 pp.
2. Y. M. Chiew. Local Scour at Bridge Piers. Report 355. School of Engineering, University of Auckland, New Zealand, 1984.
3. H. N. Breusers, G. Nicollet, and H. W. Shen. Local Scour Around Cylindrical Piers. Journal of Hydraulic Research, Vol. 15, No. 3, 1977, pp. 211–252.
4. H. H. Chang. *Fluvial Processes in River Engineering.* Wiley, New York, 1988, 432 pp.
5. E. V. Richardson, D. B. Simons, and P. Y. Julien. *Highways in the River Environment*, 2nd ed., FHWA, U.S. Department of Transportation, 1988.
6. H. W. Shen, V. R. Schneider, and S. Karake. Local Scour Around Bridge Piers. *Journal of the Hydraulics Division, ASCE*, Vol. 95, No. HY6, 1969, pp. 1919–1939.
7. B. W. Melville. Local Scour at Bridge Sites. Report 117. School of Engineering, University of Auckland, New Zealand, 1975.
8. Baker. Local Scour at Bridge Piers in Nonuniform Sediment. Report 402. School of Engineering, University of Auckland, New Zealand, 1986.
9. A. J. Raudkivi. Functional Trends of Scour at Bridge Piers. *Journal of Hydraulic Engineering, ASCE*, Vol. 112, No. 1, 1986, pp. 1–13.
10. P. A. Johnson. *The Probability of Bridge Failure Due to Pier Scour.* Ph.D. dissertation, University of Maryland, College Park, 1990, 231 pp.
11. C. M. White. Equilibrium of Grains on the Bed of a Stream. *Proc., Royal Society* (London), Series A, Vol. 174, 1940, p. 322.
12. F. M. Henderson. *Open Channel Flow.* Macmillan, New York, 1966, pp. 476–481.

13. R. Ariathurai and K. Arulanandan. Erosion Rates of Cohesive Soils. *Journal of the Hydraulics Division, ASCE*, Vol. 104, No. HY2, 1978, pp. 279–283.
14. Y. H. Chen and B. A. Anderson. *Development of a Methodology for Estimating Embankment Damage Due to Flood Overtopping.* Report FHWA-RD-86-126. FHWA, U.S. Department of Transportation, 1987.
15. L. J. Tison. Erosion Autour de Piles de Pont en Riviere. Annales des Travaux Publics de Belgique, Vol. 41, No. 6, pp. 813–871.
16. E. M. Laursen and A. Toch. Model Studies of Scour Around Bridge Piers and Abutments—Second Progress Report. *HRB, Proc.*, Vol. 31, 1956, pp. 82–87.
17. J. Chabert and P. Engeldinger. Etude des Affouillements Autour des Piles de Ponts. Lab. Nat. d'Hydr. Chatou, France, Oct. 1956.
18. E. M. Laursen. The Total Sediment Load of Streams. *Journal of the Hydraulics Division, ASCE*, No. HY1, 1958, pp. 1530–1536.
19. P. Todorovic. Stochastic Models of Floods. Water Resources Research, Vol. 14, No. 2, 1978, pp. 345–356.
20. C. Cunnane. A Note on the Poisson Assumption in Partial Duration Series Models. *Water Resources Research*, Vol. 15, No. 2, 1979, pp. 489–494.
21. M. North. Time-Dependent Stochastic Model of Floods. *Journal of the Hydraulics Division, ASCE*, Vol. 106, No. HY5, 1980, pp. 649–665.
22. J. F. Cruise and K. Arora. A Hydroclimatic Application Strategy for the Poisson Partial Duration Model. *Water Resources* Bulletin, Vol. 26, No. 3, 1990, pp. 431–442.

Publication of this paper sponsored by Committee on Hydrology, Hydraulics, and Water Quality.